NORTHWESTERN UNIVERSITY

Carbon Cycling of Glaciated Landscapes on Modern and Geologic Timescales: Investigation with Strontium and Carbon Isotope Geochemistry

A DISSERTATION

SUBMITTED TO THE GRADUATE SCHOOL

IN PARTIAL FULFILLMENT OF THE REQUIREMENTS

for the degree

DOCTOR OF PHILOSOPHY

Field of Earth and Planetary Sciences

By

M. Grace Andrews

EVANSTON, ILLINOIS

December 2017

Abstract

The studies presented in this dissertation combine radiogenic and stable strontium isotope ratios ($^{87}Sr/^{86}Sr$ and $\delta^{88/86}Sr$, respectively), radiogenic and stable carbon isotope ratios ($\Delta^{14}C$ and $\delta^{13}C$, respectively), and bulk ion geochemistry to trace the sources and cycling of C in three glaciated environments (New Zealand, Iceland, and Greenland). A primary focus is the characterization of chemical weathering, and the effect that weathering in these locations has on long-term atmospheric CO_2 concentrations and global climate. I also investigate biogeochemical cycling of major cations and C, both for the impact on dissolved chemical weathering products and on short-term C fluxes, the latter being relevant for anthropogenic climate change. One of the main tools used in these studies, namely $\delta^{88/86}Sr$ values, is a novel isotopic tracer. I developed a method for the measurement of $\delta^{88/86}Sr$ values by thermal ionization mass spectrometry. This method generates data with external error bars 50% less than many other methods, while using an order of magnitude less sample. Cumulatively, these studies provide critical new insight into the controls on $\delta^{88/86}Sr$ values at Earth's surface.

My research in Fiordland, New Zealand quantified the sources and controls on riverine cations using Sr isotopes and bulk ion geochemistry. Rivers have high $\delta^{88/86}Sr$ values relative to local bedrock, and may be accounted for by the preferential uptake of light Sr isotopes by plants. This was one of the first studies to demonstrate mass-dependent fractionation of Sr isotopes by plants, and proposes that $\delta^{88/86}Sr$ values could be used as a biogeochemical cycling tracer.

Furthermore, Sr isotopes and bulk ion geochemistry in Icelandic rivers indicate that solutes are largely controlled by the weathering of hydrothermal calcite. Glacial rivers have substantially higher quantities of calcite-derived cations, likely due to increased physical erosion. A model of the long-term carbon cycle that incorporates a subsurface silicate weathering flux

demonstrates that weathering of hydrothermal calcite will not result in long-term atmospheric CO_2 sequestration.

Additionally, I investigated subglacial discharge from the Russell Glacier, Greenland Ice Sheet with Sr isotopes and bulk ion geochemistry. Solute geochemistry is best explained by the preferential weathering of silicate minerals such as K-feldspar. This result is in contrast to the commonly held assumption that ice sheets largely weather carbonate and sulfide minerals. Ice sheets may therefore sequester more atmospheric CO_2 on long timescales than previously realized.

Finally, C isotopes and bulk ion geochemistry of subglacial discharge from the Russell Glacier, Greenland Ice Sheet reveal that dissolved C is sourced from supraglacial inputs (~50%), carbonate weathering (~20 – 40%), and respiration of organic matter by microbes (~10 – 30%). The amount of microbially-respired C varies across the melt season based on the input of young organic material from the supraglacial environment. The amount of young organic C transferred to the subglacial environment may increase in the future. This could drive an increase in dissolved CO_2, which may evade to the atmosphere and exacerbate climate change.

Acknowledgements

This dissertation reflects the hard work of countless people. I would like to thank, first and foremost, my advisor, Dr. Andrew Jacobson. Andy shared with me his tremendous scientific expertise, his professional experience and guidance, and his love of all things isotopic. I am deeply grateful for the opportunity to have worked and learned with him. Furthermore, I would like to thank the fellow members of the Jacobson Group: students, post-docs, and lab managers, past and present. It is only by acting and thinking as a team that great science gets done. In particular, however, I would like to thank Dr. Gregory Lehn, with whom I worked closely throughout my tenure at Northwestern. He was a mentor, a compatriot, and a friend, all in one.

I must also acknowledge the suite of other mentors and collaborators I have had over the years. Dr. Ethan Baxter, my undergraduate research advisor, got me hooked on isotope geochemistry a decade ago and has been a constant supporter of my career ever since. My Ph.D. committee members, Dr. Yarrow Axford and Dr. Steven Jacobsen, as well as the greater EPS faculty, have been incredible sources of advice, encouragement, and education. My scientific collaborators have enhanced and enriched my knowledge base and our publications, for which I thank them. The work presented in this thesis also could not have been done without the long days put in by my multiple field assistants and the efforts of the EPS Administrative Staff.

Finally, I would like to thank my friends in the EPS department. We spent many hours together in the department and in the pub, and I believe both were essential for the successful completion of my degree.

Dedication

This dissertation is dedicated to my beloved partner, Josh. As much as my soul is in these pages, he is here too. Josh has listened to me ramble endlessly about isotopes and carbon for over six years. He has shared the joy and excitement of scientific discovery with me, and has toasted each accepted manuscript. He was equally my support for the mundane and daily things. He cooked dinner for me when nights in the laboratory went too late, and he has sat through practice runs of every talk I have ever given. However, he was also subject to the hard parts of my Ph.D. He waited patiently for me to come home when fieldwork took me away for months at a time, and he wiped tears from my eyes when the stress became too much to bear. Now that I have finished my degree, he has moved to a different continent to allow me to keep pursuing my dreams. I am grateful for this opportunity to thank Josh, the love of my life, and the invisible force behind all of my work.

Table of Contents

List of Tables

List of Figures

Chapter 1

Introduction and Overview

1.1 Introduction

The carbon (C) cycle describes the processes by which C is exchanged between Earth's geologic, hydrologic, atmospheric, and biologic reservoirs. The processes which comprise the C cycle operate on different timescales, ranging from days to millions of years. Over geological timescales, the chemical weathering of continental silicate rocks controls atmospheric CO_2 levels (Berner et al., 1983). Silicate weathering transforms CO_2 to HCO_3^- while releasing dissolved cations, such as Ca^{2+} and Mg^{2+} to rivers. These solutes are transported to the ocean where calcium carbonate precipitation sequesters CO_2 (Berner et al., 1983). On human timescales, atmospheric CO_2 sequestration via chemical weathering is negligible. Rather, atmospheric CO_2 levels are in large part controlled by biological processes. Because atmospheric CO_2 concentrations regulate global temperatures via the greenhouse effect, quantifying silicate chemical weathering and its controls is critical for understanding how Earth became and remains habitable on geologic timescales, while identifying biogeochemical C cycle feedbacks and their controls is essential for assessing how the Earth may respond to anthropogenic climate change.

Much of this dissertation is dedicated to understanding the C cycle through radiogenic and stable strontium (Sr) isotope geochemistry. Sr is a tracer for Ca because Sr^{2+} readily substitutes for Ca^{2+} due to its identical charge and similar ionic radius. Ca is an essential nutrient for life, and the key cation released during silicate chemical weathering. As a proxy for Ca, the transformation of Sr across Earth's surface can therefore shed light on both biogeochemical cycling and chemical weathering.

Sr has four naturally occurring isotopes: ^{84}Sr, ^{86}Sr, ^{87}Sr, and ^{88}Sr. ^{87}Sr is radiogenic and produced by the β-decay of ^{87}Rb, which has a half-life of 48.8 Myr, while the remaining Sr isotopes are stable (Faure and Mensing, 2005). The radiogenic Sr isotope ratio ($^{87}Sr/^{86}Sr$) has been an essential tool in geology since the 1960's (e.g. Gast, 1960, Dasch 1969) and today, $^{87}Sr/^{86}Sr$ values can be readily measured to ±10 ppm (2σSD, this dissertation). In chemical weathering studies, $^{87}Sr/^{86}Sr$ ratios are used to fingerprint riverine Sr sources and quantify their relative contributions to the dissolved load. This is possible because primary geologic materials (e.g. silicate and carbonate minerals) have different $^{87}Sr/^{86}Sr$ ratios based on their initial Rb content and age, while secondary materials (e.g. dust, soil, rain) have unique $^{87}Sr/^{86}Sr$ ratios derived from the particular combination of primary sources that contribute to them (Banner, 2004).

Furthermore, advances in mass spectrometry have facilitated the recent development of the field of stable Sr isotope geochemistry, which has seen increasing scientific interest since its advent a decade ago (Fig. 1.1). This interest stems from the fact that unlike $^{87}Sr/^{86}Sr$ ratios, stable Sr isotope values (denoted as $\delta^{88/86}Sr$) preserve mass-dependent fractionation. At the onset of my PhD program (2012), a limited number of data suggested that certain low-temperature processes such as calcite precipitation and plant uptake of Sr could fractionate $\delta^{88/86}Sr$ values (de Souza et al., 2010; Krabbenhöft et al., 2010; Ohno and Hirata, 2007; Rüggeberg et al., 2008). $\delta^{88/86}Sr$ values were therefore envisioned as a novel 'process' tracer, capable of recording evidence for secondary mechanisms that impact the dissolved Sr load with the benefit of being directly paired to 'source' information gleaned from well-constrained $^{87}Sr/^{86}Sr$ ratios.

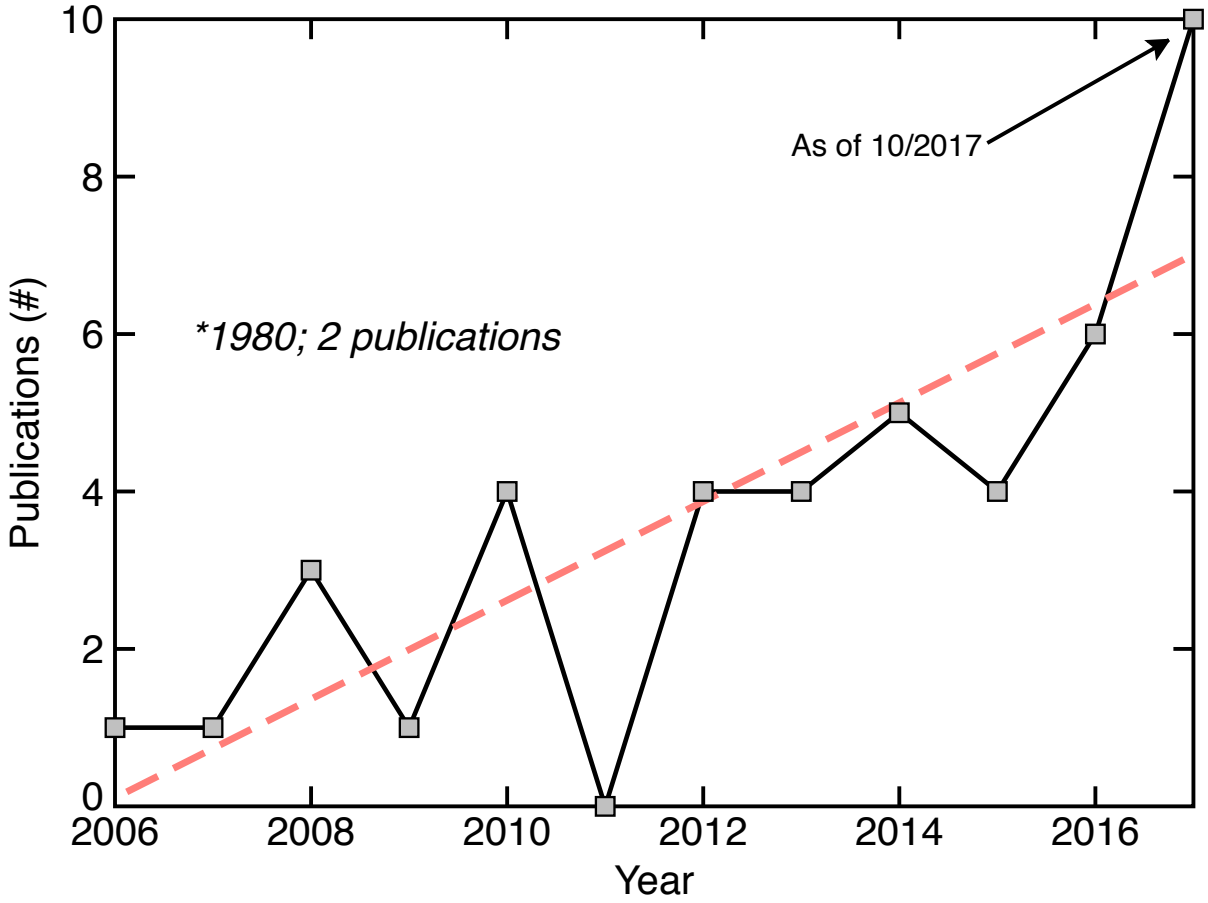

Figure 1.1. Number of papers reporting stable Sr isotope measurements ($\delta^{88/86}$Sr values) through time.

This dissertation embodies, to some degree, the rapid early evolution of the field of stable Sr isotope geochemistry. Ideas regarding which processes fractionate $\delta^{88/86}$Sr values, as well as the relative significance of these mechanisms in the natural world shift throughout the dissertation with key new findings from my own studies and the contemporaneous work of other researchers in the field. With the goal of better understanding both the short- and long-term C cycles, I present three studies that use Sr isotopes to investigate the sources of dissolved Sr, and controls on dissolved Sr concentrations, in rivers from glaciated terranes spanning New Zealand, Iceland, and Greenland. Appendix A summarizes the TIMS method for measurement of $\delta^{88/86}$Sr

values I developed, which generates data with external error bars of ±20 ppm (2σSD), 50% less than the TIMS methods published a decade ago (Krabbenhöft et al., 2009), while using an order of magnitude less sample. Additionally, I present a fourth companion study that uses C isotopes to investigate the sources of dissolved C, and controls on dissolved C concentrations, in Greenlandic rivers. Two of these studies are drawn from previously published works. Chapter 2 and Appendix A were published as Andrews et al. (2016), while Chapter 3 and Appendix B were published as Andrews and Jacobson (2017).

1.2 Chapter 2: Radiogenic and stable Sr isotope ratios ($^{87}Sr/^{86}Sr$, $\delta^{88/86}Sr$) as tracers of riverine cation sources and biogeochemical cycling in the Milford Sound region of Fiordland, New Zealand

This chapter reports radiogenic Sr isotope ratios ($^{87}Sr/^{86}Sr$), stable Sr isotope ratios ($\delta^{88/86}Sr$), and major ion concentrations for river, rock, sediment, soil, and plant samples collected from the Cleddau and Hollyford catchments in the Milford Sound region of Fiordland, New Zealand. The catchments primarily drain gabbro, but some tributaries access limestone and volcanogenic sediments. The goal of the study was to understand controls on riverine $\delta^{88/86}Sr$ values in a landscape with multiple factors that may influence chemical weathering, including dense vegetation, high rainfall, and abundant, freshly-eroded Holocene fluvio-glacial and landslide debris.

Rivers draining gabbro have higher $\delta^{88/86}Sr$ values than bedrock, by as much as ~0.14‰, and the $\delta^{88/86}Sr$ values strongly correlate with molar Ca/Sr ratios ($R^2 = 0.69$). Leaching of rocks and sediment reveals no evidence for the preferential dissolution of minerals having high $\delta^{88/86}Sr$ values and Ca/Sr ratios. In-stream Sr isotope fractionation seems unlikely because comparison

against $^{87}Sr/^{86}Sr$ and Ca/Sr ratios demonstrates that riverine $\delta^{88/86}Sr$ values conservatively trace water-mass mixing. The riverine data are best explained by the input of soil water, which is distinct from potential bedrock end-members (i.e., silicates and carbonates) based on $\delta^{88/86}Sr$ but indistinguishable in terms of Ca/Sr and $^{87}Sr/^{86}Sr$. While strontium isotope fractionation during secondary mineral formation and pedogenesis is possible, clay mineral formation is minor and most soils are poorly developed. Instead, soil water $\delta^{88/86}Sr$ values more likely reflect plant uptake. Plant samples yielded a wide range of $\delta^{88/86}Sr$ values, but on average, they are lower than those for bedrock, consistent with the expectation that plants preferentially incorporate lighter Sr isotopes. Mass-balance constraints, together with $^{87}Sr/^{86}Sr$ ratios, indicate that soil water $\delta^{88/86}Sr$ values are ~0.30‰ higher than bedrock $\delta^{88/86}Sr$ values, and mixing calculations show that the plant-fractionated soil water pool contributes ~27% of the riverine Sr. For tributaries accessing limestone and volcanogenic sediments, Ca/Sr and $^{87}Sr/^{86}Sr$ ratios appear consistent with two-component mixing between silicate and carbonate weathering, but $\delta^{88/86}Sr$ values reveal a third contribution from soil water inputs, similar to gabbro catchments.

The results of this study suggest that Sr isotopes behave conservatively during water mass mixing and stream transport but non-conservatively in soil, where plant uptake can elevate soil water $\delta^{88/86}Sr$ values relative to bedrock. Plant uptake, or related biogeochemical processes, such as ion-exchange on organic matter surfaces, also appear to modify soil water Ca/Sr ratios. Many studies use $^{87}Sr/^{86}Sr$ and Ca/Sr ratios to apportion riverine solutes between silicate and carbonate weathering, but Ca/Sr ratios may be non-conservative in densely vegetated areas. The stable Sr isotope tracer shows promise for resolving riverine cation sources, as well as effects from biological cycling.

1.3 Chapter 3: The radiogenic and stable Sr isotope geochemistry of basalt weathering in Iceland: Role of hydrothermal calcite and implications for long-term climate regulation

Several studies have examined the geochemistry of Icelandic rivers to quantify the relationship between basalt weathering and long-term climate regulation. Recent research has suggested that the chemical weathering of hydrothermal and metamorphic calcite contributes significant quantities of HCO_3^- to the Icelandic riverine flux (Jacobson et al., 2015). Because the HCO_3^- derives from volcanic CO_2 that was sequestered in mineral form prior to atmospheric injection, the strength of the basalt weathering feedback occurring in Iceland may be lower than previously realized. To test these hypotheses, we analyzed the radiogenic and stable Sr isotope composition ($^{87}Sr/^{86}Sr$ and $\delta^{88/86}Sr$) of the same suite of water, rock, and mineral samples as examined in Jacobson et al. (2015), and we developed a simple model of the long-term C cycle that considers the transformation of volcanic CO_2 to HCO_3^- during subsurface silicate weathering, which is a precursor to hydrothermal calcite formation.

Interpretations based on $^{87}Sr/^{86}Sr$ and Ca/Sr ratios suggest that conservative, three-component mixing between basalt, calcite, and atmospheric deposition adequately explains river geochemistry. On average, the $\delta^{88/86}Sr$ values of glacial and non-glacial rivers (0.414‰ and 0.388‰, respectively) are generally higher than those for basalt (0.276‰); however, calcite $\delta^{88/86}Sr$ values (0.347‰) are also higher than those for basalt and span the range of riverine values. Thus, riverine $\delta^{88/86}Sr$ values are also consistent three-component mixing between basalt, calcite, and atmospheric deposition. Isotopic fractionation is not required to explain riverine trends. Finally, model equations for the long-term C cycle demonstrate that subsurface silicate weathering reduces the magnitude of the volcanic CO_2 degassing flux, which in turn causes the atmosphere to stabilize at lower pCO_2 values compared to the case where no subsurface silicate

weathering occurs. However, the proportion of the net volcanic C flux introduced to the atmosphere-ocean system as HCO_3^- after subsurface silicate weathering does not regulate long-term climate. Because hydrothermal calcite simply sequesters some of this HCO_3^- and delays its transmission to the atmosphere-ocean system until it dissolves at the surface later in time, it can be concluded the weathering of hydrothermal calcite bearing non-atmospheric C also has no effect on long-term climate regulation. Icelandic riverine HCO_3^- fluxes should be corrected for the hydrothermal calcite weathering contribution prior to quantifying atmospheric CO_2 consumption rates by basalt weathering at the Earth's surface.

1.4 Chapter 4: Controls on the solute geochemistry of subglacial discharge from the Russell Glacier, Greenland Ice Sheet determined by radiogenic and stable Sr isotope ratios

During the 2014 and 2015 melt seasons, we used radiogenic and stable Sr isotope ratios ($^{87}Sr/^{86}Sr$ and $\delta^{88/86}Sr$) to examine controls on solute acquisition in subglacial discharge from the Russell Glacier, a land-terminating lobe of the Greenland Ice Sheet (GrIS) located in southwestern Greenland. Subglacial discharge $^{87}Sr/^{86}Sr$ ratios are higher than those for bedload and suspended sediment digests, but broadly similar to bedload sediment leachates. Complementary analyses of mineral separates suggest that the preferential dissolution of silicate minerals such as biotite, chlorite, K-feldspar, and/or hornblende could account for subglacial discharge $^{87}Sr/^{86}Sr$ ratios. On average, subglacial discharge $\delta^{88/86}Sr$ values are ~0.10‰ higher than those for bedload and suspended sediment digests, which are similar and yield a narrow range of $\delta^{88/86}Sr$ values. The sediment data suggest that isotopic fractionation during secondary mineral formation and adsorption cannot satisfactory explain the elevated subglacial discharge $\delta^{88/86}Sr$ values. Within a given rock, mineral separates display a wide range of $\delta^{88/86}Sr$ values

(~0.40‰). We find that preferential dissolution of K-feldspar, hornblende, apatite, and titanite could elevate subglacial discharge $\delta^{88/86}Sr$ values. Considering the radiogenic and stable Sr isotope data together, preferential weathering of both high $^{87}Sr/^{86}Sr$ and $\delta^{88/86}Sr$ value minerals, namely K-feldspar and hornblende, can fully account for the geochemistry of subglacial discharge.

Subglacial discharge from the Russell Glacier feeds the proglacial Akuliarusiarsuup Kuua River (AKR). Along a 32km transect of the AKR from the GrIS margin towards the coast, riverine $^{87}Sr/^{86}Sr$ ratios increase from ~0.722 to ~0.747 in a step-wise pattern. Increases in $^{87}Sr/^{86}Sr$ ratios correspond to known locations of other subglacial discharge inputs to the AKR, such that solute geochemistry appears to be controlled by mixing from point sources. Lengths of the downstream transect with no additional hydrological inputs have little variation in major cation concentrations or $^{87}Sr/^{86}Sr$ ratios. This suggests that proglacial chemical weathering is negligible and likely does not contribute significantly to GrIS carbon cycling on either short or long timescales.

In general, this study supports the recent contention that, in contrast to valley glaciers which are largely dominated by carbonate and sulfide weathering regardless of primary bedrock, GrIS subglacial discharge has a significant contribution of cations from silicate mineral weathering (Graly et al., 2016; Graly et al., 2014). The impact of glaciers and ice sheets on long-term global climate may therefore be different, and atmospheric CO_2 drawdown from ice sheet chemical weathering could be higher than previously realized.

1.5 Chapter 5: Linkages between the supraglacial and subglacial carbon cycles at the margin of the Greenland Ice Sheet

Melting of the Greenland Ice Sheet (GrIS) has accelerated in recent decades. Given the close association of the water and carbon (C) cycles, melting of the GrIS may also drive local and global C cycle feedbacks. However, few studies have quantified such feedbacks, which may have important implications for predicting future climate. Here, we investigated seasonal and interannual C cycling at the margin of the Russell Glacier, southwestern Greenland. By synthesizing isotopic analyses of water ($\delta^{18}O$) and C ($\delta^{13}C$ and $\Delta^{14}C$) with geomicrobiological observations, we present evidence for previously unknown connections between the GrIS's supra- and sub-glacial dissolved C cycles. Supraglacial streams have variable concentrations of dissolved organic carbon (DOC) and are the dominant source of DOC in subglacial discharge. Supraglacial stream dissolved inorganic carbon (DIC) concentrations are uniform and sourced from a spatially and temporally constant mixture of microbially-respired organic C (~25%) and atmospheric C (~75%). Microbial communities inhabiting supraglacial streams are primarily photosynthentic organisms and aerobic heterotrophs, consistent with DIC sources. Supraglacial inputs account for ~40 – 50% of subglacial DIC. The remaining subglacial DIC derives from carbonate weathering and microbial CO_2 production, with the latter source attributable to abundant anaerobic heterotrophs and hydrogen-oxidizing lithotrophic communities observed in subglacial discharge. Furthermore, we find that supraglacial streams deliver young DOC to the subglacial environment during snowmelt and periodic rain events. These short-lived pulses of organic C may drive heterotrophic microbial respiration, with the cumulative effect being a seasonal shift in the source of basal DIC, from microbial- to carbonate-dominated.

Chapter 2

Radiogenic and stable Sr isotope ratios ($^{87}Sr/^{86}Sr$, $\delta^{88/86}Sr$) as tracers of riverine cation sources and biogeochemical cycling in the Milford Sound region of Fiordland, New Zealand

2.1 Introduction

Radiogenic Sr isotope ratios ($^{87}Sr/^{86}Sr$) are widely used to trace the sources and cycling of Sr at scales ranging from soils to entire watersheds (Banner, 2004; Blum et al., 2002; Capo et al., 1998; Drouet et al., 2005; Jacobson et al., 2002; Palmer and Edmond, 1992; Pett-Ridge et al., 2009; Probst et al., 2000). The relative proportions of exchangeable or dissolved Sr originating from different end-members, such as silicate or carbonate bedrock, atmospheric deposition, and anthropogenic inputs, are often assessed using $^{87}Sr/^{86}Sr$ and Ca/Sr ratios (Belanger et al., 2012; Blum et al., 2002; Jacobson and Blum, 2000; Pett-Ridge et al., 2009; Pierson-Wickmann et al., 2009). This approach assumes conservative behavior, which is reasonable because the instrumental analysis of $^{87}Sr/^{86}Sr$ ratios inherently eliminates any mass-dependent Sr isotope fractionation that might occur in nature (Faure and Mensing, 2005), and other than a few notable exceptions, such as plant uptake (Bullen and Bailey, 2005; Drouet and Herbauts, 2008; Pett-Ridge et al., 2009; Poszwa et al., 2000) and zeolite ion-exchange (e.g., Fridriksson et al., 2009), most biogeochemical processes do not strongly discriminate Ca from Sr. However, with recent advances in mass-spectrometry, small variations in stable Sr isotope abundances (reported as $\delta^{88/86}Sr$) can be precisely quantified (Fietzke and Eisenhauer, 2006, Ohno and Hirata, 2006; Krabbenhoft et al., 2009, Ma et al., 2013, and Neymark et al., 2014) and are increasingly being exploited to gain further insight into the Sr cycle and its primary controls (Böhm et al., 2012; Charlier et al., 2012; de Souza et al., 2010; Fietzke and Eisenhauer, 2006; Halicz et al., 2008;

Krabbenhoft et al., 2010; Krabbenhöft et al., 2009; Ma et al., 2013; Moynier et al., 2010; Neymark et al., 2014; Ohno and Hirata, 2006; Ohno et al., 2008; Pearce et al., 2015b; Raddatz et al., 2013; Rüggeberg et al., 2008; Stevenson et al., 2014; Vollstaedt et al., 2014; Wei et al., 2013).

To date, $\delta^{88/86}$Sr values reported for terrestrial rocks vary by ~0.60‰ (Charlier et al., 2012; Ma et al., 2013) and terrestrial materials of all forms, including rocks, waters, and plants, show >2.0‰ of variation (Neymark et al., 2014). Multiple processes can fractionate Sr isotopes, including plant uptake (de Souza et al., 2010), carbonate precipitation (Böhm et al., 2012; Fietzke and Eisenhauer, 2006; Stevenson et al., 2014) and potentially, mineral dissolution and clay formation (Halicz et al., 2008; Pearce et al., 2015b; Wei et al., 2013). Analysis of $\delta^{88/86}$Sr values can complement traditional $^{87}Sr/^{86}Sr$ ratios by tracing both sources and processes, but this attribute also highlights important challenges. Because $\delta^{88/86}$Sr values can reflect multicomponent mixing, fractionation, or some combination of the two, it is necessary to identify mechanisms that elicit conservative or non-conservative isotopic behavior and to further constrain the spatial scales over which such mechanisms operate.

To improve understanding of the stable Sr isotope tracer, we analyzed $^{87}Sr/^{86}Sr$ ratios, $\delta^{88/86}$Sr values, and major ion concentrations for river, rock, sediment, soil, and plant samples collected from the Milford Sound region of Fiordland, New Zealand. We selected this study site for several reasons. Fiordland is largely underlain by mafic bedrock, which is thought to significantly influence the marine Sr cycle (Allegre et al., 2010) and long-term global climate (Dessert et al., 2003) when it chemically weathers. Fiordland also reflects a unique confluence of physical and biological factors that affect and promote chemical weathering. In particular, the area is recently glaciated, receives very high rainfall, and supports a dense rainforest. Finally,

Fiordland is exceptionally pristine and little is known about the geochemistry of its rivers. We investigate factors that control $\delta^{88/86}Sr$ variability at scales spanning individual soil profiles to entire catchments. We also present a new double-spike TIMS method for measuring $\delta^{88/86}Sr$ values.

2.2 Geologic and Climatic Setting

Fiordland, located on the southwest coast of the South Island, New Zealand (Fig. 2.1), contains an extensive network of steep-sided fiords produced by glacial erosion. This study focused on the Cleddau and Hollyford River catchments of the Darren Mountains within the Milford Sound region. Steep-sided (>45°) valleys extend from sea level to over 2000 m where remnants of cirque glaciers persist from more extensive late Pleistocene and Holocene glaciation. The mean annual temperature is cool (~10.4 ºC) , and rainfall rates are extremely high, between 6000 and 9000 mm/year (NIWA, 2012). Rivers and stream levels can rise meters within hours during the ~weekly heavy rainfall events, and the upper reaches of both studied catchments are frequently swept by ice, snow, and rock avalanches. The lower slopes support a dense, temperate rainforest populated by beech and podocarp trees, as well as wide variety of ferns and shrubs. Above ~1000 m, shrublands give way to widespread bare rock exposures. Thin layers of highly lithic soil, peat, and forest litter cover alluvium and colluvium in low elevation areas, where vegetation has become established on Holocene sediments. Soil horizon distinctions, apart from a surface organic-rich layer, are poorly developed and mainly reflect differences in the grain size of lithic debris.

The Cleddau River (CR) is underlain by the ~138 Myr Darren Leucogabbro (Muir et al., 1998; Turnbull, 2000) and drains northwest from Gertrudes Saddle to the Tasman Sea. The

Darren Leucogabbro consists of plagioclase (80%, An_{40-45}), pyroxene (14%), biotite (5%), magnetite (1%), and trace amounts of quartz and K-feldspar (Blattner, 1978). To the west, gabbro grades into hornblende diorite comprising plagioclase (72%, An_{43}), actinolite (12%), biotite (8%), hornblende (5%), and quartz (3%) (Blattner, 1978). However, this transition occurs gradually, at the individual outcrop scale, and gabbro remains abundant throughout the western margin of the study site. The CR catchment experiences a mean annual rainfall of 8400 mm/yr (NIWA, 2012).

The Hollyford River drains eastward from Gertrudes Saddle and in this study, is further subdivided into the Upper and Lower Hollyford River (UHR and LHR, respectively), based on predominant bedrock lithologies. The UHR primarily drains the Darren Leucogabbro, as well a minor component of the Mistake Diorite (~226Ma), before it transitions to the LHR (Blattner, 1978; Muir et al., 1998). The UHR catchment has a mean annual rainfall of 7800mm/yr (NIWA, 2012). The LHR drains a more complex basement geology. Tributaries on the western side of the LHR drain the Darren Leucogabbro, with minor contributions from the Mistake Diorite and volcanogenic metasediments belonging to the Permian Mantle Volcanics Formation (Turnbull, 2000 and references therein) . Tributaries on the eastern side of the LHR drain a suite of Permo-Triassic terranes dominated by calcalkaline volcanogenic metasediments, with minor limestone and mafic metavolcanic units (Bishop et al., 1976; Kawachi, 1974; Turnbull, 2000 and references therein). These rocks have undergone low-grade metamorphism (sub-greenschist facies) and contain metamorphic calcite, laumontite, prehnite, pumpellyite, and/or epidote. Known outcrops of the metamorphosed limestone strike north to northeastwards in the vicinity of sampling sites W12 and W31 (Fig. 2.1). Collectively, LHR tributaries that drain volcanic and

sedimentary rocks are referred to as LHR-VS. The entire LHR catchment experiences a mean annual rainfall of 6300 mm/yr (NIWA, 2012).

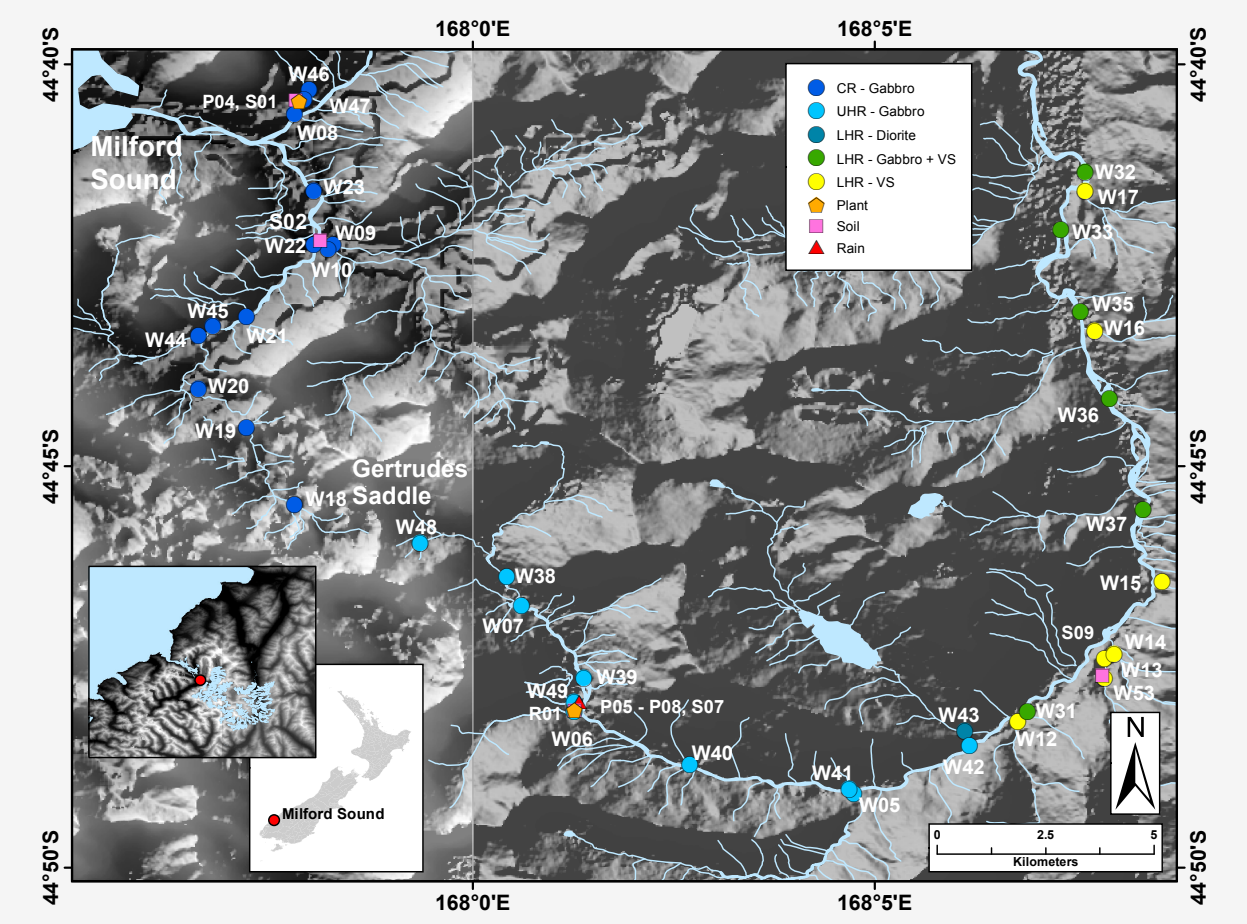

Figure 2.1. Sample location map. River water (W) samples are designated based on their catchment and bedrock, where CR = Cleddau River catchment, UHR = Upper Hollyford River catchment, LHR = Lower Hollyford River catchment, and VS = volcanic and sedimentary rock. Additionally, R = rain, S = soil, and P = plant.

2.3 Methods

2.3.1 Sample collection and field methods

River water samples (n = 37) were collected in February 2012 (Fig. 2.1). The main river stem, major and minor tributaries, as well as small overland rivulets and waterfalls, were

sampled in each catchment, when possible. Sample locations were documented with a Garmin 60CSx handheld GPS meter. River temperature and pH were measured on-site using a Mettler SevenGo Pro pH portable meter equipped with a temperature probe and a glass-body Orion 8104BNUWP Ross Ultra combination pH electrode. The electrode was calibrated daily with pH 4, 7, and 10 buffers. River water samples for the analysis of cation and Si concentrations, as well as Sr isotope ratios, were passed through 0.45µm filter capsules (Versapor membrane), collected in I-CHEM HDPE bottles, and acidified to pH <2 using concentrated, ultrapure HNO_3. River water samples for the analysis of anions and total alkalinity were passed through 0.45µm filter capsules (Versapor membrane) and collected in LDPE sample bottles. One rainwater sample was collected in an I-CHEM HDPE bottle using an HDPE funnel. The sample was filtered in the laboratory using a 0.45µm polypropylene syringe filter (Whatman Puradisc) and acidified to pH <2 using concentrated, ultrapure HNO_3. River water samples for dissolved organic carbon (DOC) concentrations were passed through 0.45µm filter capsules (Supor membrane), collected in amber, borosilicate glass vials, and acidified with ultrapure HCl to pH < 2 within 12 hours. However, results are not reported because DOC concentrations for most samples were below detection (< 0.5mg/L). Total carbonate alkalinity ($A_T = [HCO_3^-]+ 2[CO_3^{2-}]$) in µeq/L was measured by Gran Titration with standardized 0.02N HCl within 12 hours of sample collection. Given the pH range of the samples, combined with the lack of appreciable DOC, $A_T \approx [HCO_3^-]$. The uncertainty of the method was better than ±3%, as determined by repeated titrations of a gravimetrically prepared Na_2CO_3 standard. Sediment and rock samples were collected in LDPE bags. Soil samples were collected from the well-vegetated rainforest floor within the CR and the LHR-VS catchments, as well as from a grassy bank in a shrubland clearing immediately above the active river flood level beside the UHR. This latter site is in an extremely dynamic river

setting, and the vegetation represents the early colonization of a young (~hundreds of years), disturbed, fluvial sedimentary setting. Soil pits were excavated, and samples were collected from the pit walls and placed in LDPE bags. O, A, B, and C horizon samples were collected from the CR catchment, and O and A horizon samples were collected from the LHR-VS catchment. The UHR soil lacked a discernable O horizon, so the A horizon was sampled at the surface and at depth. Vegetation samples were clipped from live specimens and placed into LDPE sample bags. Tree fern foliage was collected from the same site as soil sample S01, and fern and grass foliage were collected from the same site as soil sample S07 (Fig. 2.1).

2.3.2 Sample preparation

A saw was used to remove weathering rinds from rock samples and cut the inner portion into cubes. A hammer was used to break the cubes into chips. Subsamples of the chips (~25 g) were powdered in a shatterbox equipped with tungsten carbide grinding container. Sediments were dried in an oven at 50 ºC, sieved to the <2 mm fraction, and subsamples (~10g) were powdered in a shatterbox, also equipped with a tungsten carbide grinding container. The carbonate and silicate fractions of the powdered rock and sediment samples were isolated using a sequential leaching and digestion procedure (Moore et al., 2013). To isolate the carbonate fraction, subsamples of the <2 mm fraction (~1.0 g) were reacted with 4M acetic acid and stirred on a rocker table for 6 – 8 hr. The mixtures were centrifuged, and the supernatants were passed through 0.45 μm polypropylene syringe filters (Whatman Puradisc) and collected in Teflon beakers. To confirm complete reaction of the carbonate fraction, the procedure was repeated two to three times until the leachates reached a constant pH value. For each sample, the filtered supernatants were combined, dried, and re-dissolved in 5% HNO_3. The remaining residues,

assumed to represent the silicate fraction, were dried in an oven, and ~0.1 g subsamples were reacted in a 5:3 mixture of concentrated HF and HNO_3 at 140°C, dried, refluxed in concentrated HNO_3, dried, refluxed in 6N HCl, dried, and finally, re-dissolved in 5% HNO_3. Soil samples were dried in an oven at 50 ºC and sieved to the <2 mm fraction using a nylon mesh. To isolate the exchangeable fraction, subsamples of the <2 mm fraction (~1.0 g) were reacted with 10 mL of 1M ammonium chloride (NH_4Cl), adjusted to pH = 8. The mixtures were stirred on a rocker table for 6 hr. After centrifugation, the supernatants where passed through 0.45 µm polypropylene syringe filters (Whatman Puradisc), dried, and re-dissolved in 5% HNO_3. Grass samples were dried in an oven at 50 ºC and completely digested in concentrated HNO_3. Solutions were dried, re-dissolved in 5% HNO_3, placed in a UV box until clear, and passed through 0.45 µm polypropylene syringe filters (Whatman Puradisc).

2.3.3 Elemental concentrations

Concentrations of cations and Si in river water samples, rainwater, leachates, and digestions where measured in the Aqueous Geochemistry Laboratory at Northwestern University using a Thermo-Fisher iCAP 6500 inductively coupled plasma-optical emission spectrometer (ICP-OES). NIST 1643e was repeatedly analyzed to monitor accuracy and overall data quality. Results were within ±10% of reported concentrations. Anion concentrations in river water samples were measured with a Dionex DX-120 ion chromatograph equipped with an AS15 anion-exchange column and an ASRS-300 self-regenerating suppressor. Repeated analyses of a NIST-traceable Dionex standard were within ±10% of reported concentrations. The charge balance error [CBE = $(TZ^+ - TZ^-)/(TZ^+ + TZ^-)$, where TZ^+ is the sum of cations and TZ^- is the sum of anions, in eq/L] was calculated for all river water samples. The average CBE for river

water samples is -2.56%. Saturation states with respect to calcite ($\log\Omega_{cal}$) were calculated with PHREEQC, implemented with the llnl.dat thermodynamic database (Parkhurst and Appelo, 1999), major ion concentrations, and field parameters (T, pH, and A_T).

2.3.4 Radiogenic and stable Sr isotope ratios ($^{87}Sr/^{86}Sr$ and $^{88}Sr/^{86}Sr$)

Radiogenic and stable Sr isotope ratios ($^{87}Sr/^{86}Sr$ and $^{88}Sr/^{86}Sr$) were measured in the Radiogenic Isotope Geochemistry Laboratory at Northwestern University using a Thermo-Scientific Triton Thermal Ionization Mass Spectrometer (TIMS). All procedures employed ultrapure reagents. According to an ^{84}Sr isotope dilution method, column blanks contained ~30 pg Sr (n = 13), and total procedural blanks contained ~100 pg Sr (n = 4). These levels are negligible by comparison to the amounts of sample Sr analyzed (see below). Similarly, during the analysis of $^{87}Sr/^{86}Sr$ and $^{88}Sr/^{86}Sr$ ratios, the ^{85}Rb ion beam was monitored to ensure that ^{87}Rb did not isobarically interfere with ^{87}Sr. No interferences were observed.

For the determination of $^{87}Sr/^{86}Sr$ ratios, sample aliquots containing 100 ng of Sr were dried, re-dissolved in 8M HNO_3, and eluted through inverted pipette tips packed with Eichrom Sr-Spec resin. The purified Sr fractions were dried, re-dissolved in 1.5 μL of 3N HNO_3, and loaded onto single, outgassed Re filament assemblies with 1 μL of either a Ta_2O_5 or $TaCl_5$ solution. Ion beams were collected in multi-dynamic mode. To correct for instrumental mass fractionation, the $^{86}Sr/^{88}Sr$ ratio was normalized to 0.1194 using an exponential law. Multi-dynamic mode was used because $^{87}Sr/^{86}Sr$ ratios measured in static mode began drifting soon after the TIMS was employed for stable Ca isotope research (e.g., Lehn et al., 2013). Figure A1 displays NBS 987 $^{87}Sr/^{86}Sr$ ratios collected between 2011 and 2014. Prior to analysis of Ca isotope ratios, NBS 987 $^{87}Sr/^{86}Sr$ ratios determined in static mode showed no evidence for drift.

Implantation of Ca ions into the graphite collectors appears to reduce their efficiency (Holmden and Belanger, 2010; Lehn et al., 2013). The multi-dynamic mode eliminates drift by cancelling cup efficiency factors, but drift can still be monitored because the method inherently includes isotope ratios determined in static mode (e.g., Chu et al., 2011). As shown in Figure A1, while $^{87}Sr/^{86}Sr$ ratios measured in static mode continued to drift, $^{87}Sr/^{86}Sr$ ratios collected in multi-dynamic mode remained constant. During the period of study, repeated analyses of NBS 987 yielded a mean $^{87}Sr/^{86}Sr$ ratio of 0.710251 ± 0.000010 ($\pm 2\sigma_{SD}$, n = 39). The current long-term, mean $^{87}Sr/^{86}Sr$ ratio is 0.710252 ± 0.000011 ($\pm 2\sigma_{SD}$, n = 94).

An ^{87}Sr-^{84}Sr double-spike method was used to measure $^{88}Sr/^{86}Sr$ ratios. The method was optimized according to the Monte Carlo error model presented in Lehn et al. (2013). Appendix A presents details of the data reduction procedure and optimization. The data reduction procedure accounts for abundance variations of ^{87}Sr. Sample aliquots containing 450 ng of Sr were weighed into acid-cleaned Teflon vials and spiked. The vials were capped and heated at ~90°C overnight to ensure complete sample-spike equilibration. The solutions were dried, re-dissolved in 8N HNO_3, and purified using the same elution procedure described above. After drying, the purified Sr fractions were re-dissolved in 4.5μL of 3N HNO_3. Approximately 150 – 300 ng of Sr was loaded onto outgassed, single Re filament assemblies with 1 μL of a $TaCl_5$ solution; however, for these measurements, the samples were loaded between parafilm "dams," which prevent spreading on the surface of the filament and may help minimize so-called "filament reservoir effects" (Lehn and Jacobson, 2015a; Lehn et al., 2013). In the mass spectrometer, a 6V ^{88}Sr ion beam was attained, and $^{88}Sr/^{84}Sr$, $^{87}Sr/^{84}Sr$, and $^{86}Sr/^{84}Sr$ ratios were measured in static mode for a total of 140 duty cycles, each having a 16 sec integration time. The total analysis time, including filament warm-up, is ~1 hr per sample. Runs were monitored to ensure a steady or

increasing ^{88}Sr beam, an increasing raw $^{86}Sr/^{84}Sr$ fractionation pattern, and the absence of filament reservoir effects, which can manifest as apparent "reverse-fractionation" in uncorrected ratios or trends in fractionation-corrected $^{88}Sr/^{86}Sr$ ratios (Lehn and Jacobson, 2015a). All sample (smp) $^{88}Sr/^{86}Sr$ ratios are reported in delta notation (per mil) relative to NBS 987, where $\delta^{88/86}Sr$ (in ‰) = $[(^{88}Sr/^{86}Sr)_{smp}/(^{88}Sr/^{86}Sr)_{NBS\text{-}987}-1]\times 1000$.

Drift also affects measurement of $\delta^{88/86}Sr$ values (e.g., Krabbenhoft et al., 2009) , and as shown in Figure A2, $\delta^{88/86}Sr$ values for NBS 987 changed through time. While multi-dynamic collection can eliminate cup efficiency factors when analyzing $^{87}Sr/^{86}Sr$ ratios, it cannot be used when analyzing $\delta^{88/86}Sr$ values. Therefore, an offset was applied to each measurement in a session, which in turn, was defined as 40 or fewer runs, including both samples and standards. Similar to the approach adopted for the determination of $\delta^{44/40}Ca$ values (e.g., Hindshaw et al., 2011, Lehn et al., 2013), the session offset was calculated as the difference between the mean $\delta^{88/86}Sr$ value of 6 – 8 NBS 987 runs and the "true" NBS 987 $\delta^{88/86}Sr$ value, which is simply 0‰. To confirm the accuracy of the drift correction, 2 – 4 IAPSO seawater standards were analyzed during each session.

Measured internal precisions ($2\sigma_{SEM}$) for samples and standards range from 0.007 – 0.011‰. After correcting for drift, NBS 987 yielded $\delta^{88/86}Sr = 0.000 \pm 0.004$‰ ($2\sigma_{SEM}$, n = 77, Fig. A3), and IAPSO seawater yielded $\delta^{88/86}Sr = 0.396 \pm 0.005$‰ ($2\sigma_{SEM}$, n = 54, Fig. A4). In addition, four USGS rock standards (AGV-1, BIR-1, BHVO-1, and G-2) were analyzed (Table 2.1). AGV-1 yielded $\delta^{88/86}Sr = 0.300 \pm 0.004$‰ ($2\sigma_{SEM}$, n = 6), BIR-1 yielded $\delta^{88/86}Sr = 0.299 \pm 0.008$‰ ($2\sigma_{SEM}$, n = 6), BHVO-1 yielded $\delta^{88/86}Sr = 0.267 \pm 0.008$‰ ($2\sigma_{SEM}$, n = 12), and G-2 yielded $\delta^{88/86}Sr = 0.335 \pm 0.003$‰ ($2\sigma_{SEM}$, n = 8). These results agree well with previously

published values (Charlier et al., 2012; Ma et al., 2013; Moynier et al., 2010). The standard data correspond to a global, external reproducibility of ±0.020‰ ($2\sigma_{SD}$), which is the uncertainty assigned to samples.

Table 2.1. Sr standard data

Standard	$\delta^{88/86}$Sr (‰)	2σSD (‰)	2σSEM (‰)	*n*	$^{87}Sr/^{86}Sr$
NBS 987	0.000	0.018	0.004	77	0.71025
IAPSO	0.396	0.020	0.005	54	0.70918
AGV-1	0.300	0.009	0.004	6	0.70404
BIR-1	0.299	0.020	0.008	6	0.70314
BHVO-1	0.267	0.024	0.008	12	0.70349
G-2	0.335	0.007	0.003	8	0.70977

2.3.5 Correction for atmospheric inputs in river samples

River solute concentrations were corrected for atmospheric inputs using Eq. (2.1):

$$[i]^{*}_{riv} = [i]_{riv} - [\mathrm{Cl}]_{riv} \times \left(\frac{i}{\mathrm{Cl}}\right)_{rain} \tag{2.1}$$

where $[i]_{riv}^{*}$ is the concentration of element *i* in river water, corrected for atmospheric inputs (μmol/L), $[i]_{riv}$ is the measured concentration of *i* in river water (μmol/L), $[\mathrm{Cl}]_{riv}$ is the measured concentration of Cl in river water (μmol/L), and $(i/\mathrm{Cl})_{rain}$ is the molar ratio of element *i* to Cl in rainwater. The $(i/\mathrm{Cl})_{rain}$ ratio was calculated using rainwater sample R01. This approach assumes that Cl in river water is derived solely from atmospheric inputs. This assumption is reasonable because neither evaporites nor hot springs exist in the area. The element Sr was below detection

limit (< 1 ppb) in sample R01. Therefore, Sr concentrations in river water were not corrected for atmospheric inputs.

2.4 Results

2.4.1 Sr isotope and Ca/Sr geochemistry of rocks, sediments, soils, and plants

Table 2.2 reports elemental concentrations, molar Ca/Sr ratios, $^{87}Sr/^{86}Sr$ ratios, and $\delta^{88/86}Sr$ values for rocks, sediments, soils, and plants. Leachates of rocks and sediments from the CR and UHR catchments have, on average, an $^{87}Sr/^{86}Sr$ ratio of 0.70470 ± 0.00080 ($\pm 1\sigma_{SD,}$ n = 6), a Ca/Sr ratio of 0.33 ± 0.10 μmol/nmol ($\pm 1\sigma_{SD,}$ n = 24), and a $\delta^{88/86}Sr$ value of 0.267 ± 0.087‰ ($\pm 1\sigma_{SD,}$ n = 6). The corresponding digests of the silicate residues yield an average $^{87}Sr/^{86}Sr$ ratio of 0.70394 ± 0.00016 ($\pm 1\sigma_{SD,}$ n = 6), a Ca/Sr ratio of 0.19 ± 0.02 μmol/nmol ($\pm 1\sigma_{SD,}$ n = 24), and a $\delta^{88/86}Sr$ of 0.265 ± 0.052‰ ($\pm 1\sigma_{SD,}$ n = 6). The $^{87}Sr/^{86}Sr$ ratios measured for the Darren Leucogabbro are similar to results reported elsewhere (Blattner and Graham, 2000).

Relative to the rock and sediment digests, soil exchangeable fractions in the CR and UHR catchments have a high $^{87}Sr/^{86}Sr$ ratio of 0.70626 ± 0.00045 ($\pm 1\sigma_{SD,}$ n = 3) but a comparable Ca/Sr ratio of 0.15 ± 0.02 μmol/nmol ($\pm 1\sigma_{SD,}$ n = 3). Also relative to the rock and sediment digests, A horizon exchangeable fractions from a grass covered soil in the UHR catchment have a low $\delta^{88/86}Sr$ value of 0.223 ± 0.023‰ ($\pm 1\sigma_{SD,}$ n = 2), while the O horizon from one forest floor soil in the CR catchment has a relatively high $\delta^{88/86}Sr$ value of 0.369‰. The average plant $^{87}Sr/^{86}Sr$ ratio of 0.70642 ± 0.00097 ($\pm 1\sigma_{SD,}$ n = 5) is higher than that for rock and sediment digests but similar to that for the soil exchangeable fractions. Relative to the rock and sediment

digests, as well as the soil exchangeable fractions, plants have a high Ca/Sr ratio of 0.42 ± 0.17 μmol/nmol ($\pm 1\sigma_{SD,}$ n = 5) and a low $\delta^{88/86}$Sr value of 0.196 ± 0.234‰ ($\pm 1\sigma_{SD,}$ n = 5).

Leachates of rocks and sediment from LHR-VS catchments have, on average, an $^{87}Sr/^{86}Sr$ ratio of 0.70754 ± 0.00051 ($\pm 1\sigma_{SD,}$ n = 3), a Ca/Sr ratio of 0.97 ± 0.59 μmol/nmol ($\pm 1\sigma_{SD,}$ n = 7), and a $\delta^{88/86}$Sr value of 0.261 ± 0.023‰ ($\pm 1\sigma_{SD,}$ n = 3). Digests of the corresponding silicate residues yielded an average $^{87}Sr/^{86}Sr$ ratio of 0.70582 ± 0.00074 ($\pm 1\sigma_{SD,}$ n = 3), a Ca/Sr ratio of 0.25 ± 0.05 μmol/nmol ($\pm 1\sigma_{SD,}$ n = 7), and a $\delta^{88/86}$Sr value of 0.260 ± 0.025‰ ($\pm 1\sigma_{SD,}$ n = 3). The O horizon exchangeable fraction from one forest floor soil has an $^{87}Sr/^{86}Sr$ ratio of 0.70580, a Ca/Sr ratio of 0.13 μmol/nmol, and a $\delta^{88/86}$Sr value of 0.308‰.

Table 2.2. Elemental and Sr isotope geochemistry of sediment and rock leachates and digests, soils, and plants

Sample	Sample Type	Fraction	Al (µmol/g)	Ba (nmol/g)	Ca (µmol/g)	Fe (µmol/g)	K (µmol/g)	Mg (µmol/g)	Na (µmol/g)	Si (µmol/g)	Sr (nmol/g)	Ca/Sr (µmol/nmol)	$^{87}Sr/^{86}Sr$	$\delta^{88/86}Sr$ (‰)
Sediments														
Cleddau catchment														
FLNZ12 W08	gabbro	Leachate	28.3	86.8	19.6	20.8	7.8	21.6	6.2	17.6	49.8	0.39	nd	nd
		Digest	2801.4	2457.7	1229.4	1147.3	211.6	1106.9	1098.7	3.0	7455.9	0.16	nd	nd
FLNZ12 W09	gabbro	Leachate	20.7	72.2	12.7	16.4	6.0	14.6	4.1	14.3	31.5	0.40	nd	nd
		Digest	2784.4	2900.7	1152.4	1075.5	282.5	1020.1	1169.0	bdl	6715.6	0.17	nd	nd
FLNZ12 W10	gabbro	Leachate	10.3	50.6	8.8	7.9	3.8	5.5	2.0	5.9	23.0	0.38	0.70574	0.307
		Digest	2774.7	2015.9	1451.0	1255.5	187.3	1344.9	1015.6	1.3	7304.3	0.20	0.70402	0.285
FLNZ12 W46	gabbro	Leachate	18.6	92.9	19.2	10.1	5.3	11.2	5.0	14.3	43.4	0.44	nd	nd
		Digest	2710.7	1701.2	1447.1	1453.4	118.0	1481.9	1011.6	bdl	7047.8	0.21	nd	nd
FLNZ12 W47	gabbro	Leachate	23.8	79.9	17.8	11.3	2.0	9.5	5.1	12.1	59.7	0.30	0.70432	0.310
		Digest	3073.3	648.2	1813.3	1404.5	37.8	1608.6	814.9	4.3	9784.3	0.19	0.70375	0.289
FLNZ12 W18	gabbro	Leachate	37.4	34.0	24.6	9.7	1.7	14.2	7.5	23.0	107.5	0.23	nd	nd
		Digest	3290.8	790.5	1829.3	1158.3	56.6	1555.4	994.0	2.4	10021.1	0.18	nd	nd
FLNZ12 W19	gabbro	Leachate	41.1	25.0	30.3	10.5	0.8	11.8	6.7	25.6	127.9	0.24	nd	nd
		Digest	3116.7	649.3	1854.8	1354.6	37.0	1603.1	839.8	10.0	9775.0	0.19	nd	nd
FLNZ12 W20	gabbro	Leachate	23.6	20.6	18.1	8.7	0.6	8.6	3.9	19.5	77.8	0.23	nd	nd
		Digest	3087.7	672.5	1806.8	1307.7	41.5	1608.6	851.1	5.7	9769.2	0.18	nd	nd
FLNZ12 W21	gabbro	Leachate	20.8	53.9	18.0	9.4	3.2	10.8	3.9	17.5	60.0	0.30	nd	nd
		Digest	2821.5	868.5	1693.3	1573.7	84.9	1790.3	870.3	4.1	7921.1	0.21	nd	nd
FLNZ12 W22	gabbro	Leachate	14.6	51.2	14.3	6.7	2.4	6.3	2.4	10.7	41.9	0.34	0.70440	0.334
		Digest	2970.7	1755.4	1564.5	1296.4	127.3	1534.0	1016.3	bdl	7491.4	0.21	0.70390	0.265
FLNZ12 W23	gabbro	Leachate	19.0	68.1	13.6	13.5	4.9	12.0	3.7	13.8	36.5	0.37	nd	nd
		Digest	265.7	204.7	125.5	143.8	18.3	120.8	99.8	0.4	678.5	0.18	nd	nd
FLNZ12 W44	gabbro	Leachate	17.2	97.8	16.4	10.3	6.7	10.1	3.9	12.4	36.7	0.45	nd	nd
		Digest	2903.4	1781.0	1420.7	1285.3	185.9	1372.1	1096.7	1.2	7175.0	0.20	nd	nd

FLNZ12 W45	gabbro	Leachate	25.7	46.9	20.9	10.2	2.8	11.0	4.9	15.9	78.4	0.27	nd	nd
		Digest	3145.3	1151.8	1764.9	1302.2	75.1	1671.9	957.3	4.2	9279.7	0.19	nd	nd
UHR catchment														
FLNZ12 W05	diorite/gabbro	Leachate	nd	nd	nd	nd	nd	nd	nd	nd	nd	nd	nd	nd
		Digest	nd	nd	nd	nd	nd	nd	nd	nd	nd	nd	nd	nd
FLNZ12 W06	gabbro	Leachate	17.4	108.7	19.1	9.8	6.9	9.5	4.0	14.5	51.8	0.37	nd	nd
		Digest	2987.1	2014.0	1354.7	1025.1	161.4	1192.4	1196.1	2.2	7629.0	0.18	nd	nd
FLNZ12 W07	gabbro	Leachate	20.8	51.7	15.6	8.7	1.9	10.0	2.1	20.1	56.0	0.28	nd	nd
		Digest	3094.6	1490.7	1474.3	1023.2	86.8	1360.3	1147.4	2.0	8744.5	0.17	nd	nd
FLNZ12 W49	gabbro	Leachate	17.5	94.6	18.8	10.3	5.9	12.6	3.6	16.3	52.4	0.36	nd	nd
		Digest	2612.9	1747.9	1361.1	1213.5	132.8	1402.6	1016.1	4.7	6594.4	0.21	nd	nd
FLNZ12 W48	gabbro	Leachate	69.6	32.1	39.4	14.2	1.4	19.3	5.0	83.0	139.9	0.28	nd	nd
		Digest	2943.5	873.4	1786.2	1392.9	46.0	1811.6	898.0	1.3	8739.9	0.20	nd	nd
FLNZ12 W38	gabbro	Leachate	25.6	58.2	18.4	9.9	3.4	11.9	3.9	18.7	59.1	0.31	nd	nd
		Digest	3036.5	1335.3	1654.9	1235.5	89.2	1542.5	1021.6	5.9	8534.0	0.19	nd	nd
FLNZ12 W39	gabbro	Leachate	20.4	70.2	16.9	9.1	6.4	11.6	4.6	18.4	52.3	0.32	nd	nd
		Digest	2921.9	2453.7	1114.3	816.9	229.5	901.3	1239.9	3.0	7086.9	0.16	nd	nd
FLNZ12 W40	gabbro	Leachate	31.1	88.1	22.8	16.2	6.2	30.4	5.5	35.6	104.1	0.22	nd	nd
		Digest	3120.8	1930.9	1351.3	955.0	165.4	1291.2	1159.2	1.5	7944.3	0.17	nd	nd
FLNZ12 W41	gabbro	Leachate	105.9	114.2	58.1	104.1	11.6	271.3	14.0	106.7	287.4	0.20	0.70424	0.316
		Digest	2570.7	1095.4	1503.6	1283.5	78.2	2049.2	695.7	9.3	6861.8	0.22	0.70398	0.306
FLNZ12 W42	gabbro	Leachate	17.5	27.0	10.9	13.7	2.3	28.4	2.1	30.5	39.8	0.27	nd	nd
		Digest	2661.2	1359.1	1391.3	1239.1	129.4	1797.0	881.3	4.9	6300.6	0.22	nd	nd
LHR catchment														
FLNZ12 W43	diorite	Leachate	27.9	68.9	16.3	15.0	8.0	8.8	6.9	12.3	39.9	0.41	nd	nd
		Digest	2883.3	3498.6	722.3	821.4	451.7	372.2	1480.0	bdl	5507.3	0.13	nd	nd
FLNZ12 W12	volc/sed	Leachate	45.4	39.3	30.7	32.9	2.6	26.3	4.1	20.4	53.6	0.57	nd	nd
		Digest	2744.6	943.9	900.2	1145.8	203.3	1003.6	1014.4	0.9	3977.7	0.23	nd	nd
FLNZ12 W13	volc/sed	Leachate	19.9	80.5	652.3	13.4	4.7	11.8	2.6	10.3	292.1	2.23	0.70695	0.271
		Digest	2174.0	1730.7	447.4	605.3	283.7	489.4	1133.4	bdl	2743.2	0.16	0.70665	0.245

FLNZ12 W14	volc/sed	Leachate	20.4	126.7	25.5	13.6	6.5	13.6	2.8	13.1	31.2	0.82	nd	nd
		Digest	2686.4	2176.3	759.0	938.0	431.0	832.4	1033.0	bdl	3040.2	0.25	nd	nd
FLNZ12 W15	volc/sed	Leachate	22.9	67.7	21.3	17.3	5.0	19.4	2.3	15.0	32.3	0.66	0.70782	0.235
		Digest	2784.6	1735.5	1061.0	1144.3	331.0	1001.8	1009.6	1.9	4061.4	0.26	0.70523	0.246
FLNZ12 W16	volc/sed	Leachate	14.5	71.8	202.5	29.9	2.9	197.8	1.2	16.4	174.6	1.16	nd	nd
		Digest	1451.1	1358.3	265.0	777.1	230.6	4062.6	606.8	0.2	767.5	0.35	nd	nd
FLNZ12 W17	volc/sed	Leachate	29.1	90.1	29.0	27.0	5.4	82.3	3.1	20.9	45.9	0.63	0.70784	0.277
		Digest	2502.4	1608.0	617.7	896.9	287.8	1919.0	867.4	0.2	2269.6	0.27	0.70559	0.289
FLNZ12 W53	volc/sed	Leachate	64.2	41.9	27.1	12.8	1.8	8.7	2.4	15.8	36.4	0.74	nd	nd
		Digest	2665.9	1161.3	983.5	981.6	158.7	842.7	887.4	2.2	4232.4	0.23	nd	nd
FLNZ12 W31	gabbro/volc/sed	Leachate	40.3	53.4	26.4	27.8	4.4	41.1	4.2	60.7	86.3	0.31	nd	nd
		Digest	2997.2	1472.3	1354.2	1169.7	155.2	1443.2	1032.0	2.2	7322.2	0.18	nd	nd
FLNZ12 W32	gabbro/volc/sed	Leachate	17.3	66.1	20.5	16.0	2.4	55.3	1.4	16.8	35.8	0.57	nd	nd
		Digest	2314.6	1540.9	710.5	898.0	227.1	2402.8	844.7	3.6	3202.1	0.22	nd	nd
FLNZ12 W33	gabbro/volc/sed	Leachate	22.2	58.0	20.1	23.1	4.4	56.6	2.8	31.2	46.3	0.43	nd	nd
		Digest	2495.9	1194.0	1225.1	1340.6	164.9	1942.9	865.3	2.1	5279.1	0.23	nd	nd
FLNZ12 W35	gabbro/volc/sed	Leachate	31.2	72.8	47.4	31.3	5.8	114.6	3.6	25.3	76.5	0.62	nd	nd
		Digest	2547.8	1555.1	1079.3	1053.6	193.7	1873.9	946.5	bdl	4686.8	0.23	nd	nd
FLNZ12 W36	gabbro/volc/sed	Leachate	34.4	68.5	23.5	30.9	5.6	58.4	4.2	50.2	60.1	0.39	nd	nd
		Digest	2567.6	1318.5	1303.5	1494.3	177.0	1591.2	855.6	bdl	5284.7	0.25	nd	nd
FLNZ12 W37	gabbro/volc/sed	Leachate	23.4	58.0	26.9	13.8	3.4	19.0	3.2	20.2	52.7	0.51	nd	nd
		Digest	2801.1	1377.5	1270.0	1119.3	201.2	1200.8	974.7	bdl	5256.6	0.24	nd	nd
Whole Rocks														
Cleddau catchment														
FLNZ12 W22	gabbro	Leachate	60.7	445.7	41.9	47.8	50.3	46.5	13.4	71.0	87.6	0.67	0.70565	0.104
		Digest	2930.7	3121.1	1155.8	1118.2	344.1	1121.6	1282.2	0.3	6543.9	0.18	0.70419	0.284
FLNZ12 W47	gabbro	Leachate	47.4	46.4	43.4	17.0	1.8	20.4	18.7	39.2	135.3	0.32	0.70384	0.233
		Digest	3412.7	831.5	1565.8	1076.9	45.9	1220.8	1342.7	4.5	10040.2	0.16	0.70380	0.162
LHR catchment														
FLNZ12 W17	sandstone	Leachate	102.2	58.5	25.7	79.5	10.9	61.8	6.0	63.7	15.8	1.63	nd	nd

		Digest	3211.4	1918.7	603.1	1467.3	325.8	1056.0	994.6	1.6	1909.8	0.32	nd	nd
FLNZ12 W17	siltstone	Leachate	74.1	207.9	563.1	46.0	33.6	29.1	10.3	48.6	1220.6	0.46	nd	nd
		Digest	2101.8	3521.3	242.9	476.1	518.7	352.6	959.1	0.3	1013.7	0.24	nd	nd
Soils														
Cleddau catchment														
FLNZ12 $S01_O$	0-15cm, forest	Exchangable	bdl	11.6	1.7	bdl	6.6	5.5	3.9	1.0	12.1	0.14	0.70597	0.369
FLNZ12 $S02_A$	0-39cm, forest	Exchangable	0.5	2.2	bdl	bdl	6.6	1.2	2.8	0.2	1.9	nd	nd	nd
FLNZ12 $S02_B$	39-75cm, forest	Exchangable	0.7	bdl	bdl	bdl	0.5	bdl	0.6	0.1	bdl	nd	nd	nd
FLNZ12 $S02_C$	75cm+, forest	Exchangable	1.0	15.8	bdl	bdl	bdl	bdl	0.2	0.3	1.8	nd	nd	nd
UHR catchment														
FLNZ12 $S07_{A\text{-}surface}$	3-8cm, grassy	Exchangable	1.7	126.1	4.0	bdl	2.0	0.9	0.6	13.0	21.8	0.18	0.70677	0.207
FLNZ12 $S07_{A\text{-}deep}$	20-29cm, grassy	Exchangable	1.1	58.1	1.5	bdl	0.4	0.2	0.4	0.1	10.4	0.14	0.70603	0.239
LHR catchment														
FLNZ12 $S09_O$	0-14cm, forest	Exchangable	bdl	18.0	5.0	bdl	9.1	5.7	5.1	1.6	38.2	0.13	0.70580	0.308
FLNZ12 $S09_A$	14cm+, forest	Exchangable	0.7	3.9	bdl	bdl	0.5	bdl	0.6	0.4	bdl	nd	nd	nd
Plants														
Cleddau catchment														
FLNZ12 P04	fern tree leaf	n/a	1.2	547.9	100.9	bdl	204.7	126.5	61.9	54.1	690.1	0.15	0.70646	0.251
UHR catchment														
FLNZ12 P05	fern bush leaves	n/a	11.4	117.9	39.2	bdl	460.7	77.8	3.7	-0.1	67.9	0.58	0.70529	-0.011
FLNZ12 P06	grass leaves	n/a	bdl	105.8	26.2	bdl	492.0	21.8	11.3	0.0	58.0	0.45	0.70595	0.198
FLNZ12 P07	grass leaves	n/a	bdl	332.0	54.9	bdl	307.5	55.0	0.6	45.4	145.2	0.38	0.70650	-0.015
FLNZ12 P08	grass leaves	n/a	bdl	79.8	51.0	bdl	334.9	30.5	0.7	43.1	92.0	0.55	0.70792	0.554

volc = volcanic and sed = sedimentary

nd indicates not collected or not measured, bdl indicates below detection limit, n/a indicates not applicable.

2.4.2 Major ion, Sr isotope, and Ca/Sr geochemistry of givers

Table 2.3 reports elemental concentrations, molar Ca*/Sr ratios, saturation states with respect to calcite ($\log\Omega_{cal}$), $^{87}Sr/^{86}Sr$ ratios, and $\delta^{88/86}Sr$ values for river water samples. Figures 2.2A and B plot relative abundances of major cations and anions (in equivalents) for Fiordland rivers, prior to correction for atmospheric inputs. The CR and UHR catchments draining the Darren Leucogabbro have similar average major cation and Si concentrations. On a molar basis, Si dominates (~40%), followed by Ca and Na (~25%, each) and Mg and K (<10%, each). In the LHR and the LHR-VS catchments Ca dominates (~55%), followed by Si (~25%), Na (~15%) and Mg and K (< 10%, each). The CR and UHR catchments also have similar anion concentrations. On a molar basis, HCO_3 dominates (~60%), followed by SO_4 (~30%) and Cl (~10%). In the LHR and LHR-VS catchments, HCO_3 dominates (~85%), followed by SO_4 (~10%) and Cl (~5%).

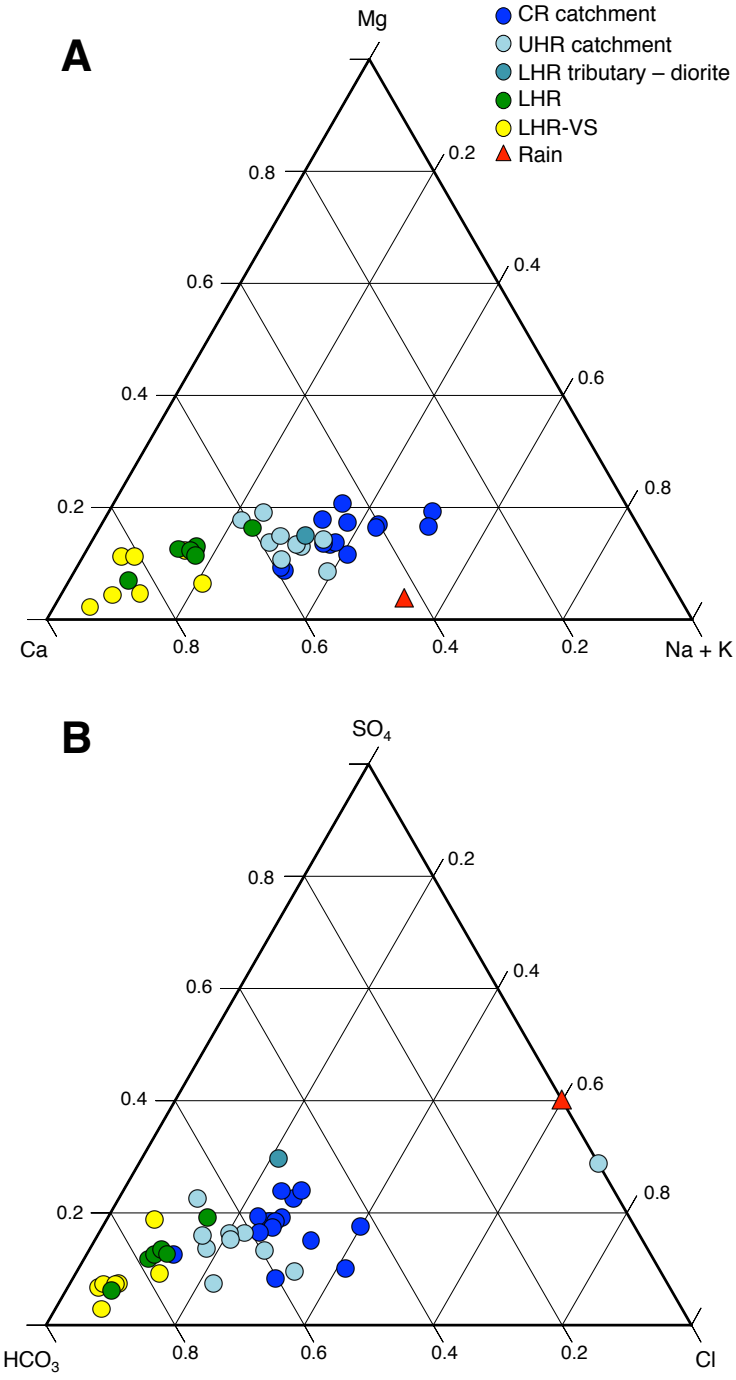

Figure 2.2. Major A) cation and B) anion composition (in equivalents) for rivers draining the Milford Sound region. Also shown is the composition of rainwater (R01). CR = Cleddau River, UHR = Upper Hollyford River, LHR= Lower Hollyford River, LHR-VS = Lower Hollyford tributaries draining volcanic and sedimentary rock. Cation and anion concentrations are not corrected for atmospheric deposition.

The Fiordland rivers and streams analyzed in this study are very dilute, and much of the major cation load appears to originate from atmospheric deposition. On average, atmospheric deposition contributed ~100% of the K. Atmospheric deposition also contributed relatively high amounts of Ca, Na, Mg, and SO_4 to the CR catchment (21, 11, 6, and 92%, respectively), the UHR catchment (16, 14, 7, and 86%, respectively), the LHR (5, 11, 3, and 61%, respectively) and the LHR-VS catchments (3, 10, 4, and 73%, respectively). All rivers are undersaturated with respect to calcite, with the exception of one LHR-VS tributary (W13), which appears at or near equilibrium. This latter tributary drains an area with limestone outcrops. Rivers draining silicate bedrock are significantly more undersaturated with respect to calcite than rivers draining sedimentary bedrock.

The CR catchment has, on average, a $^{87}Sr/^{86}Sr$ ratio of 0.70448 ± 0.00037 ($\pm 1\sigma_{SD,}$ n = 13), a Ca*/Sr ratio of 0.22 ± 0.09 μmol/nmol ($\pm 1\sigma_{SD,}$ n = 13), and a $\delta^{88/86}Sr$ value of 0.354 ± 0.018‰ ($\pm 1\sigma_{SD,}$ n = 11). The UHR catchment yielded an average $^{87}Sr/^{86}Sr$ ratio of 0.70450 ± 0.00021 ($\pm 1\sigma_{SD,}$ n = 10), a Ca*/Sr ratio of 0.34 ± 0.14 μmol/nmol ($\pm 1\sigma_{SD,}$ n = 10), and a $\delta^{88/86}Sr$ value of 0.392 ± 0.018‰ ($\pm 1\sigma_{SD,}$ n = 6). We note that the CR and UHR catchments have higher Ca*/Sr ratios and $\delta^{88/86}Sr$ values than the rock and sediment digests. The LHR has an $^{87}Sr/^{86}Sr$ ratio of 0.70567 ± 0.00041 ($\pm 1\sigma_{SD,}$ n = 6), a Ca*/Sr ratio of 0.87 ± 0.51 μmol/nmol ($\pm 1\sigma_{SD,}$ n = 6), and a $\delta^{88/86}Sr$ of 0.360 ± 0.027‰ ($\pm 1\sigma_{SD,}$ n = 6). LHR-VS catchments have an $^{87}Sr/^{86}Sr$ ratio of 0.70684 ± 0.00036 ($\pm 1\sigma_{SD,}$ n = 7), a Ca*/Sr ratio of 0.98 ± 0.34 μmol/nmol ($\pm 1\sigma_{SD,}$ n = 7), and a $\delta^{88/86}Sr$ value of 0.328 ± 0.041‰ ($\pm 1\sigma_{SD,}$ n = 7). Relative to sediment digests and leachates, LHR-VS catchments have intermediate $^{87}Sr/^{86}Sr$ and Ca*/Sr ratios but higher $\delta^{88/86}Sr$ values.

Table 2.3 Elemental, saturation state, and Sr isotope geochemistry of Fiordland rivers and rain sample

Sample	Bedrock; Sample Type	Latitude	Longitude	T (°C)	pH	Ca (μmol/L)	K (μmol/L)	Mg (μmol/L)	Na (μmol/L)	Si (μmol/L)	Sr (nmol/L)	SO_4 (μmol/L)	Cl (μmol/L)	HCO_3 (μmol/L)	Ca*/Sr (μmol/nmol)	$log\Omega_{cal}$	$^{87}Sr/^{86}Sr$	$\delta^{88/86}Sr$ (‰)
Cleddau catchment																		
FLNZ12 W08	gabbro, tributary	-44.67777	167.96317	9.6	6.96	27.9	6.5	10.3	32.6	41.7	60.5	11.0	31.0	61.9	0.38	-3.92	0.70477	nd
FLNZ12 W09	gabbro, tributary	-44.70410	167.97102	9.9	6.68	24.0	4.2	11.3	34.5	44.3	44.5	11.3	30.9	68.3	0.43	-4.22	0.70515	nd
FLNZ12 W10	gabbro, tributary	-44.70477	167.96995	10.7	6.95	25.2	5.2	10.6	48.6	52.2	70.8	9.1	40.3	61.9	0.27	-3.96	0.70484	0.355
FLNZ12 W46	gabbro, rivulet	-44.67218	167.96645	12.6	6.06	21.6	7.7	13.7	63.3	86.2	95.9	6.6	49.8	95.9	0.15	-4.69	0.70480	0.370
FLNZ12 W47	gabbro, rivulet	-44.67437	167.96530	12.1	6.67	25.7	3.9	13.1	76.3	105.9	158.6	7.5	60.9	71.5	0.10	-4.15	0.70446	0.326
FLNZ12 W18	gabbro, main stem	-44.75822	167.96377	7.4	6.27	19.3	1.6	4.7	31.5	35.8	94.7	7.1	32.1	34.2	0.15	-5.06	0.70412	0.340
FLNZ12 W19	gabbro, main stem	-44.74180	167.95333	8.8	6.94	35.7	1.3	5.3	38.1	53.6	175.8	11.9	33.9	71.2	0.17	-3.79	0.70394	0.330
FLNZ12 W20	gabbro, main stem	-44.73387	167.94275	9.4	6.95	38.1	1.0	6.0	39.8	57.2	187.2	11.2	33.8	72.1	0.18	-3.73	0.70394	0.337
FLNZ12 W21	gabbro, main stem	-44.71933	167.95282	10.5	7.05	34.3	6.0	9.3	45.8	55.9	146.1	15.1	36.1	89.5	0.20	-3.57	0.70426	0.360
FLNZ12 W22	gabbro, main stem	-44.70455	167.96797	12.7	6.99	33.0	5.3	9.4	46.6	56.2	139.2	15.8	37.8	70.3	0.20	-3.71	0.70429	0.376
FLNZ12 W23	gabbro, main stem	-44.69260	167.96675	13.1	7.07	28.9	5.4	11.2	43.7	53.8	90.2	12.6	37.6	89.4	0.26	-3.58	0.70458	0.358
FLNZ12 W44	gabbro, main stem	-44.72312	167.94285	9.1	7.02	25.7	8.3	10.4	45.7	50.6	100.4	15.6	35.8	63.0	0.20	-3.90	0.70473	0.363
FLNZ12 W45	gabbro, main stem	-44.72129	167.94562	10.5	7.03	36.8	6.2	10.0	46.7	56.9	147.2	18.0	36.8	77.4	0.21	-3.62	0.70431	0.377
UHR catchment																		
FLNZ12 W05	diorite/gabbro, tributary	-44.81757	168.07918	10	7.14	77.6	6.7	13.7	30.1	60.6	105.0	25.8	28.0	149.2	0.70	-2.92	0.70472	0.376
FLNZ12 W06	gabbro, tributary	-44.80138	168.02067	7.1	6.88	27.0	5.7	4.9	23.2	35.3	58.2	8.8	24.1	65.5	0.40	-4.03	0.70473	0.425
FLNZ12 W07	gabbro, tributary	-44.77932	168.00977	6.6	6.71	30.6	5.0	7.3	32.3	52.3	97.0	4.7	32.9	55.5	0.26	-4.22	0.70429	0.381
FLNZ12 W49	gabbro, tributary	-44.79906	168.02098	8.4	7.07	43.8	8.7	10.3	32.8	62.0	124.4	13.8	34.1	106.7	0.31	-3.40	0.70440	0.384
FLNZ12 W48	gabbro, waterfall	-44.76590	167.98908	18.5	6.44	5.0	0.5	0.8	7.0	5.0	9.1	3.1	15.5	bdl	0.28	nd	0.70492	nd
FLNZ12 W38	gabbro, main stem	-44.77265	168.00683	14.7	6.58	25.7	4.7	7.3	32.1	57.2	99.3	5.0	29.3	92.7	0.21	-4.08	0.70443	nd
FLNZ12 W39	gabbro, main stem	-44.79409	168.02235	13.1	6.61	32.7	6.1	8.0	32.1	55.6	105.0	8.8	35.9	78.6	0.26	-4.04	0.70436	nd
FLNZ12 W40	gabbro, main stem	-44.81238	168.04457	12.2	6.63	39.1	7.5	10.3	32.4	59.6	116.4	11.8	32.3	98.6	0.29	-3.86	0.70441	nd
FLNZ12 W41	gabbro, main stem	-44.81737	168.07808	8.3	7.44	48.1	8.2	16.2	32.6	67.4	137.0	12.9	33.6	128.1	0.31	-2.92	0.70434	0.387
FLNZ12 W42	gabbro, main stem	-44.80807	168.10268	9	7.44	58.3	7.7	17.0	33.1	67.8	133.5	16.4	33.6	139.6	0.40	-2.79	0.70442	0.402
LHR catchment																		
FLNZ12 W43	diorite, tributary	-44.80503	168.10217	9.4	7.19	36.8	9.1	10.6	36.5	62.8	78.7	21.7	30.7	71.5	0.41	-3.51	0.70603	nd
FLNZ12 W12	volc/sed, tributary (LHR-VS)	-44.80413	168.11234	8.7	7.69	220.7	2.9	37.6	89.9	150.5	162.1	58.8	45.3	458.1	1.32	-1.48	0.70673	0.280
FLNZ12 W13	volc/sed, tributary (LHR-VS)	-44.78977	168.13123	12.6	8.4	579.1	5.9	14.3	63.7	59.9	453.1	40.8	56.6	1068.0	1.26	0.05	0.70705	0.293
FLNZ12 W14	volc/sed, tributary (LHR-VS)	-44.78872	168.13293	12	7.73	215.0	5.7	12.1	57.0	50.5	231.7	20.3	40.0	459.8	0.90	-1.39	0.70671	0.351
FLNZ12 W15	volc/sed, tributary (LHR-VS)	-44.77403	168.14315	9.6	7.41	100.7	5.9	8.8	52.1	64.3	269.3	13.5	38.1	229.1	0.35	-2.36	0.70669	0.309

FLNZ12 W16	volc/sed, tributary (LHR-VS)	-44.72160	168.12880	14.1	8.08	534.4	9.7	72.4	66.7	71.7	692.8	46.6	65.3	1104.0	0.76	-0.27	0.70623	0.402
FLNZ12 W17	volc/sed, tributary (LHR-VS)	-44.69307	168.12658	15.3	8.4	309.9	4.0	43.2	56.5	53.2	280.8	27.4	52.6	641.9	1.07	-0.38	0.70719	0.334
FLNZ12 W53	volc/sed, rivulet (LHR-VS)	-44.79357	168.13132	11.9	7.7	431.9	4.2	21.8	74.1	86.1	352.7	14.4	71.6	907.8	1.19	-0.85	0.70727	0.331
FLNZ12 W31	gabbro/volc/sed, main stem	-44.80098	168.11528	9	7.3	56.8	8.0	15.5	36.9	69.4	116.4	20.5	32.8	139.4	0.44	-2.94	0.70494	0.371
FLNZ12 W32	gabbro/volc/sed, main stem	-44.69184	168.12737	11.1	7.67	142.3	9.3	24.4	45.4	70.1	171.2	23.9	40.6	316.8	0.80	-1.80	0.70607	0.324
FLNZ12 W33	gabbro/volc/sed, main stem	-44.70083	168.12238	10.6	7.47	109.2	9.0	20.2	42.7	72.0	146.1	21.9	36.8	267.6	0.71	-2.19	0.70565	0.353
FLNZ12 W35	gabbro/volc/sed, main stem	-44.71820	168.12622	11.6	7.73	114.9	9.2	19.8	42.4	71.0	154.1	23.9	38.9	266.0	0.71	-1.89	0.70569	0.357
FLNZ12 W36	gabbro/volc/sed, main stem	-44.73562	168.13190	12.2	7.93	104.9	8.8	16.8	42.1	70.9	141.5	20.1	39.1	237.3	0.70	-1.77	0.70562	0.351
FLNZ12 W37	gabbro/volc/sed, main stem	-44.75915	168.13893	13	7.04	318.6	10.3	26.6	59.2	93.7	164.3	22.0	49.2	611.1	1.89	-1.78	0.70604	0.405
Rain																		
FLNZ12 R01	n/a, UHR catchment	-44.79924	168.02202	nd	nd	2.0	3.4	0.2	1.7	0.2	bdl	4.5	13.2	nd	nd	nd	nd	nd

*Corrected for atmospheric inputs. See section 3.5.

volc = volcanic and sed = sedimentary

nd indicates not collected or not measured, bdl indicates below detection limit, n/a indicates not applicable

2.5 Discussion

2.5.1 The LHR catchment

The LHR provides a simplified setting to evaluate source tracing with $^{87}Sr/^{86}Sr$ ratios and $\delta^{88/86}Sr$ values because LHR water derives from the gabbro-draining UHR, which flows into the LHR, and the LHR-VS catchments on the eastern side of the river, which drain volcanic and sedimentary rocks. The LHR also receives water from gabbro-draining tributaries on the western side of the river. We were unable to sample these tributaries, but we can assume they have similar geochemistry to the UHR. Figures 2.3A and B plot riverine $^{87}Sr/^{86}Sr$ ratios and $\delta^{88/86}Sr$ values versus Ca*/Sr ratios, while Figure 2.3C shows $\delta^{88/86}Sr$ values versus $^{87}Sr/^{86}Sr$ ratios. The figures also include two-component mixing lines connecting the average values for the UHR and LHR-VS riverine end-members. The mixing lines show theoretical percentages of Sr derived from the two end-members. The percentages were calculated using the following standard two-component mixing equations:

$$\left(\mathrm{Ca^*/Sr}\right)_M = f_{UHR}\left(\mathrm{Ca^*/Sr}\right)_{UHR} + \left(1 - f_{UHR}\right)\left(\mathrm{Ca^*/Sr}\right)_{LHR-VST} \tag{2.2}$$

$$R_M = f_{UHR}R_{UHR} + \left(1 - f_{UHR}\right)R_{LHR-VST} \tag{2.3}$$

where M denotes the mixture, in this case, the LHR, f_{UHR} is the mole fraction of Sr from the UHR, and R symbolizes either $^{87}Sr/^{86}Sr$ or $\delta^{88/86}Sr$. The LHR-VS samples display considerable scatter, which is not surprising given the complex lithology of this area. Nonetheless, the LHR samples show similar patterns in both diagrams. Although one sample (W37) has an unusually high Ca*/Sr ratio, the others appear consistent with simple two-component mixing, with several

samples clustering at or near the 50% mark. To examine the patterns in slightly more quantitative terms, we orthogonally extrapolated measured LHR data points to their nearest position on the mixing lines (Jacobson et al., 2015; Moore et al., 2013). The results are illustrated in Figures 2.3A, B, and C. Results for both isotope tracers indicate that LHR-VS catchments contribute ~60% of the Sr in the LHR, while the gabbro-draining UHR, and presumably other gabbro-draining tributaries, provide the remaining 40%. We therefore conclude that $\delta^{88/86}$Sr values conservatively trace water-mass mixing, which implies that Sr isotope fractionation during in-stream transport is either negligible or nonexistent in this setting.

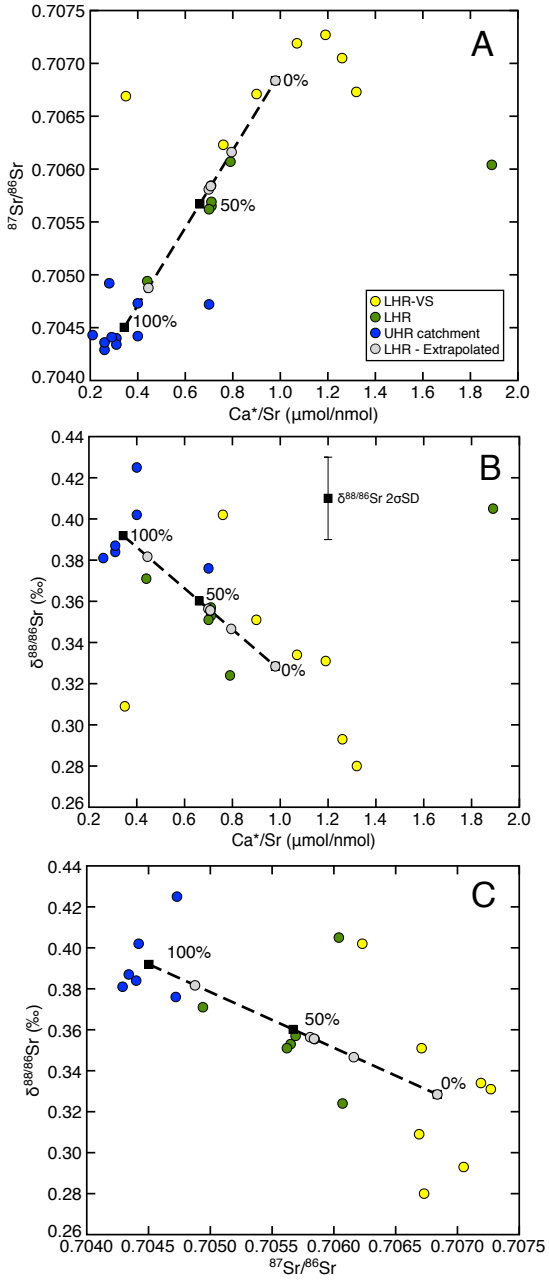

Figure. 2.3: The LHR catchment. A) $^{87}Sr/^{86}Sr$ ratios versus Ca*/Sr ratios, B) $\delta^{88/86}Sr$ values versus Ca*/Sr ratios, and C) $\delta^{88/86}Sr$ values versus $^{87}Sr/^{86}Sr$ ratios, for UHR catchment, LHR, and LHR-VS water samples. Ca concentrations have been corrected for atmospheric inputs. Error bars for $^{87}Sr/^{86}Sr$ ratios are smaller than the size of the datapoints. R^2 values correspond to water samples. Two-component mixing lines connect average values for UHR catchment and LHR-VS water samples. Percentages indicate the molar proportion of Sr in the LHR from the UHR catchment. LHR samples have been orthogonally extrapolated to the mixing lines. The LHR tributary draining predominately diorite (sample W43) is not plotted because diorite composes a minor fraction of the overall catchment lithology and was therefore not analyzed for $\delta^{88/86}Sr$ values.

2.5.2 The CR and UHR catchments

Figure 2.4 plots river, sediment, rock, soil, and plant samples from the CR and UHR catchments, which are grouped together because of their common bedrock and climatic conditions. Figure 2.4A shows $^{87}Sr/^{86}Sr$ ratios versus Ca/Sr ratios, Figure 2.4B shows $\delta^{88/86}Sr$ values versus Ca/Sr ratios, and Figure 2.4C shows $\delta^{88/86}Sr$ values versus $^{87}Sr/^{86}Sr$ ratios. In Figure 2.4A, riverine $^{87}Sr/^{86}Sr$ ratios weakly correlate ($R^2 = 0.24$) with Ca/Sr ratios. In addition, rivers have slightly higher $^{87}Sr/^{86}Sr$ ratios compared to rocks and sediment but lower $^{87}Sr/^{86}Sr$ ratios compared to plants and the soil exchangeable fractions. In Figure 2.4B, riverine $\delta^{88/86}Sr$ values show a relatively strong correlation ($R^2 = 0.69$) with Ca/Sr ratios, and rivers have higher $\delta^{88/86}Sr$ values compared to rocks and sediment. Finally, in Figure 2.4C, riverine $\delta^{88/86}Sr$ values do not strongly correlate ($R^2 = 0.16$) with $^{87}Sr/^{86}Sr$ ratios but overall, the riverine data appear to display two-component mixing between gabbro and an unidentified end-member having higher $^{87}Sr/^{86}Sr$ ratios and $\delta^{88/86}Sr$ values.

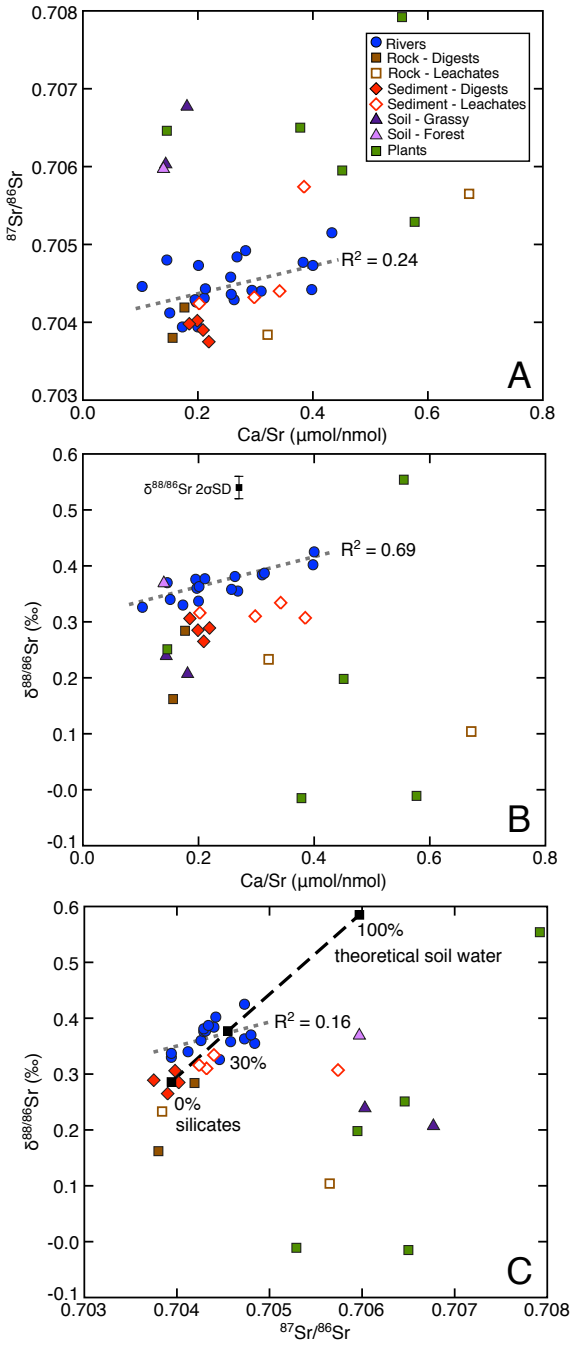

Figure. 2.4: The CR and UHR catchments. A) $^{87}Sr/^{86}Sr$ ratios versus Ca/Sr ratios, B) $\delta^{88/86}Sr$ values versus Ca/Sr ratios, and C) $\delta^{88/86}Sr$ values versus $^{87}Sr/^{86}Sr$ ratios, for CR catchment and UHR catchment water, plant, soil exchangeable fractions, as well as digests and leachates from rocks and sediment. Riverine Ca concentrations have been corrected for atmospheric inputs (Ca*). Error bars for $^{87}Sr/^{86}Sr$ ratios are smaller than the size of the datapoints. R^2 values correspond to water samples. Figure 2.4C includes a two-component mixing line between sediment silicate digests and water samples, which has been extrapolated to a theoretical soil water end-member. Percentages indicate the molar proportion of riverine Sr from soil water.

Although the aforementioned patterns are complex, it is reasonable to assume that a unifying explanation exists. In the following paragraphs, we consider and ultimately eliminate the most obvious potential explanations, such as calcite weathering, calcite precipitation, wet and dry atmospheric deposition, and bedrock weathering and pedogenesis. We then use our data to suggest that biological processes and soil water inputs provide the most likely explanation. Chemical weathering of accessory calcite can dominate riverine Sr and Ca fluxes and elevate riverine Ca/Sr ratios (e.g., Blum et al, 1998; Jacobson et al., 2015). However, the leachate data reported in Table 2.2 confirm that the Darren Leucogabbro, which composes the CR and UHR catchments, does not contain accessory calcite. The leachates yielded small amounts of Ca, but also relatively high amounts of elements associated with silicate minerals, such as Si and Na, suggesting that most, if not all, of the leachate Ca is silicate-derived.

Because calcite preferentially incorporates lighter Sr isotopes (Böhm et al., 2012; Fietzke and Eisenhauer, 2006; Stevenson et al., 2014), calcite precipitation could explain why rivers have higher $\delta^{88/86}$Sr values compared to bedrock. However, waters are highly undersaturated with respect to calcite, and our preceding analysis for the LHR tends to rule out other in-stream processes, such as ion-exchange on rock and sediment surfaces, that might fractionate Sr isotopes as well as Ca/Sr ratios.

Wet deposition of Sr is important in some settings (e.g., Miller et al., 1993; Pearce et al., 2015), but rainwater analyzed in this study had a negligible amount of Sr. Although we only analyzed one rainwater sample, we infer that wet deposition cannot explain the riverine data, but we also recognize that more detailed studies of rainwater in the region are required to test this hypothesis. Due to the proximity of the study site to the Tasman Sea, atmospheric deposition might resemble seawater at times (Halstead et al., 2000). Seawater has a $\delta^{88/86}$Sr value of

0.396‰ (see Methods), an $^{87}Sr/^{86}Sr$ ratio of ~0.70923 and a Ca/Sr ratio of ~0.11 μmol/nmol (Banner, 2004). Thus, seawater contributions could elevate riverine $\delta^{88/86}Sr$ values and $^{87}Sr/^{86}Sr$ ratios, but they do not readily explain variation in riverine Ca/Sr ratios. We are unaware of any studies that have documented the extent, source, or geochemistry of dry deposition to Fiordland. Research conducted in the nearby Southern Alps suggests that dust largely derives from local bedrock and therefore, would not greatly alter river geochemistry (Marx et al., 2008). Additionally, Fiordland's remote location precludes significant anthropogenic inputs.

A more plausible interpretation pertains to strontium isotope fractionation and/or preferential mineral dissolution during pedogenesis and secondary clay mineral formation. Halicz et al. (2008) found that terra rossa (clay) soils from the Judeau Mountains have significantly lower $\delta^{88/86}Sr$ values compared to the predominantly carbonate bedrock and suggested that pedogenesis may fractionate Sr isotopes. Uptake of lighter Sr isotopes during clay formation could explain why Fiordland rivers have higher $\delta^{88/86}Sr$ values relative to gabbro, but Fiordland soils are highly incipient and poorly developed. Furthermore, it is less clear how this mechanism would produce co-variation with riverine $^{87}Sr/^{86}Sr$ and Ca/Sr ratios, particularly as Ca and Sr are thought to behave identically during ion-exchange on clays (Lefevre et al., 1996). Laboratory studies have demonstrated that the time-dependent release of stable Ca isotope ratios during granite weathering reflects the relative solubility and dissolution kinetics of different Ca-bearing minerals having unique isotopic compositions (Ryu et al., 2011). The stable Sr isotope system may behave similarly. However, we are unaware of any studies that have addressed this topic, and the question arises whether minerals composing the Darren Leucogabbro possess sufficient stable Sr isotope variation to produce the effects observed at the watershed scale. Although not a definitive test, we note that rock and sediment leachates have slightly different

$\delta^{88/86}$Sr values compared to bulk digest values, but the differences are insufficient to explain the riverine data. Additionally, soil exchangeable fractions have relatively high $^{87}Sr/^{86}Sr$ ratios compared to bulk gabbro. The high $^{87}Sr/^{86}Sr$ ratios likely reflect the preferential dissolution of K-rich minerals, such as biotite (e.g., Blum and Erel, 1997), which represents ~5% of the Darren Leucogabbro, but exchangeable $^{87}Sr/^{86}Sr$ ratios and $\delta^{88/86}$Sr values show no discernable correlation.

We suggest that the dense temperate rainforest that covers much of Fiordland plays a key role in determining river geochemistry. Analogous to the Ca isotope system (Cenki-Tok et al., 2009; Farkas et al., 2011; Hindshaw et al., 2013b; Holmden and Belanger, 2010; Page et al., 2008; Wiegand et al., 2005), plants preferentially incorporate lighter Sr isotopes (de Souza et al., 2010). The plant foliage samples analyzed in this study display a wide range of $\delta^{88/86}$Sr values, but in general, they are low relative to the other Sr reservoirs. Preferential plant uptake of ^{86}Sr would increase the $\delta^{88/86}$Sr value of soil water, and in turn, discharge of soil water into rivers could elevate riverine $\delta^{88/86}$Sr values above those expected for bedrock weathering. Although we did not analyze soil water, we note that the $\delta^{88/86}$Sr value of the CR forest soil exchangeable fraction is high relative to bulk silicates. Furthermore, because the traditional radiogenic Sr isotope measurement eliminates natural mass-fractionation, plants, soil water, and soil exchangeable fractions should have similar $^{87}Sr/^{86}Sr$ ratios (Blum et al., 2002; Blum et al., 2000; Drouet and Herbauts, 2008). Indeed, plants and exchangeable Sr in the CR and UHR catchments have similar, relatively high, $^{87}Sr/^{86}Sr$ ratios compared to bulk gabbro. Based on these data, we interpret the riverine data plotted in Figure 2.4C to reflect two-component mixing between gabbro-derived Sr and soil water Sr, which has been isotopically fractionated by plant growth.

To estimate the soil water $\delta^{88/86}$Sr value, we fit a mixing line to the riverine data and the sediment digest end-member and extrapolated it to the forest soil exchangeable $^{87}Sr/^{86}Sr$ ratio of ~0.706 (Fig. 2.4C). This yields a soil water $\delta^{88/86}$Sr value of ~0.60‰. Although the O horizon exchangeable fraction composing the CR forest floor soil yielded a $\delta^{88/86}$Sr value of 0.369‰, an average soil water $\delta^{88/86}$Sr value of ~0.60‰ appears reasonable. This implies that soil water is, on average, ~0.30‰ heavier than silicate bedrock, which, by mass balance, would require plants to be ≥0.30‰ lighter than silicate bedrock, depending on the extent of nutrient recycling. Two plant samples (P05 and P07) exhibited a fractionation of this magnitude, and by analogy to the Ca isotope system, where within-plant fractionation typically causes leaves and flowers to have higher $\delta^{44/40}$Ca values than roots (Bagard et al., 2013; Holmden and Belanger, 2010; Page et al., 2008; Schmitt et al., 2013; Wiegand et al., 2005) we hypothesize that our plant samples (leaves only) represent the minimum extent of fractionation between soils and plants. Furthermore, de Souza et al. (2010) reported that $\delta^{88/86}$Sr values for different plant parts, such as roots, stems, leaves, and flowers, were 0.20‰ to 0.50‰ lighter than soil and rock, which supports our contention that the plant Sr reservoir in the Milford Sound region is ≥0.30‰ lighter than bedrock. Implementing Equation 2.3 with the hypothetical soil water composition, the riverine data, and the sediment digest end-member, we find that gabbro weathering provides ~73% of the riverine Sr, while ~27% originates from the plant-fractionated soil water pool. Finally, we emphasize that this calculation represents a first-order estimate of the soil water contribution, as riverine $\delta^{88/86}$Sr values likely reflect the relative size of the soil water pool, as well as the degree of biological fractionation and nutrient recycling.

Soil water inputs could also explain covariation between riverine $\delta^{88/86}$Sr values and Ca/Sr ratios (Fig. 2.4B). Soil water Ca/Sr ratios can vary due to plant uptake and ion-exchange

reactions, the latter which depend on many factors, including mineralogy, pH, and organic matter type and abundance (Pett-Ridge et al., 2009). Although the exact pathways and mechanisms require further investigation, the overall correlation between riverine $\delta^{88/86}$Sr values and Ca/Sr ratios likely reflects their coincident fractionation in soils during biogeochemical cycling. Although this hypothesis requires that soil water has, on average, higher Ca/Sr ratios than measured for the CR forest soil exchangeable fraction, multiple studies have reported differences between exchangeable and soil water Ca/Sr ratios (Drouet and Herbauts, 2008; Pett-Ridge et al., 2009; Poszwa et al., 2000), often with soil solutions having higher Ca/Sr ratios than the corresponding exchangeable fraction (Drouet and Herbauts, 2008; Poszwa et al., 2000). Because the factors affecting soil Ca/Sr ratios are multiple and complex, we suggest that $\delta^{88/86}$Sr values may be a more conservative tracer of soil water inputs to rivers.

2.5.3 The LHR-VS catchments

Figure 2.5 plots river, sediment, rock, and soil samples for the LHR-VS catchments. Compared to the CR and UHR catchments, the key difference is that LHR-VS catchments drain carbonate-bearing bedrock. According to Figure 2.5A, which shows $^{87}Sr/^{86}Sr$ ratios versus Ca/Sr ratios, rivers reflect two-component mixing between silicate and carbonate weathering, with the latter dominating over the former. This appears consistent with the local bedrock geology, as well as the fact that carbonate minerals are highly soluble and dissolve more rapidly compared to silicate minerals. However, a more complex pattern emerges when $\delta^{88/86}$Sr values are examined relative to Ca/Sr and $^{87}Sr/^{86}Sr$ ratios (Figures 2.5B and C, respectively). Similar to the CR and UHR catchments (Figures 2.4B and C), LHR-VS riverine $\delta^{88/86}$Sr values are elevated above those for bedrock, and a strong relationship exists between Ca/Sr ratios and $\delta^{88/86}$Sr values (R^2 =

0.91, after excluding one outlier sample, W15). These patterns presumably reflect contributions from soil water. We cannot completely rule out the possibility that fractionation during chemical weathering elevates riverine $\delta^{88/86}$Sr values in the Milford Sound region. However, the mechanism would have to be so fundamental as to transcend bedrock mineralogy, given that riverine $\delta^{88/86}$Sr values are higher than those for bedrock in both silicate- and carbonate-dominated catchments. In other words, we find that the LHR-VS catchments reflect three-component mixing between silicate weathering, carbonate weathering, and soil water. While the Ca and Sr in soil water originates from silicate and carbonate minerals, the influence of biogeochemical cycling would not be evident without measuring $\delta^{88/86}$Sr values. Moreover, application of conventional $^{87}Sr/^{86}Sr$ and Ca/Sr two-component mixing equations would almost certainly yield incorrect results for the proportions of Sr (and Ca) originating from silicate and carbonate weathering.

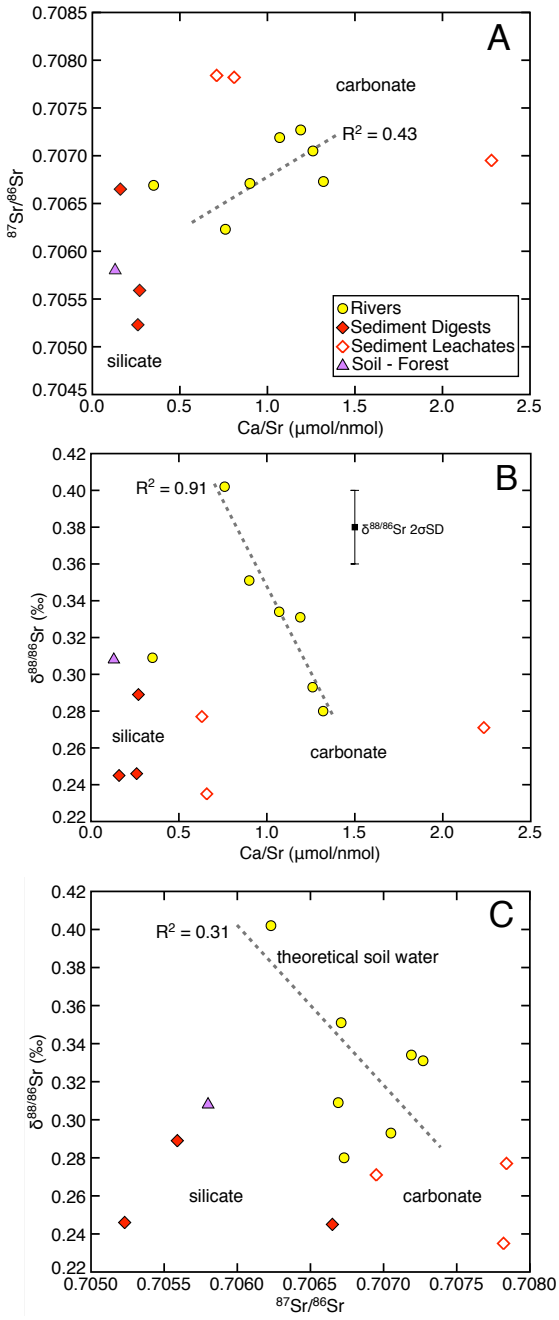

Figure. 2.5: The LHR-VS catchments. A) $^{87}Sr/^{86}Sr$ ratios versus Ca/Sr ratios, B) $\delta^{88/86}Sr$ values versus Ca/Sr ratios, and C) $\delta^{88/86}Sr$ values versus $^{87}Sr/^{86}Sr$ ratios, for LHR-VS water, soil exchangeable fractions, as well as sediment digest and leachate samples. Riverine Ca concentrations have been corrected for atmospheric inputs (Ca*). Error bars for $^{87}Sr/^{86}Sr$ ratios are smaller than the size of the datapoints. R^2 values correspond to water samples after excluding one outlier sample, W15. 'Silicate' and 'carbonate' denote the general composition for these end members, based on sediment digests and leachates, respectively. Fig 2.5C. also includes 'theoretical soil water,' which denotes the general composition of this third, hypothesized, end-member.

2.5.4 Additional evidence for the soil water hypothesis

At present, only two studies have used $\delta^{88/86}$Sr values to examine biogeochemical cycling in terrestrial systems. de Souza et al. (2010) measured $\delta^{88/86}$Sr values for bedrock, bulk soil, water, and plants from a glaciated catchment in the Swiss Alps. Ultimately, the study found that plants preferentially incorporate ^{86}Sr but due to their low abundance, do not affect bulk soil or riverine $\delta^{88/86}$Sr values, as bedrock, soil, and riverine $\delta^{88/86}$Sr values were indistinguishable. In good agreement with our findings, de Souza et al. (2010) suggested that the effect of plant fractionation would more likely be observed in soil waters, rather than bulk soil where the large reservoir of mineral-bound Sr exceeds the comparatively small pool of plant-fractionated Sr. Although the Swiss Alps study site did not reveal effects from plant growth, the authors proposed that areas with more abundant vegetation might alter the $\delta^{88/86}$Sr value of the continental weathering flux. Our results support this interpretation.

Wei et al. (2013) measured $\delta^{88/86}$Sr values for the Xijiang River in China throughout the course of a year. The Xijiang River basin experiences a tropical/subtropical climate, contains predominantly carbonate bedrock, and is populated by an evergreen forest. The study found that during warmer, rainier months, riverine $\delta^{88/86}$Sr values exceeded those for average carbonate bedrock. Although the authors did not measure $\delta^{88/86}$Sr values of local bedrock or soils, they attributed the difference to Sr isotope fractionation during drainage of surficial, silicate-derived soils. However, the seasonal trends also appear consistent with the plant-fractionated soil water hypothesis. Higher riverine $\delta^{88/86}$Sr values may simply reflect increased plant growth, Sr uptake, and attendant isotope fractionation during the summer months, combined with accelerated hydrologic discharge and flushing of soil water to the Xijiang River.

2.6 Conclusions and Implications

Rivers draining the Milford Sound region of Fiordland, New Zealand have higher $\delta^{88/86}Sr$ values compared to those expected from simple bedrock weathering. We attribute the pattern to the input of soil water, which has higher $\delta^{88/86}Sr$ values than rivers. Uptake of ^{86}Sr during plant growth provides the most likely explanation for the inferred soil water fractionation. For rivers draining gabbro, which is the predominant rock type in the study area, simple two-component mixing calculations involving $\delta^{88/86}Sr$ values suggest that 27% of the dissolved Sr originates from the soil water reservoir, while the remaining 73% is sourced directly from bedrock weathering. These are first-order estimates because the $\delta^{88/86}Sr$ value of the soil water end-member likely varies from catchment-to-catchment due to differences in soil water Sr concentrations, the degree of biological cycling, and vegetation abundance and composition. In catchments with some limestone bedrock, rivers display three-component mixing between silicate and carbonate weathering and soil water. All riverine $\delta^{88/86}Sr$ values strongly correlate with Ca/Sr ratios, which implies that the same, or related, soil biogeochemical processes that fractionate Sr isotopes also discriminate Ca from Sr. All three tracers considered in this study, namely $^{87}Sr/^{86}Sr$ ratios, Ca/Sr ratios, and $\delta^{88/86}Sr$ values conservatively trace water mass mixing, but we suggest that in heavily vegetated areas, $\delta^{88/86}Sr$ values and Ca/Sr ratios may not conservatively trace bedrock weathering sources. We note, however, that expression of the soil water signal may be limited to warmer, high-rainfall summer months. Finally, our findings for Fiordland suggest that the fractionation of Sr isotopes during plant uptake could contribute to the observation that many world rivers have higher $\delta^{88/86}Sr$ values than average bedrock (Krabbenhoft et al., 2010; Pearce et al., 2015b).

Chapter 3

The radiogenic and stable Sr isotope geochemistry of basalt weathering in Iceland: Role of hydrothermal calcite and implications for long-term climate regulation

3.1 Introduction

Over geologic timescales, the chemical weathering of silicate minerals controls atmospheric CO_2 levels and regulates global temperatures via the greenhouse effect (Berner et al., 1983; Urey, 1952). Interpretations of riverine HCO_3^- and cation fluxes suggest that basalt weathers ~2 to 10 times faster than felsic rocks, such as granite (Millot et al., 2002; Dessert et al., 2003; Schopka et al., 2011, Ibarra et al., 2016 and references therein). Because basalt composes only ~5% of Earth's continental surface area (Suchet et al., 2003), basalt weathering may account for 30% – 35% of the modern global atmospheric CO_2 consumption flux (Dessert et al., 2003). These estimates have led to the general conclusion that basaltic regions are atmospheric CO_2 consumption "hot spots" that play a disproportionately large role in regulating long-term global climate. Differential weathering of basalt and granite has been invoked to explain climate evolution during a variety of time periods throughout Earth history (Cox et al., 2016; Jagoutz et al., 2016; Kent and Muttoni, 2013; Li and Elderfield, 2013; Mills et al., 2014). To constrain controls on basalt weathering and parameterize models of the long-term C cycle, studies have been conducted in basaltic regions worldwide (Allegre et al., 2010; Das et al., 2005; Dessert et al., 2001; Gaillardet et al., 2011; Li et al., 2016; Louvat and Allegre, 1997; Navarre-Sitchler and Brantley, 2007), with a considerable focus on Iceland (Eiriksdottir et al., 2013, 2015; Eiriksdottir et al., 2008; Georg et al., 2007; Gislason et al., 1996; Gislason et al., 2009; Hindshaw et al., 2013a; Jacobson et al., 2015; Louvat et al., 2008; Moulton and Berner, 1998;

Pogge von Strandmann et al., 2008; Stefansson and Gislason, 2001; Vigier et al., 2009). However, a recent Ca isotope study has argued that a substantial proportion of the Icelandic riverine HCO_3^- flux relevant to the long-term C cycle derives from carbonate weathering (Jacobson et al., 2015). This result is not unexpected given that hydrothermal and metamorphic calcites are abundant in Icelandic basalt (Thomas et al., 2016; Wiese et al., 2008) and calcite is highly soluble and dissolves orders of magnitude faster than silicate minerals (Lerman and Wu, 2008). The data are also consistent with the observation that most rivers draining basaltic regions display major ion abundances characteristic of carbonate weathering despite the absence of sedimentary carbonate rocks (Dessert et al., 2003). A major question, then, is whether the dissolution of hydrothermal calcite in Iceland and other basaltic settings has implications for quantifying the strength of the basalt weathering feedback. This question arises from several assumptions embedded in conventional models of the long-term C cycle, including that all volcanic CO_2 is emitted into the atmosphere where the CO_2 regulates climate before weathering rocks and minerals, riverine HCO_3^- fluxes derive exclusively from chemical weathering reactions occurring at the Earth's surface, and all carbonate weathering contributions originate from the sedimentary rock reservoir, which sequesters atmospheric CO_2 that once participated in climate regulation. However, the traditional long-term C cycle paradigm does not completely describe Iceland, where the hydrothermal and metamorphic calcites that contribute HCO_3^- upon weathering sequester volcanic CO_2 prior to atmospheric injection (Jacobson et al., 2015). While hydrothermal and metamorphic calcites may simply represent an intermediate reservoir for silicate weathering byproducts (Thomas et al., 2016), a complete C accounting is required to constrain the exact impact, or lack thereof, on climate regulation.

Here, we examine the role of carbonate weathering in Iceland through the dual lenses of radiogenic and stable Sr isotope ratios ($^{87}Sr/^{86}Sr$ and $\delta^{88/86}Sr$). We analyzed the same sample set of waters, rocks, and minerals as studied in Jacobson et al. (2015). Numerous studies have used $^{87}Sr/^{86}Sr$ ratios to trace riverine sources of cations and HCO_3^- (Clow et al., 1997; Das et al., 2006; Pett-Ridge et al., 2009; Schopka et al., 2011). Much like $^{87}Sr/^{86}Sr$ ratios, $\delta^{88/86}Sr$ values can conservatively trace weathering reactions and water mass mixing (Andrews et al., 2016), but $\delta^{88/86}Sr$ values also shed light on mass-dependent fractionation effects that are eliminated during analysis of $^{87}Sr/^{86}Sr$ ratios. Plant uptake (Andrews et al., 2016; Bullen and Chadwick, 2016; de Souza et al., 2010), carbonate precipitation (Böhm et al., 2012; Fietzke and Eisenhauer, 2006; Krabbenhöft et al., 2010; Rüggeberg et al., 2008; Shalev et al., 2017; Stevenson et al., 2014; Vollstaedt et al., 2014), and mineral dissolution and clay precipitation (Chao et al., 2015; Cox et al., 2016; Halicz et al., 2008; Pearce et al., 2015b) all have potential to fractionate Sr isotopes. In this way, the stable Sr isotope system can simultaneously trace source and process. Furthermore, a comparison of $^{87}Sr/^{86}Sr$ ratios, $\delta^{88/86}Sr$ values, and $\delta^{44/40}Ca$ values for the same sample set presents a unique opportunity to test the validity of assumptions regarding the similar geochemical behavior of Sr and Ca during cycling at the Earth's surface. Finally, we develop a simple one-box model for the atmosphere-ocean system to investigate the role of hydrothermal calcite weathering in the long-term C cycle. We specifically address the sources of C (i.e., volcanic vs. atmospheric) that compose calcite and hence, riverine HCO_3^-, as well as the age of the calcite undergoing weathering.

3.2 Geologic and climatic setting

Iceland is a subaerial exposure of the North Atlantic Igneous Province that lies along the Mid Atlantic Ridge between latitudes 63° and 68°N and longitudes 25° and 13°W. Basalt composes ~80% – 85% of the bedrock (Gislason et al., 1996) with ~50% produced during the Tertiary (Johannesson, 2014). The oldest exposed rocks have an age of ~13 Myr (Neuhoff et al., 2000), and volcanism continues in the modern-day. Icelandic basalt has a relatively homogeneous composition, primarily low magnesium/ferrobasalt or olivine tholeitte (Gislason et al., 1996; Neuhoff et al., 2000). Tertiary Icelandic basalt also contains an abundance of secondary minerals, including calcite (e.g., Iceland spar) and zeolites (e.g., heulandite and stilbite, among others) produced by hydrothermal alteration and burial metamorphism (Neuhoff et al., 2000; Walker, 1960). Glaciers cover ~11% of Iceland (Norodahl and Petursson, 2005). Hydrologically, surface runoff dominates in Tertiary areas due to low bedrock permeability (Gislason et al., 1996). Bedrock in young, active volcanic zones has higher permeability, and groundwater inputs dominate (Gislason et al., 1996). In glaciated areas, meltwater feeds rivers (Gislason et al., 1996). There are also 33 localized high-temperature hydrothermal springs scattered throughout Iceland (Armannsson, 2016). The mean annual temperature in Iceland is 4°C. Mean annual precipitation ranges from ~3000 – 4000 mm on the south coast to <400 mm in the north. Vegetation covers 23% of the land surface area (Hindshaw et al., 2013) and largely consists of grassland.

3.3 Methods

3.3.1 The sample set

Jacobson et al. (2015) provides a full description of the water, mineral, and rock samples analyzed in the present study, including their collection, handling, and preparation protocols, as well as their elemental and Ca isotope geochemistry. Briefly, nineteen waters were collected from locations throughout Iceland (Fig. 3.1). These consist of three non-glacial rivers, seven glacial rivers, and nine groundwaters. Additionally, six basalt samples were acquired from the Icelandic Institute of Natural History, and twenty-five mineral samples were obtained from a variety of sources, including the Icelandic Institute of Natural History, the Smithsonian Institute, the University of Iceland, and the Natural History Museum in Reykjavik. The mineral samples consist of fifteen calcite samples, six heulandite samples, and five stilbite samples, many of which were previously analyzed in Fridriksson et al. (2001, 2004, 2009).

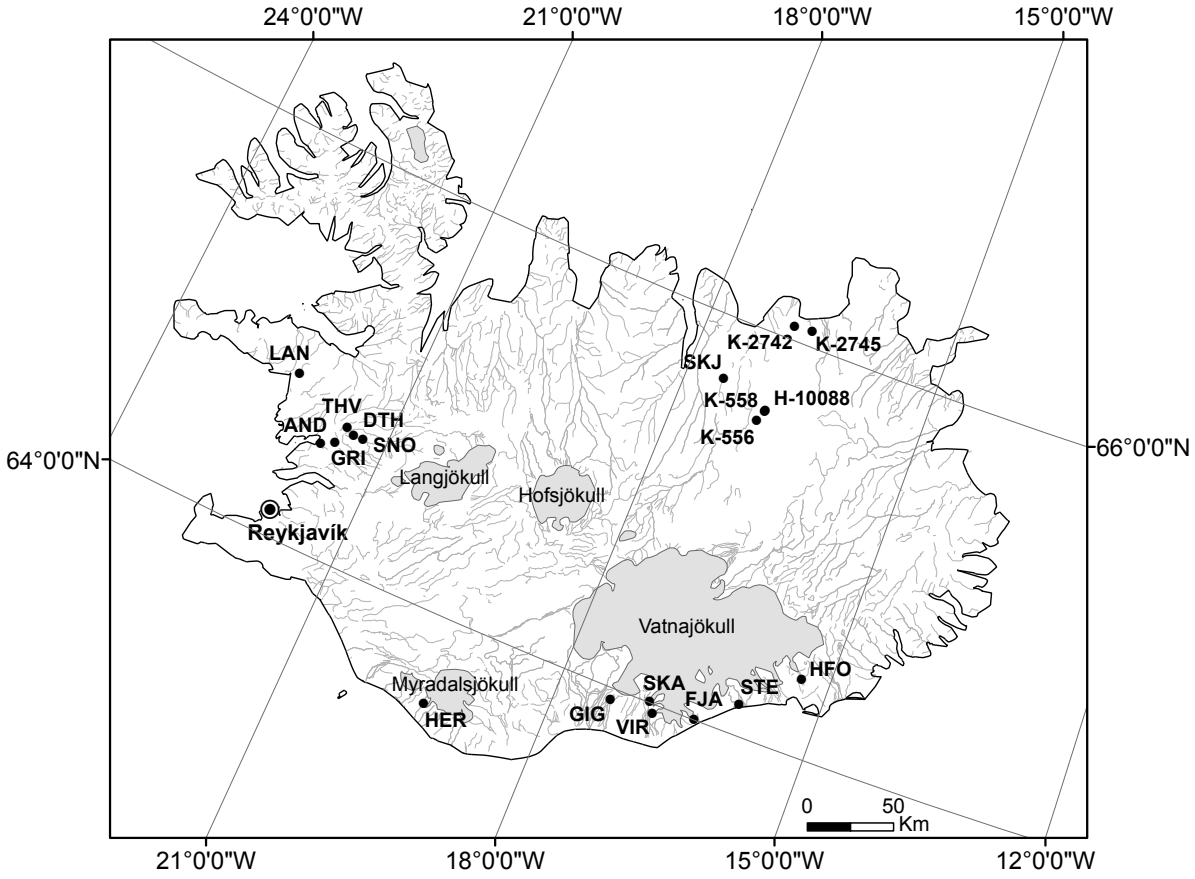

Figure 3.1: Map of Iceland showing water sample locations.

3.3.2 Radiogenic and stable Sr isotope ratios

Radiogenic and stable Sr isotopes ($^{87}Sr/^{86}Sr$ and $^{88}Sr/^{86}Sr$, respectively) were measured in the Radiogenic Isotope Geochemistry Clean Laboratory at Northwestern University (NU) using a Thermo-Scientific Triton Thermal Ionization Mass Spectrometer (TIMS). The analyses followed the procedures outlined in Andrews et al. (2016), with a few minor modifications as described below. According to an ^{84}Sr isotope dilution method, column blanks contained 27 pg Sr (n = 2), and one total procedural blank contained 27 pg Sr. These levels are negligible compared to the amounts of Sr analyzed (see below). In brief, for the determination of $^{87}Sr/^{86}Sr$ ratios, sample

aliquots containing 50 – 100 ng of Sr were weighed into acid-cleaned Teflon vials, dried, re-dissolved in 8M HNO_3, and eluted through inverted pipet tips packed with Eichrom Sr-Spec resin. The purified Sr fractions were dried, re-dissolved in 1.5 μL of 3N HNO_3, and loaded onto single, outgassed Re filament assemblies with 1 μL of a $TaCl_5$ solution between parafilm "dams." 8V ion beams were collected in multi-dynamic mode for 110 duty cycles. To correct for instrumental mass fractionation, the $^{86}Sr/^{88}Sr$ ratio was normalized to 0.1194 using an exponential law. During the period of study, repeated analyses of NBS 987 yielded a mean $^{87}Sr/^{86}Sr$ ratio of 0.71025 ± 0.00001 ($\pm 2\sigma_{SD}$, n = 20). The current, long-term mean $^{87}Sr/^{86}Sr$ ratio is 0.71025 ± 0.00001 ($\pm 2\sigma_{SD}$, n = 123).

An ^{87}Sr-^{84}Sr double-spike method was used to measure $^{88}Sr/^{86}Sr$ ratios. The method was optimized according to the Monte Carlo error model first presented in Lehn et al. (2013) for the analysis of $^{44}Ca/^{40}Ca$ ratios and later adapted in Andrews et al. (2016) for the analysis of $^{88}Sr/^{86}Sr$ ratios. Sample aliquots containing 50 – 150 ng of Sr were weighed into acid-cleaned Teflon vials and spiked. The vials were capped and heated at ~90°C overnight to ensure complete sample-spike equilibration. The solutions were dried, re-dissolved in 8N HNO_3, and purified using the same elution procedure described above. After drying, the purified Sr fractions were re-dissolved in 1.5μL of 3N HNO_3 and loaded onto outgassed, single Re filament assemblies, also between parafilm "dams" with 1 μL of a $TaCl_5$ solution. In the mass spectrometer, a 6V ^{88}Sr ion beam was attained, and $^{88}Sr/^{84}Sr$, $^{87}Sr/^{84}Sr$, and $^{86}Sr/^{84}Sr$ ratios were measured in static mode for a total of 160 duty cycles, each having a 16 sec integration time. Ultimately, 140 cycles were used for the data reduction. Runs were carefully monitored to ensure a steady or increasing ^{88}Sr beam, an increasing raw $^{86}Sr/^{84}Sr$ fractionation pattern, and the absence of filament reservoir effects, which can manifest as apparent "reverse-fractionation" in

uncorrected ratios or trends in fractionation-corrected $^{88}Sr/^{86}Sr$ ratios (Lehn and Jacobson, 2015b). All sample (smp) $^{88}Sr/^{86}Sr$ ratios are reported in delta notation (per mil) relative to NBS 987, where $\delta^{88/86}Sr$ (in ‰) = $[(^{88}Sr/^{86}Sr)_{smp}/(^{88}Sr/^{86}Sr)_{NBS\text{-}987} - 1] \times 1000$. Measured internal precisions ($2\sigma_{SEM}$) for samples and standards range from 0.007 to 0.010‰, with an average of 0.008‰.

Collector cup drift affects measurement of $\delta^{88/86}Sr$ values, so an offset was applied to each measurement in a session, which in turn, was defined as 40 or fewer runs, including both samples and standards. The session offset was calculated as the difference between the mean $\delta^{88/86}Sr$ value of 6 – 8 NBS 987 runs and the "true" NBS 987 $\delta^{88/86}Sr$ value, which is 0‰. To confirm the accuracy of the drift correction, 2 – 4 IAPSO seawater standards were analyzed during each session. During the period of study, NBS 987 yielded $\delta^{88/86}Sr = 0.000 \pm 0.006$‰ ($2\sigma_{SEM}$, $n = 31$), and IAPSO seawater yielded $\delta^{88/86}Sr = 0.396 \pm 0.007$‰ ($2\sigma_{SEM}$, $n = 13$). These data correspond to an external reproducibility of ±0.018‰ ($2\sigma_{SD}$) for NBS 987 and ±0.013‰ ($2\sigma_{SD}$) for IAPSO seawater. The current, long-term external reproducibility for both the NBS 987 and IAPSO standards is ±0.018‰ ($n = 108$ and $n = 67$, respectively). Because the stable Sr isotope data reduction procedure employs measured radiogenic Sr isotope ratios, errors must be propagated to arrive at the overall uncertainty for $\delta^{88/86}Sr$ values. The global, external reproducibility for $\delta^{88/86}Sr$ values ($2\sigma SD^{global}_{\delta 88/86Sr}$) is calculated with the equation:

$$2\sigma SD^{global}_{\delta 88/86Sr} = \sqrt{\left(2\sigma SD^{NBS}_{\delta 88/86Sr}\right)^2 + \left(2\sigma SD^{NBS}_{87/86Sr}\right)^2}, \quad (3.1)$$

where $2\sigma SD^{NBS}_{\delta 88/86Sr}$ is the long-term external reproducibility for NBS 987 stable Sr isotope measurements (±0.018‰), and $2\sigma SD^{global}_{87/86Sr}$ is the long-term external reproducibility for

NBS 987 radiogenic Sr isotope measurements, converted to per mil (±0.010‰). Based on equation (3.1), we apply a global uncertainty of ±0.020‰ ($2\sigma_{SD}$) to all samples in the dataset.

3.4 Results

3.4.1 $^{87}Sr/^{86}Sr$ and Ca/Sr ratios

Table 3.1 reports Ca and Sr concentrations, Ca/Sr ratios, $^{87}Sr/^{86}Sr$ ratios, and $\delta^{88/86}Sr$ values for waters. Table 3.2 reports Ca and Sr concentrations, Ca/Sr ratios, $^{87}Sr/^{86}Sr$ ratios, $\delta^{88/86}Sr$ values, and $\delta^{44/40}Ca$ values for rocks and minerals. Ca and Sr concentrations, as well as $\delta^{44/40}Ca$ values, were previously reported in Jacobson et al. (2015) but are provided here to facilitate discussion. Basalt bedrock has, on average, an $^{87}Sr/^{86}Sr$ ratio of 0.70318 ± 0.00005 ($1\sigma_{SD}$, n = 6) and a Ca/Sr ratio of 1.04 ± 0.54 μmol/nmol ($1\sigma_{SD}$, n = 6). The basalt $^{87}Sr/^{86}Sr$ ratio is identical, within uncertainty, to that reported in Hindshaw et al. (2013a). Compared to basalt, calcite samples have a similarly narrow range of $^{87}Sr/^{86}Sr$ ratios, producing an average $^{87}Sr/^{86}Sr$ ratio of 0.70329 ± 0.00010 ($1\sigma_{SD}$, n = 15), but a significantly greater range of Ca/Sr ratios (6.21 to 364 μmol/nmol), yielding an average Ca/Sr ratio of 53.0 ± 90.2 μmol/nmol ($1\sigma_{SD}$, n = 15). Removing calcite sample 15239 (Ca/Sr = 364 μmol/nmol) decreases the average Ca/Sr ratio to 30.7 ± 28.1 μmol/nmol ($1\sigma_{SD}$, n = 14). Heulandite samples have the same average $^{87}Sr/^{86}Sr$ ratio as calcite, 0.70328 ± 0.00007 ($1\sigma_{SD}$, n = 6) but the lowest average Ca/Sr ratio of the entire sample set, 0.04 ± 0.02 μmol/nmol ($1\sigma_{SD}$, n = 5). Finally, as compared to other lithological Sr reservoirs, stilbite samples have a modestly higher $^{87}Sr/^{86}Sr$ ratio of 0.70356 ± 0.00028 ($1\sigma_{SD}$, n = 4). Stilbite samples also have a wide range of Ca/Sr ratios (1.50 to 107 μmol/nmol), which produce a high average Ca/Sr ratio of 44.8 ± 42.6 μmol/nmol ($1\sigma_{SD}$, n = 5).

Glacial rivers have an average $^{87}Sr/^{86}Sr$ ratio of 0.70365 ± 0.00019 ($1\sigma_{SD}$, n = 7) and an average Ca/Sr ratio of 2.43 ± 1.15 μmol/nmol ($1\sigma_{SD}$, n = 7). Non-glacial rivers have the highest average $^{87}Sr/^{86}Sr$ ratio of the sample set, 0.70513 ± 0.00019 ($1\sigma_{SD}$, n = 3), and an average Ca/Sr ratio of 1.32 ± 0.44 μmol/nmol ($1\sigma_{SD}$, n = 3). Groundwaters have an average $^{87}Sr/^{86}Sr$ ratio of 0.70364 ± 0.00060 ($1\sigma_{SD}$, n = 8), but upon excluding two samples (SNO and K2745), the average $^{87}Sr/^{86}Sr$ ratio decreases to 0.70332 ± 0.00004 ($1\sigma_{SD}$, n = 6), equivalent to basalt. Groundwaters have an average Ca/Sr ratio of 1.45 ± 0.76 μmol/nmol ($1\sigma_{SD}$, n = 8).

Table 3.1

Elemental and Sr isotope data of Icelandic waters

Sample	Ca (μmol/L)	Sr (nmol/L)	Ca/Sr (μmol/nmol)	$^{87}Sr/^{86}Sr$	$\delta^{88/86}Sr$ (‰)
Non-glacial rivers					
AND	97.0	80.6	1.20	0.70530	0.390
GRI	112	61.5	1.82	0.70531	0.405
THV	140	146	0.96	0.70479	0.368
Glacial rivers					
HER	115	55.2	2.08	0.70363	0.401
SKJ	134	57.9	2.31	0.70342	0.418
STE	359	93.2	3.85	0.70382	0.472
FJA	202	178	1.13	0.70361	0.373
VIR	96.0	102	0.94	0.70391	0.269
SKA	112	36.5	3.07	0.70370	0.465
GIG	246	67.5	3.64	0.70342	0.503
Groundwater					
K2745	145	82.6	1.76	0.70480	0.315
K556	177	87.0	2.03	0.70332	0.444
K558	269	135	1.99	0.70334	0.331
H10088	405	221	1.83	0.70328	0.304
SNO	67.0	29.8	2.25	0.70438	0.366
LAN	557	665	0.84	0.70337	0.372
DTH	77.0	122	0.63	0.70337	0.459
HF-01	216	861	0.25	0.70328	0.381
Seawater					
Average	n.m.	n.m.	0.11[a]	0.70918[b]	0.396[b]

See Jacobson et al. (2015) for full description of sample locations, field parameters, other elemental concentrations, and Ca isotope values.

n.m. indicates not measured

a indicates value from Banner (2004)

b indicates value based on repearted measurements of the IAPSO seawater standard (see methods)

Table 3.2
Elemental and Ca and Sr isotope data of Icelandic rocks and minerals

Sample (description)	Ca (μmol/g)	Sr (nmol/g)	Ca/Sr (μmol/nmol)	$^{87}Sr/^{86}Sr$	$\delta^{88/86}Sr$ (‰)	$\delta^{44/40}Ca$ (‰)
Basalt						
9149 (Tholeiite)	2151	1713	1.26	0.70311	0.257	-1.06
22038 (Olivine Tholeitte)	2020	1079	1.87	0.70313	0.278	-1.05
9297 (Tholeiite)	1698	1745	0.97	0.70323	0.294	-1.06
9265 (Olivine Tholeiite)	2000	1715	1.17	0.70320	0.291	-1.07
709 (Tholeitte)	1536	2107	0.73	0.70324	0.279	-1.04
4685 (Basaltic Andesite)	1184	4410	0.27	0.70319	0.256	-1.07
Calcite						
500 (spar)	9918	256	38.7	0.70312	0.394	-0.72
6917 (spar)	10906	1625	6.71	0.70313	0.324	-0.95
7906 (spar)	9967	575	17.3	0.70332	0.386	-0.76
10303 (spar)	9687	1107	8.75	0.70334	0.359	-0.88
11622 (spar)	9916	1597	6.21	0.70321	0.432	-0.64
15239 (spar)	10045	27.6	364	0.70329	0.542	-0.62
NÍ 14320	10604	320	33.1	0.70337	n.m.	-0.69
NÍ 14525	10163	448	22.7	0.70331	0.311	-0.94
NÍ 1582	10262	146	70.3	0.70334	0.205	-0.59
NÍ 10784	9928	267	37.2	0.70334	0.412	-0.80
Bulandstindur	9192	159	57.8	0.70342	0.225	-0.78
NÍ 14632 (spar)	9908	1112	8.91	0.70337	0.288	-1.01
NÍ 14231	10130	102	99.3	0.70311	0.411	-0.68
B9435	9883	1507	6.56	0.70337	0.273	-1.18
Sturlugata	9762	588	16.6	0.70334	0.293	-1.09
Heulandite						
NI 14320	1202	58485	0.02	0.70314	0.295	-2.01
NI 14525	nd	81924	n.m.	0.70327	0.214	n.m.
NI 14692	928	15329	0.06	0.70330	0.215	-1.79
NI 1582	857	24640	0.03	0.70333	0.182	-1.83
Heul A	685	23164	0.03	0.70331	0.223	-2.24
B4133	1262	28434	0.04	0.70333	0.174	-1.72
Stilbite						
NI 14692	1363	27.0	50.5	0.70346	0.476	-1.07
NI 10784	538	358	1.50	0.70333	0.542	-1.32
Bulandstindur	1391	24.6	56.5	0.70348	0.531	-0.69
BF-10	153	18.5	8.27	0.70396	0.580	-0.90

See Jacobson et al. (2015) for full description of sample locations.
n.m. indicates not measured

3.4.2 $\delta^{88/86}$Sr values

Basalt bedrock has an average, narrowly confined, $\delta^{88/86}$Sr value of 0.276 ± 0.016‰ ($1\sigma_{SD}$, n = 6), which is similar to the $\delta^{88/86}$Sr values of the USGS Icelandic basalt standard BIR-1 and the Hawaiian basalt standard BHVO-1 (see Andrews et al., 2016). Calcite samples exhibit a wide range of $\delta^{88/86}$Sr values, from 0.205‰ to 0.542‰, with an average of 0.347 ± 0.090‰ ($1\sigma_{SD}$, n = 14), and are generally isotopically heavier than basalt. Heulandite samples have an average $\delta^{88/86}$Sr value of 0.217 ± 0.043‰ ($1\sigma_{SD}$, n = 6) and are on average, isotopically lighter than basalt. Finally, stilbite samples have an average $\delta^{88/86}$Sr value of 0.533 ± 0.043‰ ($1\sigma_{SD}$, n = 4) and represent the isotopically heaviest lithological reservoir measured for the sample set.

Glacial and non-glacial rivers, as well as groundwaters, have $\delta^{88/86}$Sr values that are, on average, higher than those for basalt. Glacial rivers have a relatively wide range of $\delta^{88/86}$Sr values producing an average of 0.414 ± 0.078‰ ($1\sigma_{SD}$, n = 7), while non-glacial rivers show less variability and have an average $\delta^{88/86}$Sr value of 0.388 ± 0.019‰ ($1\sigma_{SD}$, n = 3). Groundwaters have an average $\delta^{88/86}$Sr value of 0.371 ± 0.057‰ ($1\sigma_{SD}$, n = 8).

3.5 Discussion

3.5.1 Water geochemistry

3.5.1.1 Mixing control

Radiogenic Sr isotope ratios robustly trace source mixing because the normalizing procedure inherent to the TIMS measurement eliminates any mass-dependent fractionation that might occur in nature. Therefore, all variation in $^{87}Sr/^{86}Sr$ ratios reflects changes in the relative abundance of ^{87}Sr due to radioactive decay of ^{87}Rb. Figure 3.2 plots $^{87}Sr/^{86}Sr$ ratios versus Ca/Sr

ratios for water, rock, and mineral samples. Additional data for glacial and non-glacial rivers taken from Hindshaw et al. (2013a) are included. Here, we assume that Ca/Sr ratios conservatively trace source-mixing effects. Calcite precipitation is unlikely to affect riverine Ca/Sr ratios because the waters studied are significantly undersaturated with respect to calcite (Jacobson et al., 2015). Rivers appear to display three-component mixing between basalt and one end-member that increases $^{87}Sr/^{86}Sr$ ratios and another that increases Ca/Sr ratios. While Iceland supports vigorous hydrothermal systems, we eliminate hydrothermal water as a mixing end-member on the basis of previous studies demonstrating that such inputs are generally too small to explain river geochemistry (Vigier et al., 2009). Moreover, hydrothermal waters and rivers typically have similar Sr and Ca concentrations (Kaasalainen et al., 2015), such that by mass-balance, minor hyrothermal water inputs would not dramatically influence riverine geochemistry. We interpret the high $^{87}Sr/^{86}Sr$ ratio end-member to be atmospheric deposition of Sr with a seawater-like composition, which is expected given Iceland's proximity to the ocean and relatively small size. Hindshaw et al. (2013a) similarly identified atmospheric deposition of seawater Sr as a factor for the radiogenic Sr isotope composition of Icelandic rivers. Consistent with the interpretation of Ca isotope ratios (Jacobson et al., 2015), calcite weathering provides the most likely explanation for the end-member with high Ca/Sr ratios. Figure 3.2 shows that glacial rivers have higher relative contributions of Sr from calcite compared to non-glacial rivers, which is consistent with the expectation that higher mechanical erosion rates inherent to glacial watersheds should facilitate calcite exposure and weathering (Jacobson et al., 2015). Indeed, glacial rivers are generally closer to saturation with respect to calcite than non-glacial rivers (Jacobson et al., 2015). However, the exact proportions of Sr from silicate and carbonate weathering are difficult to quantify because calcite Ca/Sr ratios widely vary. We note that stilbite

also has high Ca/Sr ratios. While contributions from stilbite weathering cannot be entirely ruled out, significant contributions seem unlikely given that stilbite dissolves orders of magnitude slower than calcite (Chou et al., 1989; Glover et al., 2010). Groundwaters fall along the rock – mineral mixing line, with limited contributions from the third, high $^{87}Sr/^{86}Sr$ end-member. This is consistent with intuition that the high $^{87}Sr/^{86}Sr$ end-member is atmospheric deposition, which is not expected to significantly affect the Sr isotope composition of groundwater at a regional scale. Nonetheless, the two groundwater samples with higher $^{87}Sr/^{86}Sr$ ratios (samples K2745 and SNO) could reflect either localized infiltration of surface water transporting atmospherically-derived Sr (Walker, 1960) or direct incursion of seawater into hydrothermal systems (Arnorsson, 1970).

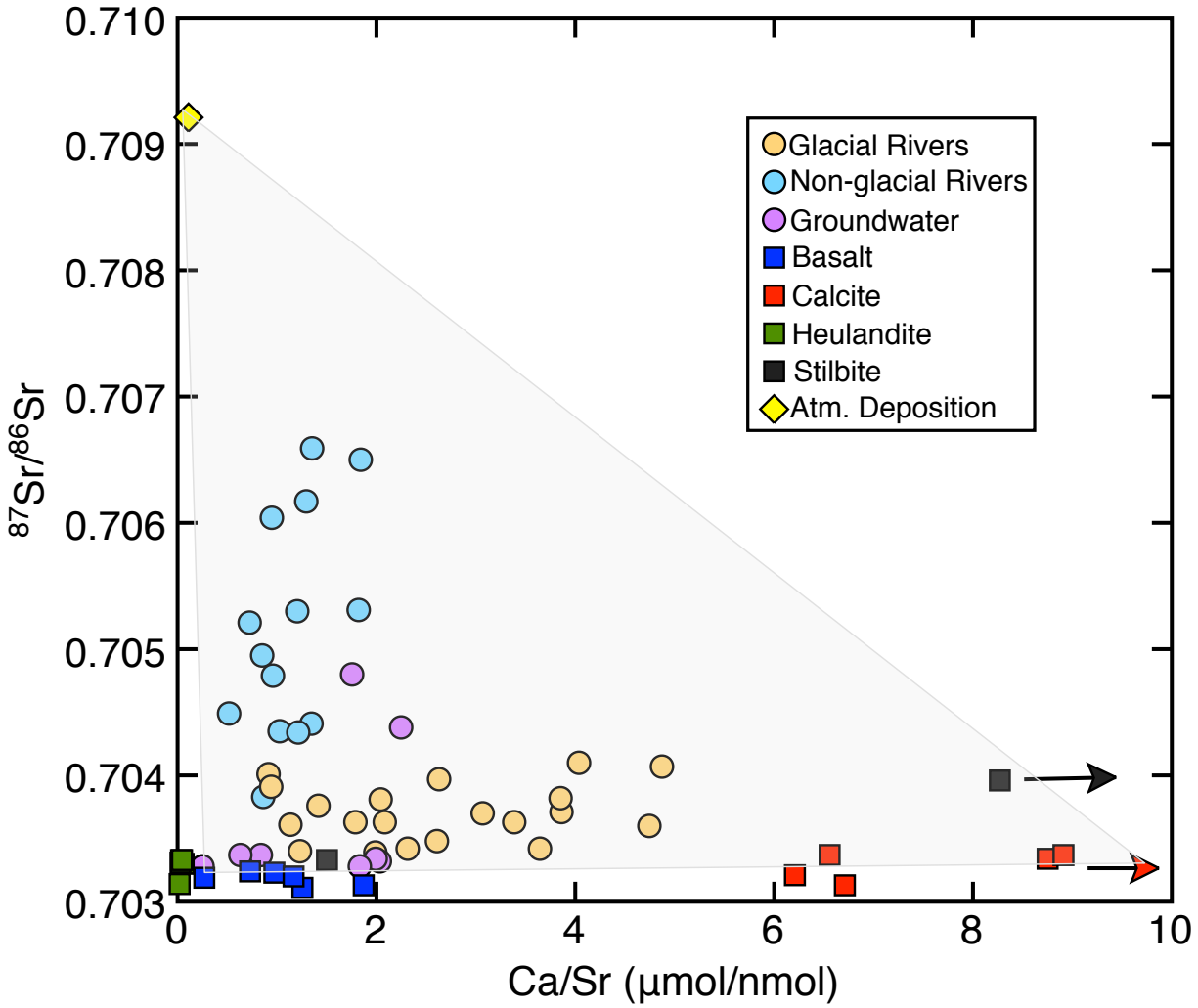

Figure 3.2: $^{87}Sr/^{86}Sr$ versus Ca/Sr ratios for Icelandic waters, rocks, and minerals. Some glacial and non-glacial river data reported in Hindshaw et al. (2013). Red arrow indicates that some calcite samples, not shown, plot to higher Ca/Sr ratios (see Table 2). Black arrow indicates that some stilbite samples, not shown, plot to higher Ca/Sr ratios (see Table 2). Gray shaded area corresponds to the basalt, calcite, and atmospheric deposition mixing regime. Riverine and groundwater Ca/Sr ratios have not been corrected for atmospheric inputs.

Figure 3.3 plots $\delta^{88/86}Sr$ values versus $^{87}Sr/^{86}Sr$ ratios for water, rock, and mineral samples. Most waters have higher $\delta^{88/86}Sr$ values than bedrock, a pattern that has been documented in several other stable Sr isotope studies (e.g., Chao et al., 2015, Pearce et al., 2015 and references therein, Andrews et al., 2016, Stevenson et al., 2016). Calcite $\delta^{88/86}Sr$ values are

also largely higher than those for basalt and span the range of riverine $\delta^{88/86}$Sr values. Because the $\delta^{88/86}$Sr value expected for atmospheric deposition falls within the range of calcite $\delta^{88/86}$Sr values, atmospheric deposition is only a constraint in $^{87}Sr/^{86}Sr$ space. Figure 3.3 is consistent with the interpretation drawn from Figure 3.2 that rivers reflect three-component mixing between basalt, calcite, and atmospheric deposition. Glacial rivers generally have higher $\delta^{88/86}$Sr values than non-glacial rivers, which is also consistent with the conclusion drawn from Figure 3.2 that glacial rivers have higher relative contributions of Sr from calcite than non-glacial rivers. As noted above, although contributions from stilbite weathering cannot be entirely ruled out, we add here that, by mass-balance, stilbite is unlikely to significantly affect riverine $\delta^{88/86}$Sr values because the mineral has very low Sr concentrations (Table 3.2). Groundwater $\delta^{88/86}$Sr values are higher than those for basalt and largely plot within the basalt – calcite regime, with the exception of the two samples noted above that show measurable contributions from the third end-member.

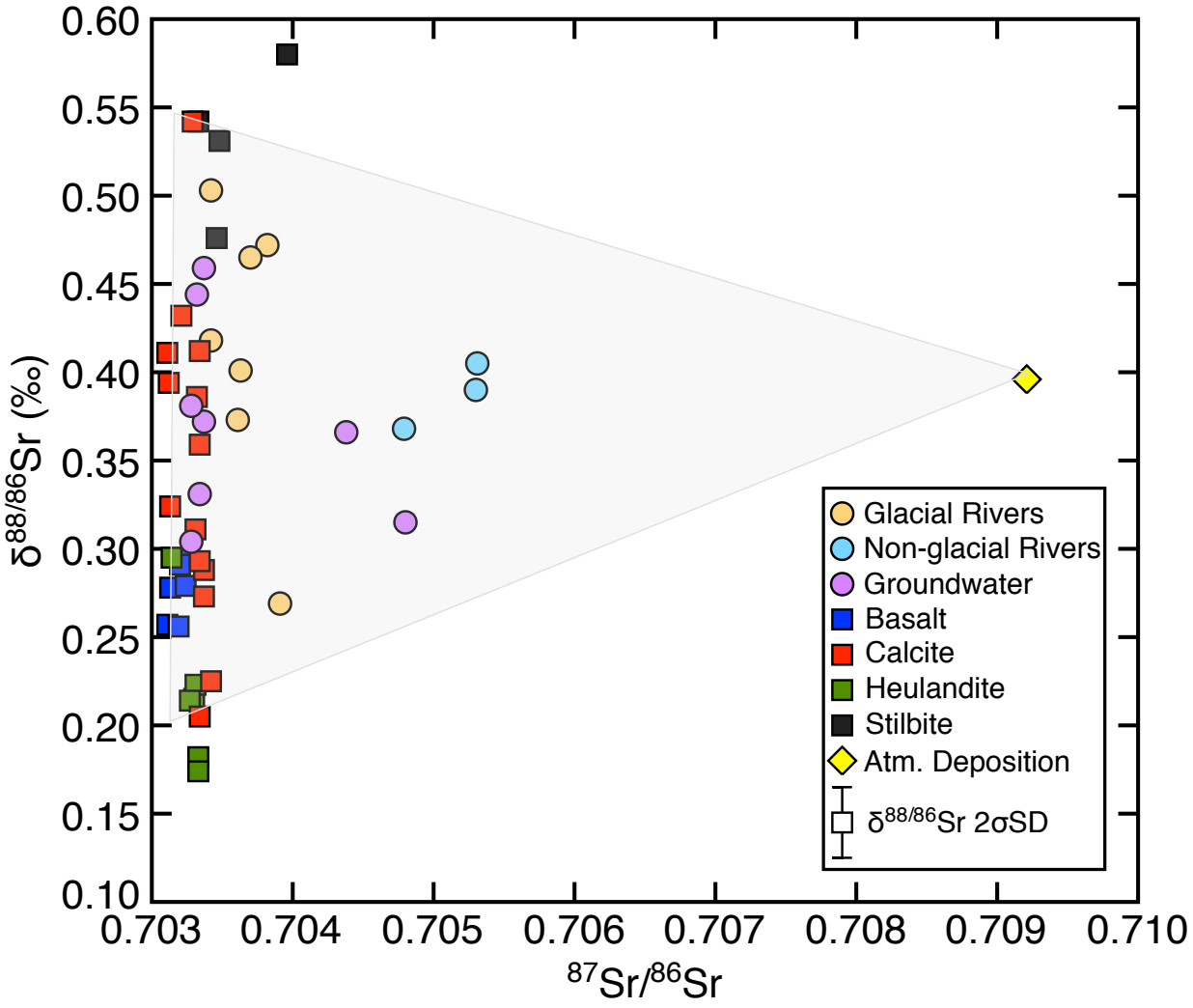

Figure 3.3: $\delta^{88/86}Sr$ values versus $^{87}Sr/^{86}Sr$ ratios for Icelandic waters, rock, and minerals. Gray shaded area corresponds to the basalt, calcite, and atmospheric deposition mixing regime.

3.5.1.2 Fractionation control

An alternative hypothesis is that riverine $\delta^{88/86}Sr$ values reflect mass-dependent fractionation. Several processes can affect the stable Sr isotope composition of surface waters, including plant uptake (Andrews et al., 2016; Bullen and Chadwick, 2016; de Souza et al., 2010), carbonate precipitation (Böhm et al., 2012; Fietzke and Eisenhauer, 2006; Krabbenhöft et al., 2010; Shalev et al., 2017; Stevenson et al., 2014; Vollstaedt et al., 2014), and potentially, mineral

dissolution and clay formation (Halicz et al., 2008; Pearce et al., 2015b; Stevenson et al., 2016; Wei et al., 2013). In Iceland, plant uptake is assumed to negligibly affect riverine $\delta^{88/86}$Sr values because vegetation is scarce. Additionally, secondary carbonate precipitation is unlikely to influence $\delta^{88/86}$Sr values because rivers are significantly undersaturated with respect to calcite (Jacobson et al., 2015). Hindshaw et al. (2013a) suggested that clay and zeolite formation, as well as adsorption onto mineral surfaces, fractionates Ca isotopes in Icelandic rivers. Similarly, Stevenson et al. (2016) concluded that preferential uptake of lighter Sr isotopes by secondary minerals modestly increased $\delta^{88/86}$Sr values (≤ 0.1‰) in the outflow draining the Lemon Creek glacier in Alaska. Preferential uptake of lighter Sr isotopes by clay minerals could explain the general observation that Icelandic rivers have higher $\delta^{88/86}$Sr values relative to basalt, but the mechanism would have to elicit more fractionation (up to 0.2‰) than observed in the Lemon Creek outflow. Furthermore, more clay formation would have to occur in glacial catchments than non-glacial catchments to explain why glacial rivers have higher $\delta^{88/86}$Sr values than non-glacial rivers. While subglacial clay formation clearly occurs (e.g., Crompton et al., 2015), Si isotope data for Icelandic rivers reveal less clay formation in glacial catchments than non-glacial catchments (Georg et al., 2007). Finally, preferential uptake of lighter Sr isotopes by zeolites is unlikely to explain the high riverine $\delta^{88/86}$Sr values relative to basalt. Fridrikkson et al. (2009) suggested that precipitation of, or ion-exchange with, heulandite increases groundwater Ca/Sr ratios because the mineral has a much higher affinity for Sr relative to Ca. Although heulandite appears to preferentially incorporate lighter Sr isotopes relative to basalt, such that it could drive groundwater to higher $\delta^{88/86}$Sr values (section 3.5.2), this process is unlikely to affect river water. In the low-temperature geothermal areas that may actively precipitate zeolites, heulandite is not a modally abundant phase (Kristmannsdottir and Tomasson, 1976). Furthermore, ion-exchange

with ancient heulandite exposed at the surface seems unlikely because the apparent heulandite – basalt fractionation factor (-0.059‰, section 3.5.2) cannot account for the magnitude of fractionation observed in rivers relative to basalt (≤ +0.227‰). Although this magnitude of fractionation could be achieved through successive water – rock(heulandite) interactions, water residence times in surficial systems are likely too short to promote the necessary reservoir effect. Additionally, stilbite appears to preferentially incorporate heavier Sr isotopes relative to basalt, such that stilbite formation would lower riverine $\delta^{88/86}$Sr values. In general, with the current dataset, we cannot identify a fractionation mechanism that reasonably explains why rivers have higher $\delta^{88/86}$Sr values than basalt. Three-component mixing between basalt, calcite, and atmospheric deposition, as suggested by the $^{87}Sr/^{86}Sr$ ratio framework, adequately accounts for the Sr isotope geochemistry of rivers. As such, we conclude that mixing provides the most likely explanation for the dataset. Three-component mixing does not eliminate the possibility of fractionation. It simply implies that if fractionation does occur, then the magnitude is smaller than the isotopic range of the mixing end-members.

3.5.2 Mineral geochemistry

Determining controls on mineral geochemistry is critical for understanding how mineral weathering controls riverine and groundwater geochemistry. Figure 3.4 plots $\delta^{44/40}$Ca versus $\delta^{88/86}$Sr values for rocks and minerals. Similar to the case for $\delta^{44/40}$Ca values (Jacobson et al., 2015), bulk basalt samples exhibit a narrow range of $\delta^{88/86}$Sr values. This suggests that the primary Sr-bearing silicate minerals composing basalt, such as plagioclase and clinopyroxene, also have a narrow range of $\delta^{88/86}$Sr values. On the other hand, the minor secondary minerals, namely heulandite, stilbite, and calcite, exhibit considerable isotopic contrast, most likely due to

mass-dependent fractionation. Assuming the Sr in heulandite and stilbite originates from basalt, the stable Sr isotope data correspond to average, effective fractionation factors ($\Delta^{88/86}Sr_{mineral - basalt}$) of -0.059‰ and 0.257‰, respectively. Similarly, assuming the Ca in heulandite and stilbite originates from basalt, the Ca isotope data correspond to average, effective fractionation factors ($\Delta^{44/40}Ca_{mineral - basalt}$) of –0.860‰ and 0.126‰, respectively. The calcite samples do not produce a well-defined average value. Rather, 11 out of 14 samples define a highly correlated and statistically significant regression line ($R^2 = 0.92$, $p < 0.0001$) that passes directly through the average basalt composition. A crucial question is then, why do the calcite $\delta^{88/86}Sr$ and $\delta^{44/40}Ca$ values linearly correlate?

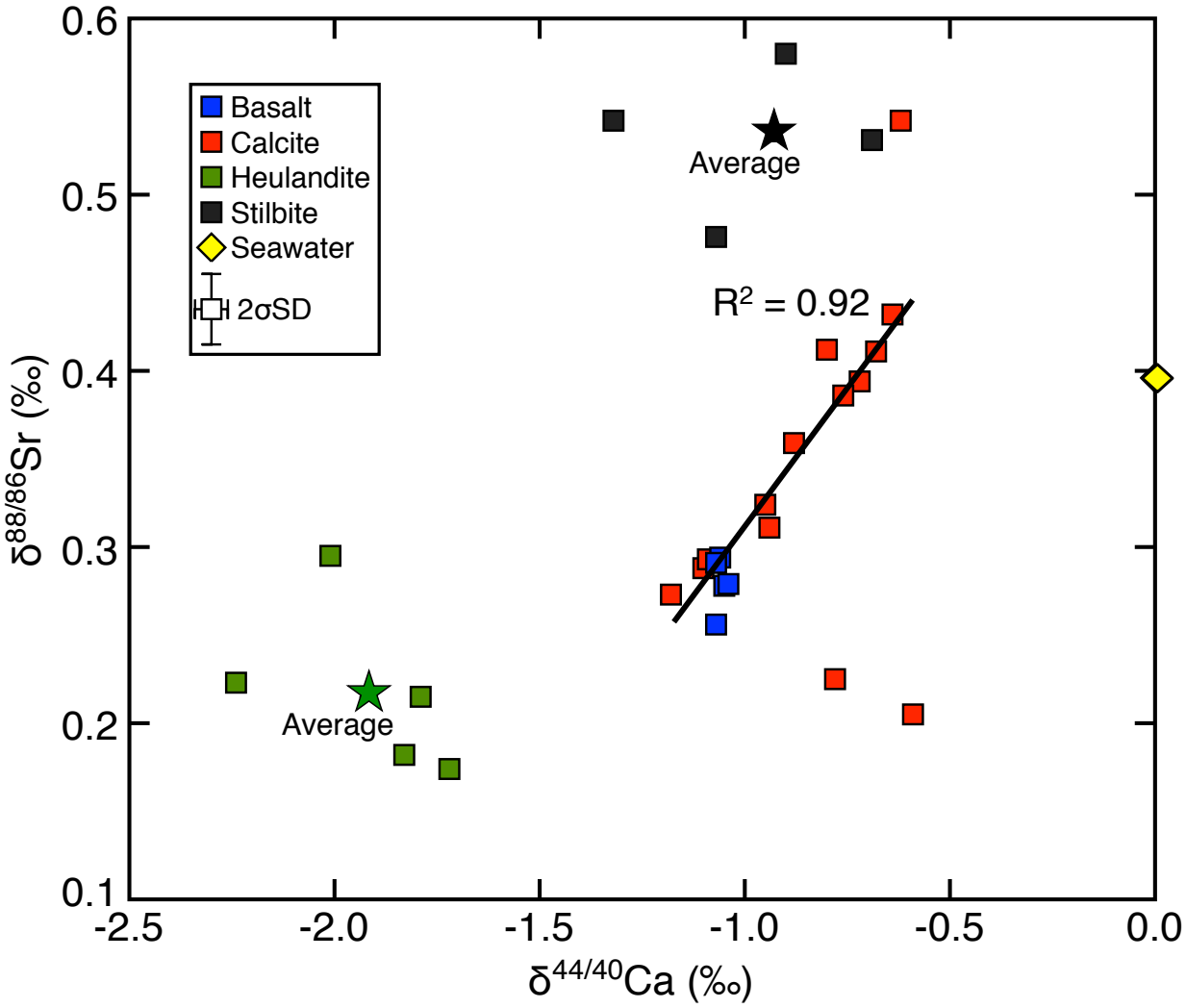

Figure 3.4: $\delta^{88/86}$Sr versus $\delta^{44/40}$Ca values for Icelandic rocks and minerals. Green star corresponds to average isotopic composition for heulandite samples, and black star corresponds to average isotopic composition for stilbite samples. Regression line and R^2 value correspond to calcites, except samples 15239, NÍ 1582, and Bulandstindur.

Beyond calcite deposits localized around active hot springs, which compose a minor fraction of Iceland's land surface area (Kristmannsdottir and Tomasson, 1976), Icelandic calcites can be broadly grouped into two categories based on their occurrence and associated phases. Much of Iceland's calcite is dispersed throughout the Tertiary flood basalts. The calcites formed during the later stages of the zeolite facies burial metamorphism pathway, which has been

extensively studied in Iceland since the 1950s (Walker, 1958) and identified in flood basalt settings worldwide (Christiansen et al., 1999; Jørgensen, 1984; Larsen et al., 1989; Murata et al., 1987; Neuhoff et al., 2000; Neuhoff et al., 1997; Schmidt, 1993; Sukheswala et al., 1974). The metabasalts reflect temperature-controlled zones defined by modally abundant index zeolites (Neuhoff et al., 2000 and references therein). Heulandite and stilbite are often co-index minerals, occupying the same zone, and are among the highest temperature (greatest depth) index zeolites (Neuhoff et al., 2000). Calcite is a minor phase throughout all zones (all depths) and is not typically described as spar (Neuhoff et al., 2000). In addition, high concentrations of calcite occur in localized, higher-grade metamorphic volcanic centers within the flood basalts (Carmichael, 1964; Mehegan et al., 1982; Walker, 1960, 1963). The volcanic centers are interpreted as volcanic complex cupolas and are marked by a core of propylitized rock containing epidote, chlorite, andradite garnet, pyrite, and calcite (Carmichael, 1964; Mehegan et al., 1982; Walker, 1960, 1963). Broad hydrothermal aureoles surrounding the propylitized cores contain abundant platy calcite, plus laumontite and quartz (Carmichael, 1964; Mehegan et al., 1982; Walker, 1960, 1963). The Helgustadir Spar Mine, the largest producer of Icelandic spar, occurs within one such aureole (Walker, 1960). Zeolites, beyond laumontite, are not commonly found as part of the volcanic center assemblages. Calcites that compose the linear correlation in Figure 3.4 include those from zeolite-zoned Tertiary flood basalts and localized volcanic aureoles, and they represent spar and non-spar varieties. Of those collected from zeolite-zoned Tertiary basalts, calcite physically separated from co-existing stilbite and heulandite, as well as calcite not paired with a zeolite mineral, plot on the line. An explanation for the linear correlation therefore requires a general mechanism applicable to the diverse sample set.

Under conditions of chemical equilibrium, wherein $\Delta^{88/86}Sr_{calcite - soln}$ and $\Delta^{44/40}Ca_{calcite - soln}$ are effectively 0‰ (Böhm et al., 2012; Fantle and DePaolo, 2007; Jacobson and Holmden, 2008), calcite preserves the isotopic composition of the solution from which it precipitates. Mixing of Sr and Ca derived from basalt and yet another, regionally extensive, end-member with higher $\delta^{88/86}Sr$ and $\delta^{44/40}Ca$ values could explain the calcite correlation. In this instance, seawater, which may have circulated in the paleo-subsurface, offers the most logical explanation. While modern seawater does not have the appropriate isotopic composition to explain the trend (Fig. 3.4), seawater likely had a different isotopic composition during the Tertiary. To represent the second reservoir, seawater would have to have a $\delta^{88/86}Sr$ value $\geq$ 0.43‰. Values this high occurred during the Phanerozoic (Vollstaedt et al., 2014). However, Tertiary seawater $\delta^{44/40}Ca$ values were lower compared to the present (Farkas et al., 2007). Because seawater $\delta^{88/86}Sr$ and $\delta^{44/40}Ca$ values tend to positively correlate (Vollstaedt et al., 2014), mixing between basalt and paleo-seawater does not offer a satisfactory explanation for the dataset.

Potentially, calcite could have precipitated from an initially basaltic solution subject to varying degrees of fractionation by secondary mineral formation (e.g., zeolites). By necessity, the secondary mineral would preferentially incorporate lighter Sr and Ca isotopes, relative to basalt, and fall along the regression line defined by calcite and basalt. Heulandite preferentially incorporates both lighter Sr and Ca isotopes relative to basalt, and the mineral has extremely high Sr concentrations relative to other reservoirs because it preferentially incorporates Sr over Ca (Fridriksson et al., 2009; Fridriksson et al., 2004; Pabalan and Beretti, 2001). By mass balance, heulandite may represent a large enough Sr reservoir within the heulandite-stilbite zeolite zone to drive groundwater, and ultimately calcite, geochemistry. The range of calcite $\delta^{88/86}Sr$ and $\delta^{44/40}Ca$ values could reflect varying degrees of progressive water-rock(heulandite) interactions, with the

highest $\delta^{88/86}$Sr and $\delta^{44/40}$Ca values reflecting precipitation from the most geochemically evolved groundwaters. Nonetheless, the basalt-calcite regression line does not pass through the heulandite samples, and it is unclear how heulandite fractionation at depth could drive the isotopic composition of calcite precipitated higher in the Tertiary lava pile, or in volcanic aureoles that lack heulandite. However, we note that laumontite in volcanic aureoles may have formed by replacement of earlier precipitated heulandite (Mehegan et al., 1982). Icelandic basalts contain other Ca- and Sr- bearing zeolites and clays formed under hydrothermal conditions, such as chabazite, thomsonite, and smectite, which could play a role in determining groundwater, and ultimately, calcite isotopic compositions.

Finally, under kinetically-controlled conditions, calcite fractionates Sr and Ca isotopes to varying degrees based largely on precipitation rate (Böhm et al., 2012; Lemarchand et al., 2004), such that the mineral no longer preserves the isotopic composition of the solution from which it forms. Therefore, the regression line could represent a kinetic mass-dependent fractionation line of calcite precipitated from an initially basaltic solution. However, at least under the low-temperature conditions that have been investigated to date, calcite incorporates lighter Sr and Ca isotopes (e.g., Lemarchand et al., 2004, Fietzke and Eisenhauer, 2006; Tang et al., 2008; Böhm et al., 2012, Stevenson et al., 2014), such that the calcites analyzed in the present study would be expected to have lower $\delta^{88/86}$Sr and $\delta^{44/40}$Ca values than basalt. Thus, precipitating calcite with relatively high $\delta^{88/86}$Sr and $\delta^{44/40}$Ca values would require a substantial reservoir effect (i.e., precipitation of other calcite with low $\delta^{88/86}$Sr and $\delta^{44/40}$Ca values) or an altogether different fractionation direction at higher temperatures, which is not consistent with the Ca isotope composition of hydrothermal calcites found in other settings (Brown et al., 2013). Barring the one calcite sample (B9435) with a marginally lighter isotopic composition than basalt, the

necessary light reservoir has not been identified. On a plot of $\Delta^{88/86}Sr_{calcite - soln}$ versus $\Delta^{44/40}Ca_{calcite - soln}$, inorganic calcites precipitated in the laboratory produce a mass-dependent fractionation line with a slope of 0.176 ± 0.04 (Böhm et al., 2012). At 0.34, the slope of the regression line in Figure 3.4 is twice as high, requiring a mechanism their either doubled the magnitude of Sr isotope fractionation or halved the magnitude of Ca isotope fractionation in calcite. In summary, we have not identified a mechanism that readily explains the correlation between calcite $\delta^{88/86}Sr$ and $\delta^{44/40}Ca$ values. Additional experiments and analyses are required to develop a more complete understanding of the complex Icelandic system.

3.5.3 The long-term C cycle

Findings presented in this study, as well as Jacobson et al. (2015), suggest that the dissolution of hydrothermal calcite controls much of the Icelandic riverine alkalinity flux relevant to the long-term C cycle. While the chemical weathering of "old" (>1 Myr) sedimentary carbonate rocks does not impact long-term climate (e.g., Berner et al., 1983), the question arises whether the same interpretation applies to hydrothermal calcite, such as that present in Iceland. To address this question, we adapted the long-term C cycle model for the atmosphere-ocean system presented in Kump and Arthur (1999) (see Appendix B). With the model, we evaluate several factors important for understanding long-term climate evolution, including the location of silicate weathering (surface vs. subsurface), the forms of C delivered to the atmosphere-ocean system (CO_2 vs. HCO_3^-), CO_2 sources that contribute to the formation of hydrothermal calcite (volcanic vs. atmospheric), and the timescale of hydrothermal calcite formation and dissolution (<1 Myr vs. >1 Myr).

Like nearly all models of the long-term C cycle (e.g., Berner, 1990; Arvidson et al., 1996; Wallmann, 2001), the Kump and Arthur (1999) model prescribes that volcanoes and mid-ocean ridges emit C into the atmosphere-ocean system as CO_2 . Here, we consider that some fraction of the total CO_2 degassed from the solid Earth can participate in hydrothermal silicate weathering reactions in the shallow subsurface (e.g., Rad et al., 2007; Dessert et al., 2009; Hurwitz et al., 2010; Rivé et al., 2013) such that volcanism, via groundwater discharge to rivers, may introduce C into the atmosphere-ocean system as alkalinity (hereafter, HCO_3^-) instead of CO_2. . Hydrothermal calcite can sequester some of the subsurface HCO_3^- (e.g., Varekamp et al., 1992; Kerrick and Caldeira, 1998; Weise et al. 2008) and delay its transmission to the atmosphere-ocean system until it dissolves later in time. In the sections that follow, we first consider the case where groundwater discharges all of the subsurface HCO_3^- to the atmosphere-ocean system (section 3.5.3.1). With the role of subsurface silicate weathering established, we then consider effects from the formation and dissolution of hydrothermal calcite (section 3.5.3.2) and apply this understanding to Iceland.

3.5.3.1 Subsurface silicate weathering

Incorporating subsurface silicate weathering into the traditional long-term C model (Eq. B8) confirms the basic premise of the Urey-Ebleman equation, namely that volcanic C must be injected into the atmosphere-ocean system as CO_2 to close the loop on the long-term C cycle. Only the balance between CO_2 inputs from volcanism and CO_2 outputs from silicate weathering directly controls long-term C stores in the atmosphere-ocean system, and hence climate, provided the ocean instantaneously responds to riverine HCO_3^- inputs by outputting calcium

carbonate (Kump and Arthur, 1999). The model framework presented here supports the contention that volcanic C introduced into the atmosphere-ocean system as HCO_3^- ($F_{volc}^{HCO_3^-}$) "short circuits" climate regulation (Rive et al., 2013). All volcanic C contributes to marine carbonate formation, but depending on the magnitude of $F_{volc}^{HCO_3^-}$ and its variation through geologic time, it follows that some fraction of the carbonate rock record may not directly relate to long-term climate feedbacks.

When the fraction of the total volcanic C flux (F_{volc}^{tot}) directed to subsurface silicate weathering ($F_{volc}^{HCO_3^-}$) equals zero, equation B11 (see Appendix B) is effectively identical to equation 13 in Kump and Arthur (1999) and other traditional formulations of the long-term C cycle. Increasing $F_{volc}^{HCO_3^-}$ reduces the fraction of the volcanic C flux input to the ocean-atmosphere system as CO_2 ($F_{volc}^{CO_2}$), which in turn reduces the surficial silicate weathering flux ($F_{w,sil}^{sur}$) because the silicate weathering feedback depends on atmospheric CO_2 (e.g., Walker et al., 1981; Berner et al., 1983; Volk et al., 1987; Caves et al., 2016). The net result is that the atmosphere achieves steady-state at lower pCO_2 levels compared to the case where all volcanic C is introduced as CO_2. All else being equal, increasing $F_{volc}^{CO_2}$ leads to a warmer climate, while increasing $F_{volc}^{HCO_3^-}$ leads to a cooler climate. Thus, it can be concluded that the two forms of volcanic C introduction to the atmosphere-ocean system cannot be treated identically.

Equation 3.2 provides an example of a typical weathering feedback function (Caves et al., 2016):

$$F_{w,sil}^{CO_2} = k\left[\log_2\left(R_{CO_2}+1\right)\right], \tag{3.2}$$

where $F_{w,sil}^{CO_2}$ is the long-term atmospheric CO_2 consumption flux from silicate weathering determined by measuring the total riverine HCO_3^- input flux (F_{riv}^{tot}), R_{CO_2} is the ratio of pCO_2 at some time *t* relative to the present-day, $\log_2$ reflects the sensitivity of the climate system to changes in pCO_2 (Knutti and Hegerl, 2008), and *k* is a constant of proportionality that reflects several other factors related to the feedback strength (e.g., the proportion of continental land area comprising basalt). Values for pCO_2 at some time *t* are determined by apportioning *M* between the atmosphere and ocean (see equation (7) in Kump and Arthur, 1999). Because equation 3.2 does not apply to hydrothermal systems and the subsurface silicate weathering flux ($F_{w,sil}^{sub}$) does not impact the C inventory of the atmosphere-ocean system (see Appendix B), $F_{w,sil}^{CO_2}$ should only equate to $F_{w,sil}^{sur}$. Thus, depending on how equation 3.2 is employed, neglecting the contribution of $F_{w,sil}^{sub}$ to F_{riv}^{tot} or setting the sum of $F_{w,sil}^{sub}$ and $F_{w,sil}^{sur}$ equal to $F_{w,sil}^{CO_2}$ would imply a higher feedback strength, higher atmospheric CO_2 levels, or a greater climate sensitivity than actually exist, which in turn becomes problematic when using modern-day calibrations of equation 3.2 to quantify paleo-conditions. Neglecting to differentiate the two different sources of riverine HCO_3^- could explain why most independently constrained estimates for $F_{volc}^{CO_2}$ (e.g., 2.3×10^{12} mol/yr; Kerrick, 2001) and $F_{w,sil}^{sur}$ (e.g., 11.7×10^{12} mol/yr; Gaillardet et al., 1999) do not agree. Most field studies assume that F_{riv}^{tot} entirely represents $F_{w,sil}^{sur}$, but owing to elevated temperatures, higher pCO_2 values, and longer water residence times inherent to hydrothermal systems (Rad et al., 2011, Thomas et al., 2016), subsurface silicate weathering rates exceed surficial silicate weathering rates, and the contribution of $F_{w,sil}^{sub}$ can be sizable (Rad et al., 2007; Dessert et al,

2009; Rivé et al., 2013). To properly calculate long-term atmospheric CO_2 consumption rates, our analysis suggests that studies should subtract $F_{w,sil}^{sub}$ from F_{riv}^{tot} and/or refrain from combining independently constrained estimates for $F_{w,sil}^{sur}$ and $F_{w,sil}^{sub}$, especially in volcanic settings where $F_{w,sil}^{sub}$ derives from ascending solid Earth CO_2.

3.5.3.2 Hydrothermal calcite

The model results (Eq. B8) demonstrate that HCO_3^- derived from subsurface silicate weathering by volcanic CO_2 does not directly regulate long-term climate. If hydrothermal calcite simply sequesters some of this HCO_3^- until it dissolves at the surface later in time, then it's reasonable to conclude that the weathering of hydrothermal calcite bearing non-atmospheric C also has no direct impact on long-term climate regulation (Jacobson et al., 2015). If the timescale of hydrothermal calcite formation and weathering is short (<1 Myr), then the transfer of volcanic C to marine carbonate rocks is delayed, but the lag is inconsequential with respect to the long-term C cycle. While calcite formation releases CO_2 to the atmosphere, calcite weathering consumes an equivalent amount of CO_2 such that no change in the atmospheric inventory occurs. This scenario is indistinguishable from the case where groundwater discharge delivers all subsurface HCO_3^- to rivers, and is akin to a climate regulation "short-circuit" (Rivé et al., 2013).

Over longer timescales (> 1 Myr), the CO_2 that hydrothermal calcite formation contributes may increase $F_{volc}^{CO_2}$, such that the atmosphere stabilizes at higher pCO_2 levels compared to the case where no hydrothermal calcite forms but still lower levels compared to the case where no subsurface silicate weathering occurs. Regardless, when considering timescales >1 Myr, identifying the source of C in hydrothermal calcite (volcanic vs. atmospheric) becomes

less critical, as the situation is more analogous to the weathering of old sedimentary carbonate rocks. Some studies have dismissed hydrothermal calcite weathering on the basis that hydrothermal calcite represents an intermediate reservoir for silicate weathering byproducts. However, sedimentary carbonate rocks may also be considered intermediate reservoirs for silicate weathering byproducts, and their role in the long-term C cycle is well understood. The weathering of sufficiently old sedimentary carbonate rocks does not affect long-term climate (e.g., Berner et al., 1983). The same logic must therefore apply to the weathering of old hydrothermal calcite. The weathering of carbonate-bearing rocks and minerals with ages >1 Myr followed by marine carbonate precipitation produces no change in atmospheric CO_2 levels. In other words, if it can be demonstrated that hydrothermal calcite contains old atmospheric C or non-atmospheric C of any age, then the carbonate weathering flux ($F_{w,carb}$) should be subtracted from F_{riv}^{tot} before calculating CO_2 consumption rates, in the same way that $F_{w,sil}^{sub}$ should be subtracted from F_{riv}^{tot}, as described above. Given that calcite dissolves orders of magnitude faster than silicate minerals, such corrections are particularly necessary if the goal is to use equation 3.2 or similar versions thereof to constrain the nature of the basalt "silicate" weathering feedback. The same logic applies to riverine fluxes of Ca^{2+} and Sr^{2+}. Appreciating that hydrothermal calcite contains cations derived from silicate mineral weathering is only relevant to the extent that riverine cations trace the sources of C (volcanic vs. atmospheric) that compose HCO_3^- (this study, Jacobson et al., 2015), which is the more important parameter for assessing feedbacks between basalt weathering and climate.

The model framework reveals only one scenario where the calcite weathering contribution may be neglected when attempting to constrain the long-term balance on

atmospheric CO_2. This is when calcite sequesters atmospheric CO_2 and forms and dissolves over relatively short timescales (<1 Myr). Calcite veins and calcite-rich surface travertine deposits precipitated from hyperalkaline springs, such as those found in the Samail Ophiolite in Oman (Kelemen and Matter, 2008; Mervine et al., 2014), offer a good example. Nonetheless, the calcites analyzed here and in Jacobson et al. (2015) did not precipitate from hyperalkaline springs, which are rare systems mostly limited to the alteration of peridotite, not basalt. Rather, the calcites formed during hydrothermal alteration associated with burial metamorphism and volcanism (section 3.5.2). Carbon isotope data, noble gas measurements, and attempts to quantify volcanic CO_2 emissions indicate that the calcites largely contain volcanic CO_2 degassed from the solid Earth prior to atmospheric injection (Armannsson, 2016; Arnorsson, 1986, 1995; Arnorsson and Stefansson, 2007; Barry et al., 2014; Marty et al., 1991; Sano et al., 1985; Thomas et al., 2016; Wiese et al., 2008). Moreover, while the absolute ages of the calcites are unknown, relative dating arguments suggest that the calcites form quickly (<1 Myr) and have approximately the same age as the basalt flows that contain them. In East Greenland, the ~55 Ma Skaergaard intrusion cuts across 55 – 57 Ma basalt flows produced by the Iceland hot spot (Neuhoff et al., 1997, Neuhoff et al., 2000 and references therein). The basalt flows contain the same zeolite zones (plus calcite) as observed in Iceland, except in an aureole surrounding the Skaergaard intrusion where prograde metamorphic reactions replaced the zeolite zones to yield higher-temperature mineral assemblages (minus calcite) (Manning et al., 1993; Neuhoff et al., 2000; Neuhoff et al., 1997). The best interpretation is that production of the zeolites and calcite predated the intrusion, which leads to the generalized conclusion that the zeolite zones form within 1 Myr after eruption of basalt and that the age of the zeolites and calcite can be considered identical to the radiometric age of the basalt (Neuhoff et al., 2000; Neuhoff et al., 1997). Most

Icelandic basalt formed during the Tertiary. Therefore, in the context of the model framework presented here, the evidence for volcanic C contained within the calcites, as well as their old age, suggest that the weathering of Icelandic calcite does not regulate long-term climate.

3.6 Conclusions

On average, Icelandic rivers have higher $\delta^{88/86}$Sr values than basalt; however, $\delta^{88/86}$Sr values for hydrothermal calcite are higher than those for basalt and span the range of riverine values. Interpreted in context with $^{87}Sr/^{86}Sr$ and Ca/Sr ratios, these results suggest that the Sr isotope geochemistry of Icelandic rivers represents three-component mixing between atmospheric deposition, basalt, and hydrothermal calcite. Glacial rivers appear to have higher relative contributions of calcite-derived Sr than non-glacial rivers, which we attribute to higher rates of physical erosion inherent to glacial watersheds that enhance calcite exposure and weathering. These findings are consistent with the interpretation of $\delta^{44/40}$Ca values determined for the same sample suite (Jacobson et al., 2015). The dominance of physical mixing does not preclude the possibility of Ca and Sr isotope fractionation. It simply implies that the magnitude of fractionation is smaller than the range of the mixing end-members. The preferential dissolution of highly weatherable trace phases, such as calcite, may contribute to the observation that many world rivers have higher $\delta^{88/86}$Sr values than local bedrock. This study also represents the first watershed-scale comparison of $\delta^{88/86}$Sr and $\delta^{44/40}$Ca values. Consistent with long-held assumptions, we find that Sr and Ca largely derive from the same sources, flow together during aqueous transport, and track the same isotope fractionation processes (or lack thereof).

Basalt and high-temperature metamorphic zeolites (e.g., heulandite and stilbite) have significantly different $\delta^{88/86}$Sr values. We interpret this as evidence for mass-dependent

fractionation. Relative to basalt, heulandite appears to preferentially incorporate lighter Sr isotopes, while stilbite incorporates heavier stable Sr isotopes. These results are consistent with the fractionation directions observed for $\delta^{44/40}$Ca values (Jacobson et al., 2015). The magnitude of the Sr isotope fractionation factor for each mineral appears to correspond to their relative affinities for Sr, wherein a greater affinity yields less fractionation. Hydrothermal and metamorphic calcites collected from locations throughout Iceland generate a highly correlated and statistically significant linear regression line between $\delta^{88/86}$Sr and $\delta^{44/40}$Ca values. The data could reflect reservoir effects stemming from fractionation by zeolites or an altogether different fractionation mechanism that remains to be elucidated.

We adapted the long-term C model from Kump and Arthur (1999) to evaluate how subsurface hydrothermal silicate weathering, as well as hydrothermal calcite formation and dissolution – such as that occurring in Iceland – influence long-term climate evolution. Transforming some fraction of the volcanic C flux to HCO_3^- during subsurface silicate weathering lowers the steady-state atmospheric CO_2 concentration obtained over geologic timescales, but the HCO_3^- flux plays no direct role in climate regulation. Hydrothermal calcite simply sequesters some of the subsurface HCO_3^-, such that the weathering of hydrothermal calcite bearing non-atmospheric C also plays no role in regulating climate. Our findings suggest that riverine HCO_3^- fluxes from Iceland should be corrected for the carbonate weathering contribution prior to calculating long-term atmospheric CO_2 consumption rates by silicate weathering.

Several studies have attempted to parameterize the sensitivity of the basalt weathering feedback by evaluating HCO_3^- concentrations and fluxes relative to temperature and runoff (Dessert et al., 2003; Li et al., 2016), but it follows from this study and Jacobson et al. (2015)

that a component of such correlations could reflect the thermodynamics and kinetics of carbonate weathering. The data and model framework reported here support the contention that the ratio of basalt-to-granite weathering may be less than 10 (Jacobson et al., 2015), which agrees well with previous conclusions deduced from numerical simulations (Berner, 2006). Finally, it is worth noting that portions of the sedimentary marine $^{87}Sr/^{86}Sr$ record have been employed to constrain climatic evolution over Earth history due to changes in the ratio of basalt-to-granite weathering (Allegre et al., 2010; Dessert et al., 2001; Li and Elderfield, 2013; Taylor and Lasaga, 1999). However, our findings for Iceland suggest that some fraction of the riverine Sr flux derives from hydrothermal calcite, which has the same $^{87}Sr/^{86}Sr$ ratio as basalt but does not impact atmospheric CO_2 levels upon weathering. More research is needed to determine whether findings for Iceland apply generally to other basaltic settings, but potentially, downturns in the $^{87}Sr/^{86}Sr$ record attributed to basalt weathering on the continents may not represent a simple proxy for atmospheric CO_2 consumption.

Chapter 4

Controls on the solute geochemistry of subglacial discharge from the Russell Glacier, Greenland Ice Sheet determined by radiogenic and stable Sr isotope ratios

4.1 Introduction

Glaciers and ice sheets are sites of substantial chemical weathering despite extremely cold temperatures (Anderson et al., 1997; Graly et al., 2014; Wadham et al., 2010 and references therein). This is largely due to high rates of physical erosion and bedrock communition that produce abundant fine-grained particles with fresh, reactive mineral surfaces (Anderson, 2005). The major ion geochemistry of discharge from valley glaciers overlying silicate bedrock largely reflects the weathering of non-silicate trace minerals, such as carbonates and sulfides (Anderson et al., 2000; Torres et al., 2017; Tranter et al., 2002b). Carbonates and sulfides contribute disproportionately to solute loads because their dissolution rates exceed those for primary, bedrock-forming silicate minerals by several orders of magnitude (Torres et al., 2017). Over geologic timescales, carbonic acid – carbonate weathering does not impact atmospheric CO_2 levels, while sulfide oxidation (sulfuric acid) – carbonate weathering yields a net release of CO_2 to the atmosphere (Berner et al., 1983; Torres et al., 2014). Nonetheless, the exact impact of glacial weathering on climate remains unclear. Previous studies have argued that chemical weathering in glacial landscapes minimally affects long-term climate (Anderson et al., 2000; Sharp et al., 1995; Tranter et al., 2002a; Tranter et al., 2002b), while more recent work points to potential climate warming (Torres et al., 2017). Regardless, a major assumption is that the geochemistry of discharge from valley glaciers represents that from ice sheets (Tranter et al., 2002a). However, while weathering fluxes from the Greenland Ice Sheet (GrIS), for example, are

comparable to those from valley glaciers, bulk ion geochemistry suggests they have significantly greater contributions of cations from silicate mineral weathering (Graly et al., 2014). Results from the Antarctic Ice Sheet indicate similar patterns (Wadham et al., 2010). These observations likely reflect the order of magnitude greater water transport distances under ice sheets compared to valley glaciers, which lead to longer water residence times and hence more extensive water/rock interactions (Graly et al., 2016; Wadham et al., 2010).

Here, we test the hypothesis that the GrIS can be a site of substantial silicate chemical weathering. We combine radiogenic and stable Sr isotope ratios ($^{87}Sr/^{86}Sr$ and $\delta^{88/86}Sr$) to track primary and secondary controls on solute acquisition in subglacial discharge from the Russell Glacier, southwestern GrIS, as well as along a ~32km transect of the Akuliarusiarsuup Kuua River, from the margin of the Russell Glacier towards the ocean. Only a few studies have reported $^{87}Sr/^{86}Sr$ ratios for GrIS runoff (Goldstein and Jacobsen, 1987; Hagedorn and Hasholt, 2004; Hindshaw et al., 2014), and presently, none have reported $\delta^{88/86}Sr$ values. Radiogenic Sr isotope ratios robustly trace solute sources (Capo et al., 1998). Primary cation reservoirs (e.g., rocks, minerals) often have distinct $^{87}Sr/^{86}Sr$ ratios (Capo et al., 1998) as do water masses that mix during stream transport (Andrews et al., 2016). Stable Sr isotope ratios offer a complementary tracer, as cation sources can also have distinct $\delta^{88/86}Sr$ values (Andrews and Jacobson, 2017; Andrews et al., 2016). In addition, $\delta^{88/86}Sr$ values may also reflect mass-dependent isotopic fractionation by a variety of processes that remove Sr and other cations from solution, including plant uptake, calcite precipitation, and, potentially, clay formation and adsorption (e.g. Andrews et al., 2016; Böhm et al., 2012; Stevenson et al., 2016). Glacial watersheds offer particularly ideal settings to refine understanding of the stable Sr isotope tracer,

as minimal amounts of vegetation imply that any evidence for fractionation can be attributed exclusively to abiotic mechanisms (de Souza et al., 2010; Stevenson et al., 2016).

4.2 Hydrologic and Geologic Setting

Our study focused on the Akuliarusiarsuup Kuua River (AKR), which drains the Russell Glacier, a land terminating lobe of the GrIS located in the Kangerlussuaq region of southwestern Greenland (Fig. 4.1). We sampled GrIS subglacial discharge from the margin (site P) along a ~32 km downstream transect toward the Kangerlussuaq Fjord (Fig. 4.1). The relatively small (~40 km^2) site P catchment is situated on the northern margin of the Russell Glacier (Lindback et al., 2015) and has an average summer discharge of ~12 m^3s^{-1} according to measurements made between 2008 and 2011 (Rennermalm et al., 2012). AKR discharge increases downstream as additional inputs feed into the system (Fig 4.1.). At ~3.4 km (site I) average summer discharge increases to ~15 m^3s^{-1}, also according to the time period between 2008 and 2011, as the AKR integrates water from Seahorse Lake (site O) and another small subglacial discharge tributary (Rennermalm et al., 2012). Discharge from yet another subglacial portal, previously studied in Dieser et al. (2014) and located between sites R and H, feeds the AKR at ~7 km. At ~13 km, the AKR gains more water as it flows directly alongside the margin of the Russell Glacier, between sites G and E. At ~17 km (site T), discharge from the Leverett Glacier provides the most substantial hydrologic input. The Leverett Glacier catchment is relatively large (~900 km^2) (Lindback et al., 2015) and has a peak summer discharge of ~300 m^3s^{-1} (2009 and 2010) (Bartholomew et al., 2011; Cowton et al., 2012). Following merger of the AKR and Leverett Glacier subglacial discharge, no additional major hydrologic inputs occur along the study transect.

Following from van Gool et al. (2002), the Russell and Leverett Glaciers overlie a geologic boundary between the southern Nagssugtoqidian Orogen to the north and the North Atlantic craton to the south. Both regionally dominated by Archaean gneisses, the southern Nagssugtoqidian Orogen is primarily amphibolite-facies, while the North Atlantic craton is largely granulite facies. A northward transition from undeformed- to deformed-Kangâmiut dykes also marks the boundary between these terranes. The northern boundary of the southern Nagssugtoqidian Orogen is the Ikertôq thrust zone, a 5 – 10 km wide belt of Paleoproterozoic paragneisses and Archaean gneisses situated directly north of the Isunnguata Sermia Glacier.

The climate of the Kangerlussuaq area is low Arctic polar desert. Temperature is strongly seasonal, with a mean summer air temperature of 10.3 °C (2001 – 11) and a mean winter air temperature of -16.1°C (2001 – 2011) (Hanna et al., 2012). Mean annual precipitation is low, 258 mm/yr (2001 – 2012) (Mernild et al., 2015). Permafrost is continuous in the proglacial area and has an active layer thickness of 0.5 m in peat and >1 m in unvegetated outwash (Yde et al., 2010).

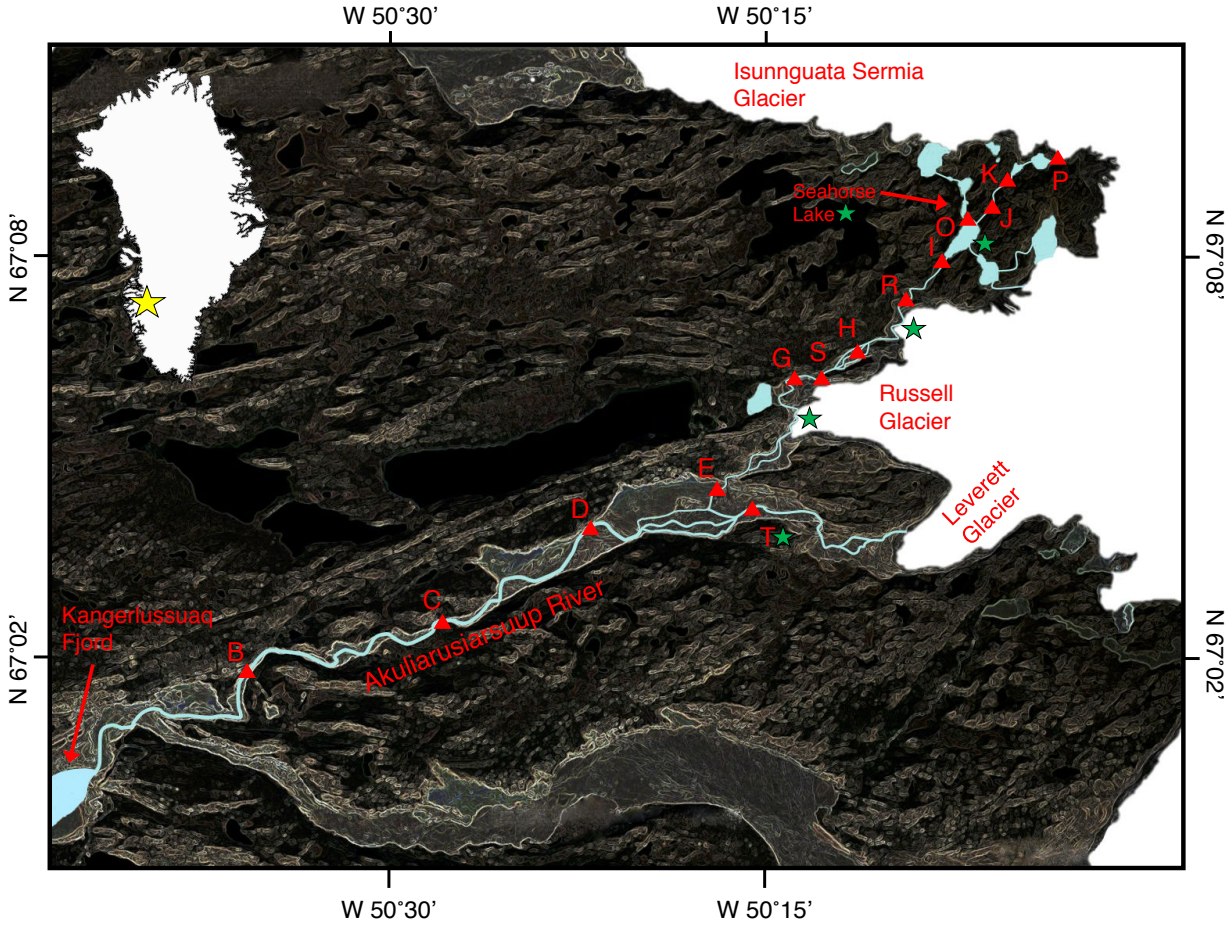

Figure 4.1: Map of field site. Red triangles indicate sample sites. Green stars indicate locations of additional hydrologic inputs to the AKR (see text). Insert map of Greenland with a yellow star indicating the location of the field site.

4.3 Methods

4.3.1 Sample collection and field methods

Subglacial discharge (site P) water samples were collected between 1 pm and 2 pm, approximately once per week, from June through August in 2014 and 2015. Major cation and anion concentrations, as well as alkalinity data, were previously reported in Andrews et al. (*in prep*). In addition, downstream transect samples of the AKR were collected within one week of each other, once per month from June through August in 2014 and once per month during June

and July in 2015. Sample locations were documented with a Garmin 60CSx handheld GPS meter. Water temperatures were measured on-site using a Mettler SevenGo Pro meter. Water samples for cation and Si concentration analyses were passed through 0.45 μm filter capsules (Versapor membrane), collected in I-CHEM HDPE bottles, and acidified to pH < 2 using concentrated, ultrapure HNO_3. Water samples for Sr isotope analyses were passed through 0.45 μm filter capsules (Versapor membrane) and collected in I-CHEM HDPE bottles. To ensure complete removal of suspended sediments, river water samples intended for stable Sr isotope analyses were filtered again in the laboratory using 0.45 μm polypropylene syringe filters (Whatman Puradisc). All Sr isotope water samples were acidified to pH < 2 using concentrated, ultrapure HNO_3. Water samples for anion concentration analyses were passed through 0.45 μm filter capsules (Versapor membrane) and collected in LDPE sample bottles. Water samples for suspended sediment analyses were collected with a pole sampler directly outside the subglacial portal (site P, Fig. 4.1). Two water samples were collected in HDPE bottles. Samples were passed through pre-weighed Whatman GF/F filters within 12 hrs after collection. The filters were dried and the total volume of water and the final filter weight were recorded and used to calculate suspended sediment concentrations. The reported concentrations (Table 4.1, 4.2) represent the average value of both samples. Bedload sediments and rock hand-samples (R01 – R04) were collected in LDPE bags during the 2014 field season. Rock R05 was collected in an LDPE bag during 2009, as part of the sampling campaign for Ryu and Jacobson (2012). Rock R05 captured the boundary between two gneisses with distinct mineralogies, one felsic and one mafic. As such, R05 was cut and processed as two separate rock samples (R05F and R05M).

4.3.2 Sample preparation

Bedload sediments were dried in an oven at 50 ºC and sieved using a 2 mm nylon mesh. To isolate the exchangeable fraction, ~10 g subsamples of the <2 mm fraction were reacted with 10 mL of 1M ammonium chloride (NH_4Cl), adjusted to pH = 8. The mixtures were shaken on a rocker table for 6 hr. After centrifugation, the supernatants where passed through 0.45 µm polypropylene syringe filters (Whatman Puradisc) into Teflon vials, dried, and re-dissolved in 5% HNO_3. Additional subsamples (~10 g) of the <2 mm fraction were powdered in a shatterbox equipped with a tungsten carbide grinding container and processed with a sequential leaching and digestion procedure. To isolate the carbonate fraction, ~1.0 g subsamples of the powder were reacted with 10 mL of 4M acetic acid and shaken on a rocker table for 6 hr. The mixtures were centrifuged, and the supernatants were passed through 0.45 µm polypropylene syringe filters (Whatman Puradisc) and collected in Teflon vials. To confirm complete reaction of the carbonate fraction, the procedure was repeated two to three times until the leachates reached a constant pH value. For each sample, the filtered supernatants were combined, dried, and re-dissolved in 5% HNO_3. The residues were then reacted with 10 mL of 1M HNO_3 and shaken on a rocker table for 6 hr. The mixtures were centrifuged and the supernatants where passed through 0.45 µm polypropylene syringe filters (Whatman Puradisc), dried, and re-dissolved in 5% HNO_3. The remaining residues, assumed to represent the silicate fraction, were dried in an oven, and ~0.1 g subsamples were digested in a 5:3 mixture of concentrated HF and HNO_3 at 140°C, dried, refluxed in concentrated HNO_3, dried, refluxed in 6N HCl, dried, and finally, re-dissolved in 5% HNO_3. No insoluble residues were observed. Suspended sediment samples (~0.1 g) were completely digested following the same procedure. A saw was used to remove weathering rinds from rock samples and cut the inner portion into cubes. A hammer was used to break the cubes

into chips. Subsamples of the chips (~25 g) were powdered in a shatterbox equipped with tungsten carbide grinding container and processed according to the sequential leaching and digestion procedure described above. The 1M HNO_3 step was not applied to rock samples R05F and R05M. Mostly pure mineral separate fractions were isolated from rock sample R05 by Apatite-to-Zircon in Viola, ID. Subsamples of each mineral separate (~0.1 g) were processed according to the silicate digestion procedure described above.

4.3.3 Elemental Concentrations

Cation and Si concentrations were measured in the SRC Environmental Analytical Laboratories, Saskatoon, Canada using either an Agilent 7500 or 7700 inductively coupled plasma mass spectrometry (ICP-MS). Quality control standards were within ±5% of reported concentrations for all elements. Anion concentrations were measured in the Aqueous Geochemistry Laboratory at Northwestern University using a Dionex DX-120 ion chromatograph (IC) equipped with an AS15 anion-exchange column and an ASRS-300 self-regenerating suppressor. Measured values for NIST-traceable Dionex standards were within ±10% of reported concentrations for all elements. Total alkalinity was calculated by cation and anion concentration charge-balance ($ALK_{CB} = TZ^+ - TZ^-$), where TZ^+ is the sum of cations and TZ^- is the sum of anions, both in μeq/L. ALK_{CB} is assumed equivalent to carbonate alkalinity ($ALK_{CARB} \approx [HCO_3]$), as the relatively low DOC concentrations (Andrews et al., *in prep*) preclude significant contributions from non-carbonate alkalinity. Temperature, ALK_{CB}, and DIC concentrations (Andrews et al., *in prep*) were used to calculate pH values (Plummer and Busenberg, 1982). PHREEQC, implemented with the llnl.dat thermodynamic database

(Parkhurst and Appelo, 1999), was used to calculate saturation state with respect to calcite, as well as the common clay minerals smectite, illite, and kaolinite.

4.3.4 Radiogenic and stable Sr isotope ratios

Radiogenic and stable Sr isotope ratios ($^{87}Sr/^{86}Sr$ and $^{88}Sr/^{86}Sr$, respectively) were measured in the Radiogenic Isotope Geochemistry Clean Laboratory at Northwestern University (NU) using a Thermo-Scientific Triton Thermal Ionization Mass Spectrometer (TIMS). The analyses followed the procedures outlined in Andrews et al. (2016) and Andrews and Jacobson (2017). According to an ^{84}Sr isotope dilution method, column blanks contained 34 pg Sr (n = 5), and procedural blanks contained 64 pg Sr (n = 3). These levels are negligible compared to the amounts of Sr processed and analyzed (see below).

To summarize, for the determination of $^{87}Sr/^{86}Sr$ ratios, sample aliquots containing 100 ng of Sr were weighed into acid-cleaned Teflon vials, dried, re-dissolved in 8M HNO_3, and eluted through inverted pipet tips packed with Eichrom Sr-Spec resin. The purified Sr fractions were dried, re-dissolved in 1.5 μL of 3N HNO_3, and loaded together with 1 μL of a $TaCl_5$ solution between parafilm "dams" on single, outgassed Re filament assemblies. Data were collected in multi-dynamic mode for 110 duty cycles upon achieving 8 V ^{88}Sr ion-beams. To correct for instrumental mass fractionation, the $^{86}Sr/^{88}Sr$ ratio was normalized to 0.1194 using an exponential law. During the period of study, repeated analyses of NBS 987 yielded a mean $^{87}Sr/^{86}Sr$ ratio of 0.71025 ± 0.00001 ($\pm 2\sigma_{SD}$, n = 34). The current, long-term mean $^{87}Sr/^{86}Sr$ ratio for the laboratory, using this method, is 0.71025 ± 0.00001 ($\pm 2\sigma_{SD}$, n = 133).

As described in Section 4.3.1, water samples intended for stable Sr analyses were filtered in the field and again in the laboratory, to ensure total sediment removal. $^{87}Sr/^{86}Sr$ ratios were

measured on both the once- and twice-filtered aliquots for a given sample. The resulting $^{87}Sr/^{86}Sr$ ratios randomly differed in either the fourth or fifth decimal place. These differences are negligible on the scale of $^{87}Sr/^{86}Sr$ ratios measured in this study but are consistent with the removal of small amounts of sediment and/or colloids during the second filtration. Sr concentrations in the twice-filtered aliquots were also lower than their associated once-filtered aliquots by < 10%, consistent with a small degree of sediment removal during the second filtration. When available, $^{87}Sr/^{86}Sr$ ratios of the twice-filtered aliquots are reported in Tables 1 and 2.

An ^{87}Sr-^{84}Sr double-spike method was used to measure $^{88}Sr/^{86}Sr$ ratios (Andrews et al., 2016) on the twice-filtered samples. Sample aliquots containing 100 – 150 ng of Sr were weighed into acid-cleaned Teflon vials and spiked. The solutions were dried, re-dissolved in 8N HNO_3, then purified and loaded onto single Re filament assemblies as described above. In the mass spectrometer, a 6 V ^{88}Sr ion beam was attained, and $^{88}Sr/^{84}Sr$, $^{87}Sr/^{84}Sr$, and $^{86}Sr/^{84}Sr$ ratios were measured in static mode for a total of 160 duty cycles, each having a 16 sec integration time. Ultimately, 140 cycles were used for the data reduction, which incorporated $^{87}Sr/^{86}Sr$ ratios from the twice-filtered samples. All sample (smp) $^{88}Sr/^{86}Sr$ ratios are reported in delta notation (per mil) relative to NBS 987, where $\delta^{88/86}Sr$ (in ‰) = $[(^{88}Sr/^{86}Sr)_{smp}/(^{88}Sr/^{86}Sr)_{NBS\text{-}987} - 1] \times 1000$. Measured internal precisions ($2\sigma_{SEM}$) for samples and standards range from 0.007 to 0.010‰, with an average of 0.008‰. An offset was applied to each measurement in a session to account for collector cup drift. The session offset was calculated as the difference between the mean $\delta^{88/86}Sr$ value of 6 – 8 NBS 987 runs and the "true" NBS 987 $\delta^{88/86}Sr$ value, which is 0‰. To confirm the accuracy of the drift correction, 2 – 4 IAPSO seawater standards were analyzed during each session. During the period of study, NBS 987 yielded $\delta^{88/86}Sr = 0.000 \pm 0.005$‰

($2\sigma_{SEM}$, n = 74), and IAPSO seawater yielded $\delta^{88/86}Sr = 0.397 \pm 0.007‰$ ($2\sigma_{SEM}$, n = 29). These data correspond to an external reproducibility of ±0.019‰ ($2\sigma_{SD}$) for NBS 987 and ±0.018‰ ($2\sigma_{SD}$) for IAPSO seawater. The current, long-term external reproducibility for both the NBS 987 and IAPSO standards is ±0.019‰ (n = 151 and n = 83, respectively). When radiogenic Sr isotope ratio errors are propagated through the stable Sr isotope data reduction procedure, the global, external uncertainty of the stable Sr isotope measurements is ±0.021‰ ($2\sigma_{SD}$), which is the uncertainty applied to all samples in the dataset.

4.4. Results

4.4.1 Subglacial discharge and AKR transect bulk ion geochemistry

Figure 4.2 plots the major cation and anion composition (in equivalents) of subglacial discharge and AKR transect samples. In 2014, subglacial discharge (site P, 0.1km) cations were predominately Ca and Mg, with average molar cation concentrations following the order Ca (60%), Mg (17%), K (15%), and Na (9%) (Table 4.1). Between 1km to 15.6km (sites K to E) of the AKR, proportions of Ca and Mg decreased relative to K and Na such that average molar cation concentrations followed the order Ca (54%) > K (19%) > Mg (13%) = Na (13%). Following merger with the Leverett Glacier discharge at ~17 km, AKR (sites D to B) average molar cation concentrations followed the order Na (38%) > Ca (34%) > K (21%) > Mg (7%), indicating a substantial transition to higher proportions of K and Na. The 2015 melt season produced broadly similar trends. Subglacial discharge (site P) average molar cation concentrations followed the order Ca (56%) > Mg (21%) > K (13%) > Na (11%), and between sites K and E they followed the order Ca (56%) > Mg (18%) > K (16%) > Na (11%) (Fig. 4.2; Table 4.2). After merger with the Leverett Glacier discharge (sites D to B), AKR cation

concentration followed the order Ca (37%), Na (33%), K (19%), and Mg (11%), thus demonstrating another substantial increase in the proportions of Na and K. A study conducted on the AKR in 2009 found comparable results to those presented here, in that the AKR solute load transitioned to higher proportions of Na and K, relative to Ca and Mg, after merger with Leverett Glacier discharge (Ryu and Jacobson, 2012). Molar cation concentrations for one sample of Leverett Glacier discharge followed the order Ca (40%) > Na (35%) >K (17%) >Mg (8%), and was therefore similar to the AKR after merger with Leverett Glacier discharge (sites D to B), as well as the relative abundances documented for Leverett Glacier discharge in Hindshaw et al. (2014). With average molar cation concentrations following the order Ca (47%) > Mg (21%) > Na (16%) > K (15%), the geochemistry of Seahorse Lake distinctly differs from either AKR or Leverett Glacier discharge.

Across both melt seasons, HCO_3 dominated the anion load of all samples (Table 4.1, 4.2). In 2014, Cl concentrations were below the instrumental detection limit. Subglacial discharge (site P) also had SO_4 concentrations below the instrumental detection limit, such that HCO_3 exclusively balanced the cation load. From 1km to 15.6 km of the AKR downstream transect (sites K to E), HCO_3 and SO_4 composed 98% and 2% of the molar anion load. After merger with Leverett Glacier discharge (sites D to B), HCO_3 and SO_4 composed 89% and 11% of the molar anion load. During 2015, subglacial discharge (site P) had measureable concentrations of Cl in early June, as well as measureable concentrations of SO_4 until mid-July, such that the average molar anion load followed the order HCO_3 (90%) > SO_4 (8%) > Cl (1%). Cl was not detected in any AKR transect samples. From sites K to E, HCO_3 and SO_4 composed 93% and 7% of the molar anion load. From sites D to B, HCO_3 and SO_4 concentrations composed 90% and 10% of the molar anion load, similar to the 2014 samples. Seahorse lake HCO_3 and SO_4 concentrations

composed 90% and 10% of the molar anion load, while anion concentrations in Leverett Glacier discharge followed the order HCO_3 (77%) > SO_4 (15%) > Cl (9%), similar to results reported in Hindshaw et al. (2014).

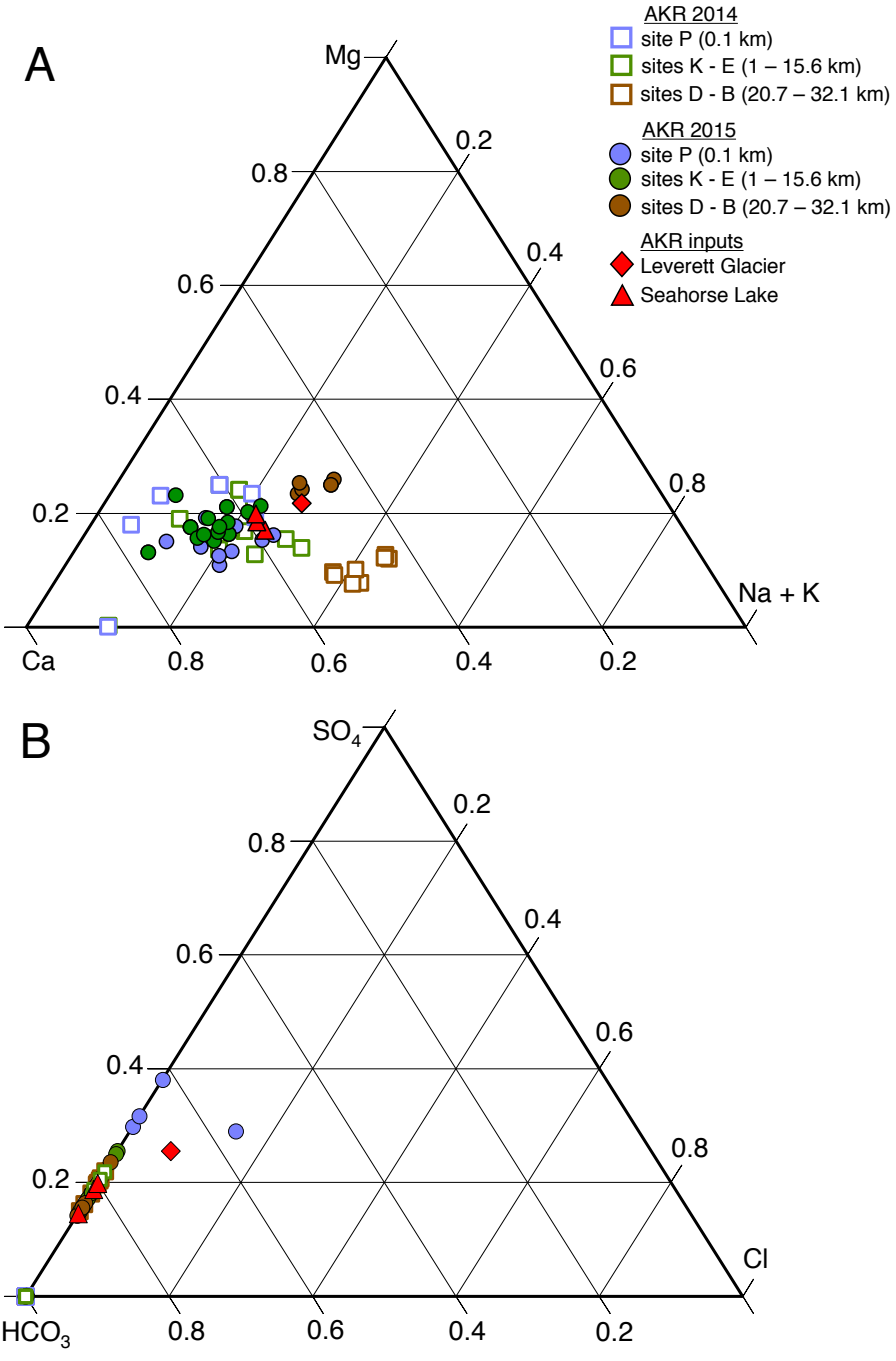

Figure 4.2: Relative proportions of major cations (A) and anions (B) in water samples, in µeq/L.

4.4.2 *Subglacial discharge and AKR transect Sr isotope geochemistry*

Tables 4.1 and 4.2 report the radiogenic and stable Sr isotope compositions of water samples from 2014 and 2015, respectively. Subglacial discharge (site P) had an average $^{87}Sr/^{86}Sr$ ratio of 0.72198 ± 0.00210 (1σSD, n = 7) in 2014 and an average $^{87}Sr/^{86}Sr$ ratio of 0.72107 ± 0.00237 (1σSD, n = 12) in 2015. There was no statistically significant change in $^{87}Sr/^{86}Sr$ ratios through time during either melt season ($p > 0.05$) (Fig. 4.3). $^{87}Sr/^{86}Sr$ ratios increased with distance from the ice sheet margin towards the ocean. After merger with Leverett Glacier discharge, the AKR (sites D through B) had an average $^{87}Sr/^{86}Sr$ ratio of 0.74718 ± 0.00068 (1σSD, n = 8) in 2014 and an average $^{87}Sr/^{86}Sr$ ratio of 0.74403 ± 0.00478 (1σSD, n = 6) in 2015. One sample of Leverett Glacier discharge had an $^{87}Sr/^{86}Sr$ ratio of 0.75438, and the average Seahorse Lake $^{87}Sr/^{86}Sr$ ratio was 0.72966 ± 0.00151 (1σSD, n = 3) during 2014 and 2015 combined. Subglacial discharge had an average $\delta^{88/86}Sr$ values of 0.386 ± 0.042 (1σSD, n = 6) in 2014 and an average $\delta^{88/86}Sr$ values of 0.362 ± 0.005 (1σSD, n = 4) in 2015. There was no statistically significant change in $\delta^{88/86}Sr$ values through time during either melt season ($p > 0.05$) (Fig. 4.3). Finally, there was no statistically significant correlation between subglacial discharge $^{87}Sr/^{86}Sr$ and $\delta^{88/86}Sr$ values ($R^2 \leq 0.1$, $p > 0.05$) during either melt season.

4.4.3 *Mineral, sediment, and bulk rock Sr isotope geochemistry*

Table 4.3 reports the radiogenic and stable Sr isotope compositions of suspended sediment, bedload sediment, bulk rock, and mineral separates. Suspended sediment had an average $^{87}Sr/^{86}Sr$ ratio of 0.70940 ± 0.00084 (1σSD, n = 8) and an average $\delta^{88/86}Sr$ value of 0.259 ± 0.015 (1σSD, n = 8). There was no statistically significant correlation between suspended

sediment $^{87}Sr/^{86}Sr$ and $\delta^{88/86}Sr$ values ($R^2 \leq 0.2$, $p > 0.05$), nor was there a statistically significant change in suspended sediment $\delta^{88/86}Sr$ values through time ($p > 0.05$) (Fig. 4.3). However, $^{87}Sr/^{86}Sr$ ratios did increase through time ($R^2 = 0.5$, $p = 0.04$) (Fig. 4.3).

Bedload sediment collected from the AKR demonstrated a wide range of leachate and digest $^{87}Sr/^{86}Sr$ ratios, from ~0.708 to ~0.758. For a given bedload sediment, the $^{87}Sr/^{86}Sr$ ratios were generally in the order digest < HAc leachate < NH_4Cl leachate = HNO_3 leachate. Bedload sediment leachate and digest $\delta^{88/86}Sr$ values ranged from 0.166‰ to 0.340‰, but in general had a well-constrained average value of 0.258 ± 0.041‰ (1σSD, $n = 16$) and was therefore similar to bulk silicate Earth (Moynier et al., 2010). Site P bedload (BL02; 0.260‰) and suspended sediment (0.259‰) digests are identical to each other within the measurement uncertainty. There was no statistically significant correlation between $^{87}Sr/^{86}Sr$ and $\delta^{88/86}Sr$ values for the collective bedload sediment leachate and digest dataset, nor for individual bedload sediment samples ($p > 0.05$).

Bulk rock leachate and digest $^{87}Sr/^{86}Sr$ ratios ranged from ~0.705 to ~1.52. Very high bulk rock $^{87}Sr/^{86}Sr$ ratios (>0.8) is consistent with the bedrock lithology (high proportion of K-bearing minerals) and Archaean age (see section 4.2). Similar to bedload sediment, for a given bulk rock the $^{87}Sr/^{86}Sr$ ratios were generally in the order digest < HAc leachate < HNO_3 leachate. Bulk rock leachate and digest $\delta^{88/86}Sr$ values ranged from 0.097‰ to 0.609‰. The average bulk rock leachate and digest value was 0.297 ± 0.152‰ (1σSD, $n = 16$) and was therefore similar to the average bedload sediment value but less well constrained. There was a statistically significant but weak correlation between $^{87}Sr/^{86}Sr$ and $\delta^{88/86}Sr$ values for the collective bulk rock leachate and digest dataset ($R^2 = 0.3$, $p = 0.03$), but not for any individual bulk rock sample ($p > 0.05$).

Mineral separates from bulk rocks R05F and R05M ranged in $^{87}Sr/^{86}Sr$ ratios from ~0.703 to ~0.727, and in $\delta^{88/86}Sr$ values from 0.220‰ to 0.633‰. There was no statistically significant correlation between $^{87}Sr/^{86}Sr$ and $\delta^{88/86}Sr$ values for the collective mineral separate dataset, nor mineral separates from individual bulk rocks ($p > 0.05$). The R05F and R05M bulk rock digests have $^{87}Sr/^{86}Sr$ ratios intermediate between relatively higher $^{87}Sr/^{86}Sr$ ratio minerals such as hornblende, chlorite, biotite, and K-feldspar, and relatively lower $^{87}Sr/^{86}Sr$ ratio minerals such as plagioclase, epidote, apatite, and titanite. Additionally, The R05F and R05M bulk rock digests have $\delta^{88/86}Sr$ values intermediate between relatively higher $\delta^{88/86}Sr$ value minerals (apatite, titanite, hornblende, and K-feldspar) and relatively lower $\delta^{88/86}Sr$ value minerals (epidote, plagioclase, chlorite).

Table 4.1 Elemental and Sr isotope geochemistry of the Akuliarusiarsuup Kuua River and Seahorse Lake during the 2014 melt season

Sample ID	Site ID	Distance (km)	Date (m/d)	T (◦C)	Ca (µmol/L)	Mg (µmol/L)	K (µmol/L)	Na (µmol/L)	Al (µmol/L)	Ba (nmol/L)	Fe (µmol/L)	Si (µmol/L)	Sr (nmol/L)	SO4 (µmol/L)	Alkalinity (µeq/L)	pH	$^{87}Sr/^{86}Sr$	$\delta^{88/86}Sr$ (‰)	Suspended Sediment (g/L)
Akuliarusiarsuup Kuua River (AKR)																			
W25	P	0.1	6/17	0.2	25.0	8.2	10.2	8.7	3.2	19.7	1.5	17.4	55.9	bdl	85	7.01	0.72596	0.332	0.12
W26	K	1.0	6/17	1.1	22.5	8.2	7.7	8.7	2.4	17.5	0.8	15.0	53.6	bdl	78	nd	0.72487	nd	nd
W27	J	2.4	6/17	2.1	22.5	8.2	7.7	8.7	3.0	19.7	1.0	16.4	52.5	bdl	78	nd	0.72496	nd	nd
W28	I	4.4	6/18	3.6	32.4	8.2	10.2	8.7	0.7	20.4	0.2	19.2	73.0	11	78	nd	0.72502	nd	nd
W30	H	9.2	6/21	2.3	29.9	8.2	10.2	8.7	2.2	17.5	1.0	16.0	58.2	bdl	95	nd	0.73141	nd	nd
W29	G	11.0	6/18	3.2	29.9	8.2	12.8	8.7	5.9	26.2	2.3	24.2	66.2	10	78	nd	0.73211	nd	nd
W31	E	15.6	6/21	1.6	32.4	8.2	15.3	21.7	7.0	18.9	2.3	27.8	58.2	11	96	nd	0.74183	nd	nd
W32	D	20.7	6/21	2.0	44.9	12.3	30.7	60.9	4.1	12.4	1.3	32.4	66.2	21	165	nd	0.74764	nd	nd
W33	C	27.2	6/22	1.5	42.4	12.3	28.1	56.5	3.3	11.7	1.0	30.3	63.9	20	155	nd	0.74674	nd	nd
W34	B	32.1	6/22	2.0	44.9	12.3	28.1	60.9	8.5	25.5	1.8	42.7	76.5	18	167	nd	0.74712	nd	nd
W44	P	0.1	6/28	0.1	20.0	8.2	5.1	8.7	9.6	32.0	3.9	25.6	60.5	bdl	70	6.92	0.71988	0.334	0.05
W55	P	0.1	7/7	0.2	20.0	8.2	5.1	4.3	1.5	15.3	0.8	13.2	49.1	bdl	66	6.79	0.72330	0.409	0.10
W65	P	0.1	7/22	0.3	10.0	bdl	2.6	bdl	0.9	7.3	0.6	6.1	27.4	bdl	23	6.20	0.72127	0.432	0.12
W66	K	1.0	7/23	1.6	10.0	bdl	2.6	bdl	2.8	13.1	1.1	10.0	28.5	bdl	23	nd	0.72112	nd	nd
W67	J	2.4	7/23	2.6	10.0	bdl	2.6	bdl	3.7	18.2	1.3	13.9	30.8	bdl	23	nd	0.72109	nd	nd
W68	I	4.4	7/23	5.5	15.0	4.1	5.1	4.3	1.9	15.3	0.7	12.8	37.7	bdl	48	nd	0.72496	nd	nd
W69	H	9.2	7/24	3.4	20.0	8.2	7.7	4.3	4.8	24.0	1.6	20.3	44.5	bdl	68	nd	0.72895	nd	nd
W70	G	11.0	7/24	4.0	20.0	8.2	7.7	4.3	4.4	23.3	1.4	18.5	46.8	bdl	68	nd	0.72914	nd	nd
W71	E	15.6	7/24	3.7	20.0	4.1	7.7	8.7	2.4	8.7	1.1	12.5	36.5	bdl	65	nd	0.73852	nd	nd
W72	D	20.7	7/25	0.9	52.4	8.2	33.2	56.5	4.1	8.7	0.7	28.8	75.3	17	177	nd	0.74663	nd	nd
W73	C	27.2	7/25	2.6	59.9	12.3	38.4	60.9	11.9	39.3	3.6	53.4	98.2	18	207	nd	0.74643	nd	nd
W74	B	32.1	7/25	3.0	54.9	8.2	33.2	56.5	1.7	8.7	0.5	28.5	78.7	22	171	nd	0.74671	nd	nd
W76	P	0.1	7/28	0.3	12.5	4.1	2.6	bdl	1.8	11.7	1.2	8.5	34.2	bdl	36	nd	0.72015	0.408	nd
W89	P	0.1	8/2	0.3	17.5	4.1	2.6	bdl	0.4	10.9	1.1	7.8	43.4	bdl	46	6.42	0.72207	nd	nd
W101	P	0.1	8/12	0.3	20.0	8.2	5.1	4.3	2.7	16.7	1.2	15.7	55.9	bdl	66	6.91	0.72124	0.403	0.07
W102	K	1.0	8/12	1.6	15.0	4.1	5.1	bdl	1.4	12.4	0.6	10.3	37.7	bdl	43	nd	0.72229	nd	nd
W103	J	2.4	8/12	2.1	17.5	4.1	5.1	4.3	1.6	13.1	0.7	12.1	42.2	bdl	53	nd	0.72175	nd	nd
W104	I	4.4	8/13	4.3	20.0	8.2	5.1	4.3	0.7	13.1	0.3	11.7	41.1	bdl	66	nd	0.72787	nd	nd
W105	H	9.2	8/13	2.7	20.0	4.1	7.7	4.3	2.1	13.1	1.1	12.5	38.8	bdl	60	nd	0.73158	nd	nd
W106	G	11.0	8/13	2.8	20.0	4.1	7.7	4.3	1.7	11.7	0.9	12.1	39.9	bdl	60	nd	0.73187	nd	nd
W107	E	15.6	8/14	2.2	29.9	8.2	12.8	17.4	2.7	10.2	1.1	18.2	53.6	bdl	107	nd	0.73960	nd	nd
W108	D	20.7	8/15	0.9	44.9	8.2	25.6	39.1	2.8	10.9	1.0	26.7	67.3	17	137	nd	0.74770	nd	nd
W109	B	32.1	8/15	1.6	47.4	8.2	25.6	43.5	2.0	9.5	0.8	26.0	73.0	20	141	nd	0.74841	nd	nd
																nd			
Seahorse Lake																			
W24	O	3.4	6/16	7.6	34.9	16.5	10.2	13.0	14.5	43.0	4.7	49.8	75.3	13	101	nd	0.72992	nd	nd

"nd" indicates no data, "bdl" indicates below instrumental detection limit. Cl concentrations not shown because all samples were bdl (< 1ppm). SO4 concentrations were bdl when < 1ppm.
Site ID and distance corresponds to Fig 1.

Table 4.2 Elemental and Sr isotope geochemistry of the Akuliarusiarsuup Kuua River, Leverett Glacier, and Seahorse Lake during the 2015 melt season

Sample ID	Site ID	Distance (km)	Date (m/d)	T (◦C)	Ca (µmol/L)	Mg (µmol/L)	K (µmol/L)	Na (µmol/L)	Al (µmol/L)	Ba (nmol/L)	Fe (µmol/L)	Si (µmol/L)	Sr (nmol/L)	Cl (µmol/L)	SO4 (µmol/L)	Alkalinity (µeq/L)	pH	$^{87}Sr/^{86}Sr$	$\delta^{88/86}Sr$ (‰)	Suspended Sediment (g/L)
Akuliarusiarsuup Kuua River (AKR)																				
W112	P	0.1	6/1	0.20	49.9	16.5	10.2	17.4	0.1	19.7	0.5	18.9	109.6	23.8	23.2	90	6.60	0.72240	nd	0.28
W125	P	0.1	6/7	0.40	79.8	24.7	12.8	26.1	1.3	41.5	1.3	33.5	251.1	bdl	36.9	174	7.03	0.71598	nd	0.12
W139	P	0.1	6/15	0.70	39.9	16.5	10.2	17.4	1.7	26.2	1.1	20.7	108.4	bdl	15.7	109	6.73	0.71899	nd	0.12
W155	P	0.1	6/22	0.30	44.9	16.5	12.8	13.0	8.9	56.8	6.3	29.9	111.8	bdl	15.6	117	6.96	0.72216	0.367	0.16
W168	P	0.1	6/28	0.3	20.0	8.2	5.1	4.3	2.1	16.0	1.3	11.7	49.1	bdl	10.4	45	6.38	0.72234	nd	0.11
W171	K	1.0	6/29	0.6	20.0	8.2	5.1	4.3	0.7	12.4	0.9	11.0	46.8	bdl	bdl	66	nd	0.72425	nd	nd
W170	J	2.4	6/29	1.7	22.5	8.2	5.1	4.3	0.6	12.4	0.7	11.0	47.9	bdl	bdl	71	nd	0.72423	nd	nd
W172	I	4.4	6/29	6.7	34.9	12.3	10.2	8.7	1.9	24.8	1.1	19.6	76.5	bdl	10.3	93	nd	0.72610	nd	nd
W173	R	6.2	6/30	3.7	29.9	8.2	7.7	8.7	0.1	18.9		15.7	68.5	bdl	7.9	77	nd	0.72823	nd	nd
W174	H	9.2	6/30	2.5	29.9	8.2	10.2	8.7	2.4	21.8	1.6	16.7	62.8	bdl	7.5	80	nd	0.73199	nd	nd
W175	S	10.0	6/30	2.8	29.9	8.2	10.2	8.7	2.1	19.7	1.3	15.7	60.5	bdl	9.0	77	nd	0.73222	nd	nd
W176	G	11.0	6/30	3.2	29.9	12.3	10.2	8.7	5.9	34.2	3.8	21.4	63.9	bdl	7.5	89	nd	0.73122	nd	nd
W177	E	15.6	6/30	2.8	27.4	8.2	10.2	13.0	2.1	10.9	1.0	15.0	49.1	bdl	9.0	77	nd	0.74082	nd	nd
W178	D	20.7	6/30	2.8	32.4	8.2	17.9	34.8	1.5	8.0	0.6	20.3	51.4	bdl	11.0	112	nd	0.74735	nd	nd
W179	C	27.2	7/1	1.6	34.9	12.3	20.5	34.8	6.3	23.3	3.2	26.7	55.9	bdl	10.6	129	nd	0.74815	nd	nd
W180	B	32.1	7/1	2.1	32.4	8.2	17.9	34.8	1.2	8.0	0.5	20.7	53.6	bdl	10.5	113	nd	0.74775	nd	nd
W182	P	0.1	7/11	0.3	27.4	16.5	7.7	8.7	8.9	49.5	8.1	22.8	71.9	bdl	19.8	65	6.38	0.72169	0.357	0.10
W198	P	0.1	7/20	0.3	15.0	4.1	2.6	bdl	1.1	11.7	1.3	7.8	33.1	bdl	bdl	41	6.41	0.72319	0.366	0.11
W202	P	0.1	7/27	0.3	20.0	8.2	5.1	bdl	3.3	23.3	3.2	13.2	47.9	bdl	bdl	61	6.52	0.72331	0.360	0.09
W205	K	1.0	7/28	0.6	15.0	4.1	5.1	bdl	0.7	10.9	0.7	8.2	37.7	bdl	bdl	43	nd	0.72318	nd	nd
W203	J	2.4	7/27	2.1	15.0	4.1	2.6	bdl	2.5	15.3	1.7	10.3	34.2	bdl	bdl	41	nd	0.72217	nd	nd
W206	I	4.4	7/28	6.0	20.0	8.2	5.1	bdl	1.5	15.3	0.9	12.1	41.1	bdl	bdl	61	nd	0.72636	nd	nd
W207	R	6.2	7/28	7.2	20.0	8.2	5.1	bdl	1.4	14.6	0.8	12.5	41.1	bdl	5.7	61	nd	0.72678	nd	nd
W208	H	9.2	7/28	3.9	44.9	12.3	10.2	8.7	1.7	24.0	1.3	18.9	109.6	bdl	10.0	113	nd	0.72365	nd	nd
W209	S	10.0	7/28	4.0	42.4	12.3	10.2	8.7	1.6	21.8	1.2	18.2	98.2	bdl	11.7	105	nd	0.72375	nd	nd
W214	G	11.0	7/29	4.9	37.4	12.3	10.2	8.7	0.3	18.2	0.3	16.4	78.7	bdl	15.1	88	nd	0.72882	nd	nd
W213	E	15.6	7/29	4.5	34.9	8.2	10.2	8.7	0.5	9.5	0.3	16.7	63.9	bdl	13.2	79	nd	0.73700	nd	nd
W212	D	20.7	7/29	2.4	49.9	12.3	23.0	39.1	3.5	14.6	1.3	27.8	77.6	bdl	22.0	143	nd	0.74184	nd	nd
W211	C	27.2	7/29	2.2	52.4	16.5	25.6	39.1	9.3	33.5	4.5	35.6	82.2	bdl	21.0	160	nd	0.74327	nd	nd
W210	B	32.1	7/29	2.4	49.9	16.5	25.6	34.8	16.7	59.0	9.0	42.7	87.9	bdl	19.2	155	nd	0.73586	nd	nd
W216	P	0.1	8/3	0.4	17.5	8.2	5.1	bdl	0.9	12.4	1.2	10.7	47.9	bdl	bdl	57	6.68	0.72130	nd	0.12
W231	P	0.1	8/10	0.3	12.5	4.1	2.6	bdl	2.2	14.6	1.5	8.5	32.0	bdl	bdl	36	6.44	0.72370	nd	0.11
W242	P	0.1	8/14	0.4	27.4	8.2	5.1	8.7	4.1	25.5	2.5	17.8	77.6	bdl	bdl	85	7.01	0.71850	nd	nd
W245	P	0.1	8/15	0.3	25.0	8.2	5.1	4.3	2.4	20.4	2.7	13.9	67.3	bdl	bdl	76	6.85	0.71927	nd	nd
Seahorse Lake																				
W169	O	3.4	6/29	7.7	32.4	16.5	10.2	8.7	14.5	57.5	7.9	39.2	66.2	bdl	8.5	100	nd	0.72804	nd	nd
W204	O	3.4	7/27	12.1	22.5	8.2	7.7	8.7	4.8	24.0	2.3	24.9	46.8	bdl	7.3	63	nd	0.73102	nd	nd
Leverett Glacier																				
W152	T	16.6	6/19	2.1	59.9	12.3	25.6	52.2	0.5	8.7	0.2	22.8	86.7	16.6	28.4	149	nd	0.75438	nd	nd

"nd" indicates no data, "bdl" indicates below instrumental detection limit. Cl and SO4 concentrations were bdl when < 1ppm. Site ID and distance corresponds to Fig. 4.1

Table 4.3 Elemental and Sr isotope geochemistry of suspended sediments, bedload sediments, bulk rocks, and mineral separates

Sample ID	Sample Description	Fraction	Ca (μmol/g)	Mg (μmol/g)	K (μmol/g)	Na (μmol/g)	Al (μmol/g)	Ba (nmol/g)	Si (μmol/g)	Sr (nmol/g)	$^{87}Sr/^{86}Sr$	$\delta^{88/86}Sr$ (‰)
Suspended Sediment												
SS112	site P - 6/1/15	digest	894.3	644.5	302.7	1274.0	2846.3	7802.3	2.7	5322.9	0.70848	0.284
SS125	site P - 6/7/15	digest	883.8	677.4	307.7	1227.8	2805.4	10009.5	0.9	5202.4	0.70871	0.254
SS139	site P - 6/15/15	digest	865.2	731.9	362.8	1297.0	2831.2	10937.8	0.0	5279.8	0.70891	0.258
SS155	site P - 6/22/15	digest	873.1	741.7	317.0	1165.8	2784.2	10359.2	0.5	5153.7	0.70915	0.268
SS168	site P - 6/28/15	digest	909.5	777.0	342.1	1209.5	2943.9	12068.0	3.4	5377.4	0.70958	0.255
SS198	site P - 7/20/15	digest	859.7	690.6	325.7	1168.6	2809.9	11009.8	0.7	5062.0	0.70975	0.270
SS202	site P - 7/27/15	digest	921.0	869.2	414.5	1229.7	3129.7	16077.0	2.3	5412.9	0.71119	0.250
SS231	site P - 8/10/15	digest	848.6	708.6	333.0	1222.8	2814.0	10261.1	1.5	5190.7	0.70945	0.232
Bedload Sediment												
SED-01	site Q	NH_4Cl leach	0.4	0.4	0.5	0.2	bdl	34.6	bdl	5.1	0.73914	0.166
		HAc leach	13.3	15.7	9.0	9.0	48.4	160.1	30.6	47.6	0.73302	0.242
		HNO_3 leach	31.6	34.0	14.7	7.3	59.6	154.6	23.5	44.1	0.74758	0.340
		digest	740.1	403.1	255.1	1270.4	2577.2	3355.4	2.3	4913.4	0.70825	0.247
SED-02	site P	NH_4Cl leach	1.3	0.3	0.2	0.1	bdl	10.4	bdl	3.7	0.72382	0.265
		HAc leach	22.0	17.9	5.7	10.7	30.5	69.0	21.9	57.9	0.71576	0.271
		HNO_3 leach	24.3	23.8	6.2	7.4	37.9	88.2	24.2	42.8	0.72157	0.305
		digest	859.8	723.1	211.7	1041.1	2427.8	2479.6	1.7	4208.5	0.70758	0.260
SED-03	site E	NH_4Cl leach	1.3	0.1	0.3	0.1	bdl	7.6	bdl	2.5	0.75085	0.225
		HAc leach	19.1	12.6	9.3	10.3	29.1	89.3	20.8	46.2	0.73722	0.267
		HNO_3 leach	19.3	24.7	10.7	6.7	39.9	102.6	22.5	33.1	0.75834	0.276
		digest	642.7	394.9	382.8	1110.4	2405.4	4689.9	1.5	3460.9	0.71646	0.283
SED-04	site D	NH_4Cl leach	1.2	0.4	0.2	0.1	bdl	8.6	bdl	3.0	0.73649	0.199
		HAc leach	16.7	12.0	6.8	10.7	27.0	81.7	18.1	50.9	0.72318	0.263
		HNO_3 leach	16.6	23.2	8.7	7.4	36.6	118.8	26.1	38.3	0.73543	0.228
		digest	653.7	364.4	261.9	1184.4	2397.2	3228.6	1.6	4233.9	0.71032	0.284
Rocks												
R01	pink gneiss	HAc leach	11.2	10.4	22.4	10.8	37.3	82.0	20.8	46.3	0.82318	0.136
		HNO_3 leach	18.7	31.9	33.1	5.5	67.7	94.6	25.7	37.2	0.98287	0.097
		digest	185.0	82.8	1139.5	1043.5	2590.8	5101.8	1.5	1601.1	0.82606	0.129
R02	gray gneiss	HAc leach	20.1	15.7	15.4	10.6	32.4	172.9	20.2	35.1	0.76086	0.268
		HNO_3 leach	26.6	70.5	65.2	6.4	104.4	742.5	24.5	21.7	1.06307	0.331
		digest	752.2	302.1	150.8	1544.8	3058.5	1509.8	3.0	3814.8	0.70672	0.299
R03	granite	HAc leach	8.2	11.2	17.0	10.4	29.7	61.9	23.0	26.9	0.88278	0.190
		HNO_3 leach	27.9	64.6	84.5	5.9	114.1	254.4	27.8	24.3	1.52397	0.094
		digest	481.2	179.9	219.1	1635.4	2785.3	1052.4	1.2	3107.1	0.72670	0.288
R04	garnet gneiss	HAc leach	66.3	32.5	8.4	6.5	43.6	97.7	22.2	71.1	0.71374	0.447
		HNO_3 leach	71.7	56.9	17.4	6.3	77.9	287.8	33.4	84.5	0.71939	0.609
		digest	1286.3	988.5	181.8	596.1	2436.1	1215.8	2.6	4039.7	0.70508	0.531
R05F	felsic gneiss	HAc leach	43.1	5.8	1.9	2.4	8.4	19.1	5.0	34.9	0.71558	0.361
		digest	270.5	321.4	572.5	1395.6	2693.1	7758.7	131.8	4006.3	0.71555	0.411
R05M	mafic gneiss	HAc leach	13.1	4.4	1.1	1.8	8.3	6.0	7.1	7.6	0.72240	0.321
		digest	1677.8	1525.0	226.8	677.7	2400.2	968.9	7.3	1345.5	0.71976	0.236
Mineral Separates												
R05F-ap	apatite	digest	9054.6	37.5	8.6	10.8	47.0	34.5	4.7	5654.5	0.70717	0.607
R05F-ep	epidote	digest	3344.7	251.5	16.1	36.0	3791.7	233.1	3.5	32141.2	0.70956	0.318
R05F-pl	plagioclase	digest	249.0	36.6	306.3	2232.8	3232.7	3079.5	4.4	5618.9	0.71206	0.352
R05F-chl	chlorite	digest	313.4	2780.9	76.4	74.7	3156.8	1168.5	5.9	419.4	0.72269	0.319
R05F-Kfs	K-feldspar	digest	21.5	11.7	2938.9	541.2	3525.5	61112.2	1.2	9324.2	0.72158	0.455
R05F-qtz	quartz	digest	123.8	26.8	85.2	663.5	1030.6	1036.5	0.3	2086.7	0.71060	0.344
R05F-ttn	titanite	digest	5145.6	70.7	2.3	25.1	450.3	90.4	8.9	1194.0	0.70773	0.533
R05F-hbl	hornblende	digest	430.5	3063.0	129.9	117.3	3502.8	nd	nd	2110.1	0.72620	nd
R05F-chl+bt	chlorite+biotite	digest	633.3	2940.2	25.8	22.6	3569.6	nd	nd	2238.6	0.72169	nd
R05M-ap	apatite	digest	6232.2	85.6	2.7	30.4	545.4	109.4	10.8	1446.2	0.70398	0.633
R05M-ep	epidote	digest	1864.4	1813.8	160.7	391.2	2088.2	503.5	1.7	1299.6	0.71652	0.220
R05M-hbl	hornblende	digest	2179.2	2275.4	207.5	514.7	2547.1	722.0	4.8	634.6	0.72652	0.339
R05M-ttn	titanite	digest	4256.6	36.3	2.2	18.6	277.9	42.2	8.1	315.3	0.70610	0.479
R05M-pl	plagioclase	digest	1085.1	107.2	418.2	1900.9	4322.3	2230.1	nd	6367.0	0.71562	nd
R05M-Kfs	K-feldspar	digest	214.8	50.7	302.0	3263.4	4207.6	2180.9	nd	4602.4	0.72046	nd

nd indicates no data, "bdl" indicates below instrumental detection limit.

4.5. Discussion

4.5.1 Controls on subglacial discharge geochemistry

4.5.1.1. Solute sources determined by $^{87}Sr/^{86}Sr$ ratios

Subglacial discharge had similar average $^{87}Sr/^{86}Sr$ ratios in 2014 and 2015 suggesting the same primary source(s) of cations during both years. However, $^{87}Sr/^{86}Sr$ ratios also varied substantially throughout both seasons (Fig. 4.3). Given that Sr concentrations in rain, snow, and supraglacial stream samples were below detection limit (Andrews et al., *in prep*), it is unlikely that surficial inputs drive variation in subglacial discharge $^{87}Sr/^{86}Sr$ ratios. The relatively constant suspended sediment $^{87}Sr/^{86}Sr$ ratios suggest that primary bedrock weathering sources did not change substantially throughout the melt seasons, despite possible changes in subglacial flowpaths (Bhatia et al., 2011) (Fig. 4.3).

To assess whether preferential mineral weathering could account for subglacial discharge $^{87}Sr/^{86}Sr$ ratios, we conducted a variety of experiments to constrain the Sr isotope geochemistry of sediment and rock samples. We assume that bedload sediment reasonably approximates the average bedrock composition in the Russell Glacier catchment, as has been previously found in glacial catchments (Anderson, 2005), although we recognize that mineralogical sorting can occur during transport. As shown in Figure 4.4A, bulk digests of suspended and bedload sediment collected directly outside the subglacial portal (BL02, site P) have similar $^{87}Sr/^{86}Sr$ and Ca/Sr ratios, while various leachates of bedload sediment have much higher $^{87}Sr/^{86}Sr$ and Ca/Sr ratios. We therefore infer that minerals with high Ca/Sr and $^{87}Sr/^{86}Sr$ preferentially dissolve, given that the leachates are largely similar the composition of subglacial discharge samples.

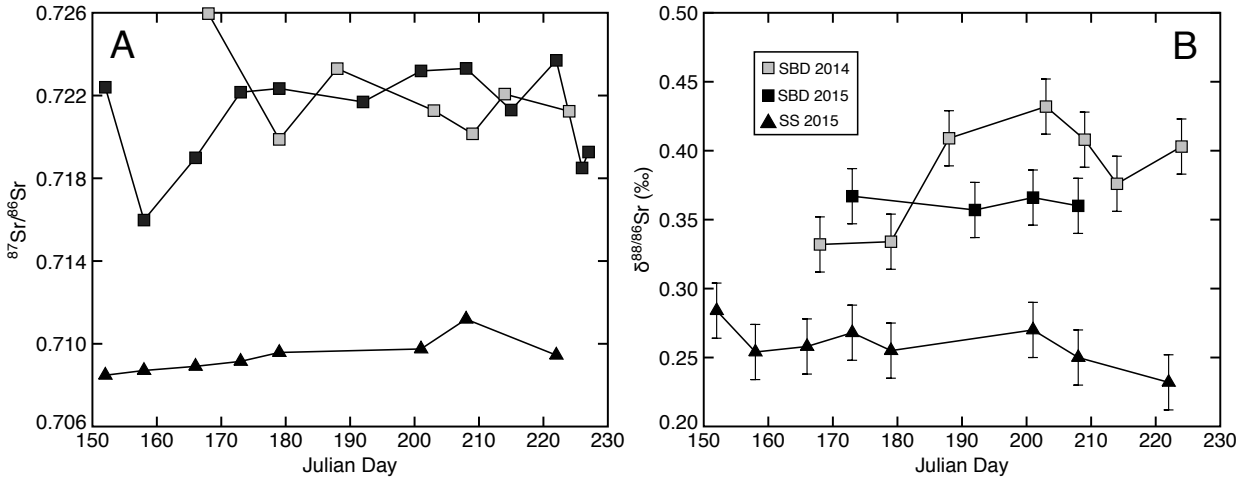

Figure 4.3: $^{87}Sr/^{86}Sr$ ratios (A) and $\delta^{88/86}Sr$ values (B) of site P subglacial discharge (SBD) and suspended sediment (SS) through time. Error bars in (B) indicate 2σSD.

To more clearly identify which minerals preferentially dissolve, we analyzed mineral separates obtained from rocks R05F and R05M (Table 4.3). Figure 4.5 plots $^{87}Sr/^{86}Sr$ and Ca/Sr ratios for R05F and R05M mineral separates, as well as their respective bulk rock digests. Given that minerals from one or two rock samples are unlikely to completely constrain the absolute radiogenic Sr isotope composition of mineral end-members in the larger site P catchment, we focus on the relative $^{87}Sr/^{86}Sr$ and Ca/Sr values of minerals in each assemblage. For example, in both assemblages hornblende has the highest $^{87}Sr/^{86}Sr$ ratio (~0.726) while apatite and titanite have relatively low $^{87}Sr/^{86}Sr$ values (< 0.708) and high Ca/Sr ratios. Plagioclase and epidote have moderate $^{87}Sr/^{86}Sr$ ratios (~0.710) as compared to other minerals, but are lower than their associated bulk rock leachates and digests. Similar trends were observed in mineral separates and whole rocks from the adjacent Leverett Glacier catchment (Hindshaw et al., 2014). Given this framework, the mineral data suggest that preferential weathering of biotite, chlorite, hornblende, and/or K-feldspar could elevate subglacial discharge $^{87}Sr/^{86}Sr$ ratios (Fig. 4.4A). Calcite weathering may also be a factor. Drill cores collected near site P contain calcite (Harper et al.,

2016), and previous studies conducted in the area have found geochemical evidence for calcite weathering contributions to the dissolved load (Andrews et al., *in prep*; Ryu and Jacobson, 2012, Graly et al., 2014, Graly et al., 2016). However, bulk rock HAc leachates, intended to characterize the rock carbonate fraction, had similar or only slightly higher $^{87}Sr/^{86}Sr$ ratios than their respective rock digests (Fig. 4.5). Furthermore, any sedimentary carbonate within the catchment would likely have very low $^{87}Sr/^{86}Sr$ ratios (Banner, 2004). Overall, we find that the weathering of biotite, chlorite, hornblende, and/or K-feldspar can reasonably account for the radiogenic Sr isotope composition of subglacial discharge.

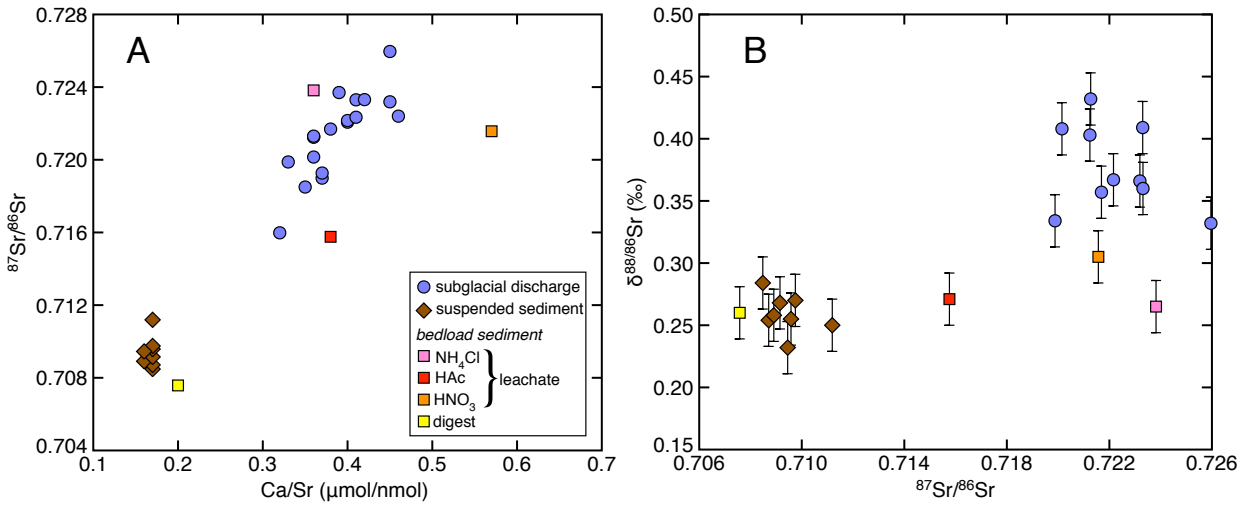

Figure 4.4: $^{87}Sr/^{86}Sr$ versus Ca/Sr ratios (A) and $\delta^{88/86}Sr$ values versus $^{87}Sr/^{86}Sr$ ratios (B) of site P subglacial discharge, suspended sediments, and bedload sediment leachates and digest. Error bars in (B) indicate 2σSD.

4.5.1.2. Solutes sources determined by $\delta^{88/86}Sr$ values

In 2014 and 2015, subglacial discharge $\delta^{88/86}Sr$ values (0.386‰ and 0.362‰, respectively) were higher than those of the site P bedload (BL02; 0.260‰) and suspended sediment (~0.259‰) digests (Fig. 4.4). Rivers across the globe often have higher $\delta^{88/86}Sr$ values

than the bedrock they drain (Pearce et al., 2015a). This phenomenon has been attributed to preferential dissolution of minerals having unique $\delta^{88/86}$Sr values (Chao et al., 2015; Andrews and Jacobson, 2017) as well as secondary mass-dependent fractionation processes. Given that preferential mineral dissolution appears to explain the radiogenic Sr isotope composition of subglacial discharge, we first evaluate whether this mechanism could also account for the stable Sr isotope composition of subglacial discharge and later assess the role of mass-dependent fractionation (see Section 4.5.2.3).

Figure 4.4B plots $\delta^{88/86}$Sr values versus $^{87}Sr/^{86}Sr$ ratios for subglacial discharge, the BL02 leachates and digest, and suspended sediments. The $\delta^{88/86}$Sr values of BL02 leachates are similar to bedload and suspended sediment digests, and lower than subglacial discharge, except for the BL02 HNO_3 leachate. The BL02 HNO_3 leachate has a statistically higher $\delta^{88/86}$Sr value than the BL02 digest and average suspended sediment, and is similar to some subglacial discharge samples. To better evaluate whether preferential mineral dissolution could control subglacial discharge $\delta^{88/86}$Sr values, we measured the $\delta^{88/86}$Sr values of mineral separates (Fig. 4.5). The stable Sr isotope composition of common silicate-rock forming minerals has not been previously reported in the literature. R05F and R05M mineral separates confirm that silicate-rock forming minerals have a wide range of $\delta^{88/86}$Sr values, and can vary by as much as 0.40‰ within a given rock. In general, the data suggest that the preferential weathering of certain mineral phases, namely K-feldspar, hornblende, apatite, and titanite, from bulk rock, could elevate subglacial discharge $\delta^{88/86}$Sr values by ≥0.10‰, which is the difference between subglacial discharge and the suspended and bedload sediment digests. It is uncertain how the weathering of trace calcite would affect riverine $\delta^{88/86}$Sr values given that there is no systematic trend in the $\delta^{88/86}$Sr values

of bulk rock HAc leachates relative to their respective digests (Table 4.3, Fig. 4.5) and data on natural, inorganic, and non-marine calcites is limited (Andrews and Jacobson, 2017). It is also unclear why the BL02 leachates and digest had such similar $\delta^{88/86}$Sr values (Fig. 4.4) given the range observed in minerals. To some extent, the more weatherable mineral phases may have been depleted from bedload sediment prior to collection (Graly et al., 2016). This might also help explain why bulk rock samples have a significantly wider range of $\delta^{88/86}$Sr values than bedload sediment, which is comparatively homogenous (Fig. 4.6). Combining the radiogenic and stable Sr isotopes analyses, the preferential weathering of minerals characterized by both high $^{87}Sr/^{86}Sr$ and $\delta^{88/86}$Sr values, namely K-feldspar and hornblende, could adequately account for the solute Sr geochemistry of subglacial discharge.

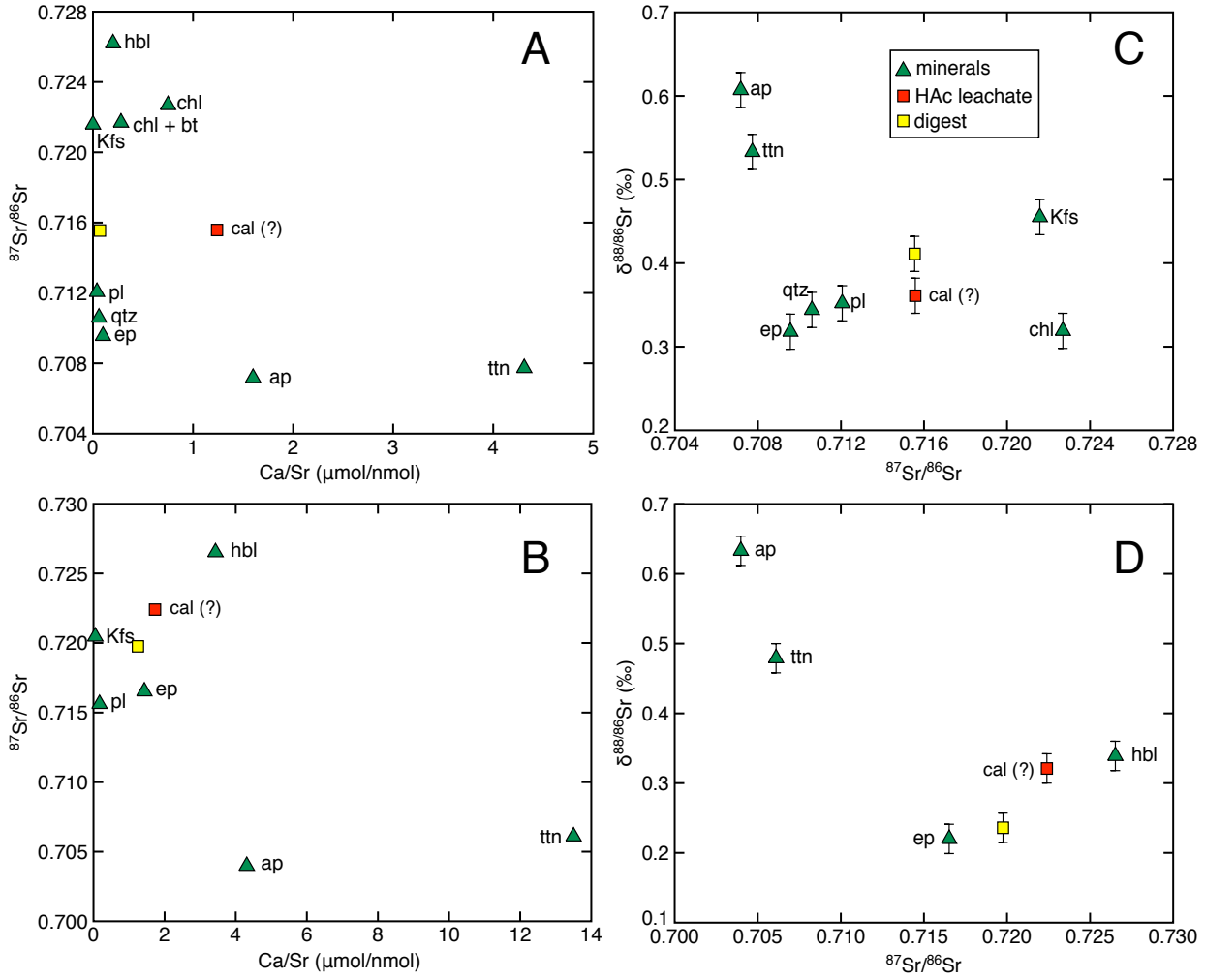

Figure 4.5: $^{87}Sr/^{86}Sr$ versus Ca/Sr ratios of R05-F (A) and R05-M (B) mineral separates and bulk rock HAc leachate and digest. $\delta^{88/86}Sr$ values versus Ca/Sr ratios of R05-F (C) and R05-M (D) mineral separates and bulk rock HAc leachate and digest. Error bars in (C) and (D) indicate 2σSD.

4.5.1.3 Secondary processes affecting solutes determined by $\delta^{88/86}Sr$ values

Multiple mass-dependent isotope fractionation mechanisms have been invoked to explain why rivers often have higher $\delta^{88/86}Sr$ values than the bedrock they drain. Here, we consider whether these mechanisms could explain subglacial discharge $\delta^{88/86}Sr$ values measured in the present study. Plant uptake can elevate riverine $\delta^{88/86}Sr$ values (Andrews et al., 2016; Bullen and

Chadwick, 2016), but we eliminate this mechanism as a factor for the present study given the absence of plants in the immediate vicinity of the Russell Glacier. Calcite precipitation can also elevate riverine $\delta^{88/86}$Sr values (Andrews et al., 2016; Bullen and Chadwick, 2016)), but discharge from the Russell Glacier is highly undersaturated with respect to calcite ($\log\Omega = -4.4$). Two studies have proposed that primary mineral weathering preferentially releases heavier Sr isotopes to solution (Pearce et al., 2015; Wei et al., 2013). However, to the extent laboratory leaching procedures simulate natural weathering, a clear pattern does not emerge when comparing leachate and digest $\delta^{88/86}$Sr values for bulk rocks and bedload sediment (Fig. 6). These data more likely reflect variations in the relative abundances of Sr-bearing minerals and their isotopic compositions.

A previous study of the Lemon Creek Glacier, Alaska reported that subglacial discharge had higher $\delta^{88/86}$Sr values than local bedrock by ~0.10‰, while suspended sediment had lower $\delta^{88/86}$Sr values than average bedrock by <0.10‰ (Stevenson et al., 2016). The study concluded that clay minerals either incorporated lighter isotopes into their lattices or adsorbed them onto their surfaces (Stevenson et al., 2016). In contrast to the findings from Stevenson et al. (2016) however, Russell Glacier suspended sediment $\delta^{88/86}$Sr values were identical to the site P bedload sediment (BL02) digest, within error bars (Fig. 4.4). There is therefore no evidence for a preferentially light clay reservoir capable of controlling subglacial discharge $\delta^{88/86}$Sr values. Suspended sediment from the adjacent Isunnguata Sermia Glacier is dominated by abraided primary silicate minerals with a very small proportion of clay (Graly et al., 2016). This could explain why Russell Glacier suspended and bedload sediment have similar $\delta^{88/86}$Sr values. Furthermore, Russell Glacier discharge is moderately supersaturated with respect to Ca-montmorillite ($\log\Omega = 1.0$), which could structurally incorporate Sr, but suspended sediment

from the adjacent Isunnguata Sermia Glacier contains only trace levels of smectite (Graly et al., 2016). Russell Glacier discharge is undersaturated with respect to illite ($\log\Omega = -1.0$) but highly supersaturated with respect to kaolinite ($\log\Omega = 4.8$). While kaolinite is not expected to incorporate much Sr, surface adsorption could be a factor. Nonetheless, Sr adsorption to kaolinite is pH dependent and dramatically reduced at low pH (Ning et al., 2017; Rafferty et al., 1981; Rani and Sasidhar, 2012). The apparent mass-dependent fractionation reported by Stevenson et al. (2016) could reflect the near order of magnitude higher pH of subglacial discharge from the Lemon Creek Glacier (~7.5) versus the Russell Glacier (~6.7). It is also possible that Lemon Creek drainage contains overall higher proportions of clay minerals. In either case, we note that Lemon Creek subglacial discharge had significantly higher $^{87}Sr/^{86}Sr$ ratios than the associated suspended sediment, much like the pattern documented for the Russell Glacier. It therefore seems equally plausible that preferential mineral weathering could explain the radiogenic and stable Sr isotope geochemistry of Lemon Creek subglacial discharge, although this hypothesis requires testing. In general, we cannot identify a mass-dependent fractionation mechanism that can reasonably account for site P subglacial discharge $\delta^{88/86}Sr$ values.

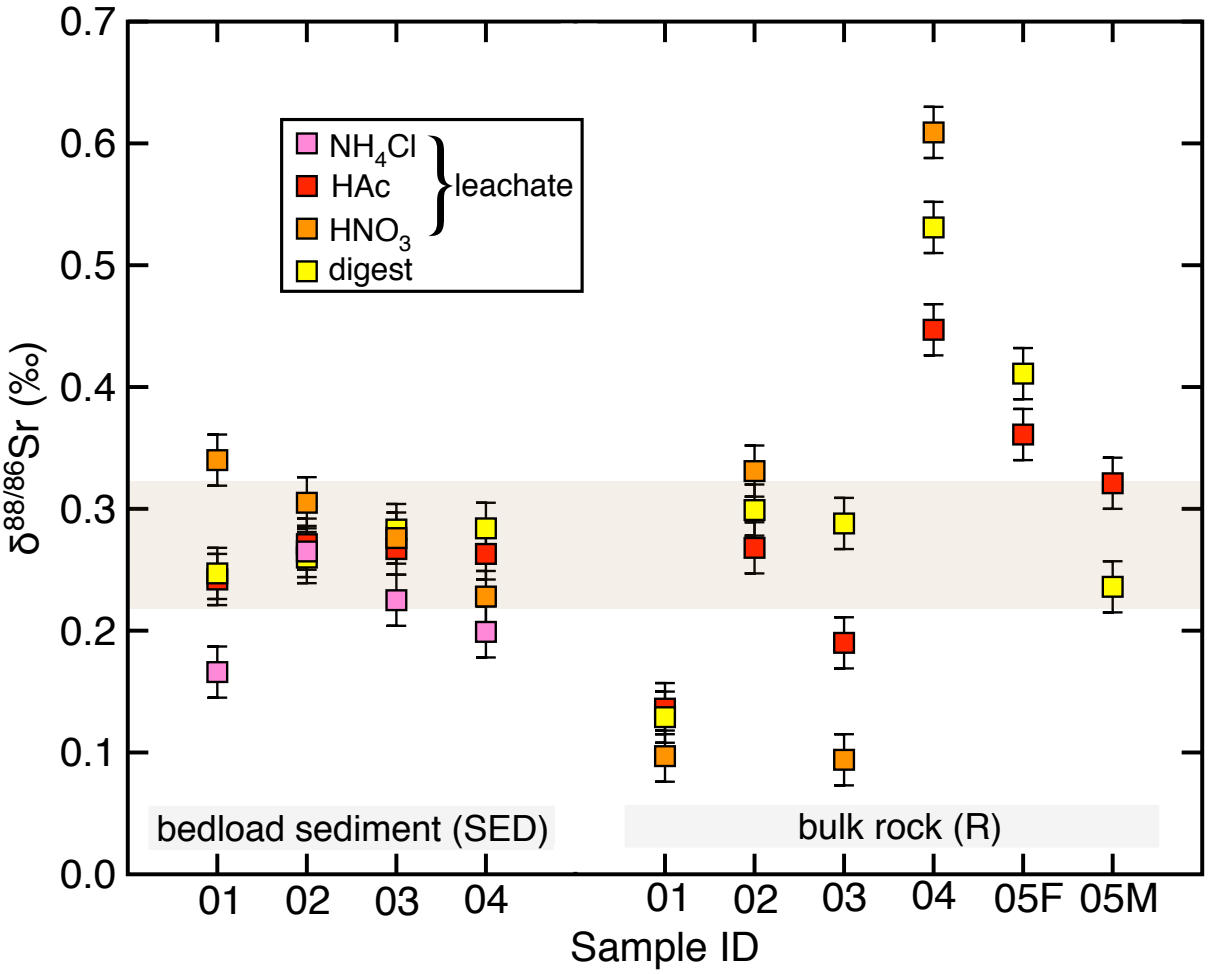

Figure 4.6: Comparison of $\delta^{88/86}Sr$ values for leachates and digest of bedload sediment and bulk rock samples. Beige shading is the bulk silicate Earth average (Moynier et al., 2010). Error bars indicate 2σSD.

4.5.2 Controls on AKR transect solute geochemistry

Along the entire ~32 km downstream transect from the GrIS margin towards the ocean, AKR $^{87}Sr/^{86}Sr$ ratios increase from ~0.722 to ~0.747 in a broadly step-wise pattern (Fig. 4.7). AKR $^{87}Sr/^{86}Sr$ values generally plateau from site P to J (0.1 km to 2.4 km), site I to R (4.4 km to 6.2 km), site H to G (9.2 km to 11 km), and site D to B (20.7 km to 32.1 km). AKR $^{87}Sr/^{86}Sr$ ratios increase at distances along the transect that follow point sources of additional subglacial discharge (Fig. 4.7). Leverett Glacier discharge and Seahorse Lake samples yielded higher

$^{87}Sr/^{86}Sr$ ratios than the AKR. AKR $^{87}Sr/^{86}Sr$ ratios versus Ca/Sr ratios strongly correlate (R^2 = 0.91 , $p < 0.0001$, n = 53) and trend from the average site P composition toward the Leverett Glacier discharge composition (Fig. 8). These results suggest that in the proglacial area, downstream changes in the AKR solute load reflects two-component mixing between site P subglacial discharge and progressively increasing contributions from water having a composition similar to Leverett Glacier discharge. The bulk cation geochemistry of the AKR and Leverett Glacier discharge also support this conclusion. The Na- and K-dominated cation composition of AKR sites D – B is similar to that of Leverett Glacier discharge, particularly in 2015 (Fig. 4.3). Additionally, during both melt seasons, the cation composition of AKR samples from sites K to E (1 km to 15.6 km) was intermediate between the chemical composition of site P subglacial discharge and that of AKR sites D – B, further suggesting two-component mixing. The dominance of the Leverett Glacier on the geochemical signature of the AKR after 16.6 km is consistent with its order of magnitude higher discharge rate as compared to the site P catchment (Bartholomew et al., 2011; Cowton et al., 2012; Rennermalm et al., 2012). Following the confluence of the AKR and Leverett Glacier discharge there are no major additional hydrological inputs to the river. Any subsequent change in AKR solute geochemistry could be attributed to in-situ weathering. However, proglacial chemical weathering appears to be negligible in the AKR because $^{87}Sr/^{86}Sr$ values and the absolute concentrations of major cations (Ca, Na, Mg, K) do not change substantially across this distance (Fig. 4.7).

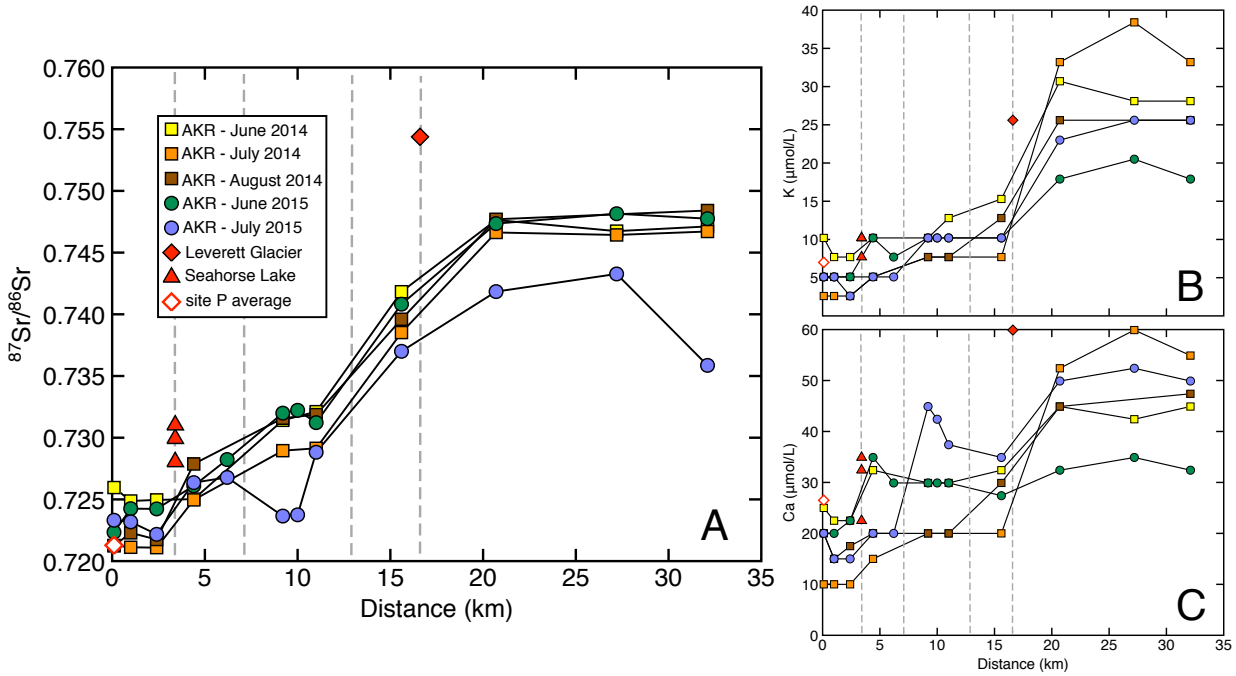

Figure 7. $^{87}Sr/^{86}Sr$ ratios (A), K concentrations (B), and Ca concentrations (C) versus distance for AKR samples. Distance moves from the ice sheet margin (0km) towards the Kangerlussuaq Fjord (see Fig. 1). Gray dashed lines indicate the downstream position of additional hydrologic inputs to the AKR, such as Seahorse Lake and Leverett Glacier discharge, also plotted.

When coupled with $^{87}Sr/^{86}Sr$ ratios, bulk cation patterns suggest that the site P catchment accesses distinctly different bedrock compared to the adjacent Leverett Glacier catchment. Site P discharge has high molar Ca/Na ratios relative to Leverett Glacier discharge (3.6 and 1.1, respectively), suggesting greater contributions from carbonate weathering. Site P discharge also has higher molar K/Na ratios than Leverett Glacier discharge (0.9 and 0.5, respectively), which could indicate more biotite and/or K-feldspar weathering, relative to plagioclase weathering. A comparison of aeromagnetic data (Fig. 3 in van Gool et al., 2002) to catchment boundaries (Fig. 1a in Lindback et al., 2015) demonstrates that the site P catchment is underlain by a small outcrop of high magnetic anomaly bedrock trending west to east, similar to the Ikertôq thrust zone. Conversely, the Leverett Glacier catchment is underlain primarily by low magnetic

anomaly bedrock trending southwest to northeast, indicative of the Southern Nagssugtoqidian Orogen. The lower $^{87}Sr/^{86}Sr$ and higher Ca/Na ratios for site P discharge may reflect differences in bedrock geology as the Ikertôq thrust zone contains large volumes of Paleoproterozoic metasediments, while the Southern Nagssugtoqidian Orogen is primarily Archaean gneisses (van Gool et al., 2002). Taken together, we find that water mass mixing plays a critical role in determining the downstream evolution of AKR discharge.

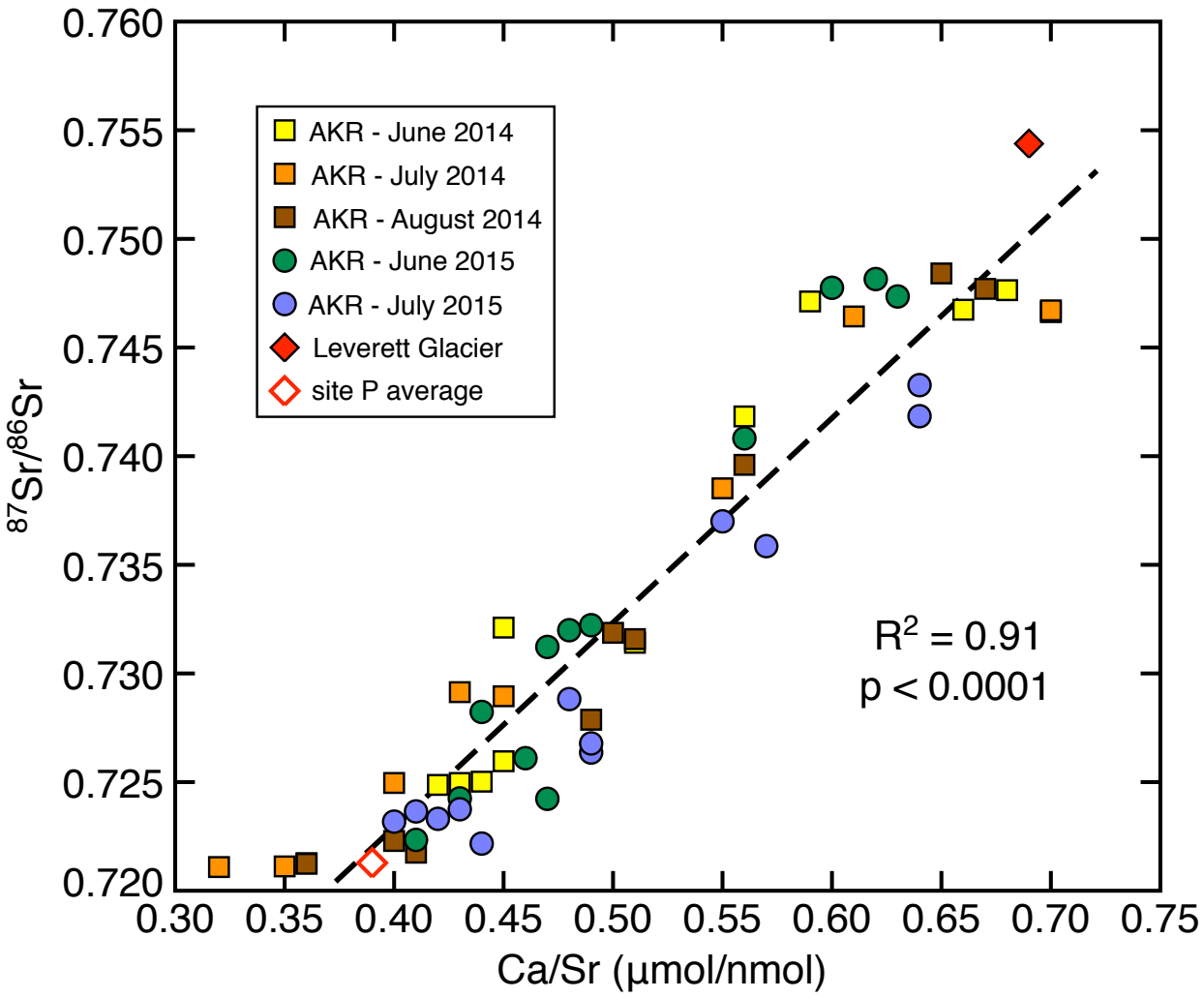

Figure 4.8: $^{87}Sr/^{86}Sr$ versus Ca/Sr ratios for AKR samples and Leverett Glacier discharge. R^2 and *p*-value correspond to the AKR regression line (black dashed line).

4.6. Conclusions and Implications

4.6.1 The role of ice sheets in long-term climate regulation

Throughout two melt seasons, we used bulk ion geochemistry and Sr isotopes to analyze the controls on solute geochemistry of subglacial discharge exiting the Russell Glacier, southwestern GrIS, and during transport through the proglacial area towards the ocean. The $^{87}Sr/^{86}Sr$ ratios of subglacial discharge, bedload sediment, suspended sediments, and mineral separates suggest that high $^{87}Sr/^{86}Sr$ silicate minerals are preferentially weathered from bedrock and could account for subglacial discharge solute geochemistry. Subglacial discharge has an average Ca/Na ratios of 3.6 which indicates that, to some extent, calcite weathering contributes to the dissolved load. However, bulk rock and bedload sediment HAc leachates are not substantially higher than their respective digests, and suggests carbonate weathering does not dominate solute geochemistry.

To further elucidate solute sources as well as secondary processes that could alter Russell Glacier subglacial discharge solute geochemistry, we analyzed the same water and rock reservoirs for $\delta^{88/86}Sr$ values. Subglacial discharge has an average $\delta^{88/86}Sr$ value higher than bedload and suspended sediment digests by ~0.10‰. Common silicate-rock forming minerals have $\delta^{88/86}Sr$ values that are different from each other by up to ~0.40‰. After evaluating whether processes such as clay formation and/or adsorption could control subglacial discharge $\delta^{88/86}Sr$ values by mass-dependent isotope fractionation, we find that solute geochemistry is best explained by the preferential weathering of high $\delta^{88/86}Sr$ value minerals. Combining our analysis of radiogenic and stable Sr isotopes, the preferential weathering of high $^{87}Sr/^{86}Sr$ and $\delta^{88/86}Sr$ value minerals, namely K-feldspar and hornblende, can fully account for the Sr geochemistry of subglacial discharge. Preferential dissolution of K-bearing minerals, such as K-feldspar, has been

previously suggested in a wide range of subglacial environments (Anderson et al., 2000; Anderson et al., 1997; Hagedorn and Hasholt, 2004; Hodson et al., 2000; Sharp et al., 2002; Stevenson et al., 2016). In general, the Sr isotope results provide a new line of evidence supporting the contention that ice sheets can be sites of substantial subglacial silicate mineral weathering.

Along a ~32km downstream transect from the GrIS margin towards the coast, AKR bulk ion geochemistry and $^{87}Sr/^{86}Sr$ values appear to be predominately controlled by water-mass mixing from point sources. Furthermore, lengths of the downstream transect with no additional hydrological inputs have little variation in major cation concentrations or $^{87}Sr/^{86}Sr$ ratios. Therefore, proglacial chemical weathering (silicate or otherwise) is likely negligible and may not contribute significantly to GrIS carbon cycling on either short or long timescales. Nevertheless, AKR bulk ion geochemistry indicates that the proportion of silicate chemical weathering, relative to other weathering regimes, is greater at the Russell and Leverett Glaciers than valley glaciers. The global average Ca/Na ratio of valley glaciers is 9.3 (Torres et al., 2017), substantially higher than the Ca/Na ratios documented here. Molar SO_4/Na ratios are considered a proxy for sulfide oxidation relative to silicate weathering. The average SO_4/Na ratio of site P subglacial discharge and the AKR after merger with Leverett Glacier discharge was 1.6 and 0.4, respectively. These values are significantly lower than the global glacier average of 3.7 (Torres et al., 2017). In general, our findings indicate that GrIS catchments have the potential to sequester more atmospheric CO_2 than valley glacier catchments due to relatively higher rates of silicate chemical weathering. This should be considered when evaluating the role of large scale glaciation on long-term global climate.

4.6.2 Developments in the stable Sr isotope tracer

Finally, this study provides new insight into the novel stable Sr isotope tracer. Given the globally ubiquitous observation that rivers often have higher $\delta^{88/86}$Sr values than the bedrock they drain (Pearce et al., 2015a), our results suggest that riverine $\delta^{88/86}$Sr values can be largely explained by the preferential dissolution of distinct mineral phases from bulk bedrock, rather than substantial low-temperature mass-dependent fractionation on the continents. This is in agreement with Chao et al. (2015), which concluded that river water from a sedimentary watershed in Taiwan had higher $\delta^{88/86}$Sr values than local bedrock due to the preferential dissolution of high $\delta^{88/86}$Sr value minerals. Laboratory experiments demonstrated that the $\delta^{88/86}$Sr value of the shale leachates decreased across a one month timespan due to the sequential dissolution of feldspar, chlorite, and illite (Chao et al., 2015). Our mineral data support their findings to the extent that feldspar weathering may elevate leachate $\delta^{88/86}$Sr values and a transition from this to chlorite weathering could yield a decrease in leachate $\delta^{88/86}$Sr values. Contrary to Stevenson et al. (2016), we find no evidence for Sr isotope fractionation via clay formation or adsorption in subglacial discharge suspended sediments. Nevertheless, processes known to fractionate stable Sr isotopes, such as calcite precipitation and plant uptake, likely play a role in determining riverine $\delta^{88/86}$Sr values in select locations.

Chapter 5

Linkages between the supraglacial and subglacial carbon cycles at the margin of the Greenland Ice Sheet

5.1 Introduction

Estimates suggest that melting of the Greenland Ice Sheet (GrIS) could significantly impact the cycling of organic and inorganic carbon (C) in the coming decades (Hood et al., 2015; Lawson et al., 2014; Ryu and Jacobson, 2012). However, these predictions are based on limited data. A handful of studies have quantified organic and inorganic C fluxes from GrIS subglacial discharge (SBD) but mainly over brief timespans (~weeks) (Bhatia et al., 2013; Dieser et al., 2014; Hagedorn and Hasholt, 2004; Hindshaw et al., 2014; Lawson et al., 2014; Ryu and Jacobson, 2012; Wimpenny et al., 2010; Yde et al., 2014). Research conducted on the GrIS surface has primarily focused on cryoconite holes, although the bare ice surface may have a substantially greater impact on the global C cycle (Cook et al., 2012; Stibal et al., 2010). Few studies have examined supraglacial streams (SPS), which traverse large spatial areas of the GrIS surface and deliver lake water, snow melt, and bare ice melt to the subglacial environment. A holistic understanding of the GrIS C cycle requires knowledge of all C reservoirs and recognition that subglacial processes inherently depend on surficial input fluxes.

To address this knowledge gap, we analyzed the geochemistry and microbial ecology of SPS and SBD sampled in tandem, from a single catchment, over the course of two melt seasons. Our study focused on a small catchment on the northern margin of the Russell Glacier, a land-terminating lobe of the GrIS located in southwestern Greenland (Fig. 5.1). We sampled SBD and SPS from June – August, 2014 and 2015. SPS and SBD samples were collected within ~24 hrs

of each other in 2014 and within ~3 hrs of each other in 2015, thus generating a series of SBD – SPS sample pairs that are comparable throughout each melt season. We sampled SPS flowing strictly through ice (SPS-Q, V-Y) as well as alongside a lateral moraine (SPS-N).

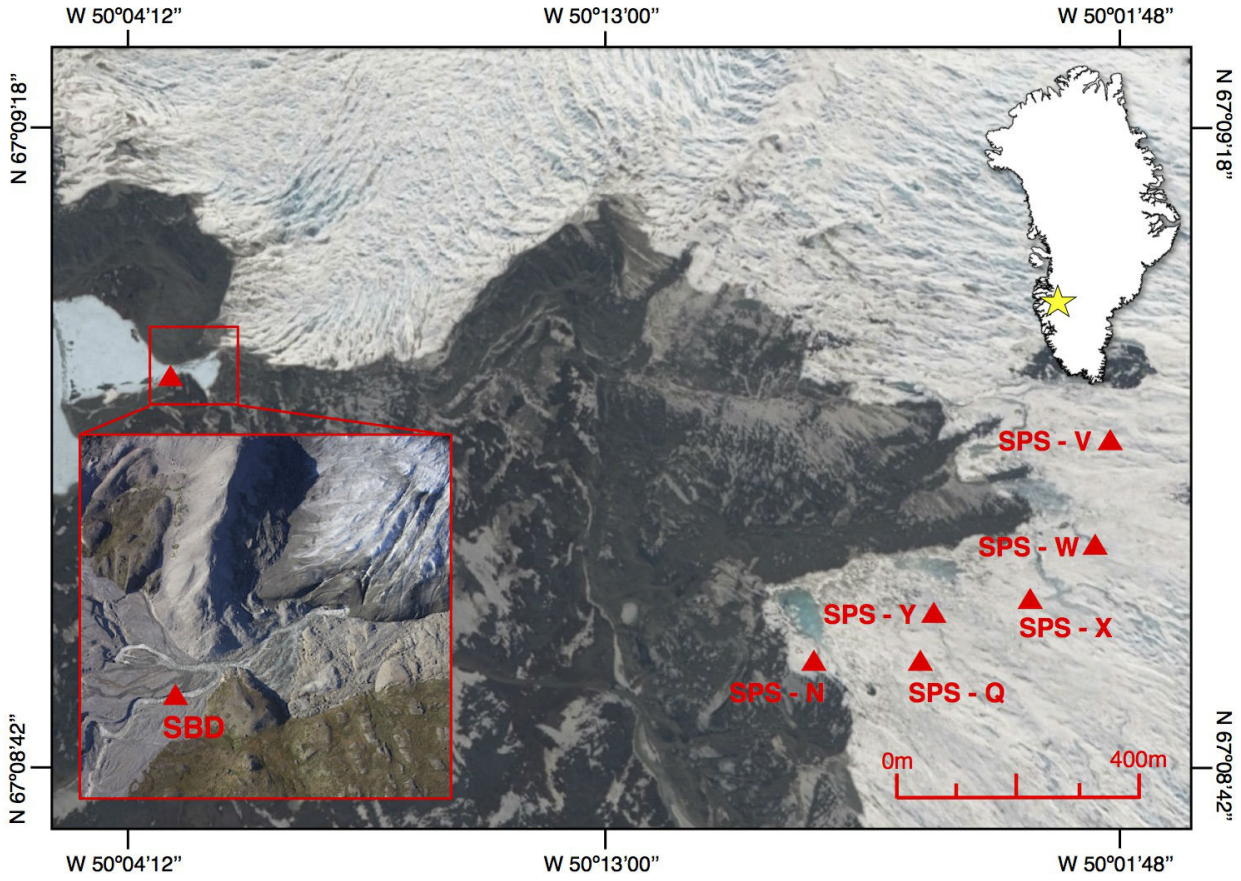

Figure 5.1. Map of field site; Russell Glacier, southwestern GrIS. Sample site locations are marked with red triangles. Location of field site within Greenland is marked with a yellow star on Greenland inset map (top-right). Aerial photograph of SBD (red square inset, bottom-left) was taken on July 29, 2015.

5.2 Setting

The Russell Glacier is located in the Kangerlussuaq region of southwestern Greenland. The study catchment is ~40 km^2 and hosts few supraglacial lakes (Lindback et al., 2015). The average summer discharge is ~12 m^3s^{-1} (2008 – 2011) (Rennermalm et al., 2012). All SPS are contained within the catchment area (Lindback et al., 2015). SBD was sampled 100 m from the ice margin (Fig. 5.1). The bedrock of the region is dominated by Archaean gneisses, primarily amphibolite- and granulite- facies (van Gool et al., 2002). Three drill cores collected from the proglacial area of the SBD portal found that fracture infillings contain between 46% and 60% calcite (Harper et al., 2016). The climate of the Kangerlussuaq area is low Arctic polar desert. Temperature is strongly seasonal, with a mean summer air temperature of 10.3 °C (2001 – 2011) and a mean winter air temperature of -16.1°C (2001 – 2011) (Hanna et al., 2012). Mean annual precipitation is low, 258 mm/yr (2001 – 2012) (Mernild et al., 2015).

5.3 Methods

5.3.1 Sample collection and field methods

SPS samples were typically collected between 11am and 12pm, while SBD samples were collected between 1pm and 2pm. Sample locations were documented with a Garmin 60CSx handheld GPS meter. Water temperatures were measured on-site using a Mettler SevenGo Pro meter. Water samples for oxygen isotope ($\delta^{18}O$) analyses were collected in LDPE sample bottles. Water samples for cation and Si concentration analyses were passed through 0.45 μm filter capsules (Versapor membrane), collected in I-CHEM HDPE bottles, and acidified to pH <2 using concentrated, ultrapure HNO_3. Water samples for anion concentration analyses were passed through 0.45 μm filter capsules (Versapor membrane) and collected in LDPE sample

bottles. Water samples for dissolved organic carbon (DOC) concentrations were passed through 0.45 μm filter capsules (Supor membrane), collected in amber, borosilicate glass vials, acidified with ultrapure HCl to pH < 2 within 12 hours, and kept in darkness until analysis. Water samples for dissolved inorganic carbon (DIC) concentrations, were passed through 0.45 μm filter capsules (Supor membrane), collected in amber, borosilicate glass vials, and kept in darkness until analysis. In 2015, an additional PTFE-rubber septum was added to each DIC concentration vial. Water samples for stable carbon isotopes ($\delta^{13}C_{DIC}$ and $\delta^{13}C_{DOC}$) and radiocarbon isotopes ($\Delta^{14}C_{DIC}$ and $\Delta^{14}C_{DOC}$) were passed through 0.45 μm filter capsules (Supor membrane), collected in amber, borosilicate glass vials, refrigerated, and kept in darkness until analysis. All samples for DIC concentrations and C isotopes were collected with no headspace. Rain samples were collected in LDPE sample bottles and passed through a 0.45 μm polypropylene filter within 24 hrs of collection. Snow samples were collected in LDPE sample bags, allowed to melt overnight, and then processed and transferred to sample bottles as outlined above.

Samples for microbial DNA sequencing were collected by passing 300 mL of stream water through 0.22 μm Sterivex filters. Sample filters were stored in sterile Whirl-Pak bags (Nasco, Fort Atkinson, WI) and immediately encased in ice. Within a few hours of collection, the samples were transferred to a -20°C freezer until shipment to the laboratory, where they were stored in an -80°C freezer until analysis. Samples for microbial cell count analyses were collected by adding 45 mL of stream water to conical tubes pre-dosed with 5mL of paraformaldehyde. Cell count samples were kept cool at all times prior to analysis.

5.3.2 Aqueous geochemistry laboratory methods

Cations and Si concentrations were measured in the SRC Environmental Analytical Laboratories, Saskatoon, Canada by inductively coupled plasma mass spectrometry (ICP-MS). Quality control standards were within ±5% of reported concentrations for all elements. Anion concentrations were measured in the Aqueous Geochemistry Laboratory at Northwestern University using a Dionex DX-120 ion chromatograph (IC) equipped with an ASRS-300 self-regenerating suppressor. Measured values for NIST-traceable Dionex standards were within ±10% of reported concentrations for all elements. DIC and DOC concentrations were measured in the Arizona Laboratory for Emerging Contaminants (ALEC) at the University of Arizona with a Shimadzu TOC-VCSH TOC/TN analyzer. Analytical errors for both DIC and DOC concentrations are ±2% based on repeated measurements of each sample. Total alkalinity was calculated by cation and anion concentration charge-balance ($ALK_{CB} = TZ^{+} - TZ^{-}$), where TZ^{+} is the sum of cations and TZ^{-} is the sum of anions, in eq/L. ALK_{CB} is assumed equivalent to carbonate alkalinity ($ALK_{CARB} \approx [HCO_3]$), as the relatively low DOC concentrations preclude significant contributions from non-carbonate alkalinity (Abril et al., 2015). $\delta^{18}O$ values were measured on a Picarro L2130-i Cavity Ring-Down Spectrometer with micro-combustion module. Samples were injected 9 times, and final data were averaged from the last four injections to eliminate any memory effects. Temperature, DIC concentrations, and ALK_{CB} were implemented with temperature-dependent equilibrium constants (Plummer and Busenberg, 1982) to calculate HCO_3 concentrations for SBD. Stable C isotope values ($\delta^{13}C_{DIC}$ and $\delta^{13}C_{DOC}$) and radio-C values ($\Delta^{14}C_{DIC}$ and $\Delta^{14}C_{DOC}$) were measured at the University of Arizona Accelerator Mass Spectrometer (AMS) Laboratory. $\delta^{13}C_{DIC}$ and $\delta^{13}C_{DOC}$ values were measured with a VG Optimal Dual Inlet Mass Spectrometer. Repeated standard analyses yielded an uncertainty of ±0.1‰.

Radio-C contents were measured by accelerator mass spectrometry following the procedure outlined in Leonard et al. (2013). Repeated measurements of each sample yielded an analytical error of ±1%.

5.3.3 Microbiology laboratory methods

DNA was extracted from the Sterivex filters using the PowerWater kit (MO BIO Laboratories, Inc.) following the manufacturer's instructions. The polymerase chain reaction (PCR) was used to generate amplicon libraries of the 16S rRNA genes from bacteria and archaea using barcoded primers (515f-806r) (Bates et al., 2011; Caporaso et al., 2011) to allow for the multiplexing of multiple samples on a single MiSeq run (Caporaso et al., 2012). PCR reactions were carried out with 5 PRIME MasterMix (Gaithersburg, MD) reagents. PCR reaction conditions were as follows: an initial denaturation step of 95 ºC for 3 minutes followed by 35 cycles of 95 ºC for 30 seconds, 55 ºC for 45 seconds, 72 ºC for 1.5 minutes. Reactions were finalized using a single extension step at 72 ºC for 10 minutes. Pooled product for each sample was then quantified using the Quant-iT PicoGreen dsDNA assay (Invitrogen). Primer dimers were removed using the UltraClean PCR Clean-Up Kit (MO BIO Laboratories, Inc.) and the amount of DNA in each sample was normalized to a final concentration of 2 ng μL^{-1}. Paired-end amplicons (151×12×151 bp) were sequenced on an Illumina MiSeq at the Environmental Sample Preparation and Sequencing Facility at Argonne National Laboratory following procedures described in Caporaso et al. (2012).

For the 14 samples, a total of 148,722 sequences were generated for an average depth of 10,623 ± 3,890 sequences per sample. Paired-end reads were joined using the PEAR algorithm (Zhang et al., 2014). Raw sequence data were demultiplexed and processed using QIIME version

1.8.0 (Caporaso et al., 2010b). Operational taxonomic units (OTUs) were picked at 97% sequence identity with UCLUST (Edgar, 2010). A representative sequence was then chosen for each OTU by selecting the most abundant sequence in that OTU. Representative sequences were aligned with PyNAST (Caporaso et al., 2010a) and taxonomy was assigned to representative sequences using the Greengenes reference database (McDonald et al., 2012). Sequence data are publicly available through MG-RAST (Meyer et al., 2008) under project number mgp79511.

Cells were counted using epifluorescence microscopy. 5 mL and 45 mL aliquots of fixed cells were filtered on to 0.22 μm black polycarbonate filters, stained with 1 mL 1 μg/mL DAPI (2-(4-amidinophenyl)-1H -indole-6-carboxamidine), then directly counted on a Zeiss Axioimager M2 upright microscope. At least 300 cells were counted for each slide.

5.3.4 Mixing calculations

We calculated the mole fraction of SPS-Q DIC originating from either heterotrophic microbial respiration (f_{microb}) or the atmosphere (f_{atm}) using the following equations for two-component mixing:

$$R_{SPS} = f_{microb}R_{microb} + f_{atm}R_{atm} \quad (5.1)$$

$$1 = f_{microb} + f_{atm} \quad (5.2)$$

where R_X is the $\delta^{13}C_{DIC}$ value of either atmospherically-derived C (R_{atm} = -6.7‰, see discussion), microbial, heterotrophically-respired C ($R_{microb} = \delta^{13}C_{DOC}$ of SPS-Q; Table 5.1, 5.2), or SPS-Q C (R_{SPS}; Table 5.1, 5.2). The calculation was conducted for each date that had paired SPS-Q $\delta^{13}C_{DOC}$ and $\delta^{13}C_{DIC}$ data.

We calculated the mole fraction of SBD DIC originating from either SPS inputs (f_{SPS}), subglacial heterotrophic microbial respiration (f_{microb}), or subglacial carbonate-mineral weathering (f_{carb}), using the following three-component mixing equations:

$$R_{SBD} = f_{SPS}R_{SPS} + f_{microb}R_{microb} + f_{carb}R_{carb} \quad (5.3)$$

$$1 = f_{SPS} + f_{microb} + f_{carb} \quad (5.4)$$

where f_{SPS} is equal to $[DIC_{SPS}]/[DIC_{SBD}]$ in mol/mol (Table 5.1, 5.2), and R_X is the $\delta^{13}C_{DIC}$ value of either SPS-Q C (R_{SPS}; Table 5.1, 5.2), microbial, heterotrophically-respired C (R_{microb} = $\delta^{13}C_{DOC}$ of SBD; Table 5.1, 5.2), or carbonate C (R_{carb} = 0‰, see below). The model was implemented for each date that had $[DIC_{SPS}]$, $[DIC_{SBD}]$, SPS-Q $\delta^{13}C_{DIC}$, and SBD $\delta^{13}C_{DIC}$ and $\delta^{13}C_{DOC}$ data. The results are plotted in Figure 4.

f_{microb} values should be considered upper limits for two reasons. First, these calculations assume that microbial methane oxidation is negligible (see discussion). Any methane oxidation would decrease f_{microb} and increase f_{carb}. Furthermore, the average $\delta^{13}C$ value of calcite from the catchment area is unknown. The average $\delta^{13}C$ value of siliciclastic continental crust is -6‰ (Sharp, 2007), and the $\delta^{13}C$ values of calcite fracture infillings from two drill cores collected in the proglacial area of the study site range from -6 to -12‰ (Harper et al., 2016). However, the average $\delta^{13}C$ of sedimentary carbonate is 0‰ (Sharp, 2007) and Paleoproterozoic metasediments are known to compose a significant portion of the bedrock ~7 km north of the catchment (van Gool et al., 2002), such that sedimentary carbonate may exist beneath the study catchment. When R_{carb} = -6‰ is applied to the model, f_{microb} is negative during the latter half of the 2014 melt season. This result could indicate that the average R_{carb} value for the catchment is higher than -6‰ and closer to 0‰. Alternatively, it may be due to the fact that SPS and SBD were sampled ~24 hrs apart in 2014, such that SPS data ($[DIC_{SPS}]$, f_{SPS}, R_{SPS}) do not perfectly correspond to the

paired SBD data ([DIC_{SBD}], R_{microb}, R_{SBD}). Applying R_{carb} = -6‰ does not change the 2015 mixing model trends but does shift f_{microb} down to ~15% of the SBD DIC load during Phase I and ~0% of the DIC load during Phase II, except during RE II when it accounts for 12% of SBD DIC. Given that DNA sequencing provides evidence for heterotrophically-respiring microbes beneath the catchment, the result that microbially-respired C accounts for ~0% of SBD DIC for a prolonged period of time during 2015 seems unlikely. In light of this analysis, we favor the hypothesis that the average R_{carb} value is higher than -6‰ and apply R_{carb} = 0‰ as an upper limit.

5.3.5 Percent covariation calculation

To assess whether two variables covaried through time, we calculated the percentage of time-steps where both variables changed, either increased or decreased, in the same direction (positive covariation) or opposing direction (negative covariation). We defined a change across a time-step as when the values of the variable at t and t +1, where t equals time, were outside the analytical error bars of the measurements.

Table 5.1. 2014 supraglacial stream and subglacial discharge geochemical data

Sample	Collection date (m/d)	T (°C)	Ca (μmol/L)	Mg (μmol/L)	K (μmol/L)	Na (μmol/L)	Al (μmol/L)	Ba (nmol/L)	Fe (μmol/L)	Si (μmol/L)	SO4 (μmol/L)	Cl (μmol/L)	Alkalinity (μeq/L)	DIC (μmol/L)	DOC (μmol/L)	$\delta^{13}C_{DIC}$ (‰)	$\Delta^{14}C_{DIC}$ (‰)	$\delta^{13}C_{DOC}$ (‰)	$\Delta^{14}C_{DOC}$ (‰)	$\delta^{18}O$ (‰)
Supraglacial stream through ice (SPS - Q)																				
W23	6/16	0	bdl	bdl	bdl	bdl	bdl	bdl	0.1	bdl	bdl	bdl	bdl	56	nm	-9.9	-297	-24.2	-325	-30.5
W41	6/27	0	bdl	bdl	bdl	bdl	0.1	4.4	0.0	1.1	bdl	bdl	bdl	53	21	-12.5	-67	-23.7	nm	-30.0
W88	8/1 (RE I)	0	bdl	bdl	bdl	bdl	0.5	10	0.1	0.7	bdl	bdl	bdl	60	42	-14.3	-330	-23.7	-106	-26.8
W99	8/11	0.1	bdl	bdl	bdl	bdl	0.1	bdl	0.0	0.7	bdl	bdl	bdl	44	35	-10.2	-124	-23.2	-307	-30.5
Supraglacial stream along lateral moraine (SPS - N)																				
W03	6/6	0.1	7.5	bdl	bdl	bdl	4.9	16.0	3.0	12	bdl	bdl	15	63	107	-10.5	-34	-25.6	-360	-29.3
W22	6/16	0	7.5	bdl	2.6	bdl	2.0	9.5	0.6	6.8	bdl	bdl	18	68	24	nm	nm	nm	nm	-30.2
W42	6/27	0.1	7.5	bdl	2.6	bdl	2.2	12	0.8	8.2	bdl	bdl	18	74	85	nm	nm	nm	nm	-30.2
W64	7/22	0	5.0	bdl	2.6	bdl	4.1	16	1.4	10	bdl	bdl	13	84	12	-10.8	-100	-24.5	-320	-30.3
W87	8/1 (RE I)	0.1	20	4.1	7.7	bdl	0.9	18	0.5	8.9	bdl	bdl	56	93	66	-9	-168	-23.7	-45	-26.4
W100	8/11	0.1	10	bdl	2.6	bdl	1.8	11	0.8	6.8	bdl	bdl	23	65	46	nm	nm	nm	nm	-30.2
Subglacial discharge (SBD)																				
W25	6/17	0.2	25	8.2	10.2	8.7	3.2	20	1.5	17	bdl	bdl	85	116	52	-12.7	-232	-24.7	-274	-26.9
W44	6/28	0.1	20	8.2	5.1	8.7	9.6	32	3.9	26	bdl	bdl	70	102	40	-10.4	-229	-25.6	-322	-27.5
W55	7/7	0.2	20	8.2	5.1	4.3	1.5	15	0.8	13	bdl	bdl	66	106	54	-9.5	-333	-25.8	-307	-28.1
W65	7/22	0.3	10	bdl	2.6	bdl	0.9	7.3	0.6	6.1	bdl	bdl	23	76	13	-9.7	-146	-25.3	-251	-28.3
W76	7/28	0.3	12	4.1	2.6	bdl	1.8	12	1.2	8.5	bdl	bdl	36	nm	nm	nm	nm	nm	nm	nm
W89	8/2	0.3	17	4.1	2.6	bdl	0.4	11	1.1	7.8	bdl	bdl	46	111	64	-8.6	-375	-24.0	-224	-27.4
W101	8/12	0.3	20	8.2	5.1	4.3	2.7	17	1.2	16	bdl	bdl	66	97	45	-3.9	-178	-25.2	-274	-27.7

"RE I" indicates the date of rain event I (see main text), "bdl" indicates that the measurement was below detection limit, and "nm" indicates the sample was not measured

Table 5.2 2015 supraglacial stream, subglacial discharge, and precipitation geochemical data

Sample (site)	Collection date (m/d)	T (°C)	Ca (µmol/L)	Mg (µmol/L)	K (µmol/L)	Na (µmol/L)	Al (µmol/L)	Ba (nmol/L)	Fe (µmol/L)	Si (µmol/L)	SO4 (µmol/L)	Cl (µmol/L)	Alkalinity (µeq/L)	DIC (µmol/L)	DOC (µmol/L)	$\delta^{13}C_{DIC}$ (‰)	$\Delta^{14}C_{DIC}$ (‰)	$\delta^{13}C_{DOC}$ (‰)	$\Delta^{14}C_{DOC}$ (‰)	$\delta^{18}O$ (‰)
Supraglacial streams through ice (SPS - Q, V - Y)																				
W138 (Q)	6/15	0	bdl	bdl	bdl	bdl	1.4	8.0	0.7	3.2	bdl	bdl	bdl	69	31	-11.1	-58	-27.1	-213	-29.7
W154 (Q)	6/22	0	bdl	bdl	bdl	bdl	0.1	bdl	0.1	0.4	bdl	bdl	bdl	62	52	nm	nm	nm	nm	-29.9
W167 (Q)	6/28	0	bdl	bdl	bdl	bdl	0.2	bdl	0.1	0.4	bdl	bdl	bdl	60	34	-11.1	-24	-25.1	-447	-31.0
W181 (Q)	7/11	0	bdl	bdl	bdl	bdl	1.1	5.1	0.4	3.2	bdl	bdl	bdl	70	40	-11.5	-63	-27.3	-420	-31.0
W195 (Q)	7/14	0	bdl	bdl	bdl	bdl	0.1	bdl	0.0	0.7	bdl	bdl	bdl	64	nm	nm	nm	nm	nm	nm
W197 (Q)	7/20	0	bdl	bdl	bdl	bdl	0.1	3.6	0.0	0.7	bdl	bdl	bdl	54	18	nm	nm	nm	nm	-31.0
W201 (Q)	7/27	0	bdl	bdl	bdl	bdl	0.5	4.4	0.2	2.1	bdl	bdl	bdl	58	49	-10.6	-78	-28.9	-465	-30.6
W215 (Q)	8/3	0	bdl	bdl	bdl	bdl	0.2	3.6	0.1	1.8	bdl	bdl	bdl	58	94	-9.7	-16	-28.8	-533	-31.1
W230 (Q)	8/10 (RE II)	0	bdl	bdl	bdl	bdl	0.1	5.1	0.0	0.7	bdl	bdl	bdl	47	7.5	-11.1	-69	-26.7	-460	-28.2
W243 (Q)	8/14	0.1	bdl	bdl	bdl	bdl	0.1	bdl	0.0	0.7	bdl	bdl	bdl	57	103	nm	nm	nm	nm	-30.5
W244 (V)	8/14	0.1	bdl	bdl	bdl	bdl	0.1	4.4	0.0	0.4	bdl	bdl	bdl	44	123	nm	nm	nm	nm	nm
W246 (W)	8/18	0	bdl	bdl	bdl	bdl	0.3	5.1	0.1	1.8	bdl	bdl	bdl	59	93	nm	nm	nm	nm	nm
W247 (X)	8/18	0	bdl	bdl	bdl	bdl	0.2	5.8	0.1	1.4	bdl	bdl	bdl	54	232	nm	nm	nm	nm	nm
W248 (Y)	8/18	0.1	bdl	bdl	bdl	bdl	0.1	4.4	0.0	0.7	bdl	bdl	bdl	53	233	nm	nm	nm	nm	nm
Supraglacial stream along lateral moraine (SPS - N)																				
W111	6/1	0.6	20	8.2	5.1	17	1.0	25	0.8	7.8	17	22	22	86	nm	-11.7	-55	-24.0	-338	-24.5
W124	6/7	0	30	8.2	7.7	4.3	0.9	20	0.6	14	bdl	bdl	88	158	nm	nm	nm	nm	nm	-28.1
W249	8/18	0.1	7.5	bdl	bdl	bdl	1.5	8.0	0.8	5.0	bdl	bdl	15	68	37	nm	nm	nm	nm	-29.6
Subglacial discharge (SBD)																				
W112	6/1	0.2	50	16	10	17	0.1	20	0.5	19	23	24	90	176	nm	-13.2	-138	-27.5	-164	-27.0
W125	6/7	0.4	80	25	13	26	1.3	42	1.3	33	37	bdl	174	235	nm	nm	nm	nm	nm	-27.4
W139	6/15	0.7	40	16	10	17	1.7	26	1.1	21	16	bdl	109	184	44	-10.9	-186	-27.8	-339	-25.3
W155	6/22	0.3	45	16	13	13	8.9	57	6.3	30	16	bdl	117	166	90	nm	nm	nm	nm	-27.2
W168	6/28	0.3	20	8.2	5.1	4.3	2.1	16	1.3	12	10	bdl	45	116	93	-12.7	-180	-29.8	-639	-28.7
W182	7/11	0.3	27	16	7.7	8.7	8.9	50	8.1	23	20	bdl	65	165	87	-8.6	-148	-27.5	-414	-28.8
W198	7/20	0.3	15	4.1	2.6	bdl	1.1	12	1.3	7.8	bdl	bdl	41	100	13	-9.5	-128	-27.9	-424	-29.1
W202	7/27	0.3	20	8.2	5.1	bdl	3.3	23	3.2	13	bdl	bdl	61	132	60	-7.8	-105	-27	-453	-28.4
W216	8/3	0.4	17	8.2	5.1	bdl	0.9	12	1.2	11	bdl	bdl	57	100	74	-8.2	-537	-27.5	-443	-28.6
W231	8/10 (RE II)	0.3	12	4.1	2.6	bdl	2.2	15	1.5	8.5	bdl	bdl	36	84	51	-11.5	-192	-27.3	-349	-26.4
W242	8/14	0.4	27	8.2	5.1	8.7	4.1	25	2.5	18	bdl	bdl	85	116	60	nm	nm	nm	nm	-28.4
W245	8/15	0.3	25	8.2	5.1	4.3	2.4	20	2.7	14	bdl	bdl	76	116	60	nm	nm	nm	nm	-27.8
Snow																				
SN01	5/31	nm	bdl	bdl	bdl	bdl	0.1	bdl	0.1	bdl	bdl	bdl	bdl	nm	nm	nm	nm	nm	nm	-23.6
SN02	5/31	nm	bdl	bdl	bdl	22	0.4	7.3	0.4	bdl	bdl	25	bdl	nm	nm	nm	nm	nm	nm	-19.2
SN03	5/31	nm	bdl	bdl	bdl	bdl	0.7	5.1	0.7	1.1	bdl	bdl	bdl	nm	nm	nm	nm	nm	nm	-24.5
Rain																				
RW01	8/9	n/a	nm	nm	nm	nm	nm	nm	nm	nm	bdl	bdl	nm	nm	nm	nm	nm	nm	nm	-18.9
RW02	8/10	n/a	nm	nm	nm	nm	nm	nm	nm	nm	bdl	bdl	nm	nm	nm	nm	nm	nm	nm	-21.8

"RE II" indicates the date of rain event II (see main text), "bdl" indicates that the measurement was below detection limit, and "nm" indicates the sample was not measured

5.4 Results and Discussion

5.4.1 Hydrologic connections between supra- and sub-glacial systems

$\delta^{18}O$ values trace the relative balance between water sources composing SPS and SBD, namely precipitation (rain and snow) and ice melt. Precipitation samples (rain and snow) collected in the present study have an average $\delta^{18}O$ value of -21.6 ± 2.6‰ ($\pm 1\sigma_{SD}$, n = 5) (Table 5.2). Previous research has found that ice collected at the terminus of the Russell Glacier has a $\delta^{18}O$ value of ~ -31‰ (Hindshaw et al., 2014). During 2014, when sample collection occurred during the peak melt season, SPS $\delta^{18}O$ values were constant, with an average of -30.2 ± 0.4‰ ($\pm 1\sigma_{SD}$, n = 8) (Fig. 5.2; Table 5.1). We therefore infer that SPS water originated from melting ice, which agrees with previous observations that on the extreme margin of the GrIS, where the SPS sites are located, rapid snow melt during the spring leaves bare ice to melt during the peak season (Chandler et al., 2015). Samples collected during a rain event on August 1 (hereafter, RE I) yielded a +4‰ excursion from the average $\delta^{18}O$ value. During 2015, sample collection began earlier in the melt season, and snow was still present on the margin of the GrIS. Accordingly, SPS demonstrated a substantial decrease in $\delta^{18}O$ values from June 1 – 22, as the source of SPS water transitioned from snow- to ice-melt. From June 28 onward, SPS $\delta^{18}O$ values plateaued at -30.7 ± 0.5‰ ($\pm 1\sigma_{SD}$, n = 7) (Fig. 5.2; Table 5.2), similar to the average value determined for the 2014 study period. Based on this shift in water sources, we designate the 2015 early melt season (June 1 – 22) as Phase I and the peak melt season (June 28 and onward) as Phase II. Samples were also collected during a rain event (hereafter, RE II), which punctuated Phase II on August 10. SPS-Q was sampled within three hours after RE II ceased, and accordingly, $\delta^{18}O$ values showed a +3‰ excursion (Fig. 5.2).

In SBD, $\delta^{18}O$ values were constant throughout 2014, with an average of -27.6 ± 0.5‰

($\pm 1\sigma_{SD}$, $n = 6$) (Fig. 5.2; Table 5.1). In 2015, SBD exhibited a similar seasonal trend as SPS, with the highest $\delta^{18}O$ values occurring during Phase I (max. -25‰) and a plateau of -28.6 ± 0.4‰ ($\pm 1\sigma_{SD}$, $n = 7$) during Phase II (Fig. 5.2; Table 5.2). SBD sampled one day after RE I did not show a positive excursion from the 2014 average $\delta^{18}O$ value; however, SBD sampled within six hours after RE II ceased yielded a +2‰ excursion from the average Phase II 2015 $\delta^{18}O$ value. Taken together, these results indicate that much of SBD water originates from SPS water, which enters the subglacial environment via crevasses and moulins (Bhatia et al., 2011), but SPS inputs to the subglacial environment have relatively short residence times, ≥ 6hrs but < 24 hrs, at least later in the melt season when the RE's occurred. The moderately higher average SBD $\delta^{18}O$ values, as compared to SPS, point to either additional SPS inputs from higher in the ablation zone or a contribution from basal ice melt (Bhatia et al., 2011).

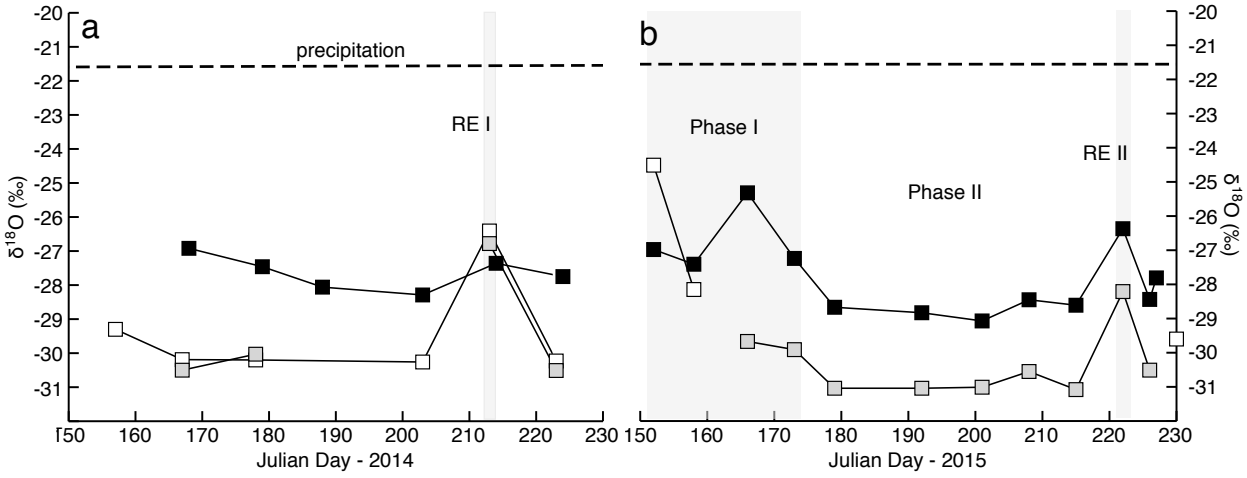

Figure 5.2. Hydrological connections between precipitation, supraglacial streams, and subglacial discharge. $\delta^{18}O$ values of SPS and SBD across the 2014 (a) and 2015 (b) melt seasons. Gray shading indicates periods when SPS and SBD $\delta^{18}O$ values had a positive excursion from their respective seasonal averages. These positive excursions correspond with known rain events (RE I (a) and II (b)), or are interpreted as distinct hydrological periods (Phase I and II, 2015 (b)). The dashed line indicates the average $\delta^{18}O$ value of precipitation samples measured for this study.

5.4.2 Inorganic and organic C concentrations of supra- and sub-glacial systems

Dissolved inorganic C (DIC) concentrations in SPS-Q and V-Y were largely constant seasonally, interannually, and spatially, with an average of 57 ± 7 μmol/L ($\pm 1\sigma_{SD}$, n = 18) for 2014 and 2015 combined (Fig. 5.3, Table 5.1, 5.2). DIC concentrations in SPS-N were more variable, as might be expected due to interaction with the moraine. We therefore assume that SPS-Q and V-Y represent the larger SPS DIC reservoir. In 2014, DIC concentrations in SBD were constant with an average value of 101 ± 14 μmol/L ($\pm 1\sigma_{SD}$, n = 6), while in 2015, DIC values decreased from a maximum of 235 μmol/L to a minimum 84 μmol/L as the melt season progressed (Fig. 5.3; Table 5.1). Major cation concentrations produced similar seasonal trends and were generally constant throughout 2014 and Phase II 2015, but decreased during Phase I 2015 (Fig. 5.3; Table 5.1, 5.2). Although SPS DIC concentrations varied minimally, 2015 SPS-Q and SBD DIC concentrations significantly correlate (R^2 = 0.81, p = 0.001, n = 9), indicating that SPS contributed DIC to SBD and that SPS inputs influenced SBD DIC fluctuations. The 2014 SPS-Q and SBD DIC concentrations also correlate (R^2 = 0.71), but the trend has a high p value (p = 0.1), likely due to the low sample resolution (n = 4). Dissolved organic C (DOC) concentrations in SPS varied significantly seasonally, interannually, and spatially, with an average of 69 ± 61 μmol/L ($\pm 1\sigma_{SD}$, n = 23) for 2014 and 2015 combined (Fig. 5.3; Table 5.1, 5.2). SBD DOC concentrations produced a similar average value of 56 ± 23 μmol/L ($\pm 1\sigma_{SD}$, n = 16) for both years combined (Fig. 5.3; Table 5.1, 5.2). Neither SPS nor SBD displayed a discernable shift in DOC concentrations between Phase I and II 2015 (Fig. 5.3). SPS and SBD DOC concentrations do not statistically correlate (p = 0.5). The absence of a correlation likely reflects the spatial heterogeneity of SPS DOC concentrations. Nevertheless, 80% of upturns and

downturns in the data positively co-vary (n = 10; see methods) (Fig. 5.3), consistent with the expectation that SPS inputs contribute to fluctuations in SBD DOC concentrations.

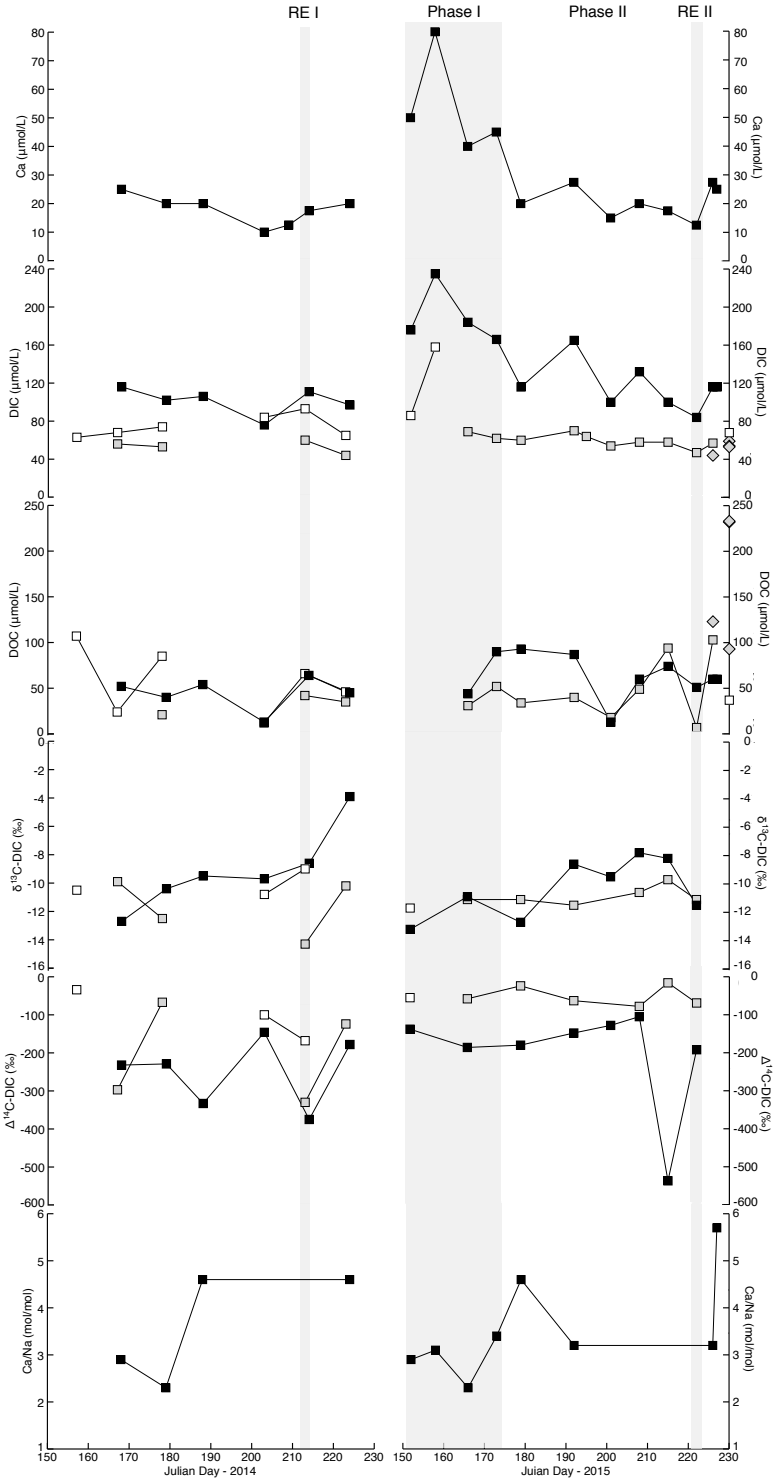

Figure 5.3. C cycle geochemical tracers (concentrations and isotopic values) for SPS and SBD compared across the 2014 and 2015 melt seasons. Gray shading corresponds to either RE I or II, or Phase I 2015, as indicated.

5.4.3. Sources of C in supra- and sub-glacial systems

In addition to their similar DOC concentrations, SPS and SBD sample pairs have similar radio-C values ($\Delta^{14}C_{DOC}$), with an average absolute difference between them of 82 ± 62‰ ($\pm 1\sigma_{SD}$, $n = 9$) for both 2014 and 2015 combined (Fig. 5.3; Table 5.1, 5.2). This difference is small considering the range of possible $\Delta^{14}C$ values (e.g. modern to radio-C dead). Combined, these observations suggest that much of the SBD DOC originates from SPS inputs (Bhatia et al., 2013) with minimal contributions from overridden soils and other basal C stocks, which would provide DOC with lower $\Delta^{14}C_{DOC}$ values (Bhatia et al., 2013). However, SBD DIC concentrations were consistently higher than those of SPS-Q and V-Y (Fig. 5.3; Table 5.1, 5.2). Assuming that SPS DIC behaves conservatively during transport to the subglacial environment, SPS inputs accounted for ~50% of SBD DIC in 2014 and Phase II 2015, and ~40% during Phase I 2015, which implies that the remaining fraction must have originated from the subglacial environment. Radio-C values of DIC ($\Delta^{14}C_{DIC}$) also point to an additional source of basal DIC. During 2014 and 2015, SPS-Q had relatively modern $\Delta^{14}C_{DIC}$ values (≥ -100‰), while SBD had lower (i.e., older) $\Delta^{14}C_{DIC}$ values (≥ -500‰) (Fig. 5.3; Table 5.1, 5.2). The "old" C in SBD could originate from the weathering of carbonate-bearing minerals, which would be radio-C dead (-1000‰), or the subglacial microbial respiration of DOC. The SBD $\Delta^{14}C_{DOC}$ values are consistent with a mechanism where SBD DOC could account for the SBD $\Delta^{14}C_{DIC}$ values, if organic C was transferred to the inorganic DIC pool.

The stable C isotope composition of DIC ($\delta^{13}C_{DIC}$) offers additional constraints on the primary sources of inorganic C in the supra- and sub-glacial environments. $\delta^{13}C_{DIC}$ values can be used to identify DIC sources because atmospheric, carbonate, and respired organic C have distinct isotopic signatures. Atmospheric CO_2 has a $\delta^{13}C$ value of ~ -8‰ (Keeling et al., 2010),

but dissolution of CO_2 gas into water under open system conditions, and subsequent partitioning among the carbonate species composing DIC, induces a fractionation that is both temperature- and species-dependent (Zhang et al., 1995). Because the alkalinity of SPS effectively equals 0 eq/L (Table 5.1, 5.2), nearly all SPS DIC occurs as CO_2. At a water temperature of ~0°C, $\Delta CO_{2(aq)} - CO_{2(g)}$ = -1.3‰, such that the $\delta^{13}C_{DIC}$ value of dissolved atmospheric CO_2 equals -6.7‰. We estimate that carbonate weathering contributes HCO_3^- with a $\delta^{13}C$ value around 0‰ (see methods), and heterotrophic microbial respiration yields CO_2 with $\delta^{13}C_{DIC}$ values roughly equivalent to $\delta^{13}C_{DOC}$ values, ~ -24‰ to -28‰ (Table 5.1, 5.2). Finally, microbial CH_4 oxidation would introduce very low $\delta^{13}C_{DIC}$ values to SBD, likely < -60‰ (Dieser et al., 2014; Templeton et al., 2006).

Much like DIC concentrations, SPS-Q $\delta^{13}C_{DIC}$ values did not vary substantially seasonally or interannually (Fig. 5.3; Table 5.1, 5.2). This indicates that the source(s) of SPS DIC are relatively constant and that the $\delta^{13}C_{DIC}$ value input to SBD from SPS is constant as well. The average $\delta^{13}C_{DIC}$ values for SPS-Q were -11.7 ± 2.1‰ ($\pm 1\sigma_{SD}$, n = 4) in 2014 and -10.9 ± 0.6‰ ($\pm 1\sigma_{SD}$, n = 6) in 2015 (Table 5.1, 5.2). These values are intermediate between microbially-respired C and atmospheric C. Dissolution of carbonate dust may also be a factor (Banta et al., 2008), but the low Ca concentrations in SPS suggest an insignificant contribution (Table 5.1, 5.2).

16S rRNA gene amplicons from SPS-Q and V-Y reveal abundant sequences most closely related to aerobic heterotrophs, supporting the contention that a significant fraction of DIC derives from respiration (Fig. 5.4a). Dominant heterotrophic families include the *Saprospiraceae*, *Acetobacteraceae*, *Sphingobacteriaceae*, *Chitinophagaceae*, and *Cytophagaceae*. Photosynthetic organisms are also abundant in SPS, namely cyanobacterial

families *Pseudanabaenales* (genus *Leptolyngbya*) and *Nostocaceae*, and eukaryotic algae (Fig. 5.4a, Fig. 5.5). Cell densities in SPS samples range from 3.4×10^3 to 1.1×10^4 cells/mL (Fig. 5.4b), which is consistent with previous reports (Stibal et al., 2015) of Greenland surface ice. Morphologies observed include coccoid, rod, and particle-associated cells (Fig. 5.6). A number of sequenced taxa are frequently detected in oligotrophic (*Caulobacterales*) and/or high radiation (e.g., *Hymenobacter*, *Deinococcus*) environments consistent with the SPS setting. *Hymenobacter* in particular has been previously found in (ant)arctic environments (Klassen and Foght, 2011). Application of a standard two-component mixing equation to the $\delta^{13}C_{DIC}$ data (Eq. 5.1, 5.2) indicates that ~24% of SPS DIC originated from microbial respiration, while the remainder originated from the atmosphere.

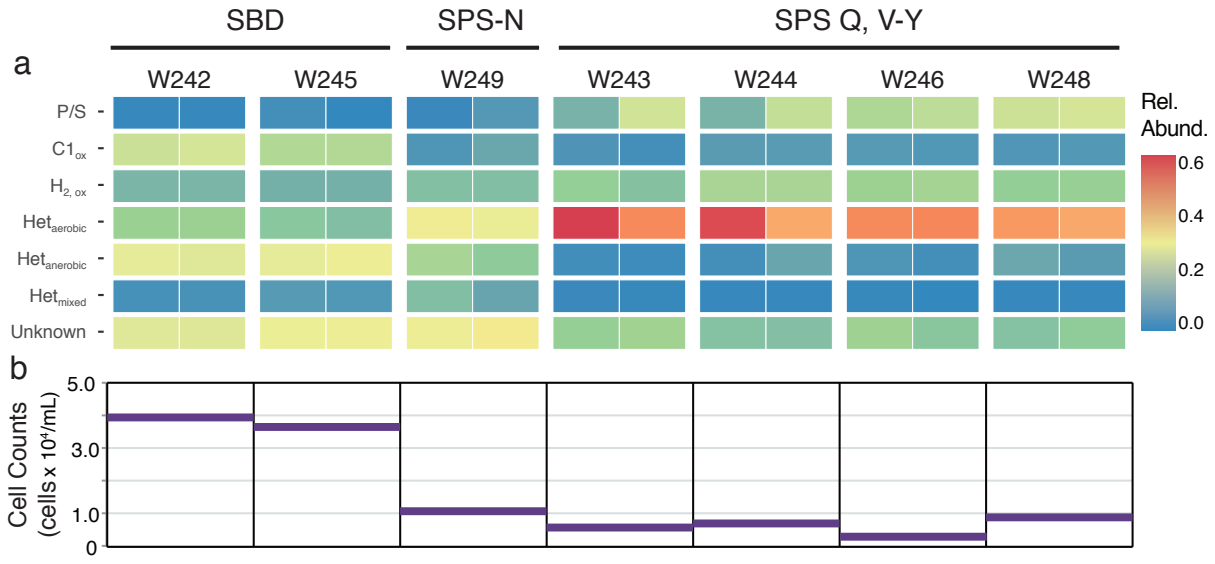

Figure 5.4. Distribution of cells and metabolisms between supraglacial streams and subglacial discharge. Heatmap showing the distribution of metabolic groups (a) determined from analysis of DNA sequencing data where P/S indicates photosynthesizers, $C1_{ox}$ indicates C1 oxidizers, $H_{2,ox}$ indicates H_2 oxidizers, $Het_{aerobic}$ indicates aerobic heterotrophs, $Het_{anaerobic}$ indicates anaerobic heterotrophs, Het_{mixed} indicates mixed heterotrophic metabolisms, and unknown indicates no discernable physiology from taxonomy. Relative abundance of cells (b) based on direct counting via epifluorescence microscopy.

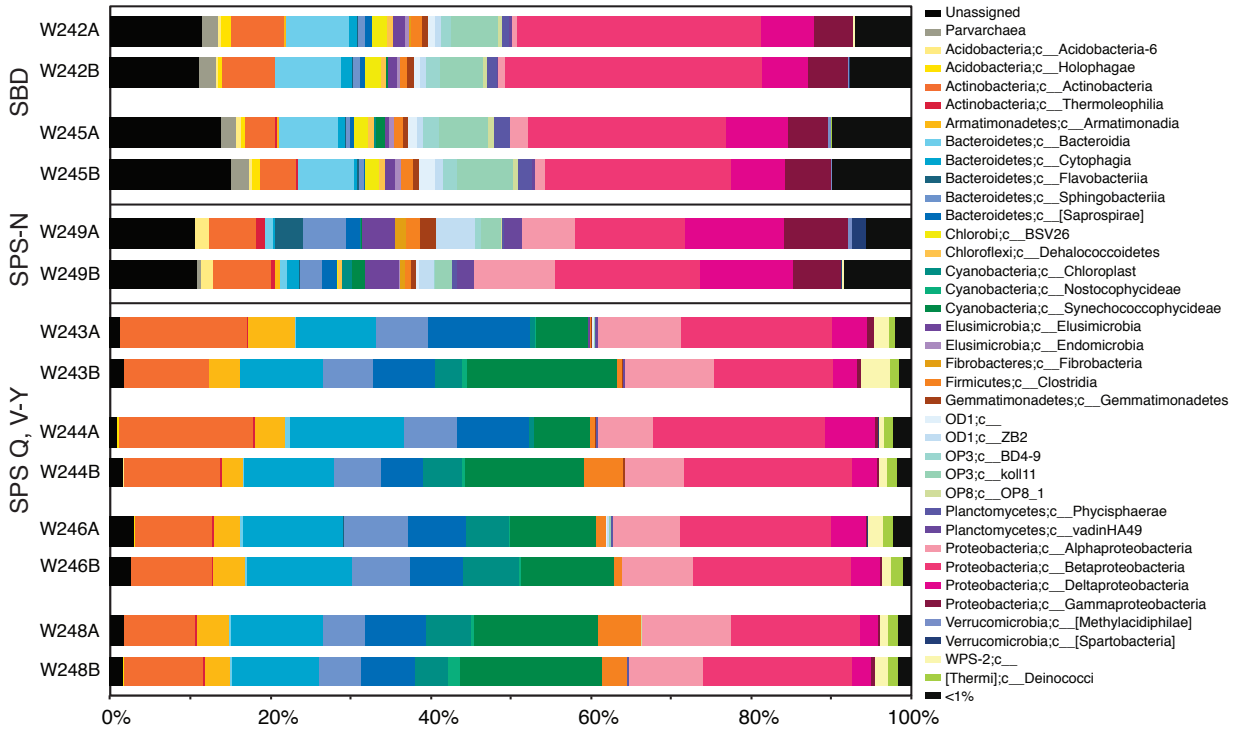

Figure 5.5. Class level taxonomy of supraglacial stream water and subglacial discharge. Relative distribution of archaeal and bacterial classes across samples sites based on amplicon sequencing of the 16S rRNA gene. Taxa comprising less than 1% are binned. Taxonomic classification is based on the Greengenes reference database (McDonald et al., 2012).

In contrast to SPS, SBD $\delta^{13}C_{DIC}$ values increased during both melt seasons, suggesting a transition from a microbially-dominated to a more atmospheric and/or carbonate-dominated signature (Fig. 5.3; Table 5.1, 5.2). DNA sequence data point to anaerobic heterotrophic respiration and C1-oxidation as inputs to the DIC pool (Fig. 5.4a). Likely heterotrophic representatives include *Actinomycetales*, *Bacteroidales*, and Candidate Phylum OP3 ('*Omnitrophica*'). C1 oxidizers include the family *Methylophilaceae* (11 to 17%) and the genus *Crenothrix* (4 to 5%), both members of the phylum *Proteobacteria*. Other notable taxa include chemolithoautotrophs common to rock-hosted environments, such as *Comaonadaceae* (H_2 oxidizers), *Gallionellaceae* (Fe oxidizers), and *Thiobacillus* (S oxidizers) (Fig. 5.4a, Fig. 5.5).

Cell counts from SBD samples are significantly higher than SPS, ranging from 3.6 to 4.0×10^4 cells/mL (Fig. 5.4b). While methanogenic archaea have been described previously as important constituents of subglacial sediments (Boyd et al., 2010), they constitute only a minor component of SBD microbial communities (~0.1% on average). The most abundant family of C1-oxidizers (*Methylophilaceae*) are known for oxidizing methanol but not methane, although they have been suggested to be important partners in a methane-oxidizing consortium (Hernandez et al., 2015). The relatively high SBD $\delta^{13}C_{DIC}$ data are consistent with these observations and do not suggest CH_4 oxidation as a significant contributor to the DIC pool.

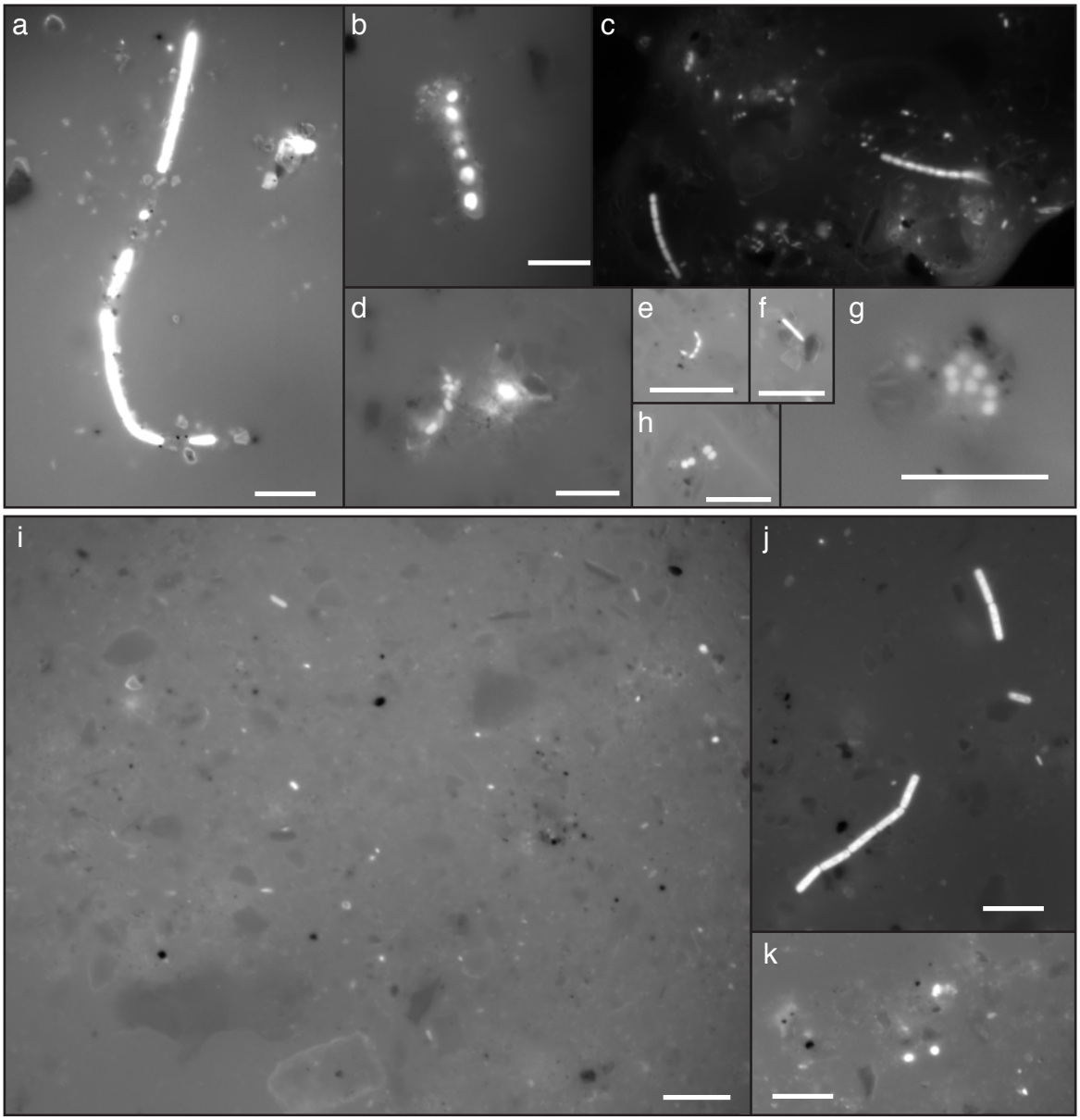

Figure 5.6. Representative microbial morphologies in supraglacial stream water and subglacial discharge. Images of DAPI stained cells from supraglacial streams (top) and subglacial discharge (bottom) samples. Note large putative phototrophs (a, b, c), particle associated cells (d, f, g), rods (c, e, f, i, j,), coccoid cells (h, g, i, k) and intracellular granules (j). Scale bars in each are 10 µm.

Riverine molar Ca/Na ratios confirm DIC inputs from carbonate weathering based on the assumption that rivers draining silicate bedrock have molar Ca/Na ratios < 1, while those draining carbonate bedrock have molar Ca/Na ratios > 50 (Gaillardet et al., 1999). Rivers draining a mixture of carbonate- and silicate-bearing rocks will have intermediate Ca/Na ratios, depending on the relative contribution of cations from each source. Although rocks in the Russell Glacier area are primarily silicates (Escher and Pulvertaft, 1995), the average molar Ca/Na ratio of SBD was 3.6 ± 1.1 ($\pm 1\sigma_{SD}$, n = 12) across 2014 and 2015 (Table 5.1, 5.2). This value is consistent with the weathering of calcite, which occurs as a trace phase within the silicate rocks composing the study region (Harper et al., 2016).

We employed the $\delta^{13}C_{DIC}$ values in a three-component mixing model to calculate the relative contributions of SBD DIC from SPS, carbonate weathering, and microbial respiration (Eq. 5.3, 5.4). Upper limit estimates suggest that the proportion of SBD DIC from microbial respiration declined from ~25 – 30% to ≤10% during both melt seasons except during RE II when it rebounded from ~10% to 20% (Fig. 5.7) (see methods). In 2014, a relative increase in carbonate DIC balanced the decline in microbial DIC. In 2015, a mixture of SPS and carbonate DIC balanced the decline. The model results, particularly those for 2014, suggest that the seasonal increase in SBD $\delta^{13}C_{DIC}$ values could result from either an absolute increase in carbonate weathering rates or an absolute decrease in microbial DIC production. However, the former seems unlikely given that Ca/Na ratios neither systematically increase through time ($p > 0.05$) nor correlate with DIC concentrations, $\delta^{13}C_{DIC}$ values, or the SBD fraction of carbonate DIC ($p > 0.05$) (Fig. 5.7; Fig. 5.3). We therefore conclude that changes in carbonate weathering rates, potentially due to shifts in subglacial drainage paths or water-rock interaction

times, cannot account for the seasonal shift in SBD $\delta^{13}C_{DIC}$ values and instead attribute the seasonal trends in SBD $\delta^{13}C_{DIC}$ values to a decrease in microbial DIC inputs.

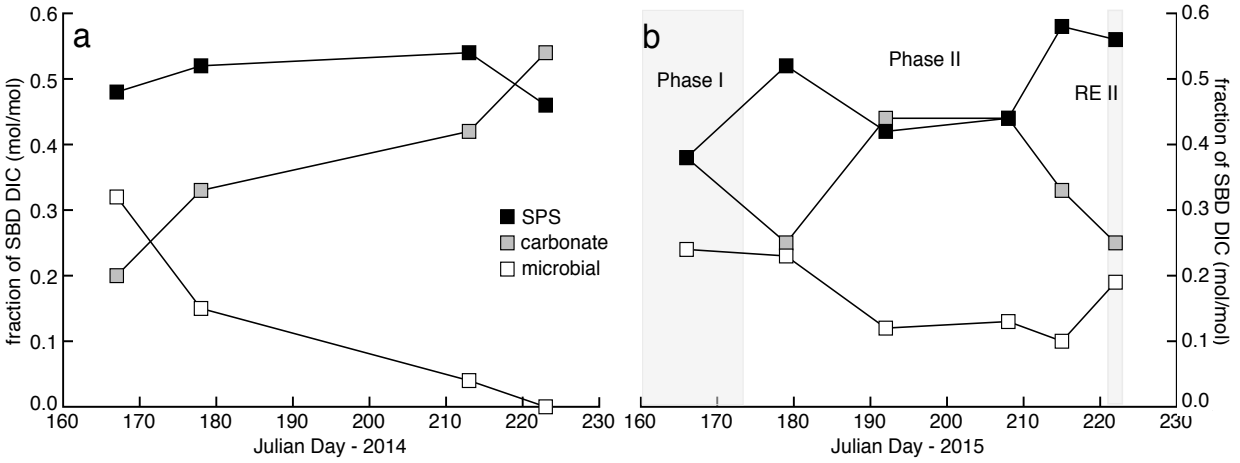

Figure 5.7. Fractional contribution of subglacial discharge DIC sources across the melt seasons. Relative fraction of SBD DIC from SPS (black squares), subglacial carbonate weathering (gray squares), and subglacial heterotrophic microbial respiration (white squares) across the 2014 (a) and 2015 (b) melt seasons. Gray shading in (b) corresponds to either Phase I 2015, or RE II as indicated. RE I is not highlighted in (a) because this event was not detected in SBD.

5.4.4. Seasonality of subglacial microbial metabolism

Previous research has suggested that microbially-sourced CO_2 may accumulate in the subglacial environment during the winter and be released early in the following melt season (Bhatia et al., 2010). Here, we suggest that the seasonal decline in microbially-sourced CO_2 may also reflect the transient nature of the labile organic C influx from the GrIS surface. When snowmelt and rain significantly contribute to SPS (e.g., Phase I of 2015, and RE I and II), $\Delta^{14}C_{DOC}$ values increase, consistent with contributions of relatively young C (Fig. 5.8a, b). Snowmelt likely contains organic C that accumulated on the GrIS surface during the previous winter, and rainfall may mobilize additional organic C from spatial extents of the surface

environment that do not otherwise reach SPS. The organic C could originate from aeolian deposition (Boggild et al., 2010) or be produced *in situ* by phototrophic CO_2 fixation. Higher $\Delta^{14}C_{DOC}$ values are simultaneously observed in SBD, consistent with the transport of SPS water and DOC to the subglacial system (Fig. 5.8a, b). Furthermore, SBD $\Delta^{14}C_{DOC}$ and SBD $\delta^{13}C_{DIC}$ upturns and downturns negatively co-vary (Fig. 5.8c, d) for 60% of the time-steps during 2014 and 2015, combined (n = 12; see methods). Additionally, by excluding one datapoint (W168), a significant correlation emerges between 2015 $\Delta^{14}C_{DOC}$ and SBD $\delta^{13}C_{DIC}$ values (R^2 = 0.87, p = 0.002, n = 7), though no such trend is observed in 2014. More data is required, but allowing for the complexity of the SBD C sources, i.e., the spatially heterogenous nature of SPS DOC inputs and the multiple sources of SBD DIC, we tentatively suggest that an influx of young, labile C to the subglacial system yields an increase in microbially-sourced DIC (Fig. 5.8a, b). The mixing model for sources of SBD DIC (Fig. 5.7) supports a rapid microbial response despite relatively short water residence times. For example, against the backdrop of seasonal declines, an increase in microbially-sourced DIC occurs during a single rain event (RE II).

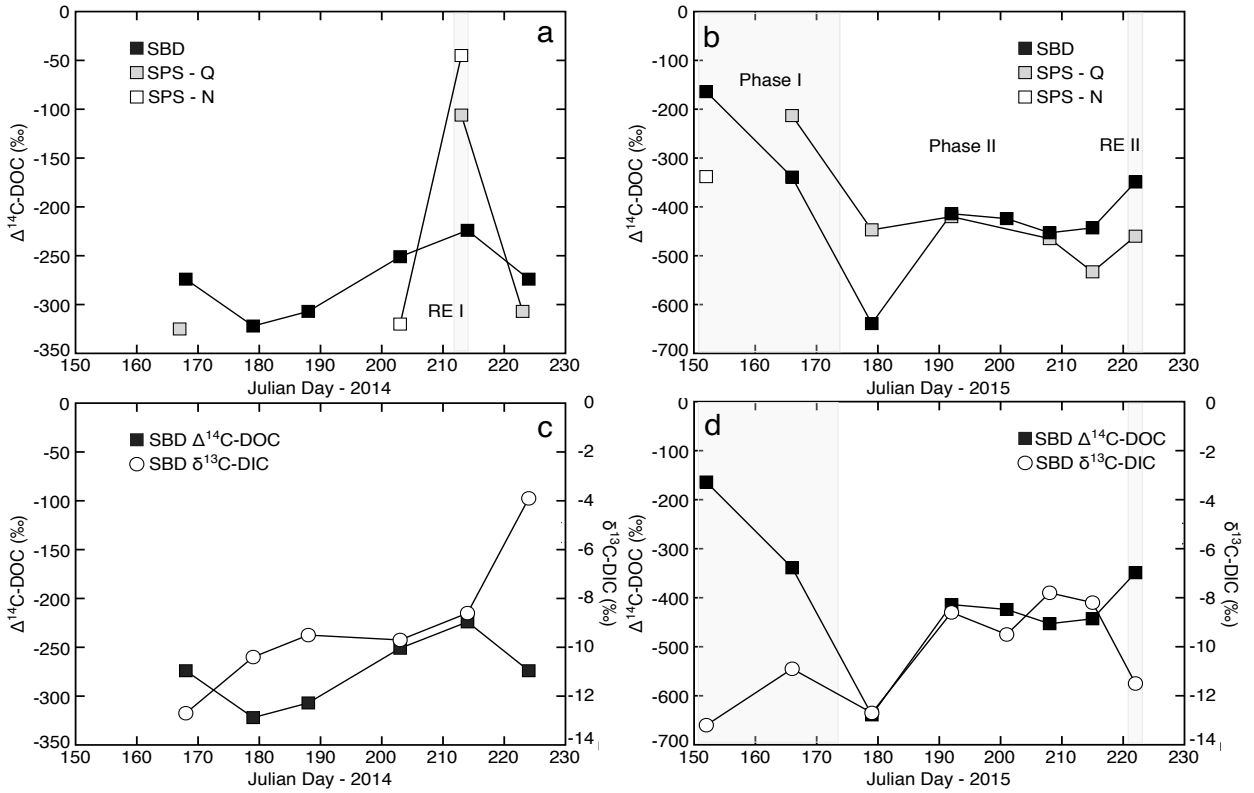

Figure 5.8. Connection between precipitation, supraglacial stream DOC, and subglacial discharge DIC. Comparison of SPS and SBD $\Delta^{14}C_{DOC}$ values across the 2014 (a) and 2015 (b) melt seasons. Comparison of SBD $\Delta^{14}C_{DOC}$ values and $\delta^{13}C_{DIC}$ values across the 2014 (c) and 2015 (d) melt seasons. Gray shading indicates RE I (a), or RE II and Phase I, 2015 as indicated (b, d). RE I is not highlighted in (c) because this event was not detected in SBD.

5.5 Conclusions

While several studies have established significant hydrological connections between the supra- and sub-glacial environments of the GrIS (this study, Bhatia et al., 2011; Doyle et al., 2015; van As et al., 2012; van As et al., 2017; Yde et al., 2004; Yde et al., 2016), the current study is the first to demonstrate intricate linkages between the C cycles of these environments. Contributions from SPS accounted for ~40 – 50% of SBD DIC and the majority of SBD DOC. Furthermore, throughout the melt season, SPS and SBD DIC concentrations correlated with high

statistical significance, even though SBD drains a significantly greater area. This is likely because SPS DIC concentrations and sources were largely constant over the spatiotemporal scales examined. One implication is that, at least in this small, marginal catchment of the GrIS, samples from one SPS reasonably approximate DIC concentrations for the larger SPS reservoir. If this holds true in catchments with more complex hydrology, comparisons between a relatively small number of SPS and SBD samples could provide important insight into extreme surface events, such as jökulhlaups. Here, we used this relationship to help isolate and constrain basal controls on SBD C outputs, namely carbonate weathering and microbial respiration. We find that subglacial microbial production of DIC composes, at most, ~30% of SBD DIC but generally declines across the melt season.

We also found that precipitation coincides with an increase of young DOC in SPS, which is then transported to SBD. We suggest that this transient input of young DOC to the subglacial environment drives seasonal trends in subglacial microbial CO_2 production. These results suggest a new mechanism linking water flow from the supra- to sub-glacial environment to the biogeochemical cycling of C at the GrIS margin. This mechanism would increase the net export of DIC from the GrIS, as well as the proportion of DIC exported in the form of CO_2. In general, this work provides combined geochemical ($\delta^{13}C_{DIC}$) and DNA evidence for an active subglacial community of heterotrophic microorganisms, poised to convert organic matter into CO_2. Upon release to the proglacial area, SBD CO_2 will escape when the dissolved pCO_2 value exceeds that of the atmosphere. Climate simulations of the Arctic for the coming century predict that vegetation will expand in the proglacial area and rainfall events will increase in both frequency and magnitude (Normand et al., 2013; Schuenemann and Cassano, 2010). These factors may improve the quality and quantity of organic C delivered to the GrIS surface, as well as facilitate

increased transport of organic C to the subglacial system where microbial utilization may elevate SBD pCO_2 values. Furthermore, a reservoir of ancient organic matter may exist beneath the GrIS (Bierman et al., 2014). Should future decay of the GrIS access this organic C reservoir, the concentration of CO_2 in SBD could increase substantially. Our results are consistent with the hypothesis that in a warming world, SBD CO_2 may evade to the atmosphere in the proglacial area and act as a positive feedback to climate change (Ryu and Jacobson, 2012). Given the extremely low ionic-strength of SBD, high-precision data, including direct pCO_2 measurements that are internally consistent with carbonate equilibria calculations, are required to constrain the exact effects climate change may have on this contribution to the global carbon cycle.

Chapter 6

Conclusions

With large water fluxes and high sediment loads, glaciated terranes play a unique role in controlling the Earth's carbon cycle on both short and long timescales. They can be sites of active biogeochemical cycling (Chap. 2, 5) as well as significant silicate chemical weathering (Chap. 2, 3, 4). However, quantifying the carbon cycle at these locales is complicated by the influence of carbonate chemical weathering (Chap. 2, 3, 5), distinguishing between water-mass mixing (Chap. 2, 4), and the potentially non-conservative nature of molar Ca/Sr ratios (Chap. 2).

Stable Sr isotopes have proved a valuable tool for understanding the global carbon cycle and Earth surface processes. The research presented in Chapter 2 demonstrated the potential for stable Sr isotopes to trace biogeochemical cycling in catchments with abundant vegetation. A long-term biogeochemical cycling $\delta^{88/86}$Sr signature in the dissolved load will only be present in circumstances were Sr uptake by plants, coupled with catchment export of biotic solids, outpaces litter degradation and return of dissolved Sr (Uhlig et al., 2017). This requirement for non-steady state Sr cycling should be carefully considered in future studies.

Stable Sr isotopes were also essential in identifying riverine Sr – and by extension Ca – sources. In the chemical weathering studies presented in Chapter 3 and 4, key cation sources, such as calcite and silicate minerals, were similar in traditional $^{87}Sr/^{86}Sr$ ratios, but distinct in $\delta^{88/86}$Sr values. In the future, paired stable and radiogenic Sr isotopes could be a powerful technique for cation source tracing, particularly in locations such as the Himalayas where silicate bedrock and calcite minerals are known to have indistinguishable $^{87}Sr/^{86}Sr$ ratios (Jacobson and Blum, 2000).

Finally, there is a globally ubiquitous observation that rivers have higher $\delta^{88/86}$Sr values than the bedrock over which the drain (Pearce et al., 2015a). In contrast to the majority of the published literature, the stable Sr isotope studies presented here favor the hypothesis that this can be largely explained by the preferential dissolution of distinct mineral phases from bulk bedrock, rather than substantial low-temperature mass-dependent fractionation on the continents (Chap 3, 4). This hypothesis has multiple broader implications. Firstly, our data support the conclusion that stable Sr isotopes are subject to high-temperature mass-dependent fractionation during mantle differentiation such that silicate minerals have a wide range of $\delta^{88/86}$Sr values (Chap. 3, 4). This may partly explain why Earth's mantle has a lower average $\delta^{88/86}$Sr value than the crust, based on hydrothermal fluid and crustal rock analyses, respectively (Pearce et al., 2015a). Additionally, because the global riverine $\delta^{88/86}$Sr signature is largely homogenous (Pearce et al., 2015a), and assuming that it is not dramatically altered by low-temperature fractionation, the $\delta^{88/86}$Sr value of the riverine input flux to the ocean is likely largely constant over geologic time, and potentially only altered by significant increases in sedimentary carbonate weathering. This highly constrained system facilitates the use of $\delta^{88/86}$Sr values in marine sediments as a robust oceanic Sr output flux tracer, and a tool for assessing paleo ocean chemistry and climate.

References

Abril, G., Bouillon, S., Darchambeau, F., Teodoru, C.R., Marwick, T.R., Tamooh, F., Omengo, F.O., Geeraert, N., Deirmendjian, L., Polsenaere, P., Borges, A.V., 2015. Technical Note: Large overestimation of pCO(2) calculated from pH and alkalinity in acidic, organic-rich freshwaters. Biogeosciences 12, 67-78.

Allegre, C.J., Louvat, P., Gaillardet, J., Meynadier, L., Rad, S., Capmas, F., 2010. The fundamental role of island arc weathering in the oceanic Sr isotope budget. Earth Plan. Sci. Lett. 292, 51-56.

Anderson, S.P., 2005. Glaciers show direct linkage between erosion rate and chemical weathering fluxes. Geomorphology 67, 147-157.

Anderson, S.P., Drever, J.I., Frost, C.D., Holden, P., 2000. Chemical weathering in the foreland of a retreating glacier. Geochim. Cosmochim. Acta 64, 1173-1189.

Anderson, S.P., Drever, J.I., Humphrey, N.F., 1997. Chemical weathering in glacial environments. Geology 25, 399-402.

Andrews, M.G., Jacobson, A.D., 2017. The radiogenic and stable Sr isotope geochemistry of basalt weathering in Iceland: Role of hydrothermal calcite and implications for long-term climate regulation. Geochim. Cosmochim. Acta 215, 247-262.

Andrews, M.G., Jacobson, A.D., Lehn, G.O., Horton, T.W., Craw, D., 2016. Radiogenic and stable Sr isotope ratios (Sr-87/Sr-86, delta Sr-88/86) as tracers of riverine cation sources and biogeochemical cycling in the Milford Sound region of Fiordland, New Zealand. Geochim. Cosmochim. Acta 173, 284-303.

Armannsson, H., 2016. The fluid geochemistry of Icelandic high temperature geothermal areas. Appl. Geochem. 66, 14-64.

Arnorsson, S., 1970. Geochemical studies of thermal waters in the Southern Lowlands of Iceland. Geothermics 2, 547 - 552.

Arnorsson, S., 1986. Chemistry of gases associated with geothermal activity and volcanism in Iceland - a review. J. Geophys. Res. - Solid 91, 2261-2268.

Arnorsson, S., 1995. Geothermal systems in Iceland: Structure and conceptual models. 1. High-temperature areas. Geothermics 24, 561-602.

Arnorsson, S., Stefansson, A., 2007. Fluid-fluid interactions in geothermal systems, in: Liebscher, A., Heinrich, C.A. (Eds.), Fluid-Fluid Interactions, pp. 259-312.

Arvidson, R.S., Mackenzie, F.T., Guidry, M., 2006. MAGic: A Phanerozoic model for the geochemical cycling of major rock-forming components. Am. J. Sci. 306, 135-190.

Bagard, M.L., Schmitt, A.D., Chabaux, F., Pokrovsky, O.S., Viers, J., Stille, P., Labolle, F., Prokushkin, A.S., 2013. Biogeochemistry of stable Ca and radiogenic Sr isotopes in a larch-covered permafrost-dominated watershed of Central Siberia. Geochim. Cosmochim. Acta 114, 169-187.

Banner, J.L., 2004. Radiogenic isotopes: systematics and applications to earth surface processes and chemical stratigraphy. Earth-Science Reviews 65, 141-194.

Banta, J.R., McConnell, J.R., Edwards, R., Engelbrecht, J.P., 2008. Delineation of carbonate dust, aluminous dust, and sea salt deposition in a Greenland glaciochemical array using positive matrix factorization. Geochem. Geophy. Geosy. 9.

Barry, P.H., Hilton, D.R., Furi, E., Halldorsson, S.A., Gronvold, K., 2014. Carbon isotope and abundance systematics of Icelandic geothermal gases, fluids and subglacial basalts with implications for mantle plume-related CO2 fluxes. Geochim. Cosmochim. Acta 134, 74-99.

Bartholomew, I., Nienow, P., Sole, A., Mair, D., Cowton, T., Palmer, S., Wadham, J., 2011. Supraglacial forcing of subglacial drainage in the ablation zone of the Greenland ice sheet. Geophys. Res. Lett. 38.

Basu, A.R., Jacobsen, S.B., Poreda, R.J., Dowling, C.B., Aggarwal, P.K., 2001. Large groundwater strontium flux to the oceans from the bengal basin and the marine strontium isotope record. Science 293, 1470-1473.

Bates, S.T., Berg-Lyons, D., Caporaso, J.G., Walters, W.A., Knight, R., Fierer, N., 2011. Examining the global distribution of dominant archaeal populations in soil. ISME J. 5, 908-917.

Belanger, N., Holmden, C., Courchesne, F., Cote, B., Hendershot, W.H., 2012. Constraining soil mineral weathering Sr-87/Sr-86 for calcium apportionment studies of a deciduous forest growing on soils developed from granitoid igneous rocks. Geoderma 185, 84-96.

Berner, R.A., 1990. Atmospheric carbon-dioxide levels over Phanerzoic time. Science 249, 1382-1386.

Berner, R.A., 2006. Inclusion of the weathering of volcanic rocks in the GEOCARBSULF model. Am. J. Sci. 306, 295-302.

Berner, R.A., Lasaga, A.C., Garrels, R.M., 1983. The carbonate-silicate geochemical cycle and its effect on atmospheric carbon-dioxide over the past 100 million years. Am. J. Sci. 283, 641-683.

Berner, R.A.a.M., K. A., 1996. Chemical weathering and controls on atmospheric O2 and CO2: Fundamental principles were enunciated by J.J. Ebelman in 1845. Geochim. Cosmochim. Acta 60, 1633 - 1637.

Bhatia, M.P., Das, S.B., Kujawinski, E.B., Henderson, P., Burke, A., Charette, M.A., 2011. Seasonal evolution of water contributions to discharge from a Greenland outlet glacier: insight from a new isotope-mixing model. J. Glaciol. 57, 929-941.

Bhatia, M.P., Das, S.B., Longnecker, K., Charette, M.A., Kujawinski, E.B., 2010. Molecular characterization of dissolved organic matter associated with the Greenland ice sheet. Geochim. Cosmochim. Acta 74, 3768-3784.

Bhatia, M.P., Das, S.B., Xu, L., Charette, M.A., Wadham, J.L., Kujawinski, E.B., 2013. Organic carbon export from the Greenland ice sheet. Geochim. Cosmochim. Acta 109, 329-344.

Bierman, P.R., Corbett, L.B., Graly, J.A., Neumann, T.A., Lini, A., Crosby, B.T., Rood, D.H., 2014. Preservation of a Preglacial Landscape Under the Center of the Greenland Ice Sheet. Science 344, 402-405.

Blattner, P., 1978. Geology of the crystalline basement between Milford Sound and the Hollyford Valley, New Zealand. New Zealand Journal of Geology and Geophysics 21, 33-47.

Blattner, P., Graham, I.J., 2000. New Zealand's Darran complex and Mackay Intrusives - Rb-Sr whole-rock isochrons in the Median Tectonic Zone. Am. J. Sci. 300, 603-629.

Blum, J.D., Erel, Y., 1997. Rb-Sr isotope systematics of a granitic soil chronosequence: The importance of biotite weathering. Geochim. Cosmochim. Acta 61, 3193-3204.

Blum, J.D., Klaue, A., Nezat, C.A., Driscoll, C.T., Johnson, C.E., Siccama, T.G., Eagar, C., Fahey, T.J., Likens, G.E., 2002. Mycorrhizal weathering of apatite as an important calcium source in base-poor forest ecosystems. Nature 417, 729-731.

Blum, J.D., Taliaferro, E.H., Weisse, M.T., Holmes, R.T., 2000. Changes in Sr/Ca, Ba/Ca and Sr-87/Sr-86 ratios between trophic levels in two forest ecosystems in the northeastern USA. Biogeochemistry 49, 87-101.

Boggild, C.E., Brandt, R.E., Brown, K.J., Warren, S.G., 2010. The ablation zone in northeast Greenland: ice types, albedos and impurities. J. Glaciol. 56, 101-113.

Böhm, F., Eisenhauer, A., Tang, J.W., Dietzel, M., Krabbenhoft, A., Kisakürek, B., Horn, C., 2012. Strontium isotope fractionation of planktic foraminifera and inorganic calcite. Geochim. Cosmochim. Acta 93, 300-314.

Boyd, E.S., Skidmore, M., Mitchell, A.C., Bakermans, C., Peters, J.W., 2010. Methanogenesis in subglacial sediments. Environ. Microbiol. Rep. 2, 685-692.

Brown, S.T., Kennedy, B.M., DePaolo, D.J., Hurwitz, S., Evans, W.C., 2013. Ca, Sr, O and D isotope approach to defining the chemical evolution of hydrothermal fluids: Example from Long Valley, CA, USA. Geochim. Cosmochim. Acta 122, 209-225.

Bullen, T., Chadwick, O., 2016. Ca, Sr and Ba stable isotopes reveal the fate of soil nutrients along a tropical climosequence in Hawaii. Chem. Geol. 422, 25-45.

Bullen, T.D., Bailey, S.W., 2005. Identifying calcium sources at an acid deposition-impacted spruce forest: a strontium isotope, alkaline earth element multi-tracer approach. Biogeochemistry 74, 63-99.

Capo, R.C., Stewart, B.W., Chadwick, O.A., 1998. Strontium isotopes as tracers of ecosystem processes: theory and methods. Geoderma 82, 197-225.

Caporaso, J.G., Bittinger, K., Bushman, F.D., DeSantis, T.Z., Andersen, G.L., Knight, R., 2010a. PyNAST: a flexible tool for aligning sequences to a template alignment. Bioinformatics 26, 266-267.

Caporaso, J.G., Kuczynski, J., Stombaugh, J., Bittinger, K., Bushman, F.D., Costello, E.K., Fierer, N., Pena, A.G., Goodrich, J.K., Gordon, J.I., Huttley, G.A., Kelley, S.T., Knights, D., Koenig, J.E., Ley, R.E., Lozupone, C.A., McDonald, D., Muegge, B.D., Pirrung, M., Reeder, J., Sevinsky, J.R., Tumbaugh, P.J., Walters, W.A., Widmann, J., Yatsunenko, T., Zaneveld, J., Knight, R., 2010b. QIIME allows analysis of high-throughput community sequencing data. Nat. Methods 7, 335-336.

Caporaso, J.G., Lauber, C.L., Walters, W.A., Berg-Lyons, D., Huntley, J., Fierer, N., Owens, S.M., Betley, J., Fraser, L., Bauer, M., Gormley, N., Gilbert, J.A., Smith, G., Knight, R., 2012. Ultra-high-throughput microbial community analysis on the Illumina HiSeq and MiSeq platforms. ISME J. 6, 1621-1624.

Caporaso, J.G., Lauber, C.L., Walters, W.A., Berg-Lyons, D., Lozupone, C.A., Turnbaugh, P.J., Fierer, N., Knight, R., 2011. Global patterns of 16S rRNA diversity at a depth of millions of sequences per sample. Proc. Natl. Acad. Sci. USA 108, 4516-4522.

Carmichael, I.S.E., 1964. The petrology of Thingmuli, a Tertiary volcano in eastern Iceland. J. Petrol. 5, 435 - 460.

Caves, J.K., Jost, A.B., Lau, K.V., Maher, K., 2016. Cenozoic carbon cycle imbalances and a variable weathering feedback. Earth Plan. Sci. Lett. 450, 152 - 163.

Cenki-Tok, B., Chabaux, F., Lemarchand, D., Schmitt, A.D., Pierret, M.C., Viville, D., Bagard, M.L., Stille, P., 2009. The impact of water-rock interaction and vegetation on calcium isotope fractionation in soil- and stream waters of a small, forested catchment (the Strengbach case). Geochim. Cosmochim. Acta 73, 2215-2228.

Chandler, D.M., Alcock, J.D., Wadham, J.L., Mackie, S.L., Telling, J., 2015. Seasonal changes of ice surface characteristics and productivity in the ablation zone of the Greenland Ice Sheet. Cryosphere 9, 487-504.

Chao, H.C., You, C.F., Liu, H.C., Chung, C.H., 2015. Evidence for stable Sr isotope fractionation by silicate weathering in a small sedimentary watershed in southwestern Taiwan. Geochim. Cosmochim. Acta 165, 324-341.

Charlier, B.L., Nowell, G.M., Parkinson, I.J., Kelley, S.P., Pearson, D.G., Burton, K.W., 2012. high temperature strontium stable isotope behaviour in the early solar system and planetary bodies. Earth Plan. Sci. Lett. 329-330, 31-40.

Chou, L., Garrels, R.M., Wollast, R., 1989. Comparative study of the kinetics and mechanisms of dissolution of carbonate minerals. Chem. Geol. 78, 269-282.

Christiansen, F.G., Boesen, A., Bojensen-Koefoed, J., Dallhoff, F., Dam, G., Neuhoff, P.S., Pedersen, A.K., Pedersen, G.K., Stannius, L.S., Zinck-Joergensen, K., 1999. Petroleum geological activities onshore West Greenland in 1997. Geol. Greenl. Surv. Bull. 180, 10-17.

Chu, Z.Y., Yang, Y.H., Guo, J.H., Qiao, G.S., 2011. Calculation methods for direct internal mass fractionation correction of spiked isotopic ratios from multi-collector mass spectrometric measurements. Int. J. Mass. Spectrom. 299, 87-93.

Clow, D.W., Mast, M.A., Bullen, T.D., Turk, J.T., 1997. Sr87/Sr86 as a tracer of mineral weathering reactions and calcium sources in an alpine/subalpine watershed, Loch Vale, Colorado. Water Resour. Res. 33, 1335-1351.

Cook, J.M., Hodson, A.J., Anesio, A.M., Hanna, E., Yallop, M., Stibal, M., Telling, J., Huybrechts, P., 2012. An improved estimate of microbially mediated carbon fluxes from the Greenland ice sheet. J. Glaciol. 58, 1098-1108.

Cowton, T., Nienow, P., Bartholomew, I., Sole, A., Mair, D., 2012. Rapid erosion beneath the Greenland ice sheet. Geology 40, 343-346.

Cox, G.M., Halverson, G.P., Stevenson, R.K., Vokaty, M., Poirier, A., Kunzmann, M., Li, Z.X., Denyszyn, S.W., Strauss, J.V., Macdonald, F.A., 2016. Continental flood basalt weathering as a trigger for Neoproterozoic Snowball Earth. Earth Plan. Sci. Lett. 446, 89-99.

Crompton, J.W., Flowers, G.E., Kirste, D., Hagedorn, B., Sharp, M.J., 2015. Clay mineral precipitation and low silica in glacier meltwaters explored through reaction-path modelling. J. Glaciol. 61, 1061-1078.

Das, A., Krishnaswami, S., Kumar, A., 2006. Sr and Sr-87/Sr-86 in rivers draining the Deccan Traps (India): Implications to weathering, Sr fluxes, and the marine Sr-87/Sr-86 record around K/T. Geochem. Geophy. Geosy. 7, 14.

Das, A., Krishnaswami, S., Sarin, M.M., Pande, K., 2005. Chemical weathering in the Krishna Basin and Western Ghats of the Deccan Traps, India: Rates of basalt weathering and their controls. Geochim. Cosmochim. Acta 69, 2067-2084.

de Souza, G.F., Reynolds, B.C., Kiczka, M., Bourdon, B., 2010. Evidence for mass-dependent isotopic fractionation of strontium in a glaciated granitic watershed. Geochim. Cosmochim. Acta 74, 2596-2614.

Dessert, C., Dupre, B., Francois, L.M., Schott, J., Gaillardet, J., Chakrapani, G., Bajpai, S., 2001. Erosion of Deccan Traps determined by river geochemistry: impact on the global climate and the Sr-87/Sr-86 ratio of seawater. Earth Plan. Sci. Lett. 188, 459-474.

Dessert, C., Dupre, B., Gaillardet, J., Francois, L.M., Allegre, C.J., 2003. Basalt weathering laws and the impact of basalt weathering on the global carbon cycle. Chem. Geol. 202, 257-273.

Dessert, C., Gaillardet, J., Dupre, B., Schott, J., Pokrovsky, O.S., 2009. Fluxes of high- versus low-temperature water-rock interactions in aerial volcanic areas: Example from the Kamchatka Peninsula, Russia. Geochim. Cosmochim. Acta 73, 148-169.

Dieser, M., Broemsen, E., Cameron, K.A., King, G.M., Achberger, A., Choquette, K., Hagedorn, B., Sletten, R., Junge, K., Christner, B.C., 2014. Molecular and biogeochemical evidence for methane cycling beneath the western margin of the Greenland Ice Sheet. ISME J. 8, 2305-2316.

Doyle, S.H., Hubbard, A., van de Wal, R.S.W., Box, J.E., van As, D., Scharrer, K., Meierbachtol, T.W., Smeets, P., Harper, J.T., Johansson, E., Mottram, R.H., Mikkelsen, A.B., Wilhelms, F., Patton, H., Christoffersen, P., Hubbard, B., 2015. Amplified melt and flow of the Greenland ice sheet driven by late-summer cyclonic rainfall. Nat. Geosci. 8, 647-+.

Drouet, T., Herbauts, J., 2008. Evaluation of the mobility and discrimination of Ca, Sr and Ba in forest ecosystems: consequence on the use of alkaline-earth element ratios as tracers of Ca. Plant and Soil 302, 105-124.

Drouet, T., Herbauts, J., Gruber, W., Demaiffe, D., 2005. Strontium isotope composition as a tracer of calcium sources in two forest ecosystems in Belgium. Geoderma 126, 203-223.

Ebelman, J., 1845. Sur les produits de la decomposition des especes minerales de la famille des silicates. Ann. Mines. 7, 3 - 66.

Edgar, R.C., 2010. Search and clustering orders of magnitude faster than BLAST. Bioinformatics 26, 2460-2461.

Eiriksdottir, E.S., Gislason, S.R., Oelkers, E.H., 2013. Does temperature or runoff control the feedback between chemical denudation and climate? Insights from NE Iceland. Geochim. Cosmochim. Acta 107, 65-81.

Eiriksdottir, E.S., Gislason, S.R., Oelkers, E.H., 2015. Direct evidence of the feedback between climate and nutrient, major, and trace element transport to the oceans. Geochim. Cosmochim. Acta 166, 249-266.

Eiriksdottir, E.S., Louvat, P., Gislason, S.R., Oskarsson, N., Hardarottir, J., 2008. Temporal variation of chemical and mechanical weathering in NE Iceland: Evaluation of a steady-state model of erosion. Earth Plan. Sci. Lett. 272, 78-88.

Escher, J.C., Pulvertaft, T.C.R., 1995. Geologic map of Greenland, 1:2500000. Geological Survey of Greenland, Copenhagen.

Fantle, M.S., DePaolo, D.J., 2007. Ca isotopes in carbonate sediment and pore fluid from ODP Site 807A: The Ca2+(aq)-calcite equilibrium fractionation factor and calcite recrystallization rates in Pleistocene sediments. Geochim. Cosmochim. Acta 71, 2524-2546.

Farkas, J., Bohm, F., Wallmann, K., Blenkinsop, J., Eisenhauer, A., van Geldern, R., Munnecke, A., Voigt, S., Veizer, J., 2007. Calcium isotope record of Phanerozoic oceans: Implications for chemical evolution of seawater and its causative mechanisms. Geochim. Cosmochim. Acta 71, 5117-5134.

Farkas, J., Dejeant, A., Novak, M., Jacobsen, S.B., 2011. Calcium isotope constraints on the uptake and sources of Ca2+ in a base-poor forest: A new concept of combining stable (delta Ca-44/42) and radiogenic (epsilon(Ca)) signals. Geochim. Cosmochim. Acta 75, 7031-7046.

Faure, G., Mensing, T.M., 2005. Isotopes: principles and applications, 3rd ed. John Wiley & Sons, Hoboken, New Jersey.

Fietzke, J., Eisenhauer, A., 2006. Determination of temperature-dependent stable strontium isotope (Sr-88/Sr-86) fractionation via bracketing standard MC-ICP-MS. Geochem. Geophy. Geosy. 7, Q08009.

Fridriksson, T., Arnorsson, S., Bird, D.K., 2009. Processes controlling Sr in surface and ground waters of Tertiary tholeiitic flood basalts in Northern Iceland. Geochim. Cosmochim. Acta 73, 6727-6746.

Fridriksson, T., Neuhoff, P.S., Arnorsson, S., Bird, D.K., 2001. Geological constraints on the thermodynamic properties of the stilbite-stellerite solid solution in low-grade metabasalts. Geochim. Cosmochim. Acta 65, 3993-4008.

Fridriksson, T., Neuhoff, P.S., Viani, B.E., Bird, D.K., 2004. Experimental determination of thermodynamic properties of ion-exchange in heulandite: Binary ion-exchange experiments at 55 and 85 degrees C involving Ca2+, Sr2+, Na+, and K+. Am. J. Sci. 304, 287-332.

Gaillardet, J., Dupre, B., Louvat, P., Allegre, C.J., 1999. Global silicate weathering and CO2 consumption rates deduced from the chemistry of large rivers. Chem. Geol. 159, 3-30.

Gaillardet, J., Louvat, P., Lajeunesse, E., 2011. Rivers from Volcanic Island Arcs: The subduction weathering factory. Appl. Geochem. 26, S350-S353.

Georg, R.B., Reynolds, B.C., West, A.J., Burton, K.W., Halliday, A.N., 2007. Silicon isotope variations accompanying basalt weathering in Iceland. Earth Plan. Sci. Lett. 261, 476-490.

Gislason, S.R., Arnorsson, S., Armannsson, H., 1996. Chemical weathering of basalt in southwest Iceland: Effects of runoff, age of rocks and vegetative/glacial cover. Am. J. Sci. 296, 837-907.

Gislason, S.R., Oelkers, E.H., Eiriksdottir, E.S., Kardjilov, M.I., Gisladottir, G., Sigfusson, B., Snorrason, A., Elefsen, S., Hardardottir, J., Torssander, P., Oskarsson, N., 2009. Direct evidence of the feedback between climate and weathering. Earth Plan. Sci. Lett. 277, 213-222.

Glover, E.T., Faanur, A., Fianko, J.R., 2010. Dissolution kinetics of stilbite at various temperatures under alkaline conditions. W. Afr. J. Appl. Ecol. 16, 95 - 105.

Goldstein, S.J., Jacobsen, S.B., 1987. THE ND AND SR ISOTOPIC SYSTEMATICS OF RIVER-WATER DISSOLVED MATERIAL - IMPLICATIONS FOR THE SOURCES OF ND AND SR IN SEAWATER. Chem. Geol. 66, 245-272.

Graly, J.A., Humphrey, N.F., Harper, J.T., 2016. Chemical depletion of sediment under the Greenland Ice Sheet. Earth Surf. Process. Landf. 41, 1922-1936.

Graly, J.A., Humphrey, N.F., Landowski, C.M., Harper, J.T., 2014. Chemical weathering under the Greenland Ice Sheet. Geology 42, 551-554.

Hagedorn, B., Hasholt, B., 2004. Hydrology, geochemistry and Sr isotopes in solids and solutes of the meltwater from Mittivakkat Gletscher, SE Greenland. Nord. Hydrol. 35, 369-380.

Halicz, L., Segal, I., Fruchter, N., Stein, M., Lazar, B., 2008. Strontium stable isotopes fractionate in the soil environments? Earth Plan. Sci. Lett. 272, 406-411.

Halstead, M.J.R., Cunninghame, R.G., Hunter, K.A., 2000. Wet deposition of trace metals to a remote site in Fiordland, New Zealand. Atmospheric Environment 34, 665-676.

Hanna, E., Mernild, S.H., Cappelen, J., Steffen, K., 2012. Recent warming in Greenland in a long-term instrumental (1881-2012) climatic context: I. Evaluation of surface air temperature records. Environmental Research Letters 7.

Harper, J., Hubbard, A., Ruskeeniemi, T., Claesson Liljedahl, L., Kontula, A., Hobbs, M., Brown, J., Dirkson, A., Dow, C., Doyle, S., Drake, H., Engstrom, J., Fitzpatrick, A., Follin, S., Frape, S., Graly, J., Hansson, K., Harrington, J., Henkemans, E., Hirschorn, S., Humphrey, N., Jansson, P., Johnson, J., Jones, G., Kinnbom, P., Kennell, L., Klint, K.E., Liimatainen, J., Lindback, K., Meierbachtol, T., Pere, T., Pettersson, R., Tullborg, E.-L., van As, D., 2016. The Greenland Analog Project: Data and Processes, Stockholm, Sweden.

Hernandez, M.E., Beck, D.A.C., Lidstrom, M.E., Chistoserdova, L., 2015. Oxygen availability is a major factor in determining the composition of microbial communities involved in methane oxidation. Peerj 3.

Hindshaw, R.S., Bourdon, B., Pogge von Strandmann, P.A.E., Vigier, N., Burton, K.W., 2013a. The stable calcium isotopic composition of rivers draining basaltic catchments in Iceland. Earth Plan. Sci. Lett. 374, 173-184.

Hindshaw, R.S., Reynolds, B.C., Wiederhold, J.G., Kiczka, M., Kretzschmar, R., Bourdon, B., 2013b. Calcium isotope fractionation in alpine plants. Biogeochemistry 112, 373-388.

Hindshaw, R.S., Reynolds, B.C., Wiederhold, J.G., Kretzschmar, R., Bourdon, B., 2011. Calcium isotopes in a proglacial weathering environment: Damma glacier, Switzerland. Geochim. Cosmochim. Acta 75, 106-118.

Hindshaw, R.S., Rickli, J., Leuthold, J., Wadham, J., Bourdon, B., 2014. Identifying weathering sources and processes in an outlet glacier of the Greenland Ice Sheet using Ca and Sr isotope ratios. Geochim. Cosmochim. Acta 145, 50-71.

Hodson, A., Tranter, M., Vatne, G., 2000. Contemporary rates of chemical denudation and atmospheric CO2 sequestration in glacier basins: An Arctic perspective. Earth Surf. Process. Landf. 25, 1447-1471.

Holmden, C., Belanger, N., 2010. Ca isotope cycling in a forested ecosystem. Geochim. Cosmochim. Acta 74, 995-1015.

Hood, E., Battin, T.J., Fellman, J., O'Neel, S., Spencer, R.G.M., 2015. Storage and release of organic carbon from glaciers and ice sheets. Nat. Geosci. 8, 91-96.

Hurwitz, S., Evans, W.C., Lowenstern, J.B., 2010. River solute fluxes reflecting active hydrothermal chemical weathering of the Yellowstone Plateau Volcanic Field, USA. Chem. Geol. 276, 331-343.

Ibarra, D.E., Caves, J.K., Moon, S., Thomas, D.L., Hartmann, J., Chamberlain, C.P., Maher, K., 2016. Differential weathering of basaltic and granitic catchments from concentration-discharge relationships. Geochim. Cosmochim. Acta 190, 265-293.

Jacobson, A.D., Andrews, M.G., Lehn, G.O., Holmden, C., 2015. Silicate versus carbonate weathering in Iceland: New insights from Ca isotopes. Earth Plan. Sci. Lett. 416, 132-142.

Jacobson, A.D., Blum, J.D., 2000. Ca/Sr and Sr-87/Sr-86 geochemistry of disseminated calcite in Himalayan silicate rocks from Nanga Parbat: Influence on river-water chemistry. Geology 28, 463-466.

Jacobson, A.D., Blum, J.D., Walter, L.M., 2002. Reconciling the elemental and Sr isotope composition of Himalayan weathering fluxes: Insights from the carbonate geochemistry of stream waters. Geochim. Cosmochim. Acta 66, 3417-3429.

Jacobson, A.D., Holmden, C., 2008. delta(44)Ca evolution in a carbonate aquifer and its bearing on the equilibrium isotope fractionation factor for calcite. Earth Plan. Sci. Lett. 270, 349-353.

Jagoutz, O., Macdonald, F.A., Royden, L., 2016. Low-latitude arc-continent collision as a driver for global cooling. Proc. Natl. Acad. Sci. USA 113, 4935-4940.

Johannesson, H., 2014. Geologic Map of Iceland, Bedrock Geology, 2nd ed. Icelandic Institute of Natural History.

Jørgensen, O., 1984. Zeolite zones in the basaltic lavas of the Faeroe Islands. Ann. Soc. Sci. Faeroensis 9, 71-91.

Kaasalainen, H., Stefansson, A., Giroud, N., Arnorsson, S., 2015. The geochemistry of trace elements in geothermal fluids, Iceland. Appl. Geochem. 62, 207-223.

Keeling, R.F., Piper, S.C., Bollenbacher, A.F., Walker, S.J., 2010. Monthly atmospheric 13C/12C isotopic ratios for 11 SIO stations, Trends: A Compendium of Data on Global Change. Carbon Dioxide Information Analysis Center, Oak Ridge National Laboratory, US Department of Energy, Oak Ridge, TN, USA.

Kelemen, P.B., Matter, J., 2008. In situ carbonation of peridotite for CO2 storage. Proc. Natl. Acad. Sci. USA 105, 17295-17300.

Kent, D.V., Muttoni, G., 2013. Modulation of Late Cretaceous and Cenozoic climate by variable drawdown of atmospheric pCO(2) from weathering of basaltic provinces on continents drifting through the equatorial humid belt. Clim. Past 9, 525-546.

Kerrick, D.M., 2001. Present and past nonanthropogenic CO2 degassing from the solid Earth. Rev. Geophys. 39, 565-585.

Kerrick, D.M., Caldeira, K., 1998. Metamorphic CO2 degassing from orogenic belts. Chem. Geol. 145, 213-232.

Klassen, J.L., Foght, J.M., 2011. Characterization of Hymenobacter isolates from Victoria Upper Glacier, Antarctica reveals five new species and substantial non-vertical evolution within this genus. Extremophiles 15, 45-57.

Knutti, R., Hegerl, G.C., 2008. The equilibrium sensitivity of the Earth's temperature to radiation changes. Nat. Geosci. 1, 735-743.

Krabbenhoft, A., Eisenhauer, A., Bohm, F., Vollstaedt, H., Fietzke, J., Liebetrau, V., Augustin, N., Peucker-Ehrenbrink, B., Muller, M.N., Horn, C., Hansen, B.T., Nolte, N., Wallmann, K., 2010. Constraining the marine strontium budget with natural strontium isotope fractionations (Sr-87/Sr-86*, delta Sr-88/86) of carbonates, hydrothermal solutions and river waters. Geochim. Cosmochim. Acta 74, 4097-4109.

Krabbenhöft, A., Eisenhauer, A., Böhm, F., Vollstaedt, H., Fietzke, J., Liebetrau, V., Augustin, N., Peucker-Ehrenbrink, B., Muller, M.N., Horn, C., Hansen, B.T., Nolte, N., Wallmann, K., 2010. Constraining the marine strontium budget with natural strontium isotope fractionations

(Sr-87/Sr-86*, delta Sr-88/86) of carbonates, hydrothermal solutions and river waters. Geochim. Cosmochim. Acta 74, 4097-4109.

Krabbenhöft, A., Fietzke, J., Eisenhauer, A., Liebetrau, V., Böhm, F., Vollstaedt, H., 2009. Determination of radiogenic and stable strontium isotope ratios ((87)/Sr(86)Sr; delta(88/86)Sr) by thermal ionization mass spectrometry applying an (87)Sr/(84)Sr double spike. J. Anal. At. Spectrom. 24, 1267-1271.

Kristmannsdottir, H., Tomasson, J., 1976. Zeolite zones in geothermal areas in Iceland, Natural Zeolites, Occurence, Properties, Use. Pergamon Press, New York, pp. 277-284.

Kump, L.R., Arthur, M.A., 1999. Interpreting carbon-isotope excursions: carbonates and organic matter. Chem. Geol. 161, 181-198.

Larsen, L.M., Watt, W.S., Watt, M., 1989. Geology and petrology of the lower Tertiary plateau basalts of the Scoresby Sund region, East Greenland. Bull. Gron. Geol. Under. 157, 164.

Lawson, E.C., Wadham, J.L., Tranter, M., Stibal, M., Lis, G.P., Butler, C.E.H., Laybourn-Parry, J., Nienow, P., Chandler, D., Dewsbury, P., 2014. Greenland Ice Sheet exports labile organic carbon to the Arctic oceans. Biogeosciences 11, 4015-4028.

Lefevre, F., Sardin, M., Vitorge, P., 1996. Migration of Ca-45 and Sr-90 in a clayey and calcareous sand: Calculation of distribution coefficients by ion exchange theory and validation by column experiments. J. Contam. Hydrol. 21, 175-188.

Lehn, G.O., Jacobson, A.D., 2015a. Optimation of a 48Ca - 43Ca double-spike MC-TIMS method for measuring Ca isotope ratios (d44/40Ca and d44/42Ca): limitations from filament reservoir mixing. J. Anal. At. Spectrom.

Lehn, G.O., Jacobson, A.D., 2015b. Optimation of a 48Ca - 43Ca double-spike MC-TIMS method for measuring Ca isotope ratios (d44/40Ca and d44/42Ca): limitations from filament reservoir mixing. J. Anal. At. Spectrom. 30, 1571-1581.

Lehn, G.O., Jacobson, A.D., Holmden, C., 2013. Precise analysis of Ca isotope ratios (delta(44/40)ca) using an optimized Ca-43-Ca-42 double-spike MC-TIMS method. Int. J. Mass. Spectrom. 351, 69-75.

Lemarchand, D., Wasserburg, G.T., Papanastassiou, D.A., 2004. Rate-controlled calcium isotope fractionation in synthetic calcite. Geochim. Cosmochim. Acta 68, 4665-4678.

Leonard, A., Castle, S., Burr, G.S., Lange, T., Thomas, J., 2013. A wet oxidation method for AMS radiocarbon analysis of dissolved organic carbon in water. Radiocarbon 55, 545-552.

Lerman, A., Wu, L., 2008. Kinetics of global geochemical cycles, Kinetics of Water-Rock Interaction. Springer, pp. 655-736.

Li, G.J., Elderfield, H., 2013. Evolution of carbon cycle over the past 100 million years. Geochim. Cosmochim. Acta 103, 11-25.

Li, G.J., Hartmann, J., Derry, L.A., West, A.J., You, C.F., Long, X.Y., Zhan, T., Li, L.F., Li, G., Qiu, W.H., Li, T., Liu, L.W., Chen, Y., Ji, J.F., Zhao, L., Chen, J., 2016. Temperature dependence of basalt weathering. Earth Plan. Sci. Lett. 443, 59-69.

Lindback, K., Pettersson, R., Hubbard, A.L., Doyle, S.H., van As, D., Mikkelsen, A.B., Fitzpatrick, A.A., 2015. Subglacial water drainage, storage, and piracy beneath the Greenland ice sheet. Geophys. Res. Lett. 42, 7606-7614.

Louvat, P., Allegre, C.J., 1997. Present denudation rates on the island of Reunion determined by river geochemistry: Basalt weathering and mass budget between chemical and mechanical erosions. Geochim. Cosmochim. Acta 61, 3645-3669.

Louvat, P., Gislason, S.R., Allegre, C.J., 2008. Chemical and mechanical erosion rates in Iceland as deduced from river dissolved and solid material. Am. J. Sci. 308, 679-726.

Ma, J.L., Wei, G.J., Liu, Y., Ren, Z.Y., Xu, Y.G., Yang, Y.H., 2013. Precise measurements of stable (delta88/86Sr) and radiogenic (87Sr/86Sr) strontium isotope ratios in geologic standard reference materials using MC-ICP-MS. Chinese Science Bulletin 58, 3111-3118.

Manning, C.E., Ingebritsen, S.E., Bird, D.K., 1993. Missing mineral zones in contact metamorphosed basalts. Am. J. Sci. 293, 894-938.

Marty, B., Gunnlaugsson, E., Jambon, A., Oskarsson, N., Ozima, M., Pineau, F., Torssander, P., 1991. Gas geochemistry of geothermal fluids, the Hengill area, southwest rift-zone of Iceland. Chem. Geol. 91, 207-225.

Marx, S.K., Kamber, B.S., McGowan, H.A., 2008. Scavenging of atmospheric trace metal pollutants by mineral dusts: Inter-regional transport of Australian trace metal pollution to New Zealand. Atmospheric Environment 42, 2460-2478.

McDonald, D., Price, M.N., Goodrich, J., Nawrocki, E.P., DeSantis, T.Z., Probst, A., Andersen, G.L., Knight, R., Hugenholtz, P., 2012. An improved Greengenes taxonomy with explicit ranks for ecological and evolutionary analyses of bacteria and archaea. ISME J. 6, 610-618.

Mehegan, J.M., Robinson, P.T., Delaney, J.R., 1982. Secondary mineralization and hydrothermal alteration in the Reydarfjordur drill core, eastern Iceland. J. Geophys. Res. 87, 6511-6524.

Mernild, S.H., Hanna, E., McConnell, J.R., Sigl, M., Beckerman, A.P., Yde, J.C., Cappelen, J., Malmros, J.K., Steffen, K., 2015. Greenland precipitation trends in a long-term instrumental climate context (1890-2012): evaluation of coastal and ice core records. International Journal of Climatology 35, 303-320.

Mervine, E.M., Humphris, S.E., Sims, K.W.W., Kelemen, P.B., Jenkins, W.J., 2014. Carbonation rates of peridotite in the Samail Ophiolite, Sultanate of Oman, constrained through C-14 dating and stable isotopes. Geochim. Cosmochim. Acta 126, 371-397.

Meyer, F., Paarmann, D., D'Souza, M., Olson, R., Glass, E.M., Kubal, M., Paczian, T., Rodriguez, A., Stevens, R., Wilke, A., Wilkening, J., Edwards, R.A., 2008. The metagenomics RAST server - a public resource for the automatic phylogenetic and functional analysis of metagenomes. BMC Bioinformatics 9.

Miller, E.K., Blum, J.D., Friedland, A.J., 1993. Determination of soil exchangeable-cation loss and weathering rates using Sr isotopes. Nature 362, 438-441.

Millot, R., Gaillardet, J., Dupre, B., Allegre, C.J., 2002. The global control of silicate weathering rates and the coupling with physical erosion: new insights from rivers of the Canadian Shield. Earth Plan. Sci. Lett. 196, 83-98.

Mills, B., Daines, S.J., Lenton, T.M., 2014. Changing tectonic controls on the long-term carbon cycle from Mesozoic to present. Geochem. Geophy. Geosy. 15, 4866-4884.

Moore, J., Jacobson, A.D., Holmden, C., Craw, D., 2013. Tracking the relationship between mountain uplift, silicate weathering, and long-term CO2 consumption with Ca isotopes: Southern Alps, New Zealand. Chem. Geol. 341, 110-127.

Moore, L.J., Murphy, T.J., Barnes, I.L., Paulsen, P.J., 1982. Absolute isotopic abundance ratios and atomic weight of a reference sample of strontium. Journal of Research of the National Bureau of Standards 87, 1-8.

Moulton, K.L., Berner, R.A., 1998. Quantification of the effect of plants on weathering: Studies in Iceland. Geology 26, 895-898.

Moynier, F., Agranier, A., Hezel, D.C., Bouvier, A., 2010. Sr stable isotope composition of Earth, the Moon, Mars, Vesta and meteorites. Earth Plan. Sci. Lett. 300, 359-366.

Muir, R.J., Ireland, T.R., Weaver, S.D., Bradshaw, J.D., Evans, J.A., Eby, G.N., Shelley, D., 1998. Geochronology and geochemistry of a Mesozoic magmatic arc system, Fiordland, New Zealand. J. Geol. Soc. 155, 1037-1052.

Murata, K.J., Formoso, M.L.L., Roisenberg, A., 1987. Distribution of zeolites in lavas of southeastern Parana Basin, state of Rio Grande do Sul, Brazil. J. Geol. 95, 455-467.

Navarre-Sitchler, A., Brantley, S., 2007. Basalt weathering across scales. Earth Plan. Sci. Lett. 261, 321-334.

Neuhoff, P.S., Fridriksson, T., Bird, D.K., 2000. Zeolite parageneses in the north Atlantic igneous province: Implications for geotectonics and groundwater quality of basaltic crust. Int. Geol. Rev. 42, 15-44.

Neuhoff, P.S., Watt, W.S., Bird, D.K., Pedersen, A.K., 1997. Timing and structural relations of regional zeolite zones in basalts of the East Greenland continental margin. Geology 25, 803-806.

Neymark, L.A., Premo, W.R., Mel'nikov, N.N., Emsbo, P., 2014. Precise determination of delta Sr-88 in rocks, minerals, and waters by double-spike TIMS: a powerful tool in the study of geological, hydrological and biological processes. J. Anal. At. Spectrom. 29, 65-75.

Ning, Z.G., Ishiguro, M., Koopal, L.K., Sato, T., Kashiwagi, J., 2017. Strontium adsorption and penetration in kaolinite at low Sr2+ concentration. Soil Science and Plant Nutrition 63, 14-17.

NIWA, 2012. New Zealand National Institute of Water and Atmospheric Research, National Climate Database.

Normand, S., Randin, C., Ohlemuller, R., Bay, C., Hoye, T.T., Kjaer, E.D., Korner, C., Lischke, H., Maiorano, L., Paulsen, J., Pearman, P.B., Psomas, A., Treier, U.A., Zimmermann, N.E., Svenning, J.C., 2013. A greener Greenland? Climatic potential and long-term constraints on future expansions of trees and shrubs. Phil. Trans. R. Soc. B 368.

Norodahl, H., Petursson, H.G., 2005. Relative sea-level changes in Iceland: new aspects of the Weichselian deglaciation of Iceland, in: Caseldine, C., Russell, A., Hardardottir, J., Knudsen, O. (Eds.), Iceland - Modern Processes and Past Environments, 1st ed. Elsevier Science, pp. 25-78.

Ohno, T., Hirata, T., 2006. Stable isotope geochemistry of strontium using MC-ICP-MS. Geochim. Cosmochim. Acta 70, A453-A453.

Ohno, T., Hirata, T., 2007. Simultaneous determination of mass-dependent isotopic Fractionation and radiogenic isotope variation of strontium in geochemical samples by multiple collector-ICP-mass spectrometry. Analytical Sciences 23, 1275-1280.

Ohno, T., Komiya, T., Ueno, Y., Hirata, T., Maruyama, S., 2008. Determination of Sr-88/Sr-86 mass-dependent isotopic and radiogenic isotope variation of Sr-87/Sr-86 in the Neoproterozoic Doushantuo Formation. Gondwana Research 14, 126-133.

Pabalan, R., Beretti, F.P., 2001. Cation-exchange properties of natural zeolites. Rev. Mineral. Geochem. 45, 453-518.

Page, B.D., Bullen, T.D., Mitchell, M.J., 2008. Influences of calcium availability and tree species on Ca isotope fractionation in soil and vegetation. Biogeochemistry 88, 1-13.

Palmer, M.R., Edmond, J.M., 1992. Controls over the Strontium isotope composition of river water. Geochim. Cosmochim. Acta 56, 2099-2111.

Parkhurst, D.L., Appelo, C.A.J., 1999. User's Guide to PHREEQC (Version 2). W4259 U.S. Geological Survey, Washington D.C.

Pearce, C.R., Parkinson, I.J., Gaillardet, J., Charlier, B.L., Mokadem, F., Burton, K.W., 2015a. Reassessing the stable (d88/86Sr) and radiogenic (87Sr/86Sr) strontium isotopic composition of marine inputs. Geochim. Cosmochim. Acta 157, 125-146.

Pearce, C.R., Parkinson, I.J., Gaillardet, J., Chetelat, B., Burton, K.W., 2015b. Characterising the stable (delta(88)/Sr-86) and radiogenic (Sr-87/Sr-86) isotopic composition of strontium in rainwater. Chem. Geol. 409, 54-60.

Pett-Ridge, J.C., Derry, L.A., Barrows, J.K., 2009. Ca/Sr and Sr-87/Sr-86 ratios as tracers of Ca and Sr cycling in the Rio Icacos watershed, Luquillo Mountains, Puerto Rico. Chem. Geol. 267, 32-45.

Pierson-Wickmann, A.C., Aquilina, L., Weyer, C., Molenat, J., Lischeid, G., 2009. Acidification processes and soil leaching influenced by agricultural practices revealed by strontium isotopic ratios. Geochim. Cosmochim. Acta 73, 4688-4704.

Plummer, L.N., Busenberg, E., 1982. The solubilities of calcite, aragonite, and vaterite in CO2-H2O solutions between 0 and 90C, and an evalution of the aqueous model for the system CaCO3-CO2-H2O. Geochim. Cosmochim. Acta 46, 1011-1040.

Pogge von Strandmann, P.A.E., Burton, K.W., James, R.H., van Calsteren, P., Gislason, S.R., Sigfusson, B., 2008. The influence of weathering processes on riverine magnesium isotopes in a basaltic terrain. Earth Plan. Sci. Lett. 276, 187-197.

Poszwa, A., Dambrine, E., Pollier, B., Atteia, O., 2000. A comparison between Ca and Sr cycling in forest ecosystems. Plant and Soil 225, 299-310.

Probst, A., El Gh'mari, A., Aubert, D., Fritz, B., McNutt, R., 2000. Strontium as a tracer of weathering processes in a silicate catchment polluted by acid atmospheric inputs, Strengbach, France. Chem. Geol. 170, 203-219.

Rad, S.D., Allegre, C.J., Louvat, P., 2007. Hidden erosion on volcanic islands. Earth Plan. Sci. Lett. 262, 109-124.

Raddatz, J., Liebetrau, V., Rüggeberg, A., Hathorne, E., Krabbenhöft, A., Eisenhauer, A., Böhm, F., Vollstaedt, H., Fietzke, J., Lopez Correa, M., Freiwald, A., Dullo, W.C., 2013. Stable Sr-isotope, Sr/Ca, Mg/Ca, Li/Ca and Mg/Li ratios in the scleractinian cold-water coral Lophelia pertusa. Chem. Geol. 352, 143-152.

Rafferty, P., Shiao, S.Y., Binz, C.M., Meyers, R.E., 1981. ADSORPTION OF SR(II) ON CLAY-MINERALS - EFFECTS OF SALT CONCENTRATION, LOADING, AND PH. Journal of Inorganic & Nuclear Chemistry 43, 797-805.

Rani, R.D., Sasidhar, P., 2012. Geochemical and thermodynamic aspects of sorption of strontium on kaolinite dominated clay samples at Kalpakkam. Environmental Earth Sciences 65, 1265-1274.

Rennermalm, A.K., Smith, L.C., Chu, V.W., Forster, R.R., Box, J.E., Hagedorn, B., 2012. Proglacial river stage, discharge, and temperature datasets from the Akuliarusiarsuup Kuua River northern tributary, Southwest Greenland, 2008-2011. Earth System Science Data 4, 1-12.

Rive, K., Gaillardet, J., Agrinier, P., Rad, S., 2013. Carbon isotopes in the rivers from the Lesser Antilles: origin of the carbonic acid consumed by weathering reactions in the Lesser Antilles. Earth Surf. Process. Landf. 38, 1020-1035.

Rüggeberg, A., Fietzke, J., Liebetrau, V., 2008. Stable strontium isotopes (delta Sr-88/86) in cold-water corals - A new proxy for reconstruction of intermediate ocean water temperatures. Earth Plan. Sci. Lett. 269, 569-574.

Ryu, J.S., Jacobson, A.D., 2012. CO2 evasion from the Greenland Ice Sheet: A new carbon-climate feedback. Chem. Geol. 320, 80-95.

Ryu, J.S., Jacobson, A.D., Holmden, C., Lundstrom, C., Zhang, Z.F., 2011. The major ion, delta Ca-44/40, delta Ca-44/42, and delta Mg-26/24 geochemistry of granite weathering at pH=1 and T=25 degrees C: power-law processes and the relative reactivity of minerals. Geochim. Cosmochim. Acta 75, 6004-6026.

Sano, Y., Urabe, A., Wakita, H., Chiba, H., Sakai, H., 1985. Chemical and isotopic compositions of gases in geothermal fluids in Iceland. Geochem. J. 19, 135-148.

Schmidt, S.T., 1993. Regional and local patterns of low-grade metamorphism in the North Shore Volcanic Group, Minnesota, USA. J. Metamorph. Geol. 11, 401-414.

Schmitt, A.D., Cobert, F., Bourgeade, P., Ertlen, D., Labolle, F., Gangloff, S., Badot, P.M., Chabaux, F., Stille, P., 2013. Calcium isotope fractionation during plant growth under a limited nutrient supply. Geochim. Cosmochim. Acta 110, 70-83.

Schopka, H.H., Derry, L.A., 2012. Chemical weathering fluxes from volcanic islands and the importance of groundwater: The Hawaiian example. Earth Plan. Sci. Lett. 339, 67-78.

Schopka, H.H., Derry, L.A., Arcilla, C.A., 2011. Chemical weathering, river geochemistry and atmospheric carbon fluxes from volcanic and ultramafic regions on Luzon Island, the Philippines. Geochim. Cosmochim. Acta 75, 978-1002.

Schuenemann, K.C., Cassano, J.J., 2010. Changes in synoptic weather patterns and Greenland precipitation in the 20th and 21st centuries: 2. Analysis of 21st century atmospheric changes using self-organizing maps. J. Geophys. Res. Atmos. 115, 18.

Shalev, N., Gavrieli, I., Halicz, L., Sandler, A., Stein, M., Lazar, B., 2017. Enrichment of Sr-88 in continental waters due to calcium carbonate precipitation. Earth Plan. Sci. Lett. 459, 381-393.

Sharp, M., Creaser, R.A., Skidmore, M., 2002. Strontium isotope composition of runoff from a glaciated carbonate terrain. Geochim. Cosmochim. Acta 66, 595-614.

Sharp, M., Tranter, M., Brown, G.H., Skidmore, M., 1995. RATES OF CHEMICAL DENUDATION AND CO2 DRAWDOWN IN A GLACIER-COVERED ALPINE CATCHMENT. Geology 23, 61-64.

Sharp, Z., 2007. Carbon in the Low-Temperature Environment, Principles of Stable Isotope Geochemistry. Pearson, Upper Saddle River, NJ, USA.

Stefansson, A., Gislason, S.R., 2001. Chemical weathering of basalts, Southwest Iceland: Effect of rock crystallinity and secondary minerals on chemical fluxes to the ocean. Am. J. Sci. 301, 513-556.

Stevenson, E.I., Aciego, S.M., Chutcharavan, P., Parkinson, I.J., Burton, K.W., Blakowski, M.A., Arendt, C.A., 2016. Insights into combined radiogenic and stable strontium isotopes as tracers for weathering processes in subglacial environments. Chem. Geol. 429, 33-43.

Stevenson, E.I., Hermoso, M., Rickaby, R.E.M., Tyler, J.J., Minoletti, F., Parkinson, I.J., Mokadem, F., Burton, K.W., 2014. Controls on stable strontium isotope fractionation in coccolithophores with implications for the marine Sr cycle. Geochim. Cosmochim. Acta 128, 225-235.

Stibal, M., Gozdereliler, E., Cameron, K.A., Box, J.E., Stevens, I.T., Gokul, J.K., Schostag, M., Zarsky, J.D., Edwards, A., Irvine-Fynn, T.D.L., Jacobsen, C.S., 2015. Microbial abundance in surface ice on the Greenland Ice Sheet. Front. Microbiol. 6, 12.

Stibal, M., Lawson, E.C., Lis, G.P., Mak, K.M., Wadham, J.L., Anesio, A.M., 2010. Organic matter content and quality in supraglacial debris across the ablation zone of the Greenland ice sheet. Ann. Glaciol. 51, 1-8.

Suchet, P.A., Probst, J.L., Ludwig, W., 2003. Worldwide distribution of continental rock lithology: Implications for the atmospheric/soil CO2 uptake by continental weathering and alkalinity river transport to the oceans. Global Biogeochem. Cy. 17.

Sukheswala, R.N., Avasia, R.K., Gangopadhyay, M., 1974. Zeolites and associated secondary minerals in the Deccan Traps of West India. Minerological Magazine 39, 658-671.

Tang, J.W., Dietzel, M., Böhm, F., Kohler, S.J., Eisenhauer, A., 2008. Sr2+/Ca2+ and Ca-44/Ca-40 fractionation during inorganic calcite formation: II. Ca isotopes. Geochim. Cosmochim. Acta 72, 3733-3745.

Taylor, A.S., Lasaga, A.C., 1999. The role of basalt weathering in the Sr isotope budget of the oceans. Chem. Geol. 161, 199-214.

Templeton, A.S., Chu, K.H., Alvarez-Cohen, L., Conrad, M.E., 2006. Variable carbon isotope fractionation expressed by aerobic CH4-oxidizing bacteria. Geochim. Cosmochim. Acta 70, 1739-1752.

Thomas, D.L., Bird, D.K., Arnorsson, S., Maher, K., 2016. Geochemistry of CO2-rich waters in Iceland. Chem. Geol. 444, 158 - 179.

Torres, M.A., Moosdorf, N., Hartmann, J., Adkins, J.F., West, A.J., 2017. Glacial weathering, sulfide oxidation, and global carbon cycle feedbacks. Proc. Natl. Acad. Sci. USA 114, 8716-8721.

Torres, M.A., West, A.J., Li, G.J., 2014. Sulphide oxidation and carbonate dissolution as a source of CO2 over geological timescales. Nature 507, 346-+.

Tranter, M., Huybrechts, P., Munhoven, G., Sharp, M.J., Brown, G.H., Jones, I.W., Hodson, A.J., Hodgkins, R., Wadham, J.L., 2002a. Direct effect of ice sheets on terrestrial bicarbonate, sulphate and base cation fluxes during the last glacial cycle: minimal impact on atmospheric CO2 concentrations. Chem. Geol. 190, 33-44.

Tranter, M., Sharp, M.J., Lamb, H.R., Brown, G.H., Hubbard, B.P., Willis, I.C., 2002b. Geochemical weathering at the bed of Haut Glacier d'Arolla, Switzerland - a new model. Hydrological Processes 16, 959-993.

Turnbull, I.M., 2000. Geology of the Wakatipu area, Institute of Geological & Nuclear Sciences 1:250000 geoloic map 18. Institute of Geological & Nuclear Sciences Limited, Lower Hutt, New Zealand.

Uhlig, D., Schuessler, J.A., Bouchez, J., Dixon, J.L., von Blanckenburg, F., 2017. Quantifying nutrient uptake as driver of rock weathering in forest ecosystems by magnesium stable isotopes. Biogeosciences 14, 3111-3128.

Urey, H., 1952. The planets, their origin and development. Yale University Press, New Haven, CT.

van As, D., Hubbard, A.L., Hasholt, B., Mikkelsen, A.B., van den Broeke, M.R., Fausto, R.S., 2012. Large surface meltwater discharge from the Kangerlussuaq sector of the Greenland ice sheet during the record-warm year 2010 explained by detailed energy balance observations. Cryosphere 6, 199-209.

van As, D., Mikkelsen, A.B., Nielsen, M.H., Box, J.E., Liljedahl, L.C., Lindback, K., Pitcher, L., Hasholt, B., 2017. Hypsometric amplification and routing moderation of Greenland ice sheet meltwater release. Cryosphere 11, 1371-1386.

van Gool, J.A.M., Connelly, J.N., Marker, M., Mengel, F.C., 2002. The Nagssugtoqidian Orogen of West Greenland: tectonic evolution and regional correlations from a West Greenland perspective. Can. J. Earth Sci. 39, 665-686.

Varekamp, J.C., Kreulen, R., Poorter, R.P.E., Vanbergen, M.J., 1992. Carbon sources in arc volcanism, with implications for the carbon cycle. Terra Nova 4, 363-373.

Vigier, N., Gislason, S.R., Burton, K.W., Millot, R., Mokadem, F., 2009. The relationship between riverine lithium isotope composition and silicate weathering rates in Iceland. Earth Plan. Sci. Lett. 287, 434-441.

Volk, T., 1987. Feedbacks between weathering and atmospheric CO2 over the last 100 million years. Am. J. Sci. 287, 763-779.

Vollstaedt, H., Eisenhauer, A., Wallmann, K., Böhm, F., Fietzke, J., Liebetrau, V., Krabbenhöft, A., Farkas, J., Tomasovych, A., Raddatz, J., Veizer, J., 2014. The Phanerozoic delta Sr-88/86 record of seawater: New constraints on past changes in oceanic carbonate fluxes. Geochim. Cosmochim. Acta 128, 249-265.

Wadham, J.L., Tranter, M., Skidmore, M., Hodson, A.J., Priscu, J., Lyons, W.B., Sharp, M., Wynn, P., Jackson, M., 2010. Biogeochemical weathering under ice: Size matters. Global Biogeochem. Cy. 24.

Walker, G.P.L., 1958. The geology of the Reydarfjordur Area, Eastern Iceland. J. Geol. Soc. 114, 367-391.

Walker, G.P.L., 1960. Zeolite zones and dike distribution in relation to the structure of the basalts of Eastern Iceland. J. Geol. 68, 515 - 528.

Walker, G.P.L., 1963. The Breiddalur central volcano, eastern Iceland. J. Geol. Soc. 119, 29 - 63.

Walker, J.C.G., Hays, P.B., Kasting, J.F., 1981. A negative feedback mechanism for the long-term stabilization of Earth's surface temperature. J. Geophys. Res. 86, 9776 - 9782.

Wallmann, K., 2001. Controls on the Cretaceous and Cenozoic evolution of seawater composition, atmospheric CO2 and climate. Geochim. Cosmochim. Acta 65, 3005-3025.

Wei, G.J., Ma, J.L., Liu, Y., Xie, L.H., Lu, W.J., Deng, W.F., Ren, Z.Y., Zeng, T., Yang, Y.H., 2013. Seasonal changes in the radiogenic and stable strontium isotopic composition of Xijiang River water: Implications for chemical weathering. Chem. Geol. 343, 67-75.

Wiegand, B.A., Chadwick, O.A., Vitousek, P.M., Wooden, J.L., 2005. Ca cycling and isotopic fluxes in forested ecosystems in Hawaii. Geophys. Res. Lett. 32, L11404.

Wiese, F., Fridriksson, T., Armannsson, H., 2008. CO2 fixation by calcite in high-temperature geothermal systems in Iceland. Technical report, ISO5-2008/003. Iceland Geosurvey, Reykjavik.

Wimpenny, J., James, R.H., Burton, K.W., Gannoun, A., Mokadem, F., Gislason, S.R., 2010. Glacial effects on weathering processes: New insights from the elemental and lithium isotopic composition of West Greenland rivers. Earth Plan. Sci. Lett. 290, 427-437.

Yde, J.C., Finster, K.W., Raiswell, R., Steffensen, J.P., Heinemeier, J., Olsen, J., Gunnlaugsson, H.P., Nielsen, O.B., 2010. Basal ice microbiology at the margin of the Greenland ice sheet. Ann. Glaciol. 51, 71-79.

Yde, J.C., Knudsen, N.T., 2004. The importance of oxygen isotope provenance in relation to solute content of bulk meltwaters at Imersuaq Glacier, West Greenland. Hydrological Processes 18, 125-139.

Yde, J.C., Knudsen, N.T., Hasholt, B., Mikkelsen, A.B., 2014. Meltwater chemistry and solute export from a Greenland Ice Sheet catchment, Watson River, West Greenland. J. Hydrol. 519, 2165-2179.

Yde, J.C., Knudsen, N.T., Steffensen, J.P., Carrivick, J.L., Hasholt, B., Ingeman-Nielsen, T., Kronborg, C., Larsen, N.K., Mernild, S.H., Oerter, H., Roberts, D.H., Russell, A.J., 2016. Stable oxygen isotope variability in two contrasting glacier river catchments in Greenland. Hydrology and Earth System Sciences 20, 1197-1210.

Zhang, J., Quay, P.D., Wilbur, D.O., 1995. Carbon-isotope fractionation during gas-water exchange and dissolution of CO2. Geochim. Cosmochim. Acta 59, 107-114.

Zhang, J.J., Kobert, K., Flouri, T., Stamatakis, A., 2014. PEAR: a fast and accurate Illumina Paired-End reAd mergeR. Bioinformatics 30, 614-620.

Appendix A

TIMS method development for stable Sr isotope measurements

A.1 Double-spike data reduction procedure

The double-spike data reduction equations are adapted from Eugster et al. (1969):

$$\left(\frac{^{87}Sr}{^{84}Sr}\right)_{dsp} = \left(\frac{^{87}Sr}{^{84}Sr}\right)_{mix} + \left[\left(\frac{^{87}Sr}{^{84}Sr}\right)_{mix} - \left(\frac{^{87}Sr}{^{84}Sr}\right)_{smp}^{tru}\right] \cdot \left[\frac{\left(\frac{^{86}Sr}{^{84}Sr}\right)_{mix} - \left(\frac{^{86}Sr}{^{84}Sr}\right)_{dsp}^{tru}}{\left(\frac{^{86}Sr}{^{84}Sr}\right)_{smp}^{tru} - \left(\frac{^{86}Sr}{^{84}Sr}\right)_{mix}}\right] \quad \text{(A1)}$$

$$\left(\frac{^{88}Sr}{^{86}Sr}\right)_{smp} = \left(\frac{^{88}Sr}{^{86}Sr}\right)_{mix} + \left[\left(\frac{^{88}Sr}{^{86}Sr}\right)_{mix} - \left(\frac{^{88}Sr}{^{86}Sr}\right)_{dsp}^{tru}\right] \cdot \left[\frac{\left(\frac{^{84}Sr}{^{86}Sr}\right)_{smp}^{tru} - \left(\frac{^{84}Sr}{^{86}Sr}\right)_{mix}}{\left(\frac{^{84}Sr}{^{86}Sr}\right)_{mix} - \left(\frac{^{84}Sr}{^{86}Sr}\right)_{dsp}^{tru}}\right] \quad \text{(A2)}$$

where *dsp*, *mix*, *tru*, and *smp* stand for double-spike, mixture (i.e., the measured composition of the double-spiked sample), true, and sample, respectively. The equations are solved iteratively. Equation A1 requires the true $^{86}Sr/^{84}Sr$ and $^{87}Sr/^{84}Sr$ ratios of the sample. For the first iteration, the true $^{86}Sr/^{84}Sr$ ratio is set to the normal value of 17.689, but because the abundance of ^{87}Sr varies due to the radioactive decay of ^{87}Rb, the $^{87}Sr/^{86}Sr$ ratio from the radiogenic Sr isotope run is multiplied by the normal $^{86}Sr/^{84}Sr$ value and input for the true $^{87}Sr/^{84}Sr$ ratio. Equation A1 subtracts the sample composition from the measured mixture composition to provide the instrumental mass-fractionated $^{87}Sr/^{84}Sr$ ratio of the double-spike. This is compared to the true double-spike $^{87}Sr/^{84}Sr$ ratio, which is previously measured on the TIMS, to calculate a fractionation factor, β, assuming fractionation follows an exponential law:

$$\left(\frac{^{a}\mathrm{Sr}}{^{b}\mathrm{Sr}}\right)_{frac} = \left(\frac{^{a}\mathrm{Sr}}{^{b}\mathrm{Sr}}\right)_{ufrac} \times \left(\frac{\mathrm{M}_{a}}{\mathrm{M}_{b}}\right)^{\beta} \quad \text{(A3)}$$

where *frac* and *ufrac* refer to fractionated and unfractionated ratios, and M_a and M_b are the exact atomic masses of Sr isotopes *a* and *b.* The calculated β value and equation A3 are then used to correct the other measured mixture ratios for instrumental mass-fractionation, prior to their use in Equation A2.

Equation A2 subtracts the spike composition from the mixture composition, after correction for instrumental mass-fractionation, to determine the $^{88}Sr/^{86}Sr$ ratio of the sample. The first iteration of Equation A2 uses the normal $^{84}Sr/^{86}Sr$ ratio of 0.05653 for the true sample ratio. The sample $^{88}Sr/^{86}Sr$ ratio (the result of equation A2) and the $^{88}Sr/^{86}Sr$ ratio of Sr normal, 8.3752, are implemented in equation A3 to estimate a value for β, which now corresponds to natural mass-fractionation. Equation A3 and the $^{86}Sr/^{84}Sr$ and $^{87}Sr/^{84}Sr$ ratios from the first iteration are then used to calculate $^{86}Sr/^{84}Sr$ and $^{87}Sr/^{84}Sr$ ratios for the sample, and these ratios are subsequently employed as the true values in the second iteration. The process is repeated for seven iterations, which corresponds to sample $^{88}Sr/^{86}Sr$ ratios converging to within less than 1 ppt.

A.2 Double-spike optimization

We used the Monte Carlo error model presented in Lehn et al. (2013) to optimize an ^{87}Sr-^{84}Sr double-spike method for measuring fractionated $^{88}Sr/^{86}Sr$ ratios. To implement the model, the double-spike composition is simulated using isotopic abundance data for ISOFLEX $^{87}SrCO_3$ and $^{84}SrCO_3$ powders (Table A1). Similarly, the sample composition is simulated using isotopic

abundance data for NBS 987 reported in Moore et al. (1982) (Table A1). The composition of the double-spike mixture is given by the equation:

$$^{84}\mathrm{Sr}_{dsp} = \frac{^{84}\mathrm{Sr}}{^{84}\mathrm{Sr} + ^{87}\mathrm{Sr}} \quad , \tag{A4}$$

where the molar abundance of ^{84}Sr ($^{84}Sr_{dsp}$) ranges from 0 to 1. Mixtures of the double-spike and sample are modeled with the equation:

$$p_{dsp} = \frac{\mathrm{Sr}_{dsp}}{\mathrm{Sr}_{dsp} + \mathrm{Sr}_{smp}} \quad , \tag{A5}$$

where the molar proportion of Sr from the double-spike (p_{dsp}) ranges from 0 to 1. From equations (A4) and (A5), the double-spike ^{87}Sr/^{84}Sr ratio and the spike/sample ratio are given by:

$$\left(\frac{^{87}\mathrm{Sr}}{^{84}\mathrm{Sr}}\right)_{dsp} = \frac{1 - ^{84}\mathrm{Sr}_{dsp}}{^{84}\mathrm{Sr}_{dsp}} \tag{A6}$$

$$\left(dsp/smp\right) = \frac{p_{dsp}}{1 - p_{dsp}} \tag{A7}$$

where $(^{87}\mathrm{Sr}/^{84}\mathrm{Sr})_{\mathrm{dsp}}$ is the double-spike ratio and *dsp/smp* is the spike/sample ratio. Both $^{84}\mathrm{Sr}_{dsp}$ and p_{dsp} are stepped in 1% increments. Spike-sample mixtures are fractionated using equation (A3) and an assumed, constant, instrumental fractionation factor ($\beta = 0.2$). The results are insensitive to the value of β. Beam voltages are calculated assuming a constant 6V ^{88}Sr ion

beam. A 16 sec integration time is applied to a static collector cup configuration. The model does not consider isobaric interferences from ^{87}Rb on ^{87}Sr because real data are not collected unless ^{87}Rb is negligible. Normally distributed errors from counting statistics and Johnson noise are randomly assigned to the theoretically derived, instrumentally fractionated ratios. Ratios have variable errors because the errors depend on signal strength. Each duty cycle generates one ^{88}Sr/^{86}Sr ratio. The model reduces theoretical data for each duty cycle and averages multiple duty cycles to calculate a mean ^{88}Sr/^{86}Sr ratio for the entire run. The internal precision is determined by doubling the standard error of the mean ratio ($2\sigma_{SEM}$). The model simulates each permutation 100 times and averages the data to arrive at the representative mean ratio and $2\sigma_{SEM}$. With these constraints, we focused on values for $^{84}Sr_{dsp}$ and p_{dsp} yielding the best internal precision in the shortest amount of time while reasonably conserving double-spike.

Table A1

Isotopic abundance of NBS 987, $^{84}SrCO_3$, $^{87}SrCO_3$, and the NU double-spike

Isotope	NBS 987[a]	$^{84}SrCO_3$[b]	$^{87}SrCO_3$[b]	NU double-spike
^{84}Sr	0.005574	0.9964	0.0001	0.73039
^{86}Sr	0.098566	0.0014	0.0082	0.00325
^{87}Sr	0.070015	0.0003	0.9126	0.24359
^{88}Sr	0.825845	0.0019	0.0791	0.02277

[a] Moore et al. (1982)

[b] Certified values from ISOFLEX.

As with the Ca isotope system (Lehn et al., 2013), statistically identical precisions are expected for a wide range of double-spike and spike/sample ratios. For 140 duty cycles, the model predicts that ^{87}Sr/^{84}Sr = 0.33 [$^{84}Sr_{dsp}$ = 3 mol/mol] and *spk/smp* = 0.36 [p_{dsp} = 0.26 mol/mol] should yield an internal precision of ±0.011‰. Table A1 reports the precise isotopic

composition of the Northwestern University (NU) double-spike calibrated against NBS 987. As reported in the main text, measured internal precisions ($2\sigma_{SEM}$) agree with the model predictions, and the long-term, external reproducibility of the method ($2\sigma_{SD}$), determined form the repeated analysis of standards, is 0.020‰, or roughly 2 times internal precision.

A.3. Radiogenic and stable Sr standards through time

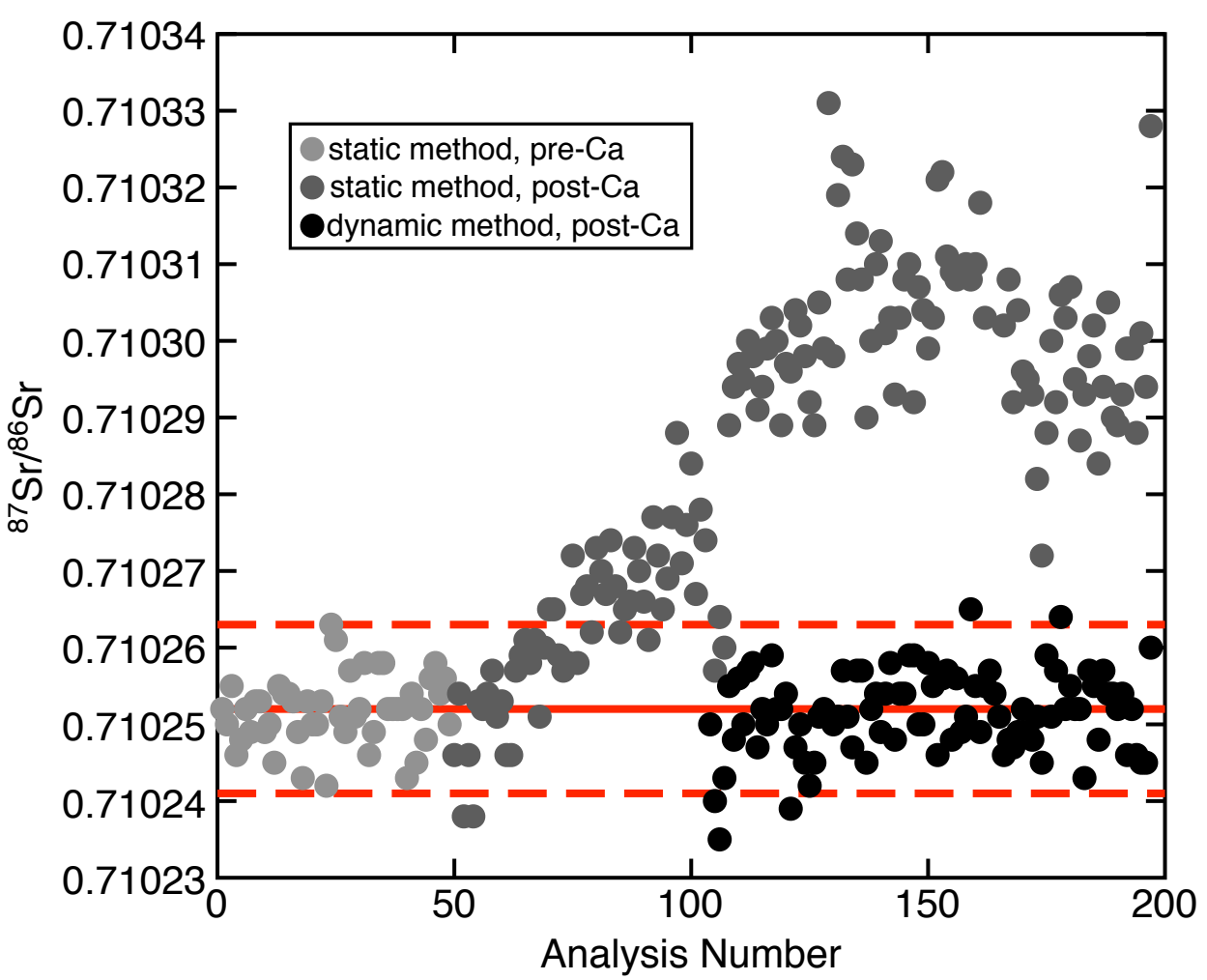

Figure A1: $^{87}Sr/^{86}Sr$ ratio for NBS 987 versus analysis number for the time period 2011 – 2014. Analysis numbers are consecutive through time. "Static method, pre – Ca" indicates $^{87}Sr/^{86}Sr$ ratios collected in static mode prior to the measurement of stable Ca isotope ratios, "static method, post – Ca" indicates $^{87}Sr/^{86}Sr$ ratios collected in either static mode (analysis #50 – 103) or the static configuration of dynamic mode (analysis #104– 197) after employing the TIMS for Ca isotope research, and "dynamic method, post – Ca" indicates $^{87}Sr/^{86}Sr$ ratios collected in dynamic mode after employing the TIMS for Ca isotope research. The solid red line shows the long-term average $^{87}Sr/^{86}Sr$ ratio for NBS 987 measured in dynamic mode, and the dashed red lines show the external reproducibility ($2\sigma_{SD}$). All samples for the current study were analyzed in dynamic mode.

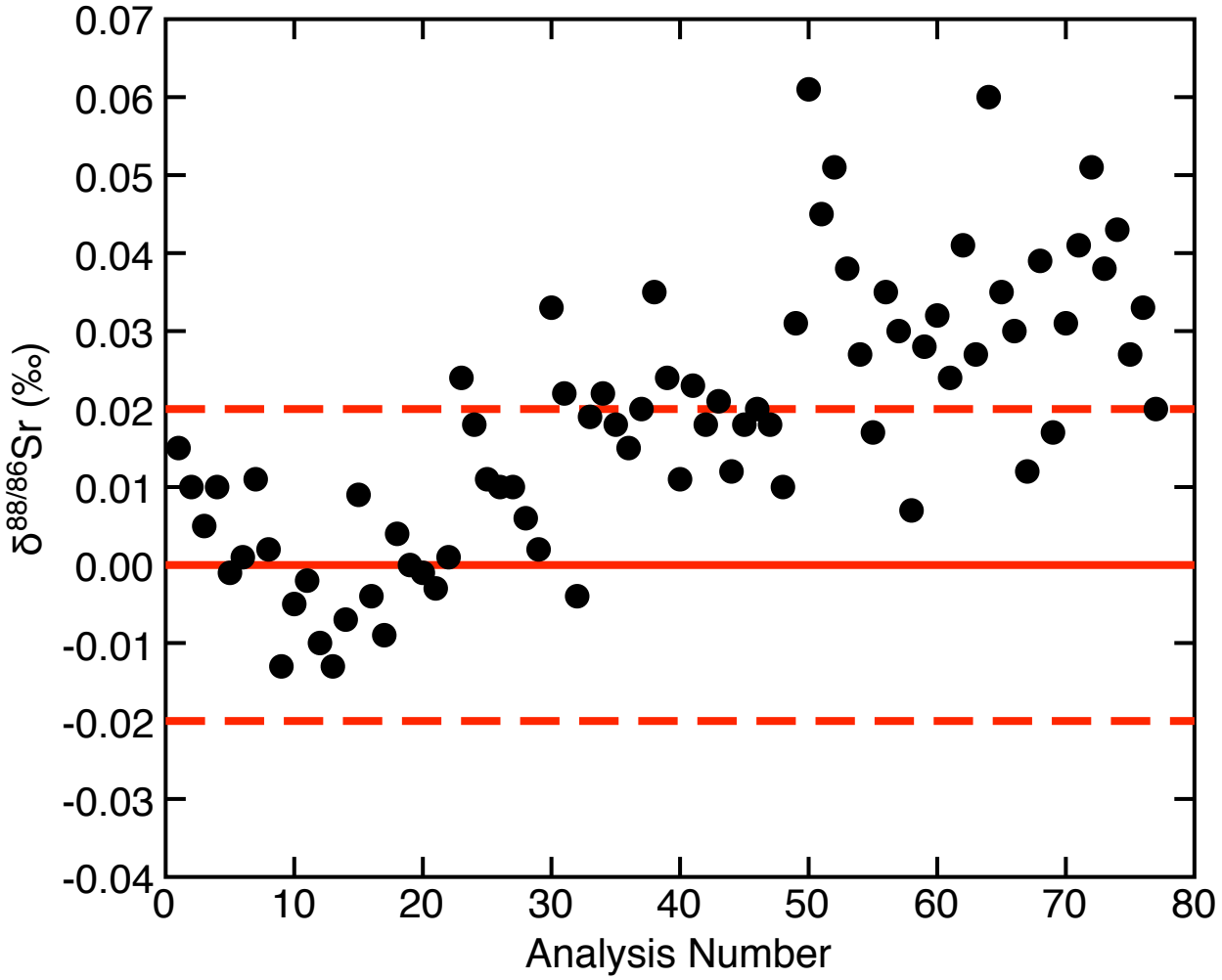

Figure A2: $\delta^{88/86}$Sr values for NBS 987 versus analysis number for the time period 2013 – 2014. The data are not drift-corrected (see text). Analysis numbers are consecutive through time. For comparison, solid red line shows the long-term, drift-corrected, average $\delta^{88/86}$Sr value, and the dashed red lines show the corresponding external reproducibility ($2\sigma_{SD}$) (see Chap. 2, Fig. A3).

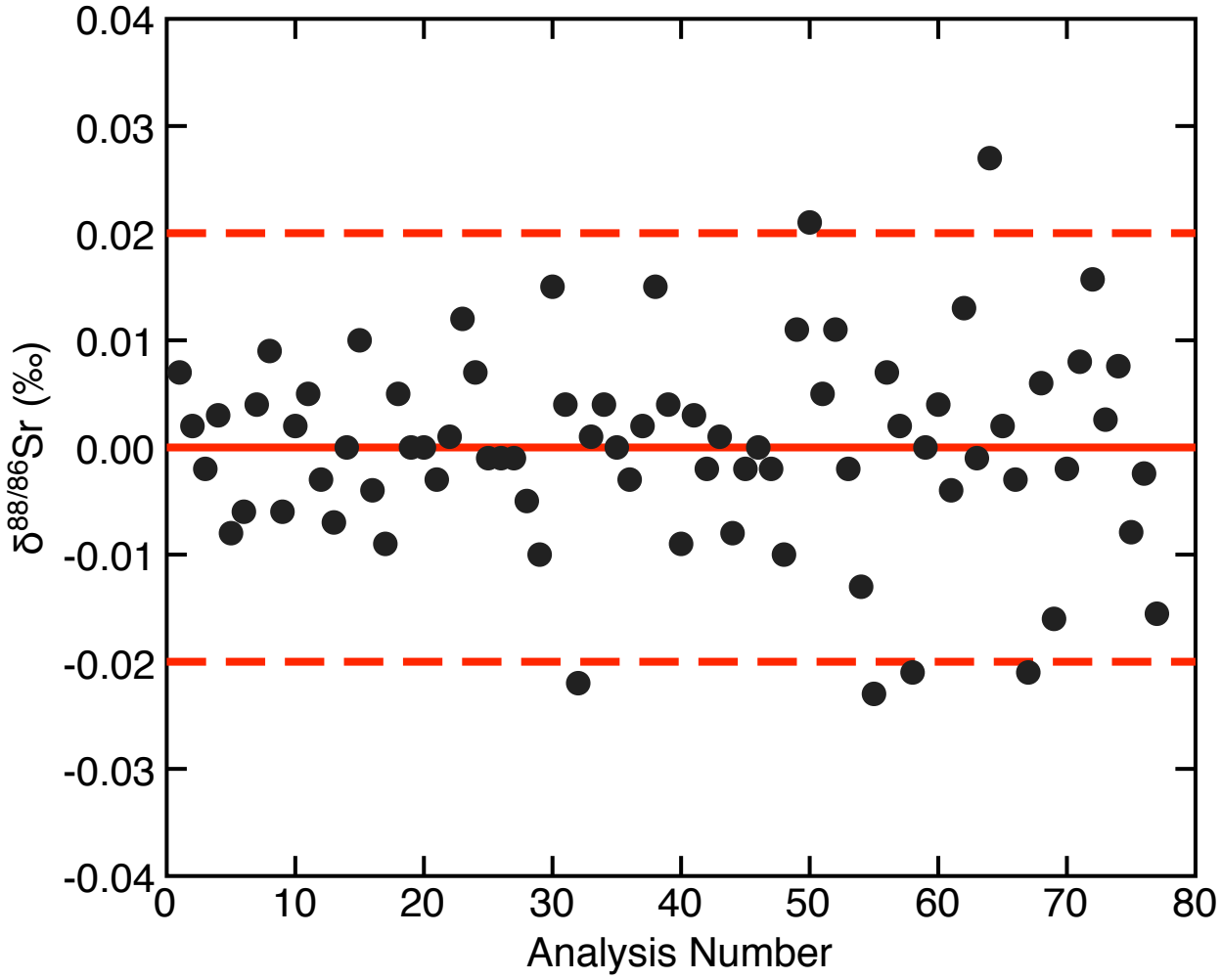

Figure A3: Drift-corrected $\delta^{88/86}$Sr values for NBS 987 versus analysis number for the time period 2013 – 2014. Analysis numbers are consecutive through time. The solid red line shows the long-term, average $\delta^{88/86}$Sr value, and the dashed red lines show the corresponding external reproducibility ($2\sigma_{SD}$).

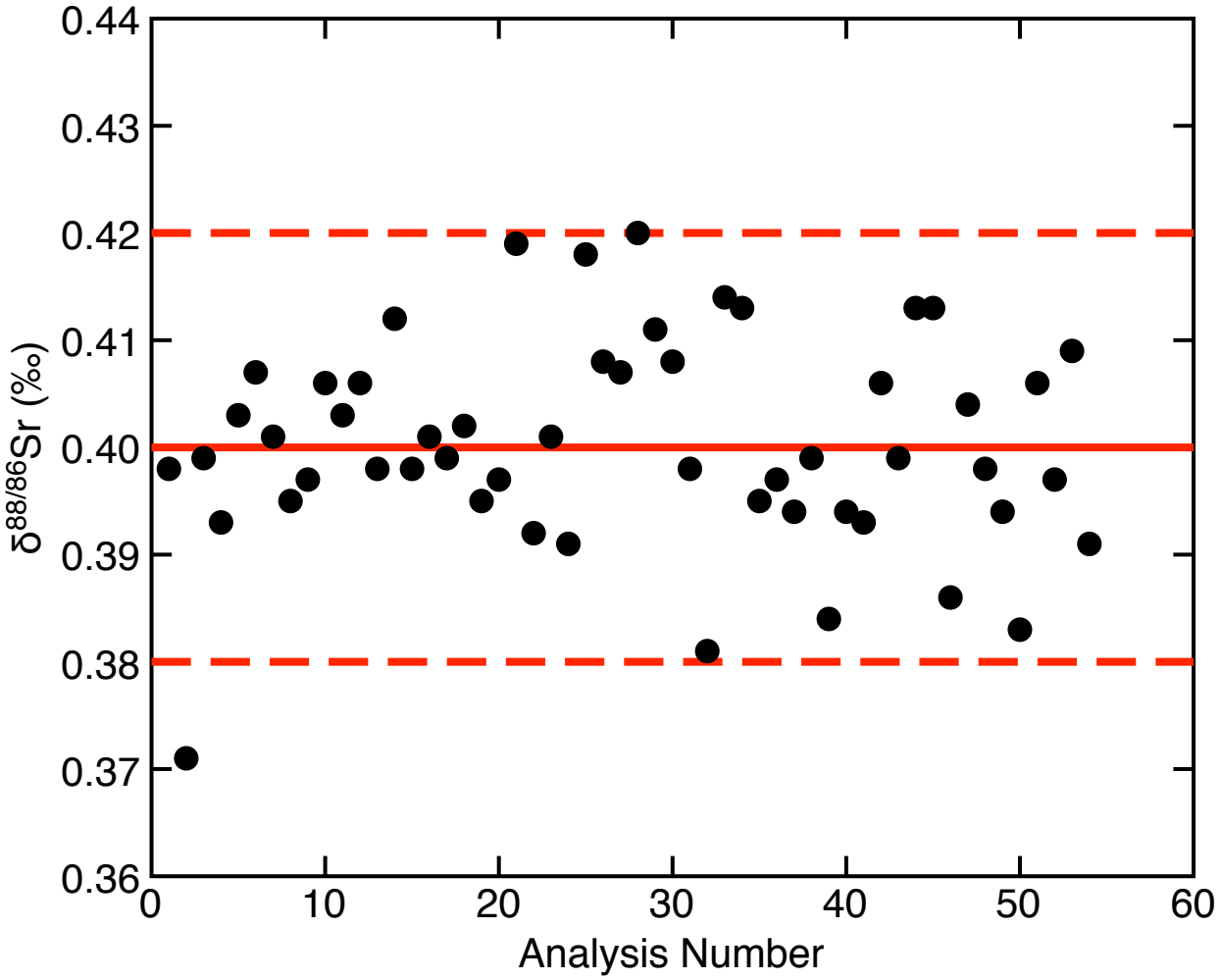

Figure A4: Drift-corrected $\delta^{88/86}$Sr values for the IAPSO seawater standard versus analysis number for the time period 2013 – 2014. Analysis numbers are consecutive through time. The solid red line shows the long-term, average $\delta^{88/86}$Sr value, and the dashed red lines show the corresponding external reproducibility ($2\sigma_{SD}$).

Appendix B

Equations for the long-term carbon cycle inclusive of a subsurface silicate weathering flux

The generalized equations for the long-term C cycle are:

$$2CO_2 + H_2O + CaSiO_3 \rightarrow Ca^{2+} + 2HCO_3^- + SiO_2 \quad \text{(B1)}$$

$$Ca^{2+} + 2HCO_3^- \rightarrow CaCO_3 + CO_2 + H_2O \quad \text{(B2)}$$

Equation B1 describes the chemical weathering of Ca-bearing silicate minerals composing terrestrial rocks, and equation B2 describes marine carbonate precipitation. The sum of the two equations yields the Urey-Ebelman equation (Berner, 1996; Ebelman, 1845; Urey, 1952). Carbonate weathering is simply the reverse of equation B2. We only consider weathering by H_2CO_3, which is the primary weathering agent in basaltic settings (e.g., Gislason, 1996; Dessert et al., 2003) , but we note that other sources of acidity (i.e., HCl and H_2SO_4) can be important in different types of volcanic regions (e.g., Dessert et al., 2009; Hurwitz et al., 2010; Schopka et al., 2011). For simplicity, we also assume that the organic C sub-cycle is balanced. Therefore, the equation describing how the mass of C (M) in the atmosphere-ocean system changes with time (t) goes as:

$$\frac{dM}{dt} = F_{volc}^{tot} + F_{w,carb} - F_{b,carb} \quad \text{(B3)}$$

where F_{volc}^{tot} is the total volcanic C input flux, $F_{w,carb}$ is the C input flux from carbonate weathering, and $F_{b,carb}$ is the marine carbonate burial output flux. The term $F_{w,carb}$ represents the weathering of old sedimentary carbonate rocks. A term for surficial silicate weathering does not appear in equation B3 because in this model formulation of the long-term C cycle where the

ocean and atmosphere are combined into one reservoir, the reaction only transforms one form of C (CO_2) into another (HCO_3^-) (Kump and Arthur, 1999).

We subdivide F_{volc}^{tot} into two components:

$$F_{volc}^{tot} = F_{volc}^{CO_2} + F_{volc}^{HCO_3^-} , \quad \text{(B4)}$$

where $F_{volc}^{CO_2}$ is the volcanic C input flux as CO_2, and $F_{volc}^{HCO_3^-}$ is the volcanic C input flux as HCO_3^- after subsurface silicate weathering. Because HCO_3^- inputs and outputs must be in quasi-steady-state over the timescale of interest, we can write (Caves et al., 2016; Kump and Arthur, 1999):

$$F_{b,carb} = F_{riv}^{tot} , \quad \text{(B5)}$$

where F_{riv}^{tot} is the total riverine HCO_3^- input flux typically measured in chemical weathering studies. The term F_{riv}^{tot} includes contributions from silicate and carbonate weathering:

$$F_{riv}^{tot} = F_{w,sil}^{tot} + F_{w,carb} , \quad \text{(B6)}$$

where $F_{w,sil}^{tot}$ is the total contribution from silicate weathering. Because atmospheric CO_2 and ascending volcanic CO_2 within the subsurface can both weather silicate minerals to produce riverine HCO_3^-, $F_{w,sil}^{tot}$ can be expanded as:

$$F_{w,sil}^{tot} = F_{w,sil}^{sur} + F_{w,sil}^{sub} , \quad \text{(B7)}$$

where $F_{w,sil}^{sur}$ is the surficial silicate weathering component derived from atmospheric CO_2, and $F_{w,sil}^{sub}$ is the subsurface silicate weathering component derived from ascending volcanic CO_2, which is equivalent to $F_{volc}^{HCO_3^-}$. Submarine groundwater discharge can introduce weathering byproducts directly to the oceans (Basu et al., 2001; Rad et al., 2007; Schopka and Derry, 2012), but we limit our analysis to rivers, which are generally considered the primary conduits linking

terrestrial weathering and seawater geochemistry. After making substitutions and simplifying, $F_{w,carb}$ cancels, as expected for typical models describing the long-term C cycle. More importantly, however, the term $F_{volc}^{HCO_3^-}$ also cancels. The final expression is simply:

$$\frac{dM}{dt} = F_{volc}^{CO_2} - F_{w,sil}^{sur} \tag{B8}$$

The two volcanic input fluxes, $F_{volc}^{CO_2}$ and $F_{volc}^{HCO_3^-}$, are linked by mass-balance, as consistent with field evidence (Rivé et al., 2013), an increase in one must necessarily come at the expense of the other. Therefore, we can write:

$$F_{volc}^{CO_2} = (1-x)\cdot F_{volc}^{tot} \tag{B9}$$

and

$$F_{volc}^{HCO_3^-} = x \cdot F_{volc}^{tot}, \tag{B10}$$

where x ranges from 0 to 1. Changing the fraction of volcanic C introduced as HCO_3^- (x) indirectly drives variation in atmosphere-ocean C stores by altering $F_{volc}^{CO_2}$. This becomes more evident by substituting equation B9 into equation B10:

$$\frac{dM}{dt} = (1-x)F_{volc}^{tot} - F_{w,sil}^{sur}, \tag{B11}$$

which is equivalent to

$$\frac{dM}{dt} = F_{volc}^{tot} - F_{volc}^{HCO_3^-} - F_{w,sil}^{sur}. \tag{B12}$$